Magnetohydrodynamic Waves
and Instabilities
in Rotating Tokamak Plasmas

One of the most promising ways to achieve controlled nuclear fusion for the commercial production of energy is the tokamak design. In such a device, a hot plasma is confined in a toroidal geometry using magnetic fields. The present generation of tokamaks shows significant plasma rotation, primarily in the toroidal direction. This plasma flow has an important impact on stability and confinement, aspects of which can be described quite well by the theory of magnetohydrodynamics (MHD).

This work contains a comprehensive theoretical analysis, supported by numerical simulations, of the MHD equilibrium, waves, and instabilities of rotating tokamak plasmas. A new general description of the thermodynamic state of the equilibrium is presented. Next, a stability criterion is derived that generalizes various previous results by including toroidal rotation. This criterion shows that a radially decreasing rotation profile can be stabilizing. The previously unknown origin of this stabilization is shown to be the Coriolis effect, with a mediating role for the pressure. Various factors that affect stability also influence stable waves and eigenmodes of the plasma. New modes that are created by rotation are found, and the effect of rotation on a type of experimentally well-known modes is described.

Finally, the step to nonlinear magnetohydrodynamics is made by extending an existing reduced MHD code to the full viscoresistive MHD equations. This allows a study of the nonlinear evolution of the equilibria, waves, and instabilities described in this thesis.

J. W. Haverkort

Magnetohydrodynamic Waves and Instabilities in Rotating Tokamak Plasmas

PROEFSCHRIFT

ter verkrijging van de graad van doctor aan de Technische Universiteit Eindhoven, op gezag van de rector magnificus, prof.dr.ir. C.J. van Duijn, voor een commissie aangewezen door het College voor Promoties in het openbaar te verdedigen op donderdag 21 maart 2013 om 16.00 uur

door

Johannes Wilhelmus Haverkort

geboren te Ruhengeri, Rwanda

Dit proefschrift is goedgekeurd door de promotor:

prof.dr.ir. B.Koren

Copromotor:
dr. H.J. de Blank

Contents

Chapter 1

Introduction

1.1   Nuclear Fusion

When two atoms approach each other, there is a chance that their nuclei will fuse. The probability that this happens becomes appreciable when the atoms are stripped of their electrons and have a large enough momentum to overcome the repelling electrical force between the positively charged nuclei. In this case the nuclei can come close enough for the shorter ranged, but much stronger, nuclear force to bind the two firmly together. Their net binding energy becomes available in the form of kinetic energy.

For nuclei heavier than those of iron, energy can be gained by breaking them up into smaller pieces. For the very heavy nuclei of uranium we make use of this nuclear *fission* in present-day nuclear reactors. From nuclear *fusion* the largest energy gain occurs for the smallest nucleus, that of the hydrogen atom. In the sun, hydrogen nuclei fuse to form helium. A long-standing hope is to reproduce a similar process on Earth for the production of virtually limitless and in principle clean energy.

Increasing the temperature of a gas, the electrons and nuclei get separated and form a *plasma*. The number of fusion reactions initially increases dramatically with temperature. The challenge is to confine a plasma hot enough to produce fusion reactions for a long enough time to produce net energy.

1.2   Tokamaks

In the sun, plasma is confined by the gravitational force. On Earth, we can alternatively use magnetic forces. Driving a current through a cylinder-shaped plasma, the resulting magnetic field exerts an inward force that can be used to confine the plasma. As a solution to the problem of end losses, the ends can be bent together to form the geometry of a torus. In a torus there are two angular directions, the *toroidal* or 'long way around' and *poloidal* or 'short way around'. The main current and magnetic field

are in the toroidal direction. Very promising results were obtained with this *tokamak* design in the 1950s in the USSR.

Presently, a worldwide effort is underway to construct the ITER tokamak in Cadarache, France. The aim of this multi-billion euro project is to show the feasibility of gaining net energy from fusion.

Thermal energy leaks away at a rate proportional to the surface area, while it is produced at a rate proportional to the volume of the plasma. Therefore, larger tokamaks can confine heat better than smaller ones. When the energy produced in the fusion reaction is sufficient to balance the heat losses, ignition is achieved. This desirable state can be reached both by *minimizing the heat losses* and *optimizing the fusion reaction*.

The heat losses in a tokamak arise primarily through turbulent structures that convect heat outwards. These turbulent motions are driven by small-scale instabilities. Understanding these instabilities potentially provides the means to reduce the heat losses. An important breakthrough was the discovery of the high-confinement mode, or H-mode [201]. In this regime the turbulent transport at the plasma edge is significantly reduced. As a consequence, high temperature and pressure gradients arise. Later investigations showed that the reduction in turbulent transport is due to the shear in plasma flows near the edge. In this way, plasma flow plays an important role in achieving the goals of fusion research.

Optimizing the fusion reaction requires attaining higher plasma pressures. Higher pressures mean higher pressure gradients, especially near the edge of an H-mode plasma. These high pressure gradients can make the plasma unstable. Another important effort is therefore oriented towards understanding and controlling such instabilities so that higher pressures can be achieved.

This thesis primarily deals with plasma rotation and stability. As a primer, we take a look at a simplified formalism to investigate stability. This is not a substitute for a thorough self-consistent stability analysis, but more an a-posteriori way to interpret and understand the outcome of such analyses. It will introduce some of the concepts and terminology that are used in the subsequent outline of this thesis.

1.3 Stability

1.3.1 Simplified formalism

Consider a fluid, like a plasma, that is in *equilibrium*. Per unit volume, Newton's equation of motion for the position $\mathbf{r}$ of a fluid element reads

$$\rho \frac{d^2 \mathbf{r}}{dt^2} = \mathbf{f}, \tag{1.3.1}$$

with ρ and $\mathbf{f}$ the mass density and force density, respectively. Equilibrium implies that fluid elements do not accelerate so that $\mathbf{f} = 0$ everywhere.

Now we investigate the *linear stability* of this equilibrium by asking what will happen when we displace the fluid element over an infinitesimal distance in the x-direction. Generally, quantities such as density and temperature may vary in this direction. In equilibrium, the fluid element has the same value for these quantities as its surroundings. For a displaced fluid element, however, not all of these quantities may adjust instantaneously. We assume a single quantity α of the fluid element remains unchanged. Starting from a position x_0, the equation of motion at the new position x then reads

$$\rho \frac{d^2 x}{dt^2} = f_x(x) - f_x(x_0) \approx \frac{\partial f_x}{\partial \alpha} \frac{\partial \alpha}{\partial x} (x - x_0). \tag{1.3.2}$$

The force on the fluid element initially linearly increases with the deviation $x - x_0$ from its initial position. This force only arises when in the background fluid α varies with x. In this case the displaced element will have a different α than the fluid surrounding it. It will therefore not satisfy the force balance. Depending on the sign of the right-hand side of Eq. (1.3.2), the element experiences either a restoring force or a force that pushes it further away from its original position. This will result in an oscillation or an instability respectively. The solution of Eq. (1.3.2) is $x - x_0 \sim \exp{(-i\omega t)}$ with the oscillation frequency squared

$$\omega^2 = \frac{1}{\rho} \frac{\partial f_x}{\partial \alpha} \frac{\partial \alpha}{\partial x}. \tag{1.3.3}$$

The condition $\omega^2 \geq 0$ provides a *linear stability criterion*. When it is not satisfied, $i\omega$ gives the growth rate of the instability.

1.3.2 Gravity

Consider the displacement of an air parcel in the atmosphere. We assume incompressibility so that the parcel's density remains constant. With x the height coordinate, $\alpha = \rho$, and the gravitational force $f_x(\rho) = \rho g < 0$ we obtain

$$\omega^2 = \frac{g\rho'}{\rho}, \tag{1.3.4}$$

where a prime denotes a derivative with respect to x. This shows that when the density decreases with height x, the atmosphere will be linearly stable against what may be called the Rayleigh-Taylor instability.

Sometimes it is more accurate is to assume that the air parcel is displaced adiabatically, without exchanging heat with its environment. In this case the quantity $\alpha = p\rho^{-\gamma}$, which is related to the entropy, remains constant. Here γ is called the *adiabatic constant*. We can assume that the pressure p of the fluid element adjusts instantaneously to the new environment. In this case, using $f_x(\alpha, p)$, Eq. (1.3.3) gives the square of the so-called *Brunt-Väisälä-frequency*

$$\omega^2 = g \left(\frac{\rho'}{\rho} - \frac{p'}{\gamma p} \right). \tag{1.3.5}$$

Typically in our atmosphere $\omega^2 < 0$ and the resulting instability drives a level of vertical turbulence. When the profiles approach the so-called 'adiabatic lapse rate', for which $\omega = 0$, the turbulence decreases.

For a tokamak we also want to know what the 'effective gravities' and gradients are that drive the turbulence. Such understanding may help to reduce the level of turbulence and thereby increase the confinement. Several of the most important sources of tokamak turbulence have been identified. The description of these micro-instabilities typically requires more detail than the single-fluid model of *magnetohydrodynamics* used in this thesis. Magnetohydrodynamics often does serve as a first approximation for the description of larger-sized instabilities. It is also the preferred model to describe the force equilibrium in a tokamak.

1.3.3   Rotation

When a fluid rotates with an angular frequency Ω around an axis at a radial distance R, the centrifugal force is given by $f_R = \rho R \Omega^2$. In the absence of a magnetic field, the conserved angular momentum density is given by $\alpha = \rho R^2 \Omega$. For a constant density, Eq. (1.3.3) with $x = R$ now gives

$$\omega^2 = \frac{\left(R^4 \Omega^2\right)'}{R^3} = R \Omega^{2'} + 4\Omega^2, \tag{1.3.6}$$

which is the square of the so-called epicyclic frequency. In the presence of a magnetic field, a radially displaced fluid element rather conserves its angular frequency than its mechanical angular momentum. This can be attributed to the spring-like nature of the magnetic field. For an incompressible fluid, we obtain from Eq. (1.3.3) with $\alpha = \rho \Omega^2$

$$\omega^2 = \frac{R \left(\rho \Omega^2\right)'}{\rho} = R \left(\frac{\rho' \Omega^2}{\rho} + \Omega^{2'}\right). \tag{1.3.7}$$

The first part is the centrifugal analogue of the Rayleigh-Taylor instability associated with Eq. (1.3.4), while the second part is known from the magnetorotational instability. The realization that a magnetic field effectively removes the stabilizing final contribution of Eq. (1.3.6) led to a breakthrough in understanding the turbulence in astrophysical accretion disks [6].

1.3.4   Interchange instability

Even when the fluid does not move as a whole, the particles that make up the fluid do. They move with a velocity v proportional to the square root of the temperature. In a strong magnetic field, the particles spiral in small circles around the field lines. When the magnetic field is curved with radius of curvature R, they will therefore experience a centrifugal force density $\rho v^2 / R \sim p / R$. Here, we assumed that the product of the density and the temperature is proportional to the pressure p. When, furthermore, we

assume that the pressure remains constant during a radial displacement, Eq. (1.3.3) indicates instability when

$$p'/R < 0. \tag{1.3.8}$$

This shows that a plasma pressure that decreases in the direction of the radius of curvature of the magnetic field provides a source of instability. For the resulting *interchange instability*, different field lines will have to change places. Because of the large energy associated with bending the field lines, this interchange can only occur at locations where the field lines have similar directions.

In a cylindrical plasma, Eq. (1.3.8) will always hold when the pressure decreases radially. Luckily in a toroidal geometry the situation is a bit better. With R the major radial coordinate, p' will be negative at the outside of the torus. According to Eq. (1.3.8) this corresponds to *unfavorable curvature*. On the inside of the torus, however, p' will be positive, providing a stabilizing contribution. The net effect is stabilizing on average. The smaller poloidal magnetic field will, however, just like in a cylinder, always provide a destabilizing contribution. The toroidal magnetic field in a tokamak therefore has to be sufficiently strong to avoid the interchange instability.

Instabilities called 'ballooning modes' are localized primarily on the outside of the torus, where the curvature is unfavorable. In this way they can still become unstable due to pressure gradients.

1.4 This Thesis

1.4.1 Goal

The primary goal of this thesis is to understand the effect that toroidal rotation has on tokamak plasma equilibria, waves, and stability. Such understanding may contribute to the larger goal of achieving nuclear fusion for the production of energy.

This thesis addresses the research questions of how toroidal rotation influences:

1. *tokamak equilibria*. What is the most general description? What description is the most relevant?

2. *stability of such equilibria*. Can a regime be identified in which toroidal rotation positively influences stability?

3. *stable waves*. Is the existence or the frequency of known modes influenced? Are there perhaps new modes that can arise due to toroidal rotation?

Rotation primarily influences the plasma equilibrium through the centrifugal force, which can be described very well by magnetohydrodynamics. Also the most basic effects of rotation on waves and instabilities through the centrifugal force, Doppler shifts, and the Coriolis effect, are expected to be primarily magnetohydrodynamic in nature. Therefore the analyses and simulations in this thesis are limited to the

framework of magnetohydrodynamics. Most of the time, the plasma is considered to be an ideal dissipationless fluid. A final goal of this work however was:

4. *To implement the magnetohydrodynamic equations in a numerical model, including various sources of dissipation.*

1.4.2 Methods

A combination of mathematical analyses and numerical computation is used. Often a theoretical analysis is supported or illustrated by a simulation. This provides confidence but also shows the boundaries of validity of the analysis. Sometimes it is the other way around, when the results from a numerical computation spark a question, or require explanation.

Finally, substantial work was performed to extend an existing tokamak physics code that solves the full MHD equations. This code, while computationally demanding, makes it possible to do fully nonlinear simulations with an extended magnetohydrodynamic model, avoiding many of the approximations that are often made analytically and numerically.

1.4.3 Outline

As holds for the analysis of plasma stability, this thesis can be naturally divided into the following parts:

- *Equilibrium description:* chapter 2.

- *Linear analysis:* chapters 2-6.

    - *The continuous spectrum:* chapter 2.
    - *Stability:* chapters 3 and 4.
    - *Waves:* chapters 5 and 6.

- *Nonlinear development:* chapter 7.

In chapter 2, tokamak equilibria including toroidal rotation are discussed. An adiabatic constant of the equilibrium is introduced that can be different from the adiabatic constant of the dynamics. In the presence of toroidal rotation in a tokamak this leads to oscillations with a Brunt-Väisälä-like frequency. Explicit expressions for this frequency are derived that are successfully compared with numerical simulations. The new equilibrium description in terms of an 'equilibrium adiabatic constant' will be used throughout this thesis.

In chapter 3, a linear stability criterion for interchange instabilities is derived, including the effects of toroidal rotation. The stabilizing Brunt-Väisälä effect, the destabilizing centrifugal Rayleigh-Taylor effect, and the magnetorotational effect all appear

in this comprehensive new stability criterion. It also contains a term that could not be interpreted in terms of known instabilities. The physical origin of this term is analyzed in chapter 4 and is revealed as a Coriolis-pressure effect.

The same mechanisms that play a role in plasma stability can sometimes also lead to stable waves. New low-frequency waves induced by toroidal rotation are described in chapter 5. The influence of toroidal rotation on a certain type of well-known plasma waves, reversed shear Alfvén eigenmodes, is analyzed in chapter 6.

Finally, chapter 7 describes the implementation of the full MHD equations into an existing nonlinear code that was based on reduced MHD equations. This numerical tool can be used to investigate whether a linear instability saturates at a certain amplitude or will contribute to the loss of energy from the plasma.

Chapters 2-6 are adapted from published journal articles. At the time of writing, chapter 7 was in preparation for submission as a journal publication. Redundancies have been removed, the notation has been streamlined, and cross-references between the chapters were added. With respect to the content, the deviations from the respective papers is fairly limited. An appendix with new material was added to chapter 5. Also, where this was not already the case, results were generalized to hold for arbitrary values of the 'equilibrium adiabatic constant'.

Chapter 2

The Brunt-Väisälä Frequency of Rotating Tokamak Plasmas

The continuous spectrum of analytical toroidally rotating magnetically confined plasma equilibria is investigated analytically and numerically. In the presence of purely toroidal flow, the ideal magnetohydrodynamic equations leave the freedom to specify which thermodynamic quantity is constant on the magnetic surfaces. Introducing a general parameterization of this quantity, analytical equilibrium solutions are derived that still posses this freedom. These equilibria and their spectral properties are shown to be ideally suited for testing numerical equilibrium and stability codes including toroidal rotation. Analytical expressions are derived for the low-frequency continuous Alfvén spectrum. These expressions still allow us to choose which quantity is constant on the magnetic surfaces of the equilibrium, thereby generalizing previous results. The centrifugal convective effect is shown to modify the lowest Alfvén continuum branch to a buoyancy frequency, or Brunt-Väisälä frequency. A comparison with numerical results for the case that respectively the specific entropy, the temperature, or the density is constant on the magnetic surfaces yields excellent agreement, showing the usefulness of the derived expressions for the validation of numerical codes.

2.1 Introduction

One of the very few viable ways to confine a plasma at the high temperatures required for nuclear fusion, is using magnetic fields. Arguably the most promising design suitable for the commercial production of energy is the tokamak, in which the plasma is confined in the shape of a torus. A tokamak force equilibrium can be described quite well by a balance between the pressure gradient, the Lorentz force, and centrifugal forces. This force balance can be described by the fluid model of magnetohydrodynamics (MHD). Assuming axisymmetry, the static MHD equations can be reduced to a single partial differential equation, called the Grad-Shafranov equation [77, 169]. The solution ψ is a stream function for the poloidal magnetic field, and can be used as a coordinate that labels the magnetic surfaces.

Given the dependence of the pressure and the toroidal magnetic field on ψ, the solution of the Grad-Shafranov equation gives ψ as a function of the spatial coordinates, completing the description of the equilibrium. Assuming this dependence to be linear, a simple polynomial solution was obtained by Solov'ev [173]. Incidentally, this solution is identical to Hill's solution for the Stokes stream function of a spherical vortex [103], which long preceded the conception of the idea of a tokamak in the 1950's. Solutions expressed in special mathematical functions were also found for a quadratic dependence [142, 102, 82] and a mixed linear and quadratic dependence [177, 129, 144, 212]. The most general linear solution is obtained in Refs. [164, 4]. More exotic dependencies yielding analytical solutions are considered in Refs. [186] and [124]. Convenient homogeneous solutions are provided in Refs. [222, 26].

In the presence of toroidal rotation, we additionally have to specify how the angular rotation frequency depends on ψ. Assuming that the ratio between the angular frequency squared and the temperature is constant and that the magnetic surfaces have constant temperature or specific entropy, analytical solutions were found for a linear [143] or a mixed linear and quadratic dependence [182] of the pressure and the toroidal magnetic field on ψ. For isothermal magnetic surfaces, solutions for a quadratic or mixed dependence were already obtained in Refs. [39, 148], or in spherical coordinates in Ref. [197]. For more general flows, solutions have been found assuming plasma incompressibility, see for example Refs. [183, 181].

All existing analytical equilibrium solutions including toroidal flow, make an assumption on which quantity is constant on the magnetic surfaces. In the present work, we assume a general parameterization of this quantity from the outset. The freedom of this choice is retained in the equilibrium equation and the subsequently derived class of analytical solutions. These analytical solutions are generalizations of those of Ref. [143] and without rotation reduce to the polynomial Solov'ev solution [173]. For numerical stability calculations, an accurate numerical representation of the equilibrium is required. In order to test the accuracy of the equilibrium solver, the Solov'ev solution is frequently used [65, 167, 136, 120, 118].

Various equilibrium codes that include toroidal rotation exist. Most of these codes assume isothermal magnetic surfaces [121, 133, 122, 41, 193, 141, 159] while some as-

sume flux surfaces of constant density [53, 194]. The equilibrium code FINESSE [8] allows in case of purely toroidal flow the freedom to choose either the temperature, the density, or the specific entropy to be constant within the magnetic surfaces [14]. Only rarely, analytical solutions have been used to test an equilibrium code including toroidal flow [141]. In the present work we will use the derived analytical solutions, to test the convergence behaviour of FINESSE.

The Solov'ev equilibrium solution [173] is also frequently used for stability calculations as a standardized reference equilibrium [136, 120, 10, 79, 165]. For stability calculations including toroidal flow, less well-defined reference test cases are generally used to benchmark numerical codes. Again, the derived analytical solutions would be ideally suited to serve as a standardized reference equilibrium including rotation.

Also in the analytical stability calculations in this work, the freedom to specify which quantity is constant on the magnetic surfaces of the equilibrium is retained. An analytical expression is derived for the low-frequency continuous Alfvén spectrum of a large aspect ratio tokamak plasma, including the effects of compressibility and toroidal rotation. This expression still allows for the choice of which quantity is constant on the magnetic surfaces of the equilibrium, and as such generalizes the results of Refs. [189, 211, 210, 204] for isothermal flux surfaces and the recent result of Ref. [131] for magnetic surfaces of constant density.

The lowest-frequency branch of the derived expression is shown to be equal to the Brunt-Väisälä-frequency associated with the centrifugal convective effect. For a tokamak plasma with magnetic surfaces of constant density, the convective instability destabilizes the continuous spectrum. Simulations show how instability spreads from a localized part of the tokamak to include almost the entire plasma for 'sonic' rotational velocities. For a tokamak with isothermal magnetic surfaces, rotation induces a gap in the continuous spectrum. Good correspondence between the continuum frequencies from numerical simulations and the derived analytical expression is obtained, showing its usefulness for the validation of stability codes.

2.2 Magnetohydrodynamic Equilibria

In this section we will introduce the considered geometry, notation, and basic equations that will be used in the rest of this thesis. Although this work primarily deals with toroidal rotation, in order to provide some context and introduce concepts that will arise in the stability analyses, Section 2.2.3 is devoted to more general equilibrium flows.

2.2.1 Equations

We depart from the ideal magnetohydrodynamic (MHD) equations. These consist of the conservation equations for momentum, mass, and energy

$$\rho\frac{\partial \mathbf{u}}{\partial t} + \rho\mathbf{u}\cdot\nabla\mathbf{u} + \nabla p - \mathbf{J}\times\mathbf{B} = 0, \tag{2.2.1a}$$

$$\frac{\partial \rho}{\partial t} + \nabla\cdot(\rho\mathbf{u}) = 0, \tag{2.2.1b}$$

$$\frac{\partial S}{\partial t} + \mathbf{u}\cdot\nabla S = 0, \tag{2.2.1c}$$

together with the reduced Maxwell equations

$$\nabla\times\mathbf{E} = -\partial\mathbf{B}/\partial t, \tag{2.2.1d}$$

$$\nabla\times\mathbf{B} = \mathbf{J}, \tag{2.2.1e}$$

$$\nabla\cdot\mathbf{B} = 0, \tag{2.2.1f}$$

and Ohm's law for ideally conducting moving media

$$\mathbf{E} = -\mathbf{u}\times\mathbf{B}, \tag{2.2.1g}$$

for the velocity $\mathbf{u}$, magnetic field $\mathbf{B}$, current density $\mathbf{J}$, pressure p, and density ρ. The quantity $S \equiv p\rho^{-\gamma}$ is a monotonic function of the specific entropy, the entropy per unit mass [70]. The electric field $\mathbf{E}$ is actually an auxiliary quantity that can be left out of the formulation by replacing Eqs. (2.2.1d) and (2.2.1g) by $\nabla\times(\mathbf{u}\times\mathbf{B}) = \partial\mathbf{B}/\partial t$. In ideal MHD the same holds for $\mathbf{J}$, which can be left out of the formulation by inserting Eq. (2.2.1e) for $\mathbf{J}$ into Eq. (2.2.1a) to give

$$\rho\frac{\partial \mathbf{u}}{\partial t} + \rho\mathbf{u}\cdot\nabla\mathbf{u} + \nabla p - (\nabla\times\mathbf{B})\times\mathbf{B} = 0, \tag{2.2.2a}$$

$$\frac{\partial \rho}{\partial t} + \nabla\cdot(\rho\mathbf{u}) = 0, \tag{2.2.2b}$$

$$\frac{\partial S}{\partial t} + \mathbf{u}\cdot\nabla S = 0, \tag{2.2.2c}$$

$$\frac{\partial \mathbf{B}}{\partial t} - \nabla\times(\mathbf{u}\times\mathbf{B}) = 0, \tag{2.2.2d}$$

$$\nabla\cdot\mathbf{B} = 0. \tag{2.2.2e}$$

The stationary ideal MHD equations then follow using $\partial/\partial t = 0$. Note that the vacuum magnetic permeability μ_0 does not appear explicitly, because it can be scaled out of the equations by a proper dimensionalization of the physical variables. The energy equation (2.2.2c) is often referred to as the adiabatic equation of state, since it states that S is constant along the flow.
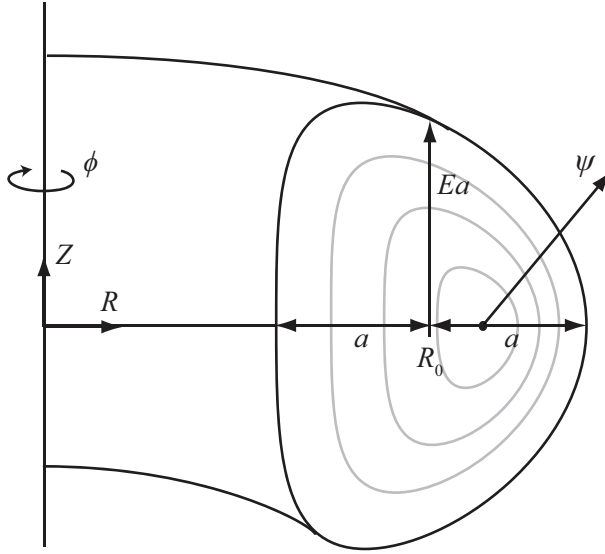
Figure 2.1:   A schematic overview of the tokamak geometry including the major radius R_0, minor radius $a = \epsilon R_0$, giving an inverse aspect ratio $\epsilon \equiv a/R_0$. In the used coordinate system (R, Z, ϕ), the direction of ϕ differs from that of the cylindrical coordinate system (R, ϕ, Z). Note that the magnetic axis, where the poloidal magnetic flux ψ has a minimum, differs from the geometrical axis at $R = R_0$ by a Shafranov shift. Note also that the ellipticity E here differs from the commonly used definition.

2.2.2   Toroidal flow

Extended Grad-Shafranov equation

We will use the coordinate system (R, Z, ϕ) shown in Fig. 2.1, commonly used for toroidal problems. This coordinate system differs from the usual cylindrical coordinate system in the direction of ϕ. We will assume axisymmetry around the Z-axis, making the toroidal angle ϕ an ignorable coordinate. Unit vectors will be denoted with a sub-scripted $\hat{\mathbf{e}}$ or using a hat. When the flow is purely toroidal $\mathbf{u} = R\Omega\hat{\mathbf{e}}_\phi$, with Ω the angular rotation frequency, the non-linear term in Eq. (2.2.2a) represents the centrifugal force density

$$-\rho\mathbf{u} \cdot \nabla\mathbf{u} = \rho\Omega^2\mathbf{R}, \tag{2.2.3}$$

where $\mathbf{R} = R\nabla R$. For purely toroidal flow, that is without flow in the poloidal plane, the stationary versions of the continuity equation (2.2.2b) and energy equation (2.2.2c) are trivially satisfied due to axisymmetry. In order to further reduce the resulting equations, we split the magnetic field and current density in a toroidal and poloidal

part as follows

$$\mathbf{B} = \nabla\phi \times \nabla\psi + F\nabla\phi, \tag{2.2.4a}$$

$$\mathbf{J} = \nabla F \times \nabla\phi + \Delta^*\psi\nabla\phi, \tag{2.2.4b}$$

where $\nabla\phi = \hat{\mathbf{e}}_\phi/R$. Here ψ and $F \equiv RB_\phi$ are stream functions of the poloidal part of $\mathbf{B}$ and $\mathbf{J}$ respectively. For $F = 0$, Eq. (2.2.4a) would describe the magnetic field of a point dipole. Because $\mathbf{B} \cdot \nabla\psi = 0$, the magnetic field lies within surfaces of constant ψ, which can therefore be used to label the magnetic surfaces as indicated in Fig. 2.1. The quantity ψ can be seen to be proportional to the poloidal magnetic flux, by integrating Eq. (2.2.4a) over an axisymmetric strip S of width $\Delta\psi$. Using $\nabla\phi \times \nabla\psi = -\nabla \times (\psi\nabla\phi)$ and Green's theorem we obtain for the poloidal magnetic flux

$$\int_S \mathbf{B} \cdot d\mathbf{S} = \int_S \nabla\phi \times \nabla\psi \cdot d\mathbf{S} = \oint_{\partial S} \psi\nabla\phi \cdot d\mathbf{l} = 2\pi\Delta\psi. \tag{2.2.5}$$

The toroidal current density $J_\phi = \Delta^*\psi/R$ in Eq. (2.2.4b) is expressed in terms of the elliptic Grad-Shafranov operator defined by

$$\Delta^*\psi \equiv R^2\nabla \cdot \left(R^{-2}\nabla\psi \right) = R\frac{\partial}{\partial R}\left(\frac{1}{R}\frac{\partial\psi}{\partial R} \right) + \frac{\partial^2\psi}{\partial Z^2}, \tag{2.2.6}$$

to ensure that Ampère's law, Eq. (2.2.1e), is satisfied. Using again $\nabla\phi \times \nabla\psi = -\nabla \times (\psi\nabla\phi)$ and axisymmetry, Equation (2.2.4a) for $\mathbf{B}$ manifestly satisfies Eq. (2.2.2e), $\nabla \cdot \mathbf{B} = 0$. Equation (2.2.1g), together with Eq. (2.2.4a), yields

$$\mathbf{E} = \Omega\nabla\psi, \tag{2.2.7}$$

so that $\nabla \times \mathbf{E}$ is automatically satisfied when Ω is a function of ψ only. Quantities like Ω that depend only on the poloidal flux ψ are often called *flux functions*, or surface functions.

   With the above formulation, the only equilibrium equation that is not yet automatically satisfied is the momentum equation. A toroidal projection of Eq. (2.2.2a) with $\partial/\partial t = 0$ leads to the observation that the Lorentz force $\mathbf{J} \times \mathbf{B}$ has no toroidal component. Inserting the expressions of Eqs. (2.2.4a) and (2.2.4b) yields $(\mathbf{J} \times \mathbf{B})_\phi = \nabla\psi \cdot (\nabla F \times \nabla\phi) = 0$, so that $F = F(\psi)$ is a flux function. A second projection of the momentum equation, parallel to the poloidal magnetic field, yields

$$\left.\frac{\partial p}{\partial R}\right|_\psi = \rho R\Omega^2, \tag{2.2.8}$$

showing that the centrifugal force will be balanced exclusively by pressure gradients within the magnetic surfaces of constant ψ. A final projection of Eq. (2.2.2a) in the direction of $\nabla\psi$ gives the extended Grad-Shafranov equation [143]

$$\Delta^*\psi = -\frac{d\frac{1}{2}F^2}{d\psi} - R^2\left.\frac{\partial p}{\partial\psi}\right|_R, \tag{2.2.9}$$

which is the final equation for ideal axisymmetric equilibria with purely toroidal flow. Provided expressions for F and p are given, this elliptic equation (2.2.9) can be solved either numerically or analytically for ψ. The difference between Eq. (2.2.9) and the ordinary Grad-Shafranov equation for static equilibria is that the last term contains a partial derivative, because the pressure has to satisfy the additional equation (2.2.8). For static equilibria, the momentum equation $\nabla p = \mathbf{J} \times \mathbf{B}$ ensures $\mathbf{B} \cdot \nabla p = 0$ so that $p = p(\psi)$.

Solving for the pressure analytically

To solve Eq. (2.2.9) we need an expression for the pressure, satisfying Eq. (2.2.8). We will introduce the following general parameterization that satisfies this equation

$$p = p_0(\psi) \left(1 + \frac{\bar{R}^2 \mathcal{M}^2(\psi)}{\zeta(\psi)} \right)^{\zeta(\psi)}, \qquad (2.2.10)$$

$$\rho = \rho_0(\psi) \left(1 + \frac{\bar{R}^2 \mathcal{M}^2(\psi)}{\zeta(\psi)} \right)^{\zeta(\psi)-1}, \qquad (2.2.11)$$

where $\bar{R}^2 \equiv \left(R^2 - R_0^2 \right) / R_0^2$ and $\mathcal{M}^2(\psi) \equiv \rho_0 R_0^2 \Omega^2 / 2 p_0$. The parameter $\zeta(\psi)$ is an arbitrary non-zero flux function.

We have the freedom of specifying an arbitrary equation of state, for which we choose the ideal gas law

$$p = \rho T, \qquad (2.2.12)$$

where a constant of proportionality is absorbed in the definition of the temperature T. With Eqs. (2.2.10) and (2.2.11), the temperature can now be written as

$$T = T_0(\psi) \left(1 + \frac{\bar{R}^2 \mathcal{M}^2(\psi)}{\zeta(\psi)} \right), \qquad (2.2.13)$$

where $T_0(\psi) = p_0/\rho_0$, so that $\mathcal{M}^2(\psi) = R_0^2 \Omega^2 / 2 T_0$.

Note from Eqs. (2.2.10) and (2.2.11) that, with $\gamma_e \equiv \zeta / (\zeta - 1)$, the following quantity is a flux function

$$A(\psi) \equiv p\rho^{-\gamma_e} = p_0 \rho_0^{-\gamma_e}. \qquad (2.2.14)$$

For different ζ, or equivalently different γ_e, various physical variables can be assumed to be constant on the magnetic surfaces. In particular

$$A(\psi) = \begin{cases} \rho(\psi) & \text{for } \gamma_e \to \infty & (\zeta \to 1). \\ T(\psi) & \text{for } \gamma_e \to 1 & (\zeta \to \infty). \\ S(\psi) & \text{for } \gamma_e = \gamma & (\zeta = \gamma/(\gamma-1)). \end{cases} \qquad (2.2.15)$$

In the case of purely toroidal flow we thus find that in addition to $p_0(\psi)$, $F(\psi)$, and $\mathcal{M}(\psi)$, there is a fourth flux function $A(\psi)$, or alternatively $\zeta(\psi)$ or $\gamma_e(\psi)$, that directly influences the equilibrium solution $\psi(R, Z)$. Equation (2.2.10) for the pressure can

now be inserted into the extended Grad-Shafranov equation (2.2.9) which can then be solved separately. Note that in the limit $\zeta \to \infty$, the factor $\left(1 + \bar{R}^2 \mathcal{M}^2/\zeta\right)^\zeta$ becomes $\exp\left(\mathcal{M}^2 \bar{R}^2\right)$.

2.2.3 General equilibrium flow

Although this thesis deals primarily with the effect of toroidal equilibrium flow, selected aspects associated with poloidal flow are considered in this section. For general equilibrium flows we have to solve an algebraic (Bernoulli) equation for the density and a generalized Grad-Shafranov equation simultaneously [87]. Here, we will only discuss the effect of poloidal flow on the freedom to choose $\zeta(\psi)$ arbitrarily. In Section 2.2.3 we will finally consider an aspect of motion along the magnetic field lines that will play a role in later sections.

Poloidal flow

From Eq. (2.2.2d) it follows with $\partial/\partial t = 0$ that $\mathbf{u} \cdot \nabla \psi = 0$, implying that equilibrium plasma flow will always be within the magnetic surfaces only [220, 87]. Apart from the toroidal rotation investigated in this thesis, plasma can also rotate poloidally. The stationary versions of Eqs. (2.2.2d) and (2.2.2b) are still satisfied when a flow $\Phi(\psi)\mathbf{B}/\rho$ is added to $\mathbf{u}$ so that

$$\mathbf{u} = \frac{\Phi(\psi)}{\rho}\mathbf{B} + R\Omega(\psi)\hat{\mathbf{e}}_\phi. \tag{2.2.16}$$

Note that for non-zero Φ, Eq. (2.2.2c) requires that $\mathbf{B} \cdot \nabla S = 0$ so that the specific entropy is a flux function. This implies that γ_e in Eq. (2.2.14) can no longer be chosen arbitrarily, but assumes the value $\gamma_e = \gamma$.

When heat conduction parallel to the field lines is faster than the plasma rotates poloidally, parallel heat exchange may ensure temperature equilibration of the magnetic surfaces. For small poloidal flow velocities, the stationary adiabatic energy equation $\mathbf{u} \cdot \nabla S = 0$ may therefore be replaced by the isothermal equation $\mathbf{u} \cdot \nabla T = 0$. For the description of faster phenomena like waves and instabilities, the adiabatic equation is often more appropriate. We note that the use of these two different energy equations is equivalent to using the same energy equation, with different adiabatic constants. This is nicely facilitated by the introduction of the 'adiabatic constant' γ_e of the equilibrium, separate from the adiabatic constant γ.

Whether the flux surfaces in a tokamak will tend to be isentropic so that $\gamma_e = \gamma$, isothermal so that $\gamma_e \to 1$, or something else, will therefore depend on the strength of the mechanism that drives poloidal rotation compared to the magnitude of the parallel heat conductivity. It has even been argued [5] that an assumption of incompressible equilibrium flow may be justified for tokamak experiments. Incompressibility entails that $\nabla \cdot \mathbf{u} = 0$ so that ρ is constant on magnetic surfaces and $\gamma_e \to \infty$. The most appropriate value for γ_e depends on the specific situation under consideration and γ_e may even assume different values on different magnetic surfaces. Not unlike the way

$p_0(\psi)$ and $F(\psi)$ can be chosen to model experimentally measured profiles, $\gamma_e(\psi)$ can be specified according to experimental observations and modeling outside MHD.

Pfirsch-Schlüter factor

The amount of equilibrium flow parallel to the field lines is given by Eq. (2.2.16) as $u_{\parallel} \equiv \mathbf{B} \cdot \mathbf{u}/B = \Phi B/\rho + R\Omega B_{\phi}/B$, which is not a flux function. For a tokamak with a large aspect ratio and circular flux surfaces, using Shafranov-shifted polar coordinates (r, θ), the flux-surface-average amount of parallel flow is related to the poloidal flow u_{θ} and toroidal flow u_{ϕ} by [218]

$$\left\langle Bu_{\parallel} \right\rangle = \left\langle B_{\theta}u_{\theta} \right\rangle (1 + 2q^2) + \left\langle B_{\phi}u_{\phi} \right\rangle, \tag{2.2.17}$$

where $q = rB_{\phi}/RB_{\theta}$ is the safety factor, introduced in Section 2.3.3. An assumption used in the derivation of Eq. (2.2.17) is that $\Phi(\psi)/\rho$ is a flux function, which only holds for low flow velocities for which $\rho = \rho_0(\psi)$.

From Eq. (2.2.17) we see that the poloidal flow velocity u_{θ} comes with an unexpected additional factor $1 + 2q^2$, called the Pfirsch-Schlüter inertial enhancement factor. This can be understood from Eq. (2.2.16) by noticing that for plasma to flow in the poloidal direction, it has to move along the magnetic field and then move back toroidally to return to its original poloidal plane. This excursion creates an additional effective inertia for motion in the poloidal direction.

2.3 Analytical Equilibria with Toroidal Flow

The extended Grad-Shafranov equation introduced in the previous section will in this section be solved analytically under simplifying assumptions. To increase the versatility of the analytical solutions obtained in this way, we discuss various homogeneous solutions that may be added. Expressions for equilibrium properties like the Mach number, plasma beta, and the safety factor are subsequently derived, allowing control over the characteristics of the solutions. Finally, alternative analytical solutions are considered.

2.3.1 Derivation

Inserting Eq. (2.2.10) for the pressure into the extended Grad-Shafranov equation (2.2.9), we obtain

$$\Delta^{*}\psi = -\frac{d\frac{1}{2}F^2}{d\psi} - R^2 \frac{\partial}{\partial \psi} \left[p_0(\psi) \left(1 + \frac{\left(R^2 - R_0^2\right)\Omega^2(\psi)}{2\zeta(\psi)T_0(\psi)} \right)^{\zeta(\psi)} \right]. \tag{2.3.1}$$

In order to arrive at an analytical solution, we assume $\zeta(\psi) = \zeta$ to be constant and

$$\frac{d\frac{1}{2}F^2}{d\psi} = J, \quad \frac{dp_0}{d\psi} = P, \quad \frac{R_0^2 \Omega^2(\psi)}{2T_0(\psi)} = \mathcal{M}^2, \tag{2.3.2}$$

with J, P, and $\mathcal{M}^2$ constants. Inserting these assumptions into Eq. (2.3.1) gives

$$R\frac{\partial}{\partial R}\left(\frac{1}{R}\frac{\partial\psi}{\partial R}\right) + \frac{\partial^2\psi}{\partial Z^2} = -J - R^2 P\left(1 + \frac{\bar{R}^2\mathcal{M}^2}{\zeta}\right)^{\zeta}. \tag{2.3.3}$$

This linear partial differential equation is solved by

$$\begin{aligned}
\psi = & c_0 + c_1 P R_0^2 R^2 + c_2 P R^2 \left(Z^2 - \frac{R^2}{4}\right) - \frac{JZ^2}{2} \\
& - \frac{P R_0^4 \zeta^2}{4\mathcal{M}^2} \frac{\left(1 + \bar{R}^2\mathcal{M}^2/\zeta\right)^{\zeta+2} - \left(1 + (\zeta+2)\,\bar{R}^2\mathcal{M}^2/\zeta\right)}{(\zeta+1)\,(\zeta+2)},
\end{aligned} \tag{2.3.4}$$

where the first three terms represent a homogeneous solution and the last two terms form the particular solution. Other solutions that produce the inhomogeneous term $-J$ in Eq. (2.3.3) exist, but $-JZ^2/2$ is the most simple one.

The second term in the numerator of the last term is added to ensure that the solution behaves well in the limit $\mathcal{M} \to 0$. This term is actually a homogeneous solution that may be added or removed freely because it vanishes under the operation of Δ^*. For $\mathcal{M} = 0$, the last term of Eq. (2.3.4) becomes $-P\left(R^2 - R_0^2\right)^2/8$ so that the solution becomes equal to the well-known polynomial Solov'ev solution [173].

When the plasma flow is purely toroidal, we have the freedom to choose an arbitrary non-zero value for ζ. Using $\exp x \equiv \lim_{n\to\infty}\left(1 + x/n\right)^n$, the last term of Eq. (2.3.4) becomes in the limit $\zeta \to \infty$

$$-\frac{P R_0^4}{4\mathcal{M}^2}\left(e^{\bar{R}^2\mathcal{M}^2} - \left(1 + \bar{R}^2\mathcal{M}^2\right)\right). \tag{2.3.5}$$

The solutions for $\zeta \to \infty$ and $\zeta = \gamma/(\gamma-1)$, that is with the temperature and the specific entropy constant on magnetic surfaces respectively, were previously obtained in Ref. [143].

2.3.2   Vacuum solutions

The first three terms of the solution given by Eq. (2.3.4) satisfy the vacuum equation $\Delta^*\psi_v = 0$ so that they may be referred to as 'vacuum solutions'. An arbitrary number of vacuum solutions ψ_v can be added to Eq. (2.3.4), providing additional control over the characteristics of the solution. The poloidal magnetic flux associated with these vacuum solutions may be thought of as originating from external magnetic field coils.

Using separation of variables, $\Delta^* \psi_v = 0$ is solved by $\psi_v = f(R)g(Z)$ when $\Delta^* f = kf$ and $\Delta^* g = -kg$. The first of these equations is Bessel's equation for f/R while the second is the harmonic equation. A general separable vacuum solution can therefore be expressed as

$$\psi_v = R \sum_n \cos(k_n Z) \left[a_n J_1(k_n R) + b_n Y_1(k_n R) \right], \tag{2.3.6}$$

with k_n, a_n, and b_n free constants and J_1 and Y_1 the first order Bessel functions of the first and second kind, respectively. We choose to look at up-down symmetric solutions only, which is why in Eq. (2.3.6) only cosines were used.

Perhaps more convenient is to use a solution consisting only of polynomials [182]

$$\psi_v = R^2 \sum_{n=0}^{n_{max}} a_n \sum_{m=0}^{n} \frac{(-1)^m (R/2)^{2(n-m)} Z^{2m}}{(n-m)! (n-m+1)! (2m)!}. \tag{2.3.7}$$

The first two terms are the second and third term of Eq. (2.3.4). The third term from Eq. (2.3.7) is proportional to $R^2 \left(R^4 - 12R^2 Z^2 + 8Z^4 \right)$. An alternative non-polynomial third vacuum term is given by [222]

$$\psi_v = c_3 \left(R^2 \ln R - Z^2 \right). \tag{2.3.8}$$

2.3.3 Controlling the characteristics of the solution

Shape

The free constants c_1 and c_2 of the solution of Eq. (2.3.4) can be used to specify the aspect ratio $\epsilon^{-1} \equiv R_0/a$ and the ellipticity E of the solution shown in Fig. 2.1. When the vacuum solution of Eq. (2.3.8) is added to Eq. (2.3.4), the third free constant c_3 can be used to tune the triangularity of the plasma cross-section. To ensure a tokamak configuration, at $Z = 0$ the outermost flux surface of the plasma should go through both $R = R_0 - a$ and $R = R_0 + a$, that is $\psi_\epsilon(c_1, c_2) \equiv \psi(R_0 + a, 0) - \psi(R_0 - a, 0)$ should vanish. The value of c_1 required to ensure $\psi_\epsilon = 0$ can be obtained from

$$c_1 = \frac{-\psi_\epsilon(c_1 = 0)}{\psi_\epsilon(c_1 = 1) - \psi_\epsilon(c_1 = 0)}. \tag{2.3.9a}$$

To ensure a certain ellipticity E, defined in Fig. 2.1, we demand that at $R = R_0$ this outermost flux surface additionally goes through $Z = Ea$ and $Z = -Ea$. Because the solution of Eq. (2.3.4) only contains even powers of Z, it is top-down symmetric so that when a flux surface goes through one of these points, it automatically goes through the other point. An ellipticity E can therefore be assured by requiring that $\psi_E(c_1, c_2) \equiv \psi(R_0, Ea) - \psi(R_0 + a, 0)$ vanishes so that

$$c_2 = \frac{-\psi_E(c_2 = 0)}{\psi_E(c_2 = 1) - \psi_E(c_2 = 0)}. \tag{2.3.9b}$$

For evaluating both (2.3.9a) and (2.3.9b), the value of the other coefficient c_1 or c_2 is required. It is therefore necessary to evaluate these self-consistently, or evaluate one analytically. The other coefficient can then be calculated either analytically as well, or numerically. Calculating c_1 from Eqs. (2.3.9a) and (2.3.4) gives

$$c_1 = \frac{1}{2} \frac{R_0^2 + a^2}{R_0^2} c_2 + \frac{R_0}{16a\mathcal{M}^4} \left(f(a) - f(-a)\right) - \frac{1}{4\mathcal{M}^2} \frac{\zeta}{1 + \zeta}, \tag{2.3.10}$$

where

$$f(\alpha) = \frac{\zeta^2}{(\zeta + 1)(\zeta + 2)} \left(1 + \frac{(R_0 + \alpha)^2}{R_0^2} \frac{\mathcal{M}^2}{\zeta}\right)^{\zeta + 2}. \tag{2.3.11}$$

In the limit $\zeta \to \infty$, this becomes $f(\alpha) = \exp\left(\frac{(R_0 + \alpha)^2}{R_0^2} \mathcal{M}^2\right)$. Substituting Eq. (2.3.10) into Eq. (2.3.9b) gives

$$c_2 = \frac{\frac{J}{P} \frac{(aE)^2}{2} + \frac{R_0^4}{4\mathcal{M}^4} \left(\frac{f(a) - f(-a)}{2} \left(1 + \frac{a}{2R_0}\right) + f(0) - f(a)\right)}{a^2 R_0^2 \left(1 - \left(\frac{a}{2R_0}\right)^2 + E^2\right)}. \tag{2.3.12}$$

With this result inserted into Eq. (2.3.10) we have the closed form expressions for c_1 and c_2 ensuring a closed flux surface through $(R_0 \pm a, 0)$ and $(0, \pm Ea)$. To make the expressions dimensionless one we may choose either $R_0 = 1$ and $a = \epsilon$, or $R_0 = \epsilon^{-1}$ and $a = 1$. To control the triangularity we can add another vacuum solution proportional to c_3, for example Eq. (2.3.8), and follow the same procedure as outlined above to find c_3. Note that this does introduce additional terms in the above expressions for c_1 and c_2.

The Mach number

The assumptions of Eq. (2.3.2) impose restrictions on the kind of equilibria that the analytical solution can describe. The function F is usually approximately constant for tokamaks, with poloidal currents creating a small 'diamagnetic dip' that can be described quite well with F^2 a linear function of ψ. For a large aspect ratio tokamak plasma, the poloidal flux function ψ is an approximately quadratic function of the distance to the magnetic axis, implying that a function linear in ψ can describe approximately parabolic profiles. The second assumption of Eq. (2.3.2) therefore restricts the pressure profile to be approximately parabolic, which may be too smooth to describe certain tokamak regimes. The third assumption states that the angular frequency is proportional to the square root of T_0. This assumption has an interesting implication for the Mach number $M \equiv R\Omega/\sqrt{\gamma T} = (R/R_0)\mathcal{M}\sqrt{2T_0/\gamma T}$ which, using Eqs. (2.2.10) and (2.2.11), can be written as

$$M = \frac{R}{R_0} \frac{\sqrt{2/\gamma}\mathcal{M}}{\sqrt{1 + \bar{R}^2 \mathcal{M}^2/\zeta}}. \tag{2.3.13}$$

Note that for constant $\mathcal{M}$ the Mach number depends only on R. The denominator of Eq. (2.3.13) places a limit on the maximum Mach number that can be described. In the limit $\mathcal{M} \to \infty$ we obtain

$$M_{\max} = \sqrt{2\zeta/\gamma}. \tag{2.3.14}$$

For isothermal flux surfaces $M = \sqrt{2/\gamma}\mathcal{M}R/R_0$, so that there is no limit on M.

The plasma beta

A parameter often used to characterize a tokamak plasma is the ratio $\beta \equiv 2p/B^2$ between the pressure and the magnetic pressure. With the efficiency of a reactor increasing with increasing p and its cost increasing with increasing B^2, β is an important parameter to roughly judge the performance of a tokamak as a power plant. A high value of β is desirable. Instabilities however limit the currently achievable value to only a few percent. Typically the toroidal vacuum magnetic field B_0 at the geometrical axis and an average pressure $\langle p \rangle$ are used. Sometimes however an average β is used, defined as

$$\langle \beta \rangle \equiv 2 \frac{\int p \, d^3\mathbf{r}}{\int B^2 d^3\mathbf{r}}, \tag{2.3.15}$$

where the integration is performed over the plasma volume. From Eq. (2.2.4a), using partial integration, and finally the extended Grad-Shafranov equation (2.2.9),

$$\int B^2 d^3\mathbf{r} = \int \frac{F^2 + |\nabla \psi|^2}{R^2} d^3\mathbf{r} = \int \frac{F^2 - (\psi - \psi_e)\Delta^*\psi}{R^2} d^3\mathbf{r} \tag{2.3.16}$$

$$= \int \left((\psi - \psi_e) \left(\frac{\partial p}{\partial \psi} + \frac{1}{R^2} \frac{d\frac{1}{2}F^2}{d\psi} \right) + \frac{F^2}{R^2} \right) d^3\mathbf{r}, \tag{2.3.17}$$

where ψ_e denotes the value of ψ at the edge so that the divergence term

$$\int \nabla \cdot \left(R^{-2} (\psi - \psi_e) \nabla \psi \right) d^3\mathbf{r} = 0. \tag{2.3.18}$$

When the pressure at the plasma edge vanishes we can use the assumptions (2.3.2) to write $(\psi - \psi_e)\partial p/\partial \psi = p$ and $(\psi - \psi_e)dF^2/d\psi = F^2 - F_e^2$, where F_e denotes the value of F at the plasma edge. By Ampère's law (2.2.1e), the magnitude of the toroidal vacuum field is given by $B_0 R_0/R$ so that we have $F_e \equiv B_{\phi e} R_e = B_0 R_0 \equiv F_0$. The average β can then be written as

$$\langle \beta \rangle = \frac{2 \int p \, d^3\mathbf{r}}{\int \left(p + \frac{1}{2}R^{-2} \left(3F^2 - F_0^2 \right) \right) d^3\mathbf{r}}. \tag{2.3.19}$$

The integrals in Eq. (2.3.19) have to be calculated numerically in general. When $\mathcal{M}^2 \ll 1$, the primary 'knob' to tune $\langle \beta \rangle$ is the ratio between the pressure gradient P and $3F^2 - F_0^2$. For higher flow velocities, $\mathcal{M}$ plays an important role as well.

The safety factor

Another important parameter to characterize a tokamak equilibrium is the safety factor which, with B_p the poloidal magnetic field, is defined by

$$q \equiv \frac{1}{2\pi} \oint \frac{B_\phi}{RB_p} dl = \frac{F(\psi)}{2\pi} \oint \frac{dl}{R\,|\nabla\psi|}, \qquad (2.3.20)$$

where in the second step for the poloidal magnetic field we used $RB_p = |\nabla\psi|$ and $RB_\phi = F(\psi)$ from Eq. (2.2.4a). The integration path of Eq. (2.3.20) is along the poloidal magnetic field over one full poloidal turn. With B_ϕ/B_p the local pitch of the magnetic field line, q gives the number of toroidal turns per poloidal turn of the magnetic field. Since the magnetic field lines do not cross, $q = q(\psi)$ is a flux function.

From Eq. (2.2.5) we obtain $2\pi d\psi = RB_p dA_t$ for the infinitesimal poloidal flux through an annulus of area $dA_t = 2\pi R dR$. The infinitesimal toroidal flux through a poloidal cross-section of area $dA_p = \oint dRdl$ is given by $2\pi d\chi = B_\phi dA_p$ so that

$$q(\psi) = \frac{d\chi}{d\psi} = \frac{B_\phi}{2\pi} \frac{dA_p}{d\psi}. \qquad (2.3.21)$$

Taylor expanding $\psi(R, Z)$ to second order around the magnetic axis, where $\nabla\psi$ vanishes, yields flux surfaces with elliptical poloidal cross-sections. The cross-sectional areas satisfy $dA_p/d\psi = 2\pi/\sqrt{D}$ with $D = \det(\nabla\nabla\psi) = \psi_{RR}\psi_{ZZ} - \psi_{RZ}^2$ the discriminant, the determinant of the Hessian. The safety factor at the magnetic axis is therefore given by

$$q(\psi_m) = \frac{B_\phi}{\sqrt{\psi_{RR}\psi_{ZZ} - \psi_{RZ}^2}}. \qquad (2.3.22)$$

For up-down symmetric equilibria like the analytical equilibria of Eq. (2.3.4), ψ_{RZ} vanishes at the magnetic axis. From Eq. (2.3.4), we have at the magnetic axis $\psi_{ZZ} = 2c_2 R_m^2 - J$ and

$$\psi_{RR} = 2c_1 PR_0^2 - 3c_2 PR_m^2 + \frac{PR_0^2}{2\mathcal{M}^2}\frac{\zeta}{\zeta+1}\left[1 - \left(1 + \frac{\bar{R}_m^2\mathcal{M}^2}{\zeta}\right)^\zeta \left(1 + \bar{R}_m^2\mathcal{M}^2 \frac{3+2\zeta}{\zeta}\right)\right]. \qquad (2.3.23)$$

where $\bar{R}_m^2 = \left(R_m^2 - R_0^2\right)/R_0^2$. Note that the equation $d\psi(R,0)/dR = 0$ for the position of the magnetic axis, with $\psi(R, Z)$ from Eq. (2.3.4), cannot be solved analytically for general ζ. For $\zeta = 1$, however, we find

$$R_m^2 = R_0^2 \frac{-\left(1 + 2c_2 - \mathcal{M}^2\right) + \sqrt{\left(1 + 2c_2 - \mathcal{M}^2\right)^2 + \mathcal{M}^2\left(2 + 8c_1 - \mathcal{M}^2\right)}}{\mathcal{M}^2}. \qquad (2.3.24)$$

providing an expression for the Shafranov shift $R_m - R_0$. In the limit of $\mathcal{M} \to 0$ Eq. (2.3.24) gives $R_m/R_0 = 1 + 4c_1$.

2.3.4 Other analytical solutions

Eq. (2.3.1) can be solved analytically for other assumptions than those of Eq. (2.3.2). When we assume that $d\frac{1}{2}F^2/d\psi$ is given by $K\psi$ instead of by J, the extended Grad-Shafranov equation (2.3.1) becomes

$$\left(\Delta^* + K\right)\psi = -R^2 P \left(1 + \bar{R}^2 \mathcal{M}^2/\zeta\right)^{\zeta}, \qquad (2.3.25)$$

which has the solution [182]

$$\psi = -\frac{PR}{K^{3/2}} \sum_{n=0}^{\infty} \left[\frac{\zeta}{n} \left(\frac{\mathcal{M}^2}{\zeta K R_0^2}\right)^n S_{2n+2,1}\left(\sqrt{K}R\right) \right.$$
$$\left. + R\cos\left(k_n Z\right)\left[a_n J_1\left(R\sqrt{K - k_n^2}\right) + b_n Y_1\left(R\sqrt{K - k_n^2}\right)\right]\right], \qquad (2.3.26)$$

where a_n, b_n and k_n are free constants. The first part of Eq. (2.3.26) represents a particular solution in terms of Lommel functions $S_{\mu,\nu}$ and the second part represents a general homogeneous solution in terms of Bessel functions. This solution has the same maximum Mach number as the solution of Eq. (2.3.4) given in Eq. (2.3.14), but has a more peaked toroidal current density. An obvious drawback for practical applications is the evaluation of an infinite sequence of special functions.

Perhaps a more useful analytical solution is obtained assuming additionally that $p_0' = Q\psi$ instead of P, so that Eq. (2.3.1) becomes

$$\left(\Delta^* + K + QR^2\left(1 + \bar{R}^2\mathcal{M}^2/\zeta\right)^{\zeta}\right)\psi = 0, \qquad (2.3.27)$$

which is solved by [182]

$$\psi = \sqrt{1 + \bar{R}^2\mathcal{M}^2/\zeta}\cos\left(\sqrt{K}Z\right)\left(a J_{1/(\zeta+2)}\left(\tau\right) + b Y_{1/(\zeta+2)}\left(\tau\right)\right), \qquad (2.3.28)$$

where $\tau = \left(\sqrt{Q}R_0^2/\mathcal{M}^2\right)\left(\zeta/(\zeta + 2)\right)\left(1 + \bar{R}^2\mathcal{M}^2/\zeta\right)^{(\zeta+2)/2}$. A property of this solution is that the toroidal current $J_\phi = \Delta^*\psi/R$ is proportional to ψ. The toroidal current can therefore be made to vanish at the plasma edge, by making ψ vanish there.

2.4 The Brunt-Väisälä Frequency

The gravitational stability of an adiabatically displaced air parcel in the atmosphere depends on the vertical stratification of pressure and density. Something similar holds for plasma under the influence of the centrifugal force. By analogy, in Section 2.4.2 expressions are derived for the oscillation frequency of plasma confined to the circular magnetic surfaces of a large aspect ratio tokamak. First, we will look at the derivation of the Brunt-Väisälä frequency of Eq. (1.3.5) in more detail.

2.4.1 In the atmosphere

Imagine a horizontally stratified atmosphere in which we displace a fluid parcel a distance z in the vertical $\hat{\mathbf{e}}_z$-direction, from position 1 to position 2. The parcel, arrived at the final position 2, will not have the same thermodynamic variables as its new environment, so that we will denote these with a subscript f. When the parcel is displaced sufficiently fast there will be no heat exchange with the environment and the process will be adiabatic, that is $S_f = S_1$. The pressure however equilibrates much faster, so that we can assume $p_f = p_2$. Therefore the final density $\rho_f = (p_f/S_f)^{1/\gamma} = (p_2/S_1)^{1/\gamma}$ will differ from the ambient density ρ_2. With $g < 0$, this density difference results in a buoyancy force $g\left(\rho_f - \rho_2\right)\hat{\mathbf{e}}_z$. We can set up the equation of motion for the vertical position of the fluid parcel

$$\frac{d^2z}{dt^2} = g\frac{\rho_f - \rho_2}{\rho_f} = g\frac{S_1^{-1/\gamma} - S_2^{-1/\gamma}}{S_1^{-1/\gamma}} \approx \frac{g}{\gamma}\frac{1}{S}\frac{dS}{dz}z. \tag{2.4.1}$$

The resulting frequency of the exponential solutions $z \propto \exp\left(i\omega_{\mathrm{BV}}t\right)$ is called the buoyancy frequency, or Brunt-Väisälä (BV) frequency

$$\omega_{\mathrm{BV}}^2 \equiv -\frac{g}{\gamma}\frac{S'}{S} = g\left(\frac{\rho'}{\rho} - \frac{p'}{\gamma p}\right), \tag{2.4.2}$$

where a prime denotes differentiation with respect to z. When this squared frequency is positive, the buoyancy force is restoring and the atmosphere is stable. When however

$$g\left(\frac{\rho'}{\rho} - \frac{p'}{\gamma p}\right) < 0, \tag{2.4.3}$$

instability will result. This criterion for convective instability is known as the Schwarzschild criterion.

When the fluid parcel is displaced sufficiently slow for heat exchange with the ambient air to take place, the temperature will equilibrate as well. In this case there will no longer be a density difference with the environment, no resulting force, and no oscillations or instability.

When the fluid parcel is displaced without being able to compress, its final density will be $\rho_f = \rho_1$ so that, as in Eq. (1.3.4),

$$\omega_{\mathrm{BV, incompr.}}^2 = g\frac{\rho'}{\rho}. \tag{2.4.4}$$

2.4.2 In a tokamak

For a tokamak plasma, the issue of gravitational stability discussed above is not very relevant. Centrifugal forces however can be significant in a tokamak. Like the gravitational force, the centrifugal force is proportional to the density. In Eq. (2.2.3), the

effective gravitational acceleration is given by $g = R\Omega^2$ in the R-direction. Because of the presence of the magnetic field, the plasma is highly anisotropic. We therefore separately discuss the centrifugal convective effect on plasma perturbations normal to the magnetic surfaces and within the magnetic surfaces. In both instances, the perturbation needs to have at least a component in the direction of the centrifugal force.

Normal to the magnetic surfaces

Perturbations perpendicular to the magnetic surfaces are to a good approximation incompressible, in order to minimize the large energy associated with the compression of magnetic field lines. We consider a plasma perturbation in the horizontal $Z = 0$ plane. Using $g = R\Omega^2$ in Eq. (2.4.4) yields

$$\omega_{\text{BV},\perp}^2 = \frac{R\Omega^2\rho'}{\rho}. \tag{2.4.5}$$

This frequency squared combines with that associated with the magneto-rotational instability $\omega_{\text{MRI}}^2 = R\left(\Omega^2\right)'$ [195, 27, 6] to give, as in Eq. (1.3.7), a kinetic energy density [61]

$$\rho\omega^2 = \rho\left(\omega_{\text{BV},\perp}^2 + \omega_{\text{MRI}}^2\right) = R\left(\rho\Omega^2\right)'. \tag{2.4.6}$$

Within the magnetic surfaces

Within the magnetic surfaces, plasma perturbations that have a component in the R-direction will also experience the convective effect. Contrary to the perturbations in the $\nabla\psi$-direction, these perturbations can be compressible and will oscillate in the presence of entropy gradients as described by Eq. (2.4.2). The relevant entropy gradients are those within the magnetic surfaces, projected on the direction of the centrifugal force, that is

$$\left.\frac{\partial S}{\partial R}\right|_\psi = \left.\frac{\partial}{\partial R}\right|_\psi p_0\rho_0^{-\gamma}\left(1 + \frac{\bar{R}^2\mathcal{M}^2}{\zeta}\right)^{\zeta-\gamma(\zeta-1)} = S\left(1 - \frac{\gamma}{\gamma_e}\right)\frac{2R\mathcal{M}^2/R_0^2}{1 + \bar{R}^2\mathcal{M}^2/\zeta}, \tag{2.4.7}$$

where we used $S = p\rho^{-\gamma}$ with p and ρ from Eqs. (2.2.10) and (2.2.11) and we used the definition $\gamma_e \equiv \zeta/(\zeta - 1)$. Plasma moving along a magnetic field line has to move in the toroidal direction as well as the poloidal direction in order to move in the R-direction. This increases the effective inertia by the Pfirsch-Schlüter factor $1 + 2q^2$ as described in Section 2.2.3. The Brunt-Väisälä frequency is then decreased by one over this factor. For circular flux-surfaces another factor of $1/2$ accounts for the average directional $\left\langle(\hat{\mathbf{e}}_\theta \cdot \nabla R)^2\right\rangle = \left\langle\cos^2\theta\right\rangle = 1/2$ resulting from the fact that the plasma is restrained to move in the poloidal $\hat{\mathbf{e}}_\theta$-direction while both the centrifugal force and the entropy gradients are in the ∇R-direction. From Eq. (2.4.2), with $g = R\Omega^2$, we

can then define the average Brunt-Väisälä frequency of a tokamak with circular flux-surfaces as

$$
\begin{aligned}
\omega^2_{\text{BV, tokamak}} &\equiv -\frac{R\Omega^2}{2\left(1+2q^2\right)}\frac{1}{\gamma S}\left.\frac{\partial S}{\partial R}\right|_\psi = \frac{\gamma/\gamma_e - 1}{1 + \bar{R}^2 \mathcal{M}^2/\zeta}\frac{\left(R^2/R_0^2\right)\mathcal{M}^2\Omega^2/\gamma}{1 + 2q^2} \\
&= \left(\frac{\gamma}{\gamma_e} - 1\right)\frac{M^2\Omega^2}{2\left(1+2q^2\right)},
\end{aligned}
\tag{2.4.8}
$$

with M given by Eq. (2.3.13). As discussed in Section 2.2.3 the adiabatic constants γ_e and γ may be different, leading to stable oscillations when $\gamma_e > \gamma$ or instability when $\gamma_e < \gamma$.

2.5 Waves and Instabilities

Up to now we have been discussing plasma configurations in which the Lorentz force, the pressure force, and the centrifugal force are balanced. We do not yet know if these configurations are stable against slight deviations from equilibrium. A small perturbation may create a restoring force, resulting in a wave within the plasma. The resulting force inequilibrium caused by the perturbation may however also amplify the original perturbation, leading to instability.

First, the Eulerian approach to stability is introduced that is implemented in the numerical code of the next section. Next, a Lagrangian approach is described and used to obtain an expression for the potential energy of a plasma perturbation. Finally, an analytical expression for the low-frequency continuous Alfvén spectrum is obtained. Both these expressions contain the freedom to choose which thermodynamic quantity is constant on the equilibrium magnetic surfaces and in both the Brunt-Väisälä frequency of the previous section plays a role. As a primer, the continuous spectrum in an infinite homogeneous plasma and a cylinder are briefly revisited.

2.5.1 Primitive variables

In order to investigate the waves and instabilities in an equilibrium, we can split all quantities in an equilibrium value plus a perturbation. Inserting these quantities into the time-dependent ideal MHD equations, linear stability is investigated by retaining only terms that depend on the perturbations to first order. Because the resulting linear equations do not depend on time explicitly, we can assume normal mode solutions in which the perturbations depend on time harmonically, that is they are proportional to $\exp\left(-i\omega t\right)$. The entire system of equations can then be cast into an eigenvalue problem for the eigenvalues ω. This procedure is typically followed in numerical codes, where the radial and poloidal directions are handled with finite elements and/or spectral methods. In the case of axisymmetry, the perturbations δf of the primitive

physical variables $f = p, \rho, \mathbf{B}, \mathbf{u}$... are typically parameterized as

$$\delta f(\psi, \vartheta, \phi, t) = \sum_m \delta f_m(\psi) e^{i(m\vartheta - \omega t - n\phi)}, \tag{2.5.1}$$

where ϑ is some poloidal coordinate and the integers m and n are the poloidal and toroidal mode number, respectively. Because the equations do not depend on the toroidal coordinate ϕ explicitly, we can investigate single normal modes in the toroidal direction. The symmetry in the poloidal direction is not exact, so that in general several poloidal mode numbers have to be included in Eq (2.5.1).

2.5.2 Plasma perturbation

Another approach is to start from an infinitesimal displacement $\boldsymbol{\xi}$ of the plasma. This perturbation automatically also perturbs other quantities like the magnetic field, the pressure, and the density:

$$\delta \mathbf{B} = \nabla \times (\boldsymbol{\xi} \times \mathbf{B}), \tag{2.5.2a}$$

$$\delta \rho = -\nabla \cdot (\rho \boldsymbol{\xi}), \tag{2.5.2b}$$

$$\delta p = -\boldsymbol{\xi} \cdot \nabla p - \gamma p \nabla \cdot \boldsymbol{\xi}. \tag{2.5.2c}$$

$$\tag{2.5.2d}$$

These Eulerian perturbations follow from Eqs. (2.2.1d) and (2.2.1g), Eq. (2.2.1b), and Eqs. (2.2.1c) and (2.2.12), respectively. Inserting the perturbed quantities into the static (that is without flow) time-dependent ideal MHD equations gives an equation of motion for $\boldsymbol{\xi}$:

$$\rho \ddot{\boldsymbol{\xi}} = \mathbf{F}_s(\boldsymbol{\xi}), \tag{2.5.3}$$

where the static force operator is given by [12]

$$\mathbf{F}_s(\boldsymbol{\xi}) = (\nabla \times \delta \mathbf{B}) \times \mathbf{B} + (\nabla \times \mathbf{B}) \times \delta \mathbf{B} - \nabla \delta p - \delta \rho \nabla \Phi. \tag{2.5.4}$$

The first two terms can be recognized as the linearised perturbed Lorentz force and the last term as the perturbed pressure force. The final term arises in the presence of a gravitational force $-\rho \nabla \Phi$. Assuming a harmonic time dependence $\ddot{\boldsymbol{\xi}} = -\omega^2 \boldsymbol{\xi}$, Eq. (2.5.3) becomes an eigenmode equation for the eigenvalues ω^2. It can be shown that $\mathbf{F}_s$ is a Hermitian operator so that the eigenvalues ω^2 are real. This implies that the frequencies ω are either purely real, corresponding to stable waves, or purely imaginary, corresponding to instabilities.

2.5.3 Frieman-Rotenberg approach

In a formalism developed by Frieman and Rotenberg [58], a Lagrangian approach is taken in which $\boldsymbol{\xi}$ describes the position of the perturbed plasma element relative to the

background flow (see Appendix 4.A.1). Assuming $\boldsymbol{\xi}$ to be of the form (2.5.1), the equation of motion changes from the static equation (2.5.3) to give (see Appendix (4.A.2))

$$-\rho\omega^2\boldsymbol{\xi} - 2i\rho\omega\mathbf{u}\cdot\nabla\boldsymbol{\xi} = \mathbf{F}(\boldsymbol{\xi}), \tag{2.5.5}$$

where, suppressing the argument $\boldsymbol{\xi}$, the total force operator $\mathbf{F} = \mathbf{F}_s + \mathbf{F}_u$, with a rotational force $\mathbf{F}_u = \nabla\cdot(\rho\boldsymbol{\xi}\mathbf{u}\cdot\nabla\mathbf{u} - \rho\mathbf{u}\mathbf{u}\cdot\nabla\boldsymbol{\xi})$.

For a toroidally rotating equilibrium with velocity $\mathbf{u} = R\Omega\hat{\mathbf{e}}_\phi$ and angular frequency vector $\boldsymbol{\Omega} = -\Omega\hat{\mathbf{e}}_Z$, we obtain after some work

$$\mathbf{F}_u = -\mathbf{R}\nabla\cdot\left(\rho\Omega^2\boldsymbol{\xi}\right) + n^2\rho\Omega^2\boldsymbol{\xi} + 2in\rho\Omega(\boldsymbol{\Omega}\times\boldsymbol{\xi}). \tag{2.5.6}$$

Equation (2.5.5) can then be rewritten in terms of the Doppler shifted frequencies $\omega_D = \omega + n\Omega$ as [198]

$$-\rho\omega_D^2\boldsymbol{\xi} - 2i\rho\omega_D\boldsymbol{\Omega}\times\boldsymbol{\xi} = \mathbf{F}_s(\boldsymbol{\xi}) - \mathbf{R}\nabla\cdot\left(\rho\Omega^2\boldsymbol{\xi}\right). \tag{2.5.7}$$

In Eq. (2.5.7) we clearly recognize the second term as the Coriolis force, the fictitious force experienced by a plasma element moving with a velocity $i\omega_D\boldsymbol{\xi}$ relative to the rotating background plasma.

2.5.4 Stability

The equation of motion, Eq. (2.5.5) or (2.5.7), is no longer a standard eigenvalue equation because the eigenvalue ω appears both linearly and quadratically. This allows the frequencies to become complex-valued. Taking the inner product of Eq. (2.5.5) or (2.5.7) with $\boldsymbol{\xi}^*$ and integrating over the entire plasma volume gives, solving for ω [58, 66]

$$\omega = \bar{V} \pm \sqrt{\bar{V}^2 + \bar{W}}, \tag{2.5.8}$$

with the Doppler-Coriolis shift $V = -\frac{1}{2}\int\rho\left(n\Omega|\boldsymbol{\xi}|^2 + i\boldsymbol{\xi}^*\cdot(\boldsymbol{\Omega}\times\boldsymbol{\xi})\right)d^3\mathbf{r}$ and the potential energy $W = -\frac{1}{2}\int\boldsymbol{\xi}^*\cdot\mathbf{F}d^3\mathbf{r}$. A bar denotes normalization with $I \equiv \frac{1}{2}\int\rho\,|\boldsymbol{\xi}|^2\,d^3\mathbf{r}$. The frequencies of Eq. (2.5.8) are real when $\bar{W} > -\bar{V}^2$, providing a stability criterion for toroidally rotating tokamak plasmas.

When the rotation is rigid, or can be considered rigid because the flow shear is insignificant over the area where the mode amplitude is non-zero, ω_D is (locally) constant. Taking the inner product of Eq. (2.5.7) with $\boldsymbol{\xi}^*$ and integrating over the entire plasma volume gives

$$\omega_D = \bar{\mathcal{V}} \pm \sqrt{\bar{\mathcal{V}}^2 + \bar{\mathcal{W}}}, \tag{2.5.9}$$

where $\mathcal{V} = -\frac{1}{2}\int i\rho\boldsymbol{\xi}^*\cdot\boldsymbol{\Omega}\times\boldsymbol{\xi}d^3\mathbf{r}$ and $\mathcal{W} = -\frac{1}{2}\int\boldsymbol{\xi}^*\cdot\left(\mathbf{F}_s(\boldsymbol{\xi}) - \mathbf{R}\nabla\cdot\left(\rho\Omega^2\boldsymbol{\xi}\right)\right)d^3\mathbf{r}$. The frequencies are real when $\bar{\mathcal{W}} > -\bar{\mathcal{V}}^2$, providing a necessary and sufficient stability criterion for rigidly rotating tokamak plasmas.

2.5.5 Potential energy

The potential energy $W = -\frac{1}{2} \int \boldsymbol{\xi}^* \cdot \mathbf{F} d^3\mathbf{r}$ can be rewritten as [70]

$$W = \frac{1}{2} \int \left(|\delta \mathbf{B}|^2 + \mathbf{J} \cdot \boldsymbol{\xi}^* \times \delta \mathbf{B} + U_n + U \right) d^3\mathbf{r}, \qquad (2.5.10)$$

where the manifestly *n*-dependent part of the rotational potential energy density is given by

$$U_n = -\boldsymbol{\xi}^* \cdot \left(n^2 \rho \Omega^2 \boldsymbol{\xi} + 2in\rho\Omega \boldsymbol{\Omega} \times \boldsymbol{\xi} \right) \qquad (2.5.11a)$$

$$= -n^2 \rho \Omega^2 |\boldsymbol{\xi}|^2 - 4in\rho\Omega \boldsymbol{\Omega} \cdot \operatorname{Re}(\boldsymbol{\xi}) \times \operatorname{Im}(\boldsymbol{\xi}) \qquad (2.5.11b)$$

and the remaining non-magnetic part of the potential energy density

$$U \equiv -(\nabla \cdot \boldsymbol{\xi}^*) \, \delta p + \boldsymbol{\xi}^* \cdot \mathbf{R} \nabla \cdot (\rho \Omega^2 \boldsymbol{\xi}), \qquad (2.5.12)$$

where the divergence term $\nabla \cdot (\boldsymbol{\xi}^* \delta p)$ was discarded because, for internal modes, it will give a vanishing surface term when integrated over the entire plasma volume. To investigate the influence of toroidal rotation on stability, we take a closer look at U,

$$U = (\nabla \cdot \boldsymbol{\xi}^*)(\boldsymbol{\xi} \cdot \nabla p + \gamma p \nabla \cdot \boldsymbol{\xi}) + \boldsymbol{\xi}^* \cdot \mathbf{R} \left(\rho \Omega^2 \nabla \cdot \boldsymbol{\xi} + \boldsymbol{\xi} \cdot \nabla(\rho \Omega^2) \right). \qquad (2.5.13)$$

Writing in components $\boldsymbol{\xi} \cdot \nabla = \xi_\psi \partial/\partial \psi + \xi_R \partial/\partial R + \xi_\phi \partial/\partial \phi$, we have

$$\boldsymbol{\xi} \cdot \nabla p = \xi_\psi \frac{\partial p}{\partial \psi} + \xi_R \rho R \Omega^2, \qquad (2.5.14)$$

where the force balance (2.2.8) was used to replace $\partial p/\partial R$ by $\rho R \Omega^2$. To rewrite the last term of Eq. (2.5.13), we use

$$\frac{\partial \rho \Omega^2}{\partial R} = \frac{\zeta - 1}{\zeta} \frac{\rho \Omega^2}{p} \frac{\partial p}{\partial R} = \frac{R \left(\rho \Omega^2\right)^2}{\gamma_e p}, \qquad (2.5.15)$$

where we used $\gamma_e \equiv \zeta/(\zeta - 1)$ and Eq. (2.2.14) for ρ. Using Eqs. (2.5.14) and (2.5.15) in Eq. (2.5.13) gives

$$U = \nabla \cdot \boldsymbol{\xi}^* \left(\xi_\psi \frac{\partial p}{\partial \psi} + \xi_R \rho R \Omega^2 + \gamma p \nabla \cdot \boldsymbol{\xi} \right) + R \xi_R^* \left(\rho \Omega^2 \nabla \cdot \boldsymbol{\xi} + \xi_\psi \frac{\partial \rho \Omega^2}{\partial \psi} + \xi_R \frac{R \rho^2 \Omega^4}{\gamma_e p} \right). \tag{2.5.16}$$

Or, rearranging terms:

$$U = \nabla \cdot \boldsymbol{\xi}^* \xi_\psi \frac{\partial p}{\partial \psi} + R \xi_R^* \xi_\psi \frac{\partial \rho \Omega^2}{\partial \psi} + \gamma p \left| \nabla \cdot \boldsymbol{\xi} + \frac{\rho \Omega^2}{\gamma p} R \xi_R \right|^2 + \left(\frac{\gamma}{\gamma_e} - 1 \right) \frac{\left| \rho \Omega^2 R \xi_R \right|^2}{\gamma p}. \tag{2.5.17}$$

The component of $\boldsymbol{\xi}$ parallel to the magnetic field is only present in the last two terms. For static equilibria these terms reduce to $\gamma p \left| \nabla \cdot \boldsymbol{\xi} \right|^2$. In order to minimize U, the parallel displacement of 'subsonic' modes whose phase velocity is smaller than the thermal velocity will ensure incompressibility of the perturbations. For supersonic modes, the parallel component will be negligible. The additional inertia associated with the parallel motion of subsonic modes will lower the frequency squared of subsonic modes by the Pfirsch-Schlüter factor. In the presence of significant toroidal flow however, the last two terms in Eq. (2.5.17) contain the parallel displacement, complicating things somewhat more.

The second term on the right-hand side of Eq. (2.5.17) should be compared with Eq. (2.4.6) resulting from a combination of the magneto-rotational instability and the convective effect of incompressible radial perturbations ξ^{ψ}. This combination was previously found in both astrophysical [6, 16] and tokamak plasmas [168]. We will encounter it again in the next chapter.

Note that the last term of Eq. (2.5.17) can be written as $(\gamma / \gamma_e - 1) \rho M^2 \Omega^2 \left| \xi_R \right|^2$. Comparing this with Eq. (2.4.8) this term can be identified as originating from the convective effect.

2.5.6 Continuous spectrum

For certain frequencies, common to a magnetic surface, the ideal MHD equations become singular. The associated eigenfunctions show singular behaviour at the corresponding magnetic surface. These singular eigenmodes can be thought of as being confined to their respective magnetic surface. Their amplitude will be non-zero over some surrounding region though. Because of the discontinuous behaviour of the eigenfunctions, the boundary conditions can always be satisfied so that each of these frequencies will be an eigenfrequency. The continuum of magnetic surfaces in this way traces out a continuum of frequencies, called the continuous spectrum [70].

The continuum modes in the presence of a one-dimensional inhomogeneity, as in a cylinder, closely resemble those waves in a homogeneous medium that have their wave vector perpendicular to the equilibrium magnetic field. As a primer to the continuous spectrum of a torus, we will shortly investigate these cases subsequently.

Infinitely extended homogeneous plasma at rest

MHD waves can most easily be described in an infinitely extended fluid at rest, with constant equilibrium variables $\mathbf{u} = 0, \mathbf{B}, p, \rho$ [70]. The ideal MHD equations (2.2.2a)-(2.2.2e) are in this case trivially satisfied, since all gradients vanish. Assuming plane wave solutions for a perturbation $\boldsymbol{\xi}$ with a spatial and time dependence proportional to $\exp{(i\mathbf{k} \cdot \mathbf{r} - i\omega t)}$, we can replace ∇ with $i\mathbf{k}$ and $\partial / \partial t$ with $-i\omega$. The equation of motion (2.5.3) for a homogeneous background medium becomes

$$- \rho \omega^2 \boldsymbol{\xi} = (i\mathbf{k} \times \delta \mathbf{B}) \times \mathbf{B} - i\mathbf{k} \delta p. \qquad (2.5.18)$$

Inserting $\delta \mathbf{B} = i\mathbf{k} \times (\boldsymbol{\xi} \times \mathbf{B})$ and $\delta p = -i\gamma p\mathbf{k} \cdot \boldsymbol{\xi}$ from Eqs. (2.5.2a) and (2.5.2c), and defining $v_s \equiv \sqrt{\gamma p/\rho}$ and $\mathbf{v}_A \equiv \mathbf{B}/\sqrt{\rho}$, we obtain

$$-\omega^2 \boldsymbol{\xi} + (\mathbf{k} \times (\mathbf{k} \times (\boldsymbol{\xi} \times \mathbf{v}_A))) \times \mathbf{v}_A + v_s^2\mathbf{k}(\mathbf{k} \cdot \boldsymbol{\xi}) = 0. \qquad (2.5.19)$$

Defining $k_\parallel \equiv \mathbf{k} \cdot \hat{\mathbf{v}}_A$, the component of Eq. (2.5.19) parallel to $\hat{\mathbf{v}}_A$ gives $\omega^2 \boldsymbol{\xi} \cdot \hat{\mathbf{v}}_A = k_\parallel v_s^2 \mathbf{k} \cdot \boldsymbol{\xi}$. Using this relation to eliminate $\boldsymbol{\xi} \cdot \hat{\mathbf{v}}_A$ and working out the triple cross-product, Eq. (2.5.19) can be written as

$$\left(\omega^2 - k_\parallel^2 v_A^2\right)\boldsymbol{\xi} + (\mathbf{k} \cdot \boldsymbol{\xi})\left[\left(v_A^2 v_s^2 \left(\frac{k_\parallel}{\omega}\right)^2 - \left(v_s^2 + v_A^2\right)\right)\mathbf{k} + k_\parallel v_A^2 \hat{\mathbf{v}}_A\right] = 0. \quad (2.5.20)$$

The component of Eq. (2.5.20) perpendicular to both $\hat{\mathbf{v}}_A$ and $\mathbf{k}$ gives the Alfvén wave frequencies $\omega_A^2 = k_\parallel^2 v_A^2$. The component of Eq. (2.5.20) parallel to $\mathbf{k}$ gives the slow (-) and fast (+) magnetosonic wave frequencies

$$\omega_{s,f}^2 = k^2\left(\frac{v_s^2 + v_A^2}{2} \pm \sqrt{\left(\frac{v_s^2 + v_A^2}{2}\right)^2 - v_s^2 v_A^2 \left(\frac{k_\parallel}{k}\right)^2}\right). \qquad (2.5.21)$$

These wave frequencies satisfy $\omega_f^2 \geq \omega_A^2 \geq \omega_s^2 \geq 0$, reflecting the strengths of the restoring forces of these waves. For fast and slow magnetosonic waves, both the plasma pressure and the magnetic pressure are disturbed; in phase and out of phase, respectively. For Alfvén waves, these pressures are not perturbed but the magnetic field line tension acts as a restoring force.

When $k_\parallel \ll k$, Eq. (2.5.21) can be expanded to give

$$\omega_s^2 \approx k_\parallel^2 \frac{v_s^2 v_A^2}{v_s^2 + v_A^2} = \omega_A^2 \frac{v_s^2}{v_s^2 + v_A^2} = \omega_A^2 \frac{\gamma p}{\gamma p + B^2} \quad \text{and} \quad \omega_f^2 \approx k^2\left(v_s^2 + v_A^2\right). \qquad (2.5.22)$$

We find that the frequencies of both the Alfvén and slow magnetosonic waves vanish when $k_\parallel = 0$. Because the frequency of the fast wave always remains finite and relatively high, it is of little interest for stability and we will not consider this wave in what follows.

A cylinder

When inhomogeneities are introduced, the continuum waves that arise satisfy $k_\parallel \ll k$. The expressions of Eq. (2.5.22) can therefore immediately be used to describe the continuum of a cylindrical plasma. In a cylinder, all quantities depend only on the radial coordinate r so that single poloidal harmonics $f \propto \exp i(m\theta - \omega t - kz)$ can be

investigated separately. The Alfvén continuum frequencies are then given by

$$\omega_{A,m}(r) = \pm k_\parallel v_A = \pm \frac{\mathbf{B} \cdot \mathbf{k}}{\sqrt{\rho}} = \pm \frac{i\mathbf{B} \cdot \nabla}{\sqrt{\rho}} e^{i(m\theta - \omega t - kz)} \tag{2.5.23}$$

$$= \pm \frac{kB_z - mB_\theta/r}{\sqrt{\rho}} = \pm \bar{\omega}_A \left(n - \frac{m}{q(r)} \right).$$

In the last expression we introduced $q(r) = rB_z/R_0 B_\theta$, $\bar{\omega}_A(r) = B_z/\sqrt{\rho}R_0$ and $n = kR_0$ to establish the correspondence between a periodic cylinder with length $2\pi R_0$ and a large aspect ratio torus with cylindrical cross-section. In this case n becomes the integer toroidal mode number introduced in Eq. (2.5.1) and B_z is replaced by B_ϕ. The cylindrical slow continuum frequencies are given by $\omega_s(r) = \pm \omega_0 (nq - m)$ with from Eq. (2.5.22)

$$\omega_0 = \frac{\bar{\omega}_A}{q} \sqrt{\frac{\gamma p}{\gamma p + B^2}} \approx \frac{\bar{\omega}_A}{q} \sqrt{\frac{1}{2}\gamma\beta} = \frac{\sqrt{\gamma T}}{q R_0}. \tag{2.5.24}$$

The approximation of Eq. (2.5.24) holds for $\beta \equiv 2p/B^2 \ll 1$. Both of the continuum frequencies vanish at the rational surface where $q = m/n$, indicating marginal stability in the absence of magnetic field line bending. It turns out that the only effect of poloidal flow u_θ and longitudinal flow u_z on the cylindrical continuum frequencies is a Doppler shift to $\omega_D \equiv \omega + mu_\theta/r + ku_z$.

A torus

In a torus, the poloidal angle is no longer an angle of symmetry. Whenever $n - m/q = \pm(n - m'/q)$ so that $\omega_{A,m} = \omega_{A,m'}$ and $\omega_{s,m} = \omega_{s,m'}$, toroidal coupling between poloidal harmonics ensures that these cylindrical frequency crossings are avoided and a spectral gap appears. The gaps due to $|m - m'| = 1, 2, 3, \ldots$ are associated with poloidal variation of the equilibrium due to toroidicity, ellipticity, triangularity, etc.

In a torus there is also a coupling when $\omega_{A,m} = \omega_{s,m'}$, which for $\beta \ll 1$ occurs approximately at the rational surface $q = m/n$ at a frequency

$$\omega \approx (m - m') \omega_0. \tag{2.5.25}$$

The continuous spectrum is substantially modified by all this coupling. As in a cylinder, rotation shifts the eigenfrequencies ω to a Doppler shifted frequency $\omega_D \equiv \omega + n\Omega$. Because in a torus the centrifugal force is no longer perpendicular to the magnetic surfaces, rotation introduces also more substantial changes to the continuous spectrum.

For a tokamak with isothermal magnetic surfaces, a small inverse aspect ratio $\epsilon \ll 1$, a Mach number of order unity, and low β of order ϵ^2, an expression for the low-frequency continuous Alfvén spectrum close to a rational surface was obtained analytically in Refs. [189, 204]. Using the same assumptions, in Refs. [211, 210] the

eigenfrequencies of axisymmetric $m = n = 0$ modes were derived[1]. According to for example Ref. [203], at the rational surface these frequencies are equal to those of continuum modes with non-zero m, n. Repeating the procedure of Refs. [211, 210] for arbitrary $\gamma_e = \zeta/(\zeta - 1)$, we derived[2] the eigenfrequencies $\omega_D = 0$, $\omega_D = \omega_0^2$, and $\omega_D^2 = \tilde{\omega}_\pm^2$, where

$$\tilde{\omega}_\pm^2 = \frac{\omega_0^2}{2} \left(\tilde{a}_1 \pm \sqrt{\tilde{a}_1^2 - \tilde{a}_2} \right), \tag{2.5.26a}$$

and

$$\tilde{a}_1 = 1 + 2q^2 \left(1 + \frac{4\mathcal{M}^2}{\gamma} + \frac{\mathcal{M}^4}{\gamma\gamma_e} \right), \tag{2.5.26b}$$

$$\tilde{a}_2 = \frac{8q^2\mathcal{M}^4}{\gamma} \left(\frac{1}{\gamma_e} - \frac{1}{\gamma} \right). \tag{2.5.26c}$$

In the limit $\gamma_e \to 1$ for isothermal magnetic surfaces, this result agrees with that of Refs. [189, 203, 204] for the low-frequency Alfvén continuum. In the limit $\gamma_e \to \infty$ for magnetic surfaces of constant density the recent result of Ref. [131] for axisymmetric modes is recovered. The present result generalizes these particular results to arbitrary γ_e.

For small flow velocities $\mathcal{M}^2 \ll 1$, we obtain from Eq. (2.5.26a)

$$\tilde{\omega}_-^2 \approx \left(\frac{1}{\gamma_e} - \frac{1}{\gamma} \right) \frac{\mathcal{M}^2 \Omega^2}{1 + 2q^2}, \tag{2.5.27}$$

which is equal to the Brunt-Väisälä frequency $\omega_{\text{BV, tokamak}}^2$ of Eq. (2.4.8). This clearly shows that the flow-induced continuum gap for $\gamma > \gamma_e$ between $\omega_D = -\tilde{\omega}_-$ and $\tilde{\omega}_-$ can be attributed to the convective effect, as was suggested in Ref. [190, 189].

In the absence of flow, the frequencies of Eq. (2.5.26a) are given by $\tilde{\omega}_-^2 = 0$ and $\tilde{\omega}_+^2 = (1 + 2q^2)\omega_0^2$. The so-called beta-induced continuum gap between $\omega_D = -\tilde{\omega}_+$ and $\tilde{\omega}_+$ was first found in Refs. [36, 187]. Note the similarity with the slow-Alfvén coupling frequency (2.5.25), the difference being half the Pfirsch-Schlüter factor $1 + 2q^2$. This toroidal effect influences the continuum modes through the curvature of the magnetic field within the magnetic surfaces, called the geodesic curvature. Modes with $m = n = 0$ with $\omega_D \approx \tilde{\omega}_+$ are therefore referred to as Geodesic Acoustic Modes (GAMs) [216]. For non-zero m, n they are referred to as Beta-induced Alfvén Eigenmodes (BAEs) [98, 187]. The observation that the continuum frequencies $\tilde{\omega}_\pm$ are the

---

[1]The result of Refs. [211, 210] for axisymmetric modes however differs from that of Refs. [189, 204] for general mode number continuum modes. This can be attributed to an erroneous factor of -2 in the exponential dependence of the density of Ref. [211], of which only the minus sign was corrected in Ref. [210]. In addition, a factor 2 is missing in the second term in Eq. (16) of Ref. [210].

[2]The difference in the derivation of Eq. (2.5.26a) compared to the result of Refs. [211, 210] for $\gamma_e \to 1$ and [131] for $\gamma_e \to \infty$, pertains to evaluation of the advection of ρ and S by the perturbed velocity $\mathbf{v}$ lying within the magnetic surfaces. Using the general parameterization of Eqs. (2.2.10) and (2.2.11), for general γ_e we find $\mathbf{v} \cdot \nabla S = (\gamma_e - \gamma)(S/\rho)\mathbf{v} \cdot \nabla\rho$ and $\mathbf{v} \cdot \nabla\rho = v_R \rho R \Omega^2/\gamma_e T$.

same for zero and non-zero m, n is therefore referred to as the GAM/BAE degeneracy.

We note that for $\mathcal{M} = 0$ the zero-frequency continuum modes $\tilde{\omega}_- = 0$ can be thought of as equilibrium flows described by Eq. (2.2.16). These flows are the linear counterpart of zonal flows. We finally note that, away from the resonant surface, the coefficients $\tilde{a}_1$ and $\tilde{a}_2$ acquire additional terms $(m/q - n)^2 / \gamma \beta$ and $2 (m/q - n)^2 \gamma \beta q^2$, respectively, to account for the effect of magnetic field line bending [189].

2.6 Numerical Calculations

In this section we numerically analyze the waves and instabilities arising in the analytical equilibria of Eq. (2.3.4). The discrete spectrum of global modes and instabilities arising in these equilibria will be investigated in chapters 5 and 3, respectively. Here, we will focus on the low-frequency continuous MHD spectrum. In particular we look at the continuum frequencies $\omega_D^2 = \tilde{\omega}_-^2$ given by Eq. (2.5.26a). We consider the cases $\gamma_e = \gamma$, $\gamma_e \to 1$, and $\gamma_e \to \infty$ corresponding to isentropic, isothermal, and isochoric magnetic surfaces.

2.6.1 Solvers

To obtain a numerical representation of the analytical equilibria in the coordinates required for the stability analysis, the equilibrium code FINESSE [8] is used. This FINite Element Solver for Stationary Equilibria, can calculate equilibria with general equilibrium flows in several geometries. In case of purely toroidal flow, in this code we can choose a constant γ_e so that the quantity $A(\psi) = p\rho^{-\gamma_e}$ from Eq. (2.2.14) is a flux function. The limits $\gamma_e \to \infty$ and $\gamma_e \to 1$, for isochoric and isothermal flux surfaces respectively, are included as special cases [14]. Other dedicated equilibrium codes that include both toroidal and poloidal flow are CLIO [167] and FLOW [81]. FINESSE uses a Galerkin approach with isoparametric bi-cubic Hermite basis functions for quartic convergence behaviour.

The linear stability code PHOENIX [15] is used to numerically investigate the continuous spectra. This mixed spectral and finite element code was developed from the CASTOR code [120] by including the ability to treat arbitrary equilibrium flow. The linearised MHD equations result in a generalized eigenvalue problem that is efficiently solved in PHOENIX using the iterative Jacobi-Davidson algorithm [172]. The singular continuum eigenfunctions, obviously, cannot be resolved by the continuous finite element basis functions. The associated eigenfrequencies however can be accurately found by replacing the basis functions by well-ordered constants [158].

2.6.2 Equilibria

The equilibria considered in this section are those of Eq. (2.3.4). The coefficients c_1 and c_2 are adjusted using Eqs. (2.3.10) and (2.3.12) to give an inverse aspect ratio $\epsilon = 0.1$

and ellipticity $E = 1$. The constant $\mathcal{M}^2 = R_0^2 \Omega^2 / 2T_0$ from Eq. (2.3.2) is adjusted to yield a desired central Mach number $M_0 \equiv M(R = R_0)$. The ratio P/J is used to give a β-profile ranging from zero at the plasma edge to a maximum of approximately 0.005. The constant J is obtained as an eigenvalue by the solver so that a normalized flux function ψ between zero at the magnetic axis and one at the edge is obtained [8]. The overall magnitude of ψ was used to rescale the safety factor q. The resulting relatively flat q-profile was centered around $q = 2$ positioned at $s \approx 0.68$, where

$$s \equiv \sqrt{\frac{\psi - \psi_m}{\psi_e - \psi_m}}, \tag{2.6.1}$$

with ψ_e and ψ_m the values of ψ at the edge and the magnetic axis, respectively. A ratio of specific heats $\gamma = 5/3$ was used in all the calculations. The parametric dependencies of Ω, T_0, and ρ_0 are restrained by the ideal gas law $p_0 = \rho_0 T_0$ and the assumption that $\mathcal{M}$ is constant. First, the remaining freedom is used to investigate the effect of rigid rotation, for which T_0 is constant. In Section 2.6.4, Ω^2, T_0, and p_0 are assumed to be of the same form so that ρ_0 is constant.

2.6.3 Convergence

For equilibria including toroidal flow, the analytical solutions of Eq. (2.3.4) are ideally suited to test the accuracy and convergence behaviour of a numerical solver. In this section we show the results of such a test for the equilibrium code FINESSE [8]. The equilibria described in the previous section were used with flux surfaces of constant density, so that the analytical expression Eq. (2.3.24) for the location of the magnetic axis could be used. This allowed the analytical solution to be compared with the numerical solution, which is scaled between zero on the magnetic axis and one at the plasma edge. A central Mach number $M_0 = 1$ was used.

In Fig. 2.2 the difference between the analytical and the numerical solution is shown in both the L^2 and the L^∞ norm, that is the root mean square of the difference and the maximum difference. Both measures of the error go down with the number N of radial and poloidal elements approximately as $1/N^4$, demonstrating fourth order convergence up to a very small error of less than 10^{-10}.

2.6.4 Continuous spectra

In this section, we will investigate the solutions of Eq. (2.3.4) for $\zeta = 1$, $\zeta \to \infty$, and $\zeta = \gamma/(\gamma - 1)$, resulting in magnetic surfaces with constant density, temperature, and specific entropy, respectively.

Isentropic magnetic surfaces

Figure 2.3 shows part of the continuous spectrum for the case that the specific entropy is constant on the magnetic surfaces. As discussed in Section 2.2.3, this may be
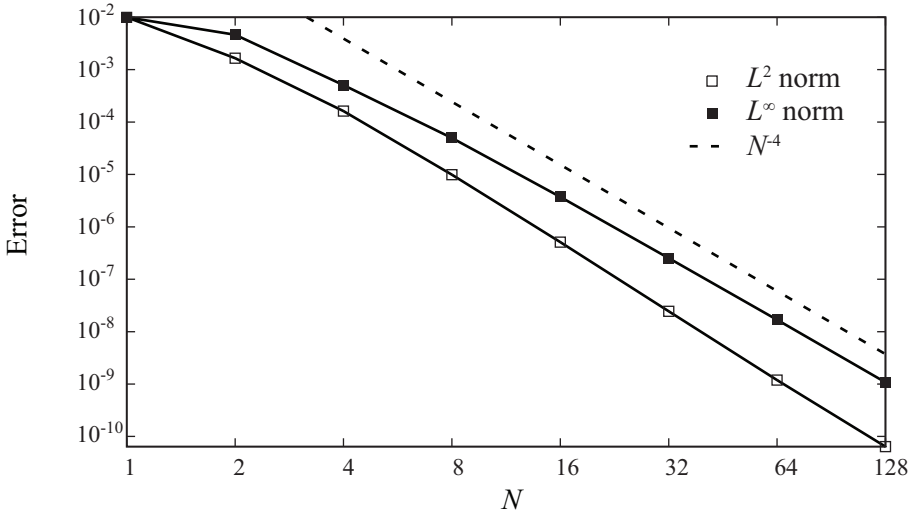
Figure 2.2: The L^n-norm difference $\|\psi_{\text{num.}} - \psi_{\text{an.}}\|_n$ between the numerical solution $\psi_{\text{num.}}$ and the analytical solution $\psi_{\text{an.}}$ of Eq. (2.3.4) with $\zeta = 1$, as a function of the number of finite elements N in the radial and the poloidal direction.
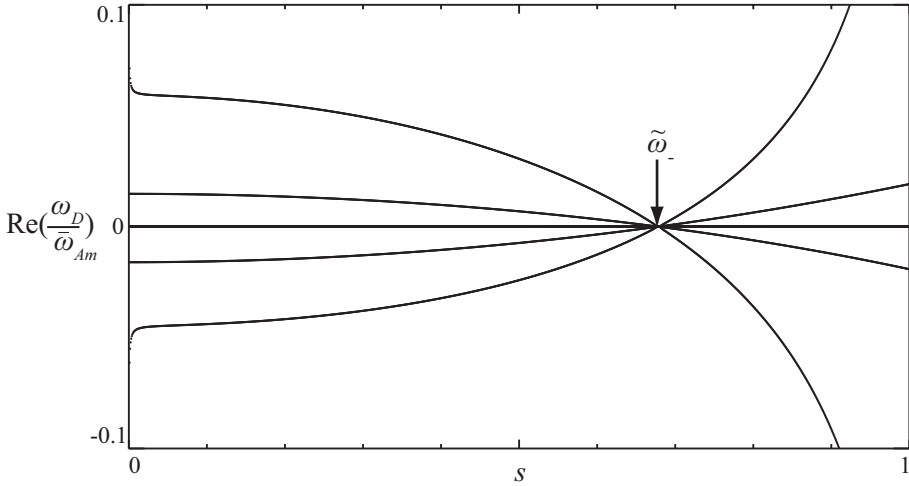
Figure 2.3: The Doppler shifted frequency ω_D normalized by $\bar{\omega}_{Am} \equiv \bar{\omega}_A(\psi_m)$, as a function of the radial coordinate s. The frequencies of the shown $n = 1$-continuum branches vanish at the rational surface at $s \approx 0.68$. The analytical equilibrium solution with isentropic flux surfaces is used with a central Mach number $M_0 = M(R = R_0) = 1$.

appropriate in the presence of significant poloidal flow. The frequencies are Doppler

shifted and non-dimensionalized with $\bar{\omega}_{Am}$, which is $\bar{\omega}_A = B_\phi / \sqrt{\rho_0} R$ evaluated at the magnetic axis. The continuum frequencies are displayed as a function of the radial coordinate s of Eq. (2.6.1), which vanishes at the magnetic axis and assumes the value $s = 1$ at the plasma edge.

Three different continuum branches are shown. The modes with a vanishing Doppler-shifted frequency represent the Eulerian entropy continuum [70]. The two other continua in Fig. 2.3 correspond to the cylindrical continua of Section 2.5.6. The lowest-frequency branch corresponds to slow magnetosonic waves, while the higher frequency branch corresponds to Alfvén waves. As elaborated in Section 2.5.6, compressibility and toroidicity allow Alfvén waves to couple with the slow magnetosonic waves so that the continua acquire a mixed slow-Alfvén polarization. Some cylindrical characteristics however remain, such as the diverging frequency of the Alfvén-like branch towards the plasma edge where the density vanishes.

A toroidal mode number $n = 1$ was used so that in a cylinder, according to Section 2.5.6, the frequency of modes with a poloidal mode number $m = 2$ vanish at the rational surface $q = m/n = 2$. Close to the rational surface, the Alfvén-like frequency branch is described by $\omega_D = \pm\tilde{\omega}_-$ from Eq. (2.5.26a). In a toroidal plasma with isentropic flux surfaces we have $\gamma = \gamma_e$ so that $\tilde{a}_2$ of Eq. (2.5.26c) vanishes. According to Eq. (2.5.26a), $\tilde{\omega}_-$ vanishes in this case at the rational surface as well. As explained in Section 2.4.2, this is due to the fact that without entropy gradients the convective effect is absent.

Isothermal magnetic surfaces

Fig. 2.4 shows the same part of the spectrum as Fig. 2.3, but now the limit $\zeta \to \infty$ is taken in the equilibrium solution (2.3.4) so that the magnetic surfaces become isothermal. The lowest frequency branch is only slightly affected, while the higher frequency branch is lifted upwards. These two continuum frequencies are accurately described by $\omega_D = \pm\tilde{\omega}_-$ from Eq. (2.5.26a). Rotation lifts these continuum frequencies to a finite buoyancy frequency or Brunt-Väisälä frequency due to the negative entropy gradients in the direction of the centrifugal force within the isothermal magnetic surfaces [189].

Fig. 2.5 shows the half-width of the flow-induced continuum gap obtained from the numerical computations, as a function of the Mach number $M_0 \equiv M(R_0)$. These numerical results are compared with the analytical result for $\tilde{\omega}_-$ of Eq. (2.5.26a) and the approximation of Eq. (2.5.27), for low Mach numbers. Surprisingly good correspondence with $\tilde{\omega}_-$ is found up to sonic Mach numbers, even though the aspect ratio $\epsilon = 0.1$ only just satisfies the assumption $\epsilon \ll 1$ used in the derivation of this analytical result. For higher Mach numbers, the flux surfaces start to acquire significant triangularity and the computational results start to deviate slightly from the analytical expression. Due to the excellent correspondence, a comparison such as performed here provides a good standardized test for stability codes including toroidal rotation.
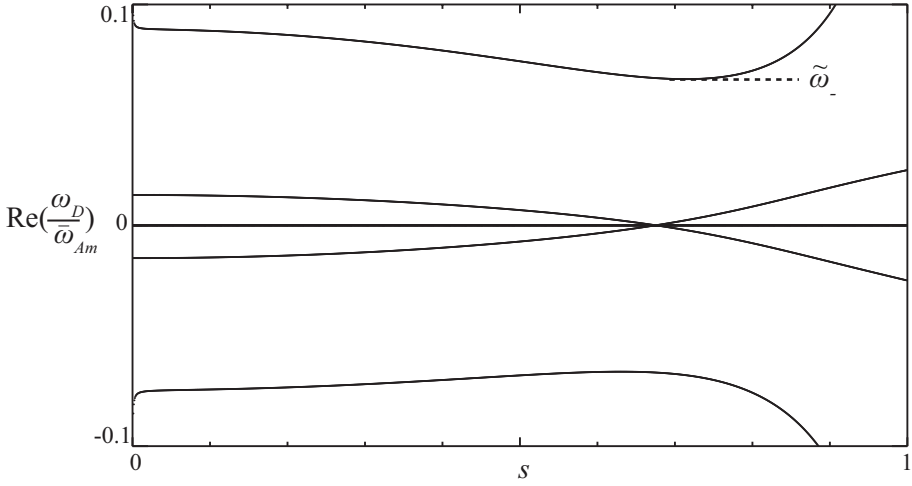
Figure 2.4: The low-frequency $n = 1$ continuous spectrum of the analytical equilibrium with isothermal flux surfaces ($\zeta \to \infty$) for $M_0 = 1$, showing the appearance of a flow-induced continuum gap due to the centrifugal convective effect.
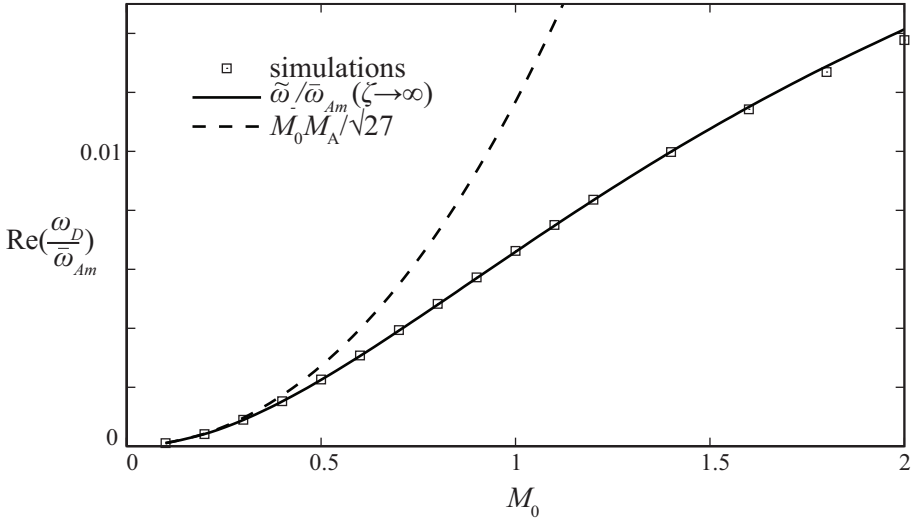
Figure 2.5: The half-width of the flow-induced continuum gap of the analytical equilibrium with isothermal magnetic surfaces as a function of the Mach number M_0. The numerical values (boxes) are compared with the analytical expression for $\tilde{\omega}_-$ from Eq. (2.5.26a) (solid line) and its approximation Eq. (2.5.27) for low M_0 (dashed line) for $q = 2$. Here $M_A = \Omega/\bar{\omega}_{Am}$ is the Alfvén Mach number.
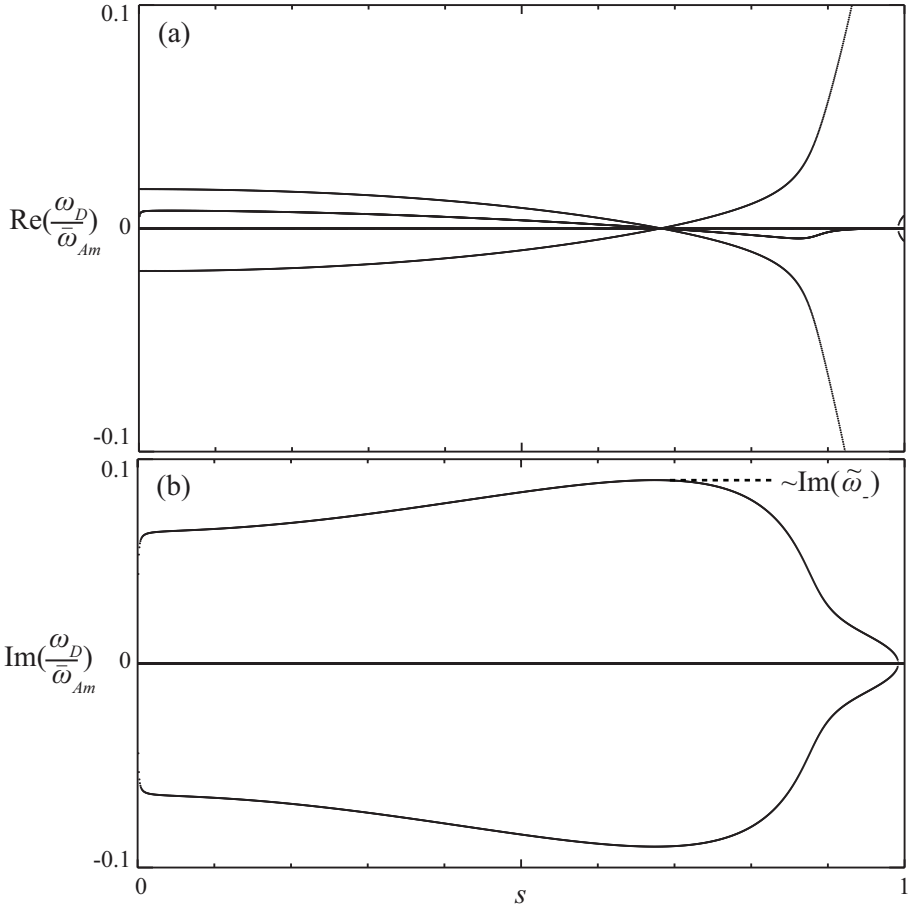
Figure 2.6:   The real (a) and imaginary (b) part of the low-frequency $n = 1$ continuous spectrum of the analytical equilibrium with isochoric flux surfaces ($\zeta = 1$) for $M_0 = 1$. Two of the four continuum branches that are stable near the plasma edge at $s = 1$ form a complex conjugate pair of unstable eigenmodes by entering the complex plane. Their common real frequency deviates slightly from the Doppler shift due to the Coriolis effect.

Isochoric magnetic surfaces

Fig. 2.6a shows again the same part of the spectrum as Figs. 2.3 and 2.4, but now for the equilibrium of Eq. (2.3.4) with $\zeta = 1$ so that the magnetic surfaces have constant density. The low-frequency slow-like branch seems similar to that of Figs. 2.3 and 2.4. Past the rational surface however, the frequency of this continuum diverges. Since the density vanishes as the edge, this is the expected behaviour for Alfvén-like waves. In the core of the plasma, the continuum frequencies are much lower than those for isentropic or isothermal flux surfaces. Apart from a very small region near the plasma
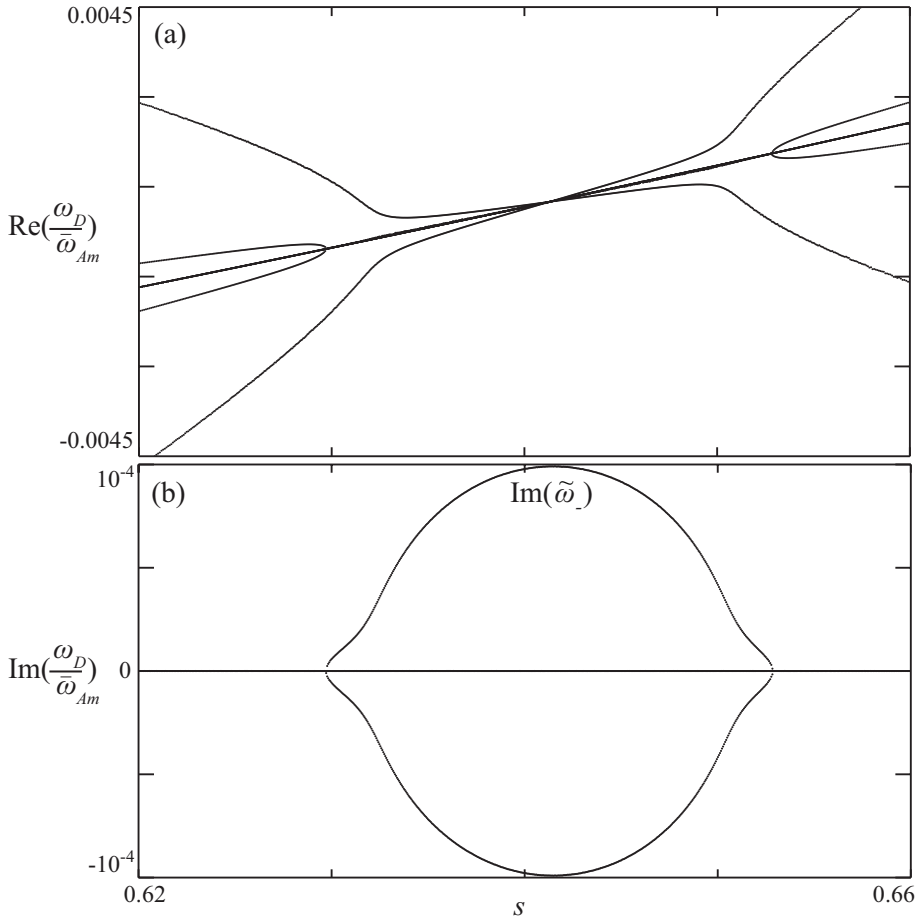
Figure 2.7: The real (a) and imaginary (b) part of the $n = 1$ low-frequency spectrum of the analytical equilibrium with constant density. For $M_0 = 0.1$ only a small part of the tokamak is unstable (note the abscissa).

edge, the slow-like continuum leaves the real axis of the complex frequency plane and acquires an imaginary component.

This imaginary component of the frequency is shown in Fig. 2.7b. As implied by Eq. (2.5.9), the unstable continuum modes turn up as a complex conjugate pair. By Eq. (2.5.1), the continuum mode with a positive imaginary part of the frequency is unstable, while the mode with a negative imaginary part is damped. Because these modes also have a real frequency, these modes oscillate while their amplitude increases (over-stable) or decreases. Note from Fig. 2.6(a) that the real part of the Doppler shifted frequency of this complex conjugate pair of modes only slightly deviates from zero, corresponding to a small Coriolis shift $\bar{V}$ in Eq. (2.5.9). Note from Fig. 2.6(b) that the
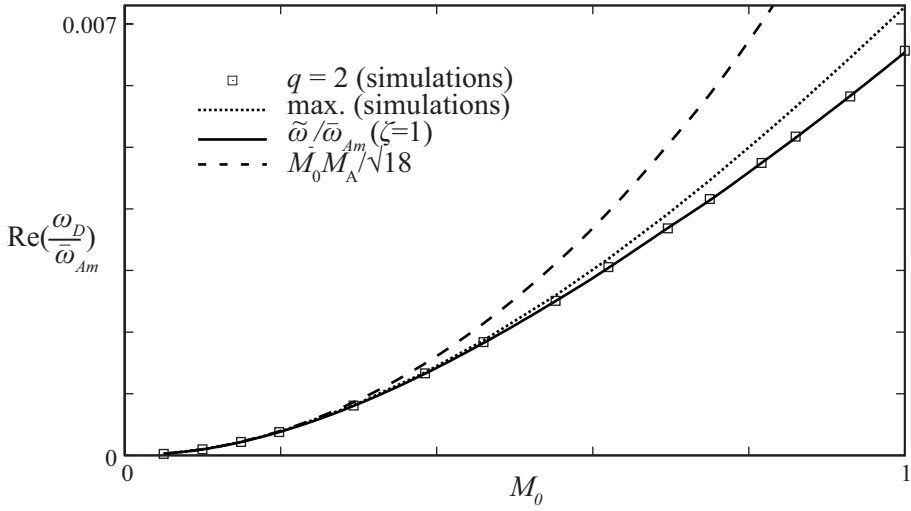
Figure 2.8: The growth rate of the unstable continuous spectrum of the constant density analytical equilibrium as a function of the Mach number M_0. The numerical values for the growth rate at the rational $q = 2$ surface (boxes) and the maximum growth rate (dotted line) are compared with the analytical expression for $\mathrm{Im}(\tilde{\omega}_-)$ of Eq. (2.5.26a) (solid line) and the approximation Eq. (2.5.27) for low M_0 (dashed line), for $q = 2$. Here $M_A \equiv \Omega/\bar{\omega}_{Am}$ is evaluated at the rational surface.

highest growth rate of the continuum modes is close to the rational surface at $s \approx 0.68$, where the magnetic field line bending vanishes. The growth rate decreases towards the plasma edge, primarily due to the effect of the decreasing density on the remaining Alfvén-like character of the modes.

Finally, we investigate the maximum growth rate of the continuous spectrum as a function of the Mach number M_0. We do this for a tokamak with a constant ρ_0 over the entire plasma. In order to satisfy the assumptions of Eq. (2.3.2), this implies that the angular frequency squared goes down towards the plasma edge like p_0. Fig. 2.9(a) shows for $M_0 = 0.1$ the continuum frequencies in a very small region around the rational surface $q = 2$. Because the angular frequency varies over the tokamak, the Doppler shift is no longer constant and the actual frequency ω is shown. The Alfvén-like continuum again becomes unstable over some part of the plasma, resulting in the imaginary part of the frequency shown in Fig. 2.9(b). When the Mach number is increased, both the maximum growth rate and the radial extent over which the continuous spectrum is unstable increase. This is shown in Figs. 2.8 and 2.9, respectively. From Fig. 2.9, the region over which the tokamak becomes unstable spreads with increasing M_0 from a tiny region close to the rational surface, to almost the en-
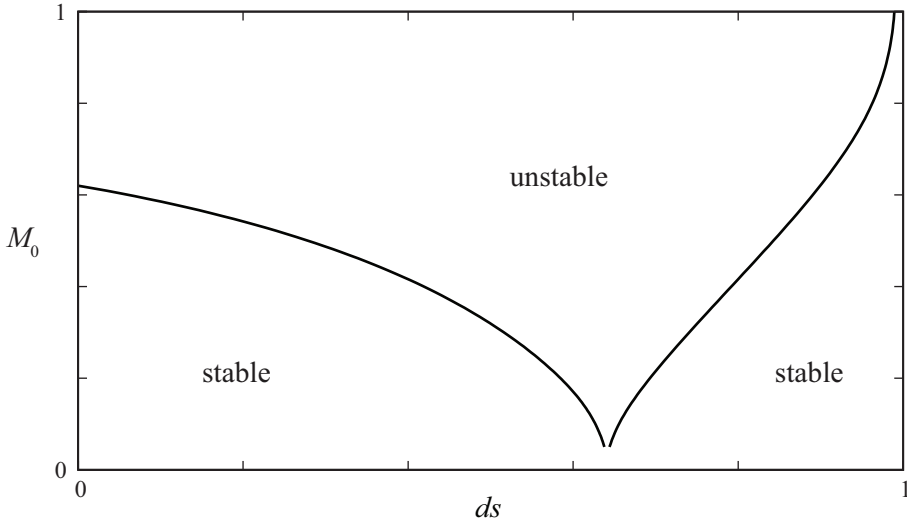
Figure 2.9: The radial extent over which the constant density analytical equilibrium is unstable, as a function of the Mach number M_0. For low M_0, only a small region near the rational surface is unstable, to spread to almost the entire tokamak for $M_0 = 1$.

tire tokamak for $M_0 = 1$.

In Fig. 2.8 the growth rate at the rational surface obtained numerically is compared to $\mathrm{Im}(\tilde{\omega}_-)$ of Eq. (2.5.26a) and the approximation of Eq. (2.5.27). Note that for constant $\mathcal{M}$ in the large aspect ratio limit the Mach number M, evaluated at the rational surface, is equal to $M_0 = M(R = R_0)$. Also shown is the maximum growth rate of the continuum, which occurs closer to the magnetic axis, where the angular frequency is higher. Excellent agreement is obtained between the numerically obtained growth rate at the rational surface and the analytical result, showing again the value of such a comparison for the validation of numerical stability codes.

2.7 Conclusions & Discussion

The axisymmetric stationary ideal MHD equations are reduced to an extended Grad-Shafranov equation (2.3.1) that allows us to specify which thermodynamic quantity is constant on the magnetic surfaces. Analytical equilibrium solutions (2.3.4) have been derived that still contain this freedom. An arbitrary number of vacuum solutions may be added, allowing control over characteristics like the aspect ratio, ellipticity, and triangularity of the equilibrium. Expressions for the Mach number, average beta, and safety factor are derived, revealing some restrictions on attainable values.

The analytical solutions have been used to demonstrate the fourth order convergence of a numerical code, showing their usefulness for testing numerical equilibrium codes including toroidal rotation.

The frequencies of the continuous Alfvén spectrum close to a rational surface of a large aspect ratio, low-β tokamak plasma have been derived including the effects of toroidicity, compressibility, and rotation. These expressions (2.5.26a) still possess the freedom to specify which thermodynamic quantity of the underlying equilibrium is constant on the magnetic surfaces.

The lowest Alfvén continuum frequency of a slowly rotating tokamak is shown to be equal to a heuristically derived expression, Eq. (2.4.8), for the Brunt-Väisälä-frequency due to the centrifugal convective effect on plasma confined to the magnetic surfaces.

Depending on which quantity is constant on the magnetic surfaces, the convective effect either lifts the continuum frequencies to a finite value or destabilizes the continuum. The analytical expressions for the flow-induced gap and the growth rate of the unstable continuum show excellent agreement with the numerical results, showing their merits for the validation of stability codes including toroidal rotation.

The present analytical spectral and equilibrium results generalize various previous results in which initial assumptions were made on which thermodynamic quantity is constant on magnetic surfaces. This work shows that in many cases no such assumption needs to be made at forehand. It is therefore recommended that, when considering purely toroidal rotation, the general parameterizations of Eqs. (2.2.10) and (2.2.11) for the pressure and the density are used to make subsequent analysis as general as possible. The same holds for numerical codes including purely toroidal rotation, where typically the specific choice of isothermal magnetic surfaces is made, unnecessarily restricting the generality offered by the MHD equations.

Chapter 3

Stability of Localized Modes in Rotating Tokamak Plasmas

The ideal magnetohydrodynamic stability is investigated of localized interchange modes in a large aspect ratio tokamak plasma. The resulting stability criterion includes the effects of toroidal rotation and rotation shear and contains various well-known limiting cases. The analysis allows for a general adiabatic index, both for the equilibrium and the dynamics, resulting in a typically stabilizing contribution from the convective effect. A further stabilizing effect from rotation exists when the angular frequency squared decreases radially more rapidly than the density. Flow shear however also decreases the stabilizing effect of magnetic shear through the Kelvin-Helmholtz mechanism. Numerical simulations reveal the merits and limitations of the performed local analysis.

3.1 Introduction.

Current tokamaks often show significant toroidal flow and flow shear, which can have a large impact on stability. Rotation was found to stabilize the resistive wall mode, see for example Ref. [37] and references therein. Flow shear is well known for its role in turbulence suppression, leading to transport barriers. A mitigating influence of flow shear has also been observed for instabilities, like tearing modes [128].

A variety of essentially hydrodynamic instabilities has been investigated experimentally in magnetically confined plasmas. The rotational or centrifugal Rayleigh-Taylor instability for example often appears in field-reversed configurations [188] and has recently been observed in a magnetic dipole experiment [134]. This instability, together with the Kelvin-Helmholtz instability [45] has been extensively studied in the 1970s and 1980s in Q-machines, see for example [117, 178]. More recently, the Kelvin-Helmholtz instability associated with flow shear has been considered to play a role in the scrape-off-layer of tokamak plasmas [62, 166, 179].

Finally, when rotation approaches the ion sound velocity, the centrifugal convective effect can play a stabilizing role. This is sometimes referred to as gyroscopic stabilization after an analogy from the original paper of Ref. [198]. Observations consistent with this predicted effect are reported for sawteeth in MAST [28, 30], TEXTOR [31], and recently for certain ideal magnetohydrodynamic modes [29].

Pressure driven instabilities put an upper limit on the maximum attainable dimensionless pressure β, thereby limiting the performance of a tokamak as an economically viable fusion energy source. In a magnetically confined toroidal plasma, various magnetohydrodynamic instabilities can only develop around rational surfaces. At these magnetic surfaces, the main poloidal and toroidal Fourier harmonics m and n of the unstable mode match the local pitch $q \approx m/n$ of the magnetic field, so that magnetic field line bending is minimal.

In this chapter we investigate the influence of toroidal rotation on interchange instabilities localized near rational surfaces. We use a large-aspect ratio expansion of the linear MHD equations to derive an insightful stability criterion. Numerical simulations serve to test and illustrate selected aspects of the analysis. Both the analytical and the numerical investigations include flow self-consistently and take into account plasma compressibility.

For high n, coupling between poloidal harmonics will enable a mode to balloon outwards into the low-field region of unfavorable curvature. Ballooning modes were found to be further destabilized by rigid rotation [88, 199], primarily by a further enhancement of the unfavorable curvature. Flow shear was often found to have a stabilizing influence [214, 147, 60]. Unless the magnetic shear is very low, this effect may however be small for sub-Alfvénic flow shear [214]. In specific cases the net effect of flow shear was found to be destabilizing [40].

It was found that, at low [140] or reversed [152] magnetic shear, over a large range of parameters the most unstable modes are low or intermediate n 'infernal modes' that can be unstable well below the ballooning mode stability limit. These ideal [219] or re-

sistive [32] modes are driven by pressure gradients and are capable of causing serious disruptions and collapses. For $m = n = 1$ this mode is called the quasi-interchange mode [215, 200], which was used to create an understanding of sawtooth oscillations.

Often a local analysis is performed in which unstable modes are assumed to be highly localized around a rational magnetic surface. An analysis of this kind led to the Mercier criterion [145]. For a tokamak plasma with circular cross-section, a large aspect ratio ϵ^{-1}, and low $\beta \sim \epsilon^2$, a simple stability criterion results [213, 170] that relates q and the maximum allowed pressure gradient to the local magnetic shear. The only difference between this toroidal result and the cylindrical Suydam crite-rion [180, 63, 83] is a stabilizing term due to the average curvature of the toroidal magnetic field. Corrections to the cylindrical result due to plasma flow were obtained in Refs. [86, 18]. Corrections to the toroidal result due to flow shear [35] or centrifugal forces [221, 207] have only been obtained separately and for a ratio of specific heats $\gamma = 1$.

We will generalize these results to include the effects of both flow shear and centrifugal forces. Furthermore, the present analysis allows for an arbitrary adi-abatic index, both for the equilibrium (γ_e) and the dynamics (γ). The most no-table effect associated with $\gamma \neq \gamma_e$ is the convective effect discussed in the previ-ous chapter. The influence of the convective effect is considered experimentally in Refs. [28, 30, 31, 29]. In analytical and numerical studies it was found to stabilize the internal kink mode [198, 206], localized modes [207], and the quasi-interchange mode [202]. We find that, depending on the specific profiles, the net effect of toroidal rotation can be stabilizing or destabilizing. The obtained stability criterion is com-pared to and supplemented with numerical simulations.

3.2 Preliminaries.

3.2.1 Mode equation

To investigate the waves and instabilities that arise in a toroidal axisymmetric equilib-rium, we consider an infinitesimal plasma perturbation

$$\boldsymbol{\xi}(r, \theta, \phi, t) = \sum_m \boldsymbol{\xi}_m(r) e^{i(m\theta - n\phi - \omega t)}. \tag{3.2.1}$$

A flux coordinate system (r, θ, ϕ) is used in which, within the magnetic surfaces la-beled by r, the field lines have a constant pitch $d\phi/d\theta = q(r) \approx rB_\phi/R_0B_\theta$ [204].

The Frieman-Rotenberg equation (2.5.7) for $\boldsymbol{\xi}$ can be simplified for a tokamak plasma with a circular cross-section and inverse aspect ratio $\epsilon \equiv a/R_0 \ll 1$. We will investigate low frequencies $\omega \sim \Omega$ and assume the ordering $\mathcal{M} \sim 1$, $m/q - n \sim \epsilon$, and $\beta \equiv 2p_0/B_0^2 \sim \epsilon^2$. The constant B_0 refers to the magnetic field at the geomet-ric axis $R = R_0$. Expanding Eq. (2.5.7) up to fourth order in ϵ, for non-zero m and n, a mode equation can be obtained for the radial component of the main harmonic

$\zeta \equiv \zeta_m^r(r)$ [204]:

$$(f\zeta')' + g\zeta = h. \tag{3.2.2}$$

Here a prime denotes d/dr and

$$f = r^3 A_1, \tag{3.2.3a}$$

$$g = r^2 A_2' - r(m^2 - 1)A_1, \tag{3.2.3b}$$

where

$$A_1 = \tilde{A}_1 + \left(\frac{m}{q} - n\right)^2, \tag{3.2.4a}$$

$$A_2 = \tilde{A}_1 - n^2 \left(\beta\left(1 - q^2\right) + q^2\alpha_k + q^2\beta_k\right), \tag{3.2.4b}$$

and where[1]

$$\tilde{A}_1 = \frac{(\omega_D^2 - \tilde{\omega}_-^2)(\omega_D^2 - \tilde{\omega}_+^2)}{\omega_A^2 \left(\omega_0^2 - \omega_D^2\right)}, \tag{3.2.5a}$$

$$\alpha_k = \frac{\omega_0^2}{\omega_A^2}\frac{4\Omega\omega_D/n}{\omega_D^2 - \omega_0^2}\left(1 + \frac{\mathcal{M}^2}{\gamma}\right), \tag{3.2.5b}$$

$$\beta_k = \beta\mathcal{M}^2\left(1 + \frac{\mathcal{M}^2}{\gamma_e}\right). \tag{3.2.5c}$$

The frequencies $\tilde{\omega}_\pm$ are given by Eq. (2.5.26a). The Doppler-shifted frequency $\omega_D(r) \equiv \omega + n\Omega$ and $\omega_A(r) \equiv B_0/\sqrt{\rho_0}R_0$.

The function h represents the coupling to the sideband harmonics $\zeta_{m\pm1}^r$ [204]. When the sideband rational surface at $q = (m+1)/n$ is not located within the plasma, this coupling term is given by

$$h = r^{m+1}\tilde{\beta}'I(\zeta), \tag{3.2.6}$$

where $\tilde{\beta} \equiv \beta\left(1 + \mathcal{M}^2\right)$, $C = \frac{1}{2}(1 + m)\left(m^2 R_0/na^{m+1}\right)^2$, and

$$I(\zeta) = \int_0^a r^{m+1}\tilde{\beta}'\zeta dr. \tag{3.2.7}$$

We note that Eq. (3.2.2) can alternatively be written in terms of $\chi \equiv r\zeta$ as

$$r(rA_1\chi')' + \chi\left(r(A_2 - A_1)' - m^2A_1\right) = h. \tag{3.2.8}$$

---

[1]The expressions provided here form the generalization to arbitrary γ_e of the results derived in Ref. [204] for $\gamma_e = 1$. The expressions for the continuum frequencies $\tilde{\omega}_\pm$ were derived in the previous chapter. They will be re-derived in the next chapter, where we will also show that the term α_k does not depend on γ_e. The term proportional to $\mathcal{M}^4$ in β_k does depend on γ_e. Heuristically, this can be understood from Eq. (3.4.1) below. The way that γ_e enters here is again through the variation of the density with R, as in Eq. (2.4.8). That these are the only instances where γ_e appears in Eq. (3.2.2), was verified using computer-algebra by repeating the analytical calculations that lead to the mode equation (3.2.2) for general γ_e [205].

In the derivation of Eq. (3.2.2) in [204] the ordering $m/q - n \sim \epsilon$ was invoked to neglect radial variation in the safety factor. Therefore in all of the above expressions, except $(m/q - n)^2$, q refers to its value m/n at the rational surface. This actually requires an additional assumption of low magnetic shear. Such modes experience little magnetic field line bending so that they can easily be unstable to interchanging adjacent plasma elements. Such interchange modes are sometimes referred to as flute instabilities. In Section 3.3 we will derive a stability criterion for such modes.

3.2.2 Continuous spectrum

The frequencies of Eq. (3.2.9) satisfy $\tilde{\omega}_-^2 \leq \omega_0^2 \leq \tilde{\omega}_+^2$. The continuous spectrum is given by those frequencies for which $A_1 = 0$ so that Eq. (3.2.2) is singular. These continuum frequencies are given by $\omega_D^2 = \omega_\pm^2$, where

$$\omega_\pm^2 = \frac{\omega_0^2}{2} \left(a_1 \pm \sqrt{a_1^2 - a_2} \right). \tag{3.2.9}$$

Here

$$a_1 = \tilde{a}_1 + \frac{\omega_A^2}{\omega_0^2} \left(\frac{m}{q} - n \right)^2, \tag{3.2.10a}$$

$$a_2 = \tilde{a}_2 + 4 \frac{\omega_A^2}{\omega_0^2} \left(\frac{m}{q} - n \right)^2, \tag{3.2.10b}$$

so that

$$A_1 = \frac{(\omega_D^2 - \omega_-^2)(\omega_D^2 - \omega_+^2)}{\omega_A^2 (\omega_0^2 - \omega_D^2)}. \tag{3.2.11}$$

3.3 Derivation of a Stability Criterion

Under certain conditions, the continuum of frequencies $\omega_D^2 = \omega_-^2(r)$ will contain an accumulation point for instabilities. As shown in the previous chapter, ω_-^2 is lifted by rotation to a finite Brunt-Väisälä frequency, associated with a stable entropy stratification. A stabilizing influence can therefore be expected for instabilities clustering at this continuum. We will consider the stability of modes that are radially highly localized, without taking into account the coupling between poloidal harmonics leading to poloidal localization. For such localized modes, the Coriolis shift [66] is much smaller than the Doppler shift so that we can assume that marginal stability holds for $\omega_D \approx 0$. When $\gamma > \gamma_e$, the ω_--continuum will not vanish at the rational surface. Modes clustering at frequencies below this continuum are therefore not automatically unstable.

3.3.1 A local mode equation

We investigate the mode equation (3.2.8) around the radial position $r = r_c$ where the coefficient $r^3 A_1$, multiplying the highest derivative of ξ, has a local minimum. Marginally stable modes will have a Doppler shifted frequency $\omega_D \approx n\Omega' x$ that vanishes at $x \equiv r - r_c = 0$. To second order in x, Eq. (3.2.4a) gives

$$A_1 = \frac{\omega_-^2 \omega_+^2}{\omega_A^2 \omega_0^2} \left(1 + \frac{(n\Omega')^2}{\omega_0^2} x^2 \right) - \frac{\omega_-^2 + \omega_+^2}{\omega_A^2 \omega_0^2} (n\Omega')^2 x^2 \tag{3.3.1}$$

$$= \frac{a_2 \omega_0^2}{4\omega_A^2} \left(1 + \frac{(n\Omega')^2}{\omega_0^2} x^2 \right) - \frac{a_1}{\omega_A^2} (n\Omega')^2 x^2 \tag{3.3.2}$$

$$= \tilde{A}_1 + \left(\frac{m}{q} - n\right)^2 + \left(\frac{\tilde{A}_1}{\omega_0^2} - \frac{\tilde{a}_1}{\omega_A^2}\right) (n\Omega')^2 x^2, \tag{3.3.3}$$

where, evaluated for $\omega_D = 0$

$$\tilde{A}_1 \equiv \frac{\tilde{a}_2 \omega_0^2}{4\omega_A^2} = \left(\frac{1}{\gamma_e} - \frac{1}{\gamma}\right) \beta \mathcal{M}^4. \tag{3.3.4}$$

For $\gamma > \gamma_e$, there will in general be a small difference $\Delta r \equiv r_c - r_s$ between the rational surface at $r = r_s$ and $x = 0$ so that $(m/q - n)^2 = (nq'/q)^2 \left(x^2 + 2x\Delta r + (\Delta r)^2\right)$. Using Eq. (3.3.3), we can write to second order in x

$$r^3 A_1 \approx r_c^3 \left(1 - \tilde{M}_A^2\right) \left(\frac{nq'}{q}\right)^2 \left(\delta^2 + x^2\right). \tag{3.3.5}$$

where, evaluated at $x = 0$:

$$\tilde{M}_A^2 \equiv M_A^2 - M_B^2 \equiv \left(\frac{q}{q'}\right)^2 \Omega'^2 \left(\frac{\tilde{a}_1}{\omega_A^2} - \frac{\tilde{A}_1}{\omega_0^2}\right) \tag{3.3.6}$$

$$\delta^2 = \frac{\tilde{A}_1}{1 - \tilde{M}_A^2} \left(\frac{q}{nq'}\right)^2. \tag{3.3.7}$$

In writing Eq. (3.3.5), we assumed that

$$\frac{(\Delta r)^2}{|1 - \tilde{M}_A^2|} \ll \delta^2 \ll r_c^2. \tag{3.3.8}$$

The first inequality was used to neglect the magnetic field line bending at $x = 0$ to write $A_1(x = 0) = \tilde{A}_1$. The second inequality was used to neglect the contribution to Eq. (3.3.5) due to the variation in r^3. Finally, we assumed the contribution of $\tilde{A}_1''$ to be negligible. The implications of the orderings of Eq. (3.3.8) will be discussed in

Sections 3.3.2 and 3.3.4, respectively. Using $\beta/\omega_0^2 = 2q^2/\gamma\omega_A^2$ we can write

$$\tilde{M}_A^2 \equiv \tilde{\alpha}_1 \left(\frac{q}{q'}\right)^2 \frac{\Omega'^2}{\omega_A^2}, \tag{3.3.9}$$

$$\tilde{\alpha}_1 = 1 + 2q^2 \left[1 + 4\mathcal{M}^2/\gamma + \mathcal{M}^4/\gamma^2\right]. \tag{3.3.10}$$

Note the small difference in this modified inertial enhancement factor $\tilde{\alpha}_1$ compared to $\tilde{a}_1$. Using Eq. (3.3.5), the mode equation (3.2.2) can locally be written as

$$\left(\left(\delta^2 + x^2\right)\xi'\right)' + D\xi = \tilde{h}, \tag{3.3.11}$$

where $\tilde{h} \equiv h(q/nq')^2/\left(1 - \tilde{M}_A^2\right)$ and, evaluated at $x = 0$,

$$D = \frac{\delta^2}{A_1}\frac{g}{r^3} = \frac{rA_2' - \left(m^2 - 1\right)\tilde{A}_1}{1 - \tilde{M}_A^2}\frac{1}{r^2}\left(\frac{q}{nq'}\right)^2. \tag{3.3.12}$$

With $\omega_D = n\Omega'x$, the quantity α_k' at $x = 0$ is given by

$$\alpha_k' = -\frac{4\Omega\Omega'}{\omega_A^2}\left(1 + \frac{\mathcal{M}^2}{\gamma}\right) = -2\beta\mathcal{M}^2\frac{\Omega'^2}{\Omega^2}\left(1 + \frac{\mathcal{M}^2}{\gamma}\right). \tag{3.3.13}$$

We note that instead of Eq. (3.2.2) the mode equation (3.2.8) for $\chi = r\xi$ could have been used. Where $(rA_1)' = 0$, we can write $r\left(A_2 - A_1\right)' - m^2A_1 = rA_2' - \left(m^2 - 1\right)A_1$, yielding again Eq. (3.3.11) and Eq. (3.3.12).

3.3.2 Localized mode solutions

The solutions to the local equation (3.3.11) are

$$\xi(x) = c_1 P_\nu\left(\frac{ix}{\delta}\right) + c_2 Q_\nu\left(\frac{ix}{\delta}\right) + \frac{\tilde{h}}{D}, \tag{3.3.14}$$

where the degree of the Legendre functions P and Q is $\nu = -1/2 + \sqrt{1/4 - D}$. When $\gamma = 1$ or $\mathcal{M} = 0$, δ vanishes and these solutions become $x^{\nu\pm}$ with $\nu_\pm = -1/2 \pm \sqrt{1/4 - D}$. For $D > 1/4$ these solutions are rapidly oscillating and diverging near $x = 0$. The solution (3.3.14) has a characteristic length scale δ. In line with the local character of the present analysis, Eq. (3.3.8) requires that $\delta \ll r_c$. From Eq. (3.3.7) we see that magnetic shear ensures mode localization, especially for high n. Also, the closer the mode frequency is to that of the continuum, as measured by $\tilde{A}_1$, the more localized they become.

3.3.3 A local stability criterion

When the degree ν is real, the solution (3.3.14) is radially non-oscillatory so that stability is ensured. This is the case when $D < 1/4$, which yields the stability criterion

$$\left(1 - \tilde{M}_A^2\right) \frac{r}{4} \left(\frac{q'}{q}\right)^2 > -\beta'(1 - q^2) + q^2 \left(S_\gamma + S_C + S_k\right), \tag{3.3.15}$$

where, evaluated at $x = 0$ for $\omega_D = 0$

$$S_\gamma = \frac{1}{m^2} \left(\tilde{A}_1' - \frac{m^2 - 1}{r} \tilde{A}_1\right), \tag{3.3.16}$$

$$S_C = -\alpha_k' = 2\beta\mathcal{M}^2 \left(1 + \frac{\mathcal{M}^2}{\gamma}\right) \frac{\Omega^{2'}}{\Omega^2}, \tag{3.3.17}$$

$$S_k = -\beta_k' = -\left[\beta\mathcal{M}^2 \left(1 + \frac{\mathcal{M}^2}{\gamma_e}\right)\right]'. \tag{3.3.18}$$

Alternatively, the multiplicative factor $1 - \tilde{M}_A^2$ can be taken into account by adding $q^2 S_s$ to the right-hand side of Eq. (3.3.15), where

$$S_s = \frac{r}{4} \frac{\tilde{\alpha}_1}{q^2} \frac{\Omega'^2}{\omega_A^2}. \tag{3.3.19}$$

3.3.4 Ordering

Within the ordering used in the derivation of Eq. (3.2.2), the terms in the stability criterion (3.3.15) are all of order $\beta \sim \epsilon^2$. The dimensionless flow $\mathcal{M}$ and flow shear $\tilde{M}_A$ can both be of order unity. The conditions (3.3.8) used in the derivation of Eq. (3.3.15) introduce some additional restrictions on the quantities involved. The second inequality of Eq. (3.3.8), $\delta^2 \ll r_c^2$, requires

$$\left(\frac{1}{\gamma_e} - \frac{1}{\gamma}\right) \beta\mathcal{M}^4 \ll |1 - \tilde{M}_A^2| r_c^2 \left(\frac{nq'}{q}\right)^2. \tag{3.3.20}$$

Since $a^2 \left(nq'/q\right)^2$ is of the same order as β, the analysis breaks down when either $(r_c/a)^2$ or $|1 - \tilde{M}_A^2|$ becomes too small and Eq. (3.3.20) additionally requires

$$\frac{1}{\gamma_e} - \frac{1}{\gamma} \ll 1 \quad \text{or} \quad \mathcal{M}^4 \ll 1. \tag{3.3.21}$$

In the stability condition (3.3.15) γ appears as a free parameter, whereas for high $\mathcal{M}$ Eq. (3.3.21) requires the use of $\gamma \approx \gamma_e$. We will look at the two options of Eq. (3.3.21) explicitly in the Sections 3.5.2 and 3.5.3 respectively.

Note that for low n, the assumptions of low magnetic shear and (3.3.20) makes S_γ

negligible. For $n \gg 1$, the part $S_\gamma \approx -\tilde{A}_1/r$ may however still be relevant. This is because, for $n \gg 1$, magnetic shear ensures mode localization even when $\tilde{A}_1$ increases.

When either $\mathcal{M} = 0$ or $\gamma = 1$, the continuum frequency ω_- vanishes at the rational surface so that $\omega_D = 0$ becomes a cluster point. In these particular cases, the result (3.3.15) could have been obtained in a more formal fashion using the Frobenius method [9]. This approach will be followed in chapter 6.

Using $S_\gamma \approx -\tilde{A}_1/r$ and $\beta \mathcal{M}^2 = \Omega^2/\omega_A^2$, Eq. (3.3.15) can be written

$$\frac{r}{4}\left(\frac{q'}{q}\right)^2 > -\beta' + q^2 \left[\beta \left(1 - \mathcal{M}^2 - \mathcal{M}^4/\gamma_e\right)\right]'$$

$$+ \frac{q^2}{\omega_A^2}\left(r\tilde{\alpha}_1 \left(\frac{\Omega'}{2q}\right)^2 + 2\Omega^{2\prime}\left(1 + \frac{\mathcal{M}^2}{\gamma}\right) - \left(\frac{1}{\gamma_e} - \frac{1}{\gamma}\right)\frac{\Omega^2\mathcal{M}^2}{r}\right). \qquad (3.3.22)$$

3.4 Physical Interpretation

In the absence of flow, stability criteria (3.3.15) or (3.3.22) reduce to a well-known expression for local stability, discussed in Section 3.5.1. The left-hand side of Eq. (3.3.15) or (3.3.22) shows the stabilizing effect associated with the bending of magnetic field lines. The right-hand side contains the destabilizing pressure gradient β' and the stabilizing term $q^2\beta'$, representing the average interchange effects of poloidal and toroidal magnetic field curvature respectively. The physical interpretation of the various flow terms will be discussed next.

3.4.1 The convective term S_γ

The assumption underlying the appearance of the stabilizing S_γ term, is that of adiabatic plasma motion conserving $S \equiv p\rho^{-\gamma}$. The mechanism was extensively discussed in the previous chapter. When the pressure adjusts instantaneously, an adiabatically displaced plasma element will have a relative density difference with its environment proportional to $-S'/\gamma S$. A displacement in the direction of a force g per unit mass, will therefore yield an oscillation frequency $\omega_{BV} \equiv \sqrt{-gS'/\gamma S}$. This Brunt-Väisälä-frequency or buoyancy frequency describes stable oscillations when the specific entropy function S decreases in the direction of the body force. Otherwise its gives the growth rate of instability. Plasma confined to a magnetic surface will encounter an increasing pressure (2.2.10) in the direction of the centrifugal force. When $\gamma > \gamma_e$ the specific entropy, as obtained in Eq. (2.4.8), will then be decreasing, exerting a stabilizing influence. This stabilizing centrifugal convective effect, or gyroscopic stabilization after Ref. [198], was considered for sawteeth in tokamaks in Refs. [28, 30, 31, 29].

3.4.2 The kinetic energy term S_k

Previously, this term was found in the study of ballooning modes [199], the internal kink mode [198], and localized modes [221, 207]. The term corresponds to a variation of the kinetic energy density [221]

$$\frac{\partial}{\partial r}\left(\mathbf{R}\cdot\nabla\frac{1}{2}\rho R^2\Omega^2\right) \approx \left[2p_0\mathcal{M}^2\left(1+\frac{\mathcal{M}^2}{\gamma_e}\right)\right]' = B_0^2\beta_k', \tag{3.4.1}$$

where we used Eq. (2.2.10). Typically in a tokamak both p_0 and $\mathcal{M}$ decrease radially, furthering instability by effectively diminishing the toroidal curvature term $q^2\beta'$.

The origin of S_k can be traced back to the last term in Eq. (2.5.7), which is associated with a potential energy $\xi_R^*\xi_\psi\partial\rho\Omega^2/\partial\psi$, the second term of Eq. (2.5.17). This shows that S_k requires the perturbation to have a component in the direction of the centrifugal force and the magnetic surface.

The origin of a kinetic energy gradient as a source of instability can be understood by considering a thin differentially rotating disk with a small perpendicular magnetic field, for example an astrophysical accretion disk [16]. Adding the Brunt-Väisälä-frequency squared of an incompressible plasma perturbation $R\Omega^2\rho'/\rho$ and the frequency squared $R\Omega^{2'}$ of the magnetorotational instability [195, 6] yields $R\left(\rho\Omega^2\right)'/\rho$ [168, 61] as in Eq. (1.3.7). Instability resulting from a gradient in the kinetic energy may therefore be understood as a combination of the magnetorotational instability and the convective instability.

The *incompressible* buoyancy-frequency $\omega_{\text{BV},\perp}^2 = \rho'R\Omega^2/\rho$ of Eq. (2.4.5) appears because it results from radial plasma perturbations, that are nearly incompressible due to the large energy associated with magnetic compression. This instability is analogous to the Rayleigh-Taylor instability of a fluid on top of a lighter fluid. Contrary to the magnetorotational instability, this instability is often observed in experiments, see for example [117, 178, 188, 134].

3.4.3 The Coriolis-pressure term S_C

Because this term derives from the radial variation of the Doppler shift $\omega_D' = n\Omega'$ through α_k' it is expected to play a role only for non-axisymmetric perturbations. Typically in a tokamak $\Omega^{2'} < 0$ so that S_C is stabilizing.

A potential energy term proportional to $\rho\Omega^{2'}$ was found in Refs. [199] and [198, 208] in relation to ballooning modes and the internal kink mode, respectively.

In Ref. [199], an integrated form of S_C was associated with the kinetic energy of the fluttering motion occurring as the plasma flows past the perturbation. Its origin can be traced back to the Coriolis term in Eq. (2.5.7). In the next chapter the physical mechanism behind this term will be elucidated as an interplay between the Coriolis effect and the pressure.

Different from S_s, and the shear stabilization effect found for ballooning modes [214,

147], the sign of Ω' is important for S_C. Contrary to the magnetorotational instability, S_C is stabilizing for a radially decreasing angular frequency. It may therefore be very well possible to experimentally observe the influence of this term on stability.

3.4.4 The shear term S_s

The prefactor $1 - M_A^2$ already appears in the cylindrical result [85, 86, 18], where $\tilde{a}_1 = 1$. The quantity M_A is sometimes referred to as the Alfvén Mach number and gives the ratio between the flow shear and the frequency shear of Alfvén waves. When these shears match, an instability does not bend the field lines and the magnetic shear term vanishes. In this way, flow shear effectively diminishes the stabilizing influence of magnetic field line bending. This destabilizing effect of $S_s \sim \rho\Omega'^2$ is essentially that of the Kelvin-Helmholtz instability, modified by toroidicity, rotation, and a magnetic field. For a torus, a similar term was found in [35, 96] and in [221], where it was eventually neglected due to the used ordering. Experimentally this instability has been studied in magnetically confined plasmas mainly in Q-machines, see for example Refs. [45, 117, 178].

The same quantity $1 - M_A^2$ with $\tilde{a}_1 = 1$ multiplies the highest derivative term in ballooning mode equations [214, 147] at marginal stability. For moderate flow shears this Kelvin-Helmholtz term was found to lead to shear destabilization [214, 40] of ballooning modes. For higher flow shears with $M_A \approx 1$, however, complete stabilization was obtained due to the effect of flow shear on poloidal mode coupling [60]. Nonlinearly, interchanges may also be stabilized by flow shear [89, 108].

Note that Eq. (3.3.6) reveals a stabilizing influence of the convective effect on the Kelvin-Helmholtz instability for high $\mathcal{M}^4$. The stabilizing Brunt-Väisälä term M_B^2, diminishes the destabilizing shear term M_A^2 in such a way that the $\mathcal{M}^4/\gamma\gamma_e$ term in $\tilde{a}_1$ is replaced by $\mathcal{M}^4/\gamma^2$ in $\tilde{\alpha}_1$.

3.5 Various Limiting Cases

3.5.1 No flow: $\mathcal{M} = 0$

Without rotation, $S_\gamma = S_k = S_C = 0$ so that Eq. (3.3.15) reduces to the Shafranov-Yurchenko condition [213, 170]

$$\frac{r}{4}\left(\frac{q'}{q}\right)^2 > -\beta'\left(1 - q^2\right),\tag{3.5.1}$$

which is a limiting case of the Mercier criterion [145] for large aspect ratio plasmas with a circular cross-section. In the cylindrical limit $q \to 0$, the last term vanishes so that Eq. (3.5.1) reduces to Suydam's criterion [180] for static cylindrical plasmas.

3.5.2   Some flow: $\mathcal{M}^4 \ll 1$

Neglecting terms proportional to $\mathcal{M}^4$, the stability criterion (3.3.15) can be written as

$$\frac{r}{4}\left(\frac{q'}{q}\right)^2 > -\beta'\left(1-q^2\right) + \frac{q^2}{\omega_A^2}\left(\rho\left(\frac{\Omega^2}{\rho}\right)' + \left(1+2q^2\right)\frac{r\Omega'^2}{4q^2}\right), \tag{3.5.2}$$

where $\rho\left(\Omega^2/\rho\right)' = 2\Omega^{2'} - (\rho\Omega^2)'/\rho$ derives from the sum of S_C and S_k respectively. When the angular frequency squared decreases faster than the density, this term is stabilizing. The shear term in Eq. (3.5.2) on the other hand is always destabilizing. The net effect of rotation therefore depends crucially on the specific angular frequency and density profile.

Note that the condition $\mathcal{M}^4 \ll 1$ is appropriate for most tokamak plasmas, where the rotation velocity is usually smaller than the ion sound velocity. The stability criterion (3.5.2) may be of some relevance to assess the influence of toroidal rotation on transport barriers, which typically have low magnetic shear but high flow shears. For high $\beta \sim \epsilon$ and large n, however, flow shear influences poloidal coupling, potentially leading to complete stabilization of ballooning modes [147, 214, 60].

3.5.3   Isothermal: $\gamma = \gamma_e = 1$

When instabilities arise on a slow enough time-scale for heat exchange with their environment to take place, it may be appropriate to assume $\gamma = \gamma_e = 1$. In this case, S_γ vanishes so that Eq. (3.3.15) gives with $\beta_k = \beta\mathcal{M}^2\left(1+\mathcal{M}^2\right)$

$$\frac{r}{4}\left(1-M_A^2\right)\left(\frac{q'}{q}\right)^2 > -\beta'\left(1-q^2\right) + q^2\beta_k\left(\frac{2\Omega^{2'}}{\Omega^2} - \frac{\beta_k'}{\beta_k}\right). \tag{3.5.3}$$

Apart from the new shear term involving M_A^2, this stability criterion is equal to those of Refs. [221, 207] derived for $\gamma = \gamma_e = 1$. For $\mathcal{M}^4 \ll 1$, $\beta_k \approx \beta\mathcal{M}^2 = \rho\Omega^2/B_0^2 = \Omega^2/\omega_A^2$ so that Eq. (3.5.3) can be written as

$$\frac{r}{4}\left(\frac{q'}{q}\right)^2 > -\beta' + q^2\left(\beta-\beta_k\right)' + \frac{2q^2\Omega^{2'} + r\left(1+2q^2\right)\Omega'^2/4}{\omega_A^2}. \tag{3.5.4}$$

For a rigidly rotating plasma with $\gamma = \gamma_e = 1$ as well as $\mathcal{M}^4 \ll 1$, the only effect of flow on localized modes is therefore the subtraction of the kinetic energy density from the pressure in the toroidal curvature term.

3.5.4   Cylindrical limit

In the cylindrical limit $q \to 0$, the only remaining effect of flow is through the factor $1-M_A^2$ multiplying the magnetic shear term, with $M_A = (q/q')\Omega'/\omega_A$. The resulting

stability criterion may be compared with the cylindrical result [85, 86, 18] for purely longitudinal flow, where the same factor $1 - M_A^2$ appears.

The cylindrical result however contains an additional term with a trans-slow resonance for $M_A^2 = \gamma p / (B^2 + \gamma p)$, that is absent in Eq. (3.3.15). This is due to the ordering assumed in the derivation of the mode equation (3.2.2). The missing term is $O\left(B_\theta^2 / B_\phi^2\right) = \epsilon^2$ smaller than the other terms, which is why it does not appear in the present large-aspect ratio result. This trans-slow resonance also disappears in a proper kinetic treatment [17]. Physically, within the present ordering there is no coupling between the m, n-Alfvén continuum modes and the slow magnetosonic continuum, only with its $m \pm 1, n$-sidebands. This is due to the fact that in cylindrical geometry, the slow magnetosonic sidebands cross at the rational surfaces, enhancing the interaction with the Alfvén continuum.

3.6 Simulations

To illustrate some aspects of the obtained stability criterion (3.3.15), we investigate the stability of a specific rotating equilibrium numerically. The analytical rigidly rotating isothermal equilibrium of Eq. (2.3.4) is used with $\gamma = 5/3$, $\epsilon = 0.1$, and β between zero at the plasma edge and a maximum $\beta \approx 0.015$. This resulted in a monotonically increasing q-profile, centered around $q_0 = 1$ at $r_c \approx 0.6$, where $q' \approx 0.023$. For this low shear equilibrium with constant Ω and $\mathcal{M}$, Eq. (3.3.15) predicts instability for $\mathcal{M} \ll 1$ when

$$\mathcal{M} > \sqrt{-rq'^2/4\beta'} \approx 0.1. \tag{3.6.1}$$

The ideal MHD spectrum of waves and instabilities of this equilibrium was investigated with PHOENIX [15], including 7 poloidal harmonics in the eigenvalue calculation. Convergence checks with more poloidal harmonics have been performed to ensure the accuracy of the results.

Local stability criteria, are sufficient conditions for stability only for modes that are localized only radially. Especially for high mode numbers, modes will localize also poloidally at the low-field side. We may therefore expect Eq. (3.3.15) to be a better guide for stability at low mode numbers, which is what we will focus on. As discussed at the end of Section 3.3.2, mode localization in this case has to come primarily from closeness of the mode frequencies to the continuum.

3.6.1 Quasi-interchange mode

For $m = n = 1$, a Sturmian sequence of unstable modes appears above a Mach number $M_0 = \sqrt{5/6}\mathcal{M} \approx 0.15$, consistent with Eq. (3.6.1). Fig. 3.1(b) shows the growth rate of these unstable quasi-interchange modes for various Mach numbers M_0. The real part of the Doppler shifted frequency of the instability, the Coriolis shift [66], is not
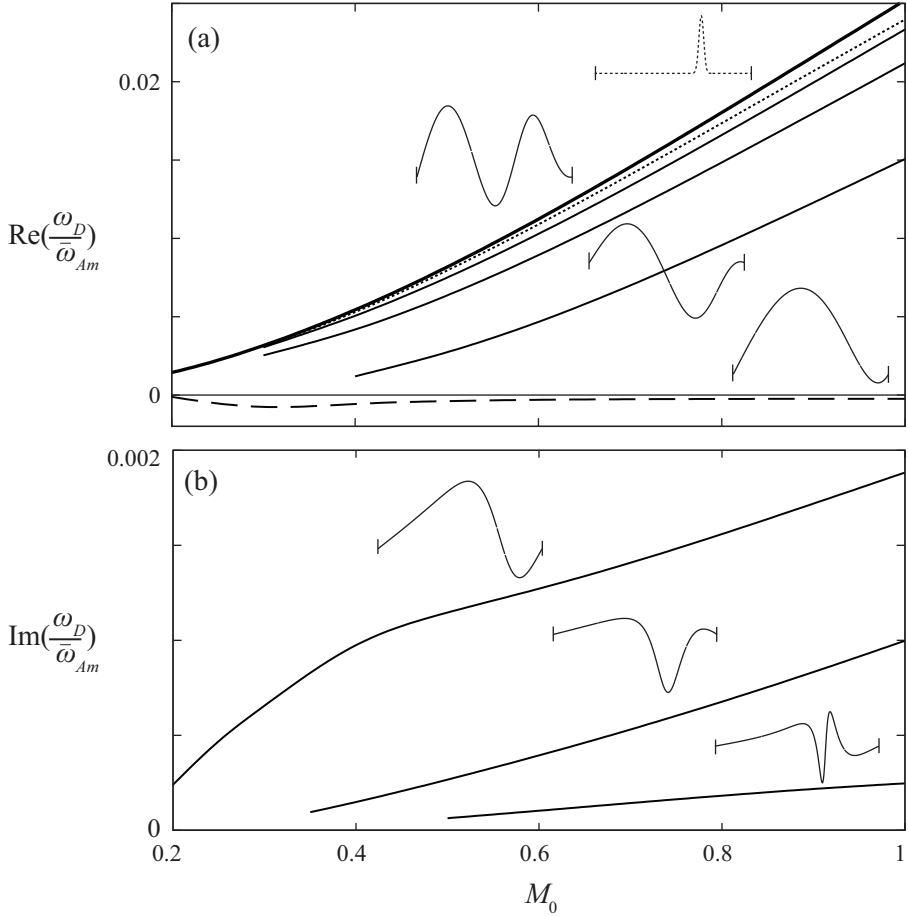
Figure 3.1:   (a) The Doppler-shifted frequency ω_D divided by $\omega_{Am} \equiv \bar{\omega}_A(\psi_m)$, of the ω_--continuum (thick line), the first zonal flow mode (dots), the first three global Alfvén modes (solid), and the most unstable interchange mode (dashes). (b) The dimensionless growth rate of the most unstable modes as a function of $M_0 = \sqrt{5/6}\mathcal{M}$. The radial perturbation of the stable and unstable modes and the poloidal perturbation of the zonal flow-modes is displayed for $M_0 = 1$. Note that the smaller the growth rate of the unstable modes, the more localized they are.

monotonic in M_0, as is shown in Fig. 3.1(a). It does become very small for marginally stable modes, justifying the use of $\omega_D = 0$ in the performed stability analysis.

3.6.2   Other modes

Fig. 3.1(a) also shows two types of modes that we will discuss in more detail in chapter 5. A Sturmian sequence of modes is present, that have a finite amplitude only in a small range around the rational surface and are polarized within the magnetic surfaces. The frequency and characteristics of these modes allows us to identify them as a type of non-axisymmetric zonal flow modes. The frequency of these modes is always somewhat below the continuum frequency $\omega_D^2 = \omega_-^2$, so that these modes were found to become slightly unstable for low M_0.

The stable global rotation-induced Alfvén modes discussed in chapter 5 appear above $M_0 \approx 0.15$, along with the unstable modes. These modes also cluster below the ω_--continuum frequency as shown in Fig. 3.1(a). The mode structure of the unstable modes is very similar to that of these stable Alfvén modes. Both modes have a single dominant poloidal mode number that is resonant with the rational surface and small sideband amplitudes.

The most significant difference is in the parallel component, which is much larger for the unstable modes. The unstable modes apparently couple more strongly with slow magnetosonic waves to form a mixed slow-Alfvén eigenmode. For higher mode numbers, the radial component becomes more significant compared to the poloidal component. Also the sideband amplitudes of the parallel component become more and more significant for higher mode numbers. For $n = 10$ for example, the $m = 9$ and $m = 11$ side bands of the parallel displacement become an order of magnitude larger than the main $m = 10$ component.

3.6.3   Infernal modes

Fig. 3.2 shows, for $M_0 = 1$, the growth rate of the first few most unstable modes with the toroidal mode numbers n from 1 to 10. Compared to $n = 1$ the maximum growth rate increases by almost two orders of magnitude, to reach a dangerously high growth rate of almost $\mathrm{Im}(\omega_D) \approx 0.1\bar{\omega}_{Am}$ for $n = 10$.

With increasing n, coupling to poloidal sideband harmonics becomes more important. For the present case, even for $n = 10$, the neighboring rational surfaces at $q = (n \pm 1)/n$ lie outside the plasma due to the low magnetic shear. The mode can minimize magnetic field line bending by shifting its poloidal sidebands in the direction of their respective rational surface. This effect is indeed observed in the simulations. These sideband amplitudes have opposite sign, to give localization at the low-field side. This weak ballooning is visible primarily in the parallel displacement, the component that does not bend the field lines.

In Fig. 3.2 the growth rate is shown for the same equilibrium, using $\gamma = 1$ in the stability calculations. The effect of $\gamma > 1$ is seen to be largest for modes with a higher
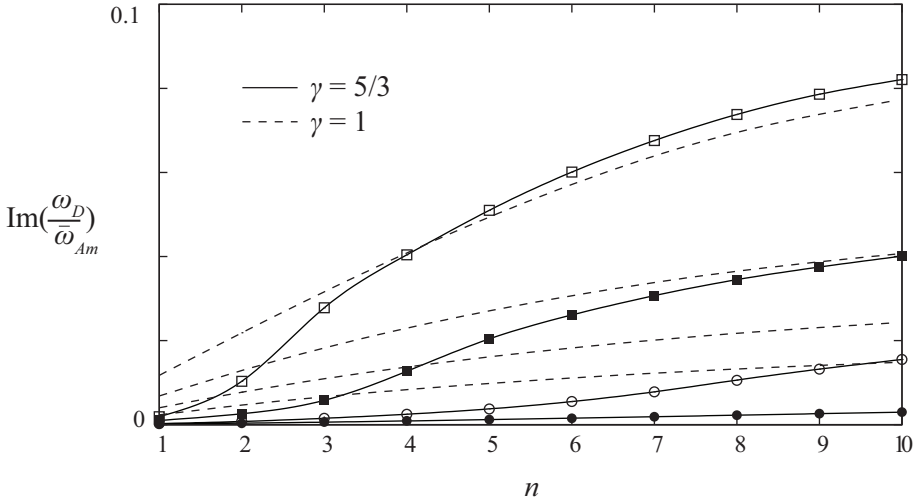
Figure 3.2: The growth rate of the first few unstable modes as a function of $n = m$ for $M_0 = 1$.

number of nodes. The stabilization is also most effective for low-m, n modes, which may be explained by the term S_γ in Eq. (3.3.16). The modes shown in Fig. 3.2 are far from marginality and not localized enough to justify the analysis of Section 3.3. The Mercier index D from Eq. (3.3.12) may however be used as a first approximation for the terms multiplying ζ in the mode equation (3.2.2). The term (3.3.16) contains a part inversely proportional to m that is stabilizing when $\tilde{A}_1' < -\tilde{A}_1/r$. For the present equilibrium this requires $|\beta'| > \beta/r$ which, for $r \approx r_s \approx 0.6$ is indeed the case.

Another observation from the data in Fig. 3.2 is that the growth rate decreases approximately exponentially with the number of nodes of the unstable modes, in agreement with the result from a boundary layer analysis [76]. Finally we note that for $n = 10$, unstable modes are already present in the absence of flow, in contrast with Eq. (3.5.1) and (3.6.1). This again shows that local criteria should not be interpreted as sufficient conditions for stability, since they do not properly take into account mode coupling.

3.7 Conclusions & Discussion

A local stability criterion (3.3.15) has been derived including the effects of toroidal rotation and rotation shear. This stability criterion reduces to various known limits. A trans-slow resonance is absent, because in the assumed ordering the Alfvén waves only couple to the slow-magnetosonic sidebands. A general adiabatic index for both the dynamics (γ) and the equilibrium (γ_e) is retained in the analysis, although for sonic rotation velocities the analysis allows only small deviations from $\gamma = \gamma_e$. For

$\gamma > \gamma_e$, the accumulation point for localized modes increases in frequency through the centrifugal convective effect. Destabilizing rotational effects may however drive the most unstable modes away in frequency faster from the accumulation point than the accumulation frequency moves away from marginality. A destabilizing effect is for example associated with flow shear. A further destabilizing term is present when the density decreases faster radially than the angular frequency squared.

The derived criterion is only a sufficient condition for stability of modes that are localized radially but not poloidally. Local criteria of this kind may therefore be regarded as necessary conditions for stability only. Numerical simulations indeed show this to be the case. Poloidal harmonics couple to create an additional destabilizing outwards ballooning effect. In relation to this point we note the work of Ref. [153], which shows that for a static cylindrical plasma within ideal MHD the effect of magnetic shear is to localize instabilities rather than to stabilize them. This is at variance with local criteria like those of Suydam and that derived in this work, showing once more the caution that should be taken in interpreting such local stability criteria.

The instabilities considered in this chapter are particularly unstable in regions of low magnetic shear, existing for example in 'hybrid' advanced tokamak scenarios. These instabilities can also arise due to the high pressure gradients near internal transport barriers, which typically arise near low mode number rational surfaces and involve low magnetic shear and high flow shear [214]. In the work of Refs. [21, 59], a local stability criterion is equal to the existence criterion for reversed shear Alfvén eigenmodes near a rational surface. The modifications due to flow discussed here, can therefore also be relevant for these modes, that show up as Alfvén cascades and are used for MHD-spectroscopy [68]. This will be the topic of chapter 6.

Chapter 4

Flow Shear Stabilization of Rotating Plasmas due to the Coriolis Effect

A radially decreasing toroidal rotation frequency can have a stabilizing effect on non-axisymmetric magnetohydrodynamic instabilities. We show that this is a consequence of the Coriolis effect that induces a restoring pressure gradient force when plasma is perturbed radially. In a rotating cylindrical plasma, this Coriolis-pressure effect is canceled by the centrifugal effect responsible for the magnetorotational instability. In a magnetically confined toroidal plasma, a large aspect ratio expansion shows that only half of the effect is canceled. This analytical result is confirmed by numerical computations. When the plasma rotates faster toroidally in the core than near the edge, the effect can contribute to the formation of transport barriers by stabilizing MHD instabilities.

4.1   Introduction

Plasma flow in present-day tokamaks is primarily beneficial. Arguably most important is the suppressing effect flow shear has on turbulence, by tearing apart the turbulent eddies. The associated reduction in thermal transport greatly benefits the goal of commercially producing energy from nuclear fusion in a tokamak. Flow shear also plays a crucial role in explaining angular momentum losses and accretion rates in astrophysical plasmas through the axisymmetric magnetorotational instability (MRI) [195, 6].

This chapter concerns an effect of flow shear caused by the influence of the Coriolis effect in rotating plasmas. It arises through a spatial variation in the Doppler shifted mode frequency. This has been overlooked in the first two analyses of localized MHD modes [221, 207]. In integrated form the effect first appeared in an analysis of the internal kink mode [198] where it was grouped with inertial terms and was denoted as "flutter". The effect also surfaced in the recent analyses of Ref. [204] and that of the previous chapter. In chapter 3 we derived a stability criterion for modes localized in the r direction, normal to the circular magnetic surfaces of a large aspect ratio tokamak plasma. For not too high rotation this result (3.5.2) can be written as:

$$\frac{rB_0^2}{4R_0^2}\left(\frac{q'}{q^2}\right)^2 > -2p'\frac{1-q^2}{q^2R_0^2} + \frac{r}{4}\frac{1+2q^2}{q^2}\rho\Omega'^2 + \rho^2\left(\frac{\Omega^2}{\rho}\right)', \qquad (4.1.1)$$

Writing

$$\rho^2\left(\frac{\Omega^2}{\rho}\right)' = 2\rho\Omega^{2'} - \rho'\Omega^2 - \rho\Omega^{2'}, \qquad (4.1.2)$$

the second term represents the centrifugal analogue of the Rayleigh-Taylor instability of a heavy fluid on top of a lighter one. The final term of Eq. (4.1.2) is responsible for the MRI, but it is canceled by the two times larger first term that is the subject of this chapter. This Coriolis-pressure term ensures that a radially decreasing angular rotation frequency is stabilizing when the destabilizing Kelvin-Helmholtz term proportional to Ω'^2 is not too large. This is the case when

$$\left|\frac{r\Omega'}{\Omega}\right| < \frac{8q^2}{1+2q^2}. \qquad (4.1.3)$$

The right-hand side of (4.1.3) ranges from 2.67 in the core of a tokamak where $q = 1$ to 4 near the edge where $q \gg 1$. First, we will investigate the effect of the Coriolis force on non-axisymmetric modes in a cylindrical geometry, to find that its influence is exactly canceled by the MRI effect. Next, we perform a large aspect ratio expansion to show that in toroidal geometry only half of the effect is canceled by the MRI. Finally, we confirm this result with linear simulations showing that the effect can stabilize interchange instabilities in the low magnetic shear core region of a tokamak plasma.

4.2 Preliminaries

We consider a rotating ideal MHD equilibrium in which the pressure force and centrifugal force are balanced by the Lorentz force and/or gravitational force

$$\nabla p = \rho \Omega^2 \mathbf{R} + (\nabla \times \mathbf{B}) \times \mathbf{B} - \rho \nabla \Phi. \tag{4.2.1}$$

We use the same (R, Z, ϕ) coordinate system as before, but we will write $z = Z$. Perturbations $\boldsymbol{\xi} \propto e^{-i(n\phi + \omega t)}$ relative to the rotating plasma, will be described by the Frieman-Rotenberg equation (2.5.7). In Appendix 4.A we provide a derivation.

4.3 Cylindrical Analysis

4.3.1 Simplified analysis

We first analyze a simple hydrodynamic cylindrical configuration in which the equilibrium quantities vary only with R. We include a gravitational field and no equilibrium magnetic field. The radial component of the force balance equation (4.2.1) then reads

$$p' = \rho \left(R\Omega^2 - \Phi' \right), \tag{4.3.1}$$

where a prime now denotes an R-derivative. To simplify the analysis, we take the incompressible limit $\nabla \cdot \boldsymbol{\xi} \to 0$, $\gamma \to \infty$ keeping $\gamma p \nabla \cdot \boldsymbol{\xi}$ finite. We consider only non-axisymmetric modes so that $n \neq 0$. The ϕ component of Eq. (2.5.7) then gives

$$\delta p = -\frac{\rho \omega_D^2}{in} R\xi_\phi - \frac{2\rho \omega_D \Omega}{n} R\xi_R. \tag{4.3.2}$$

Incompressibility $\nabla \cdot \boldsymbol{\xi} = 0$ gives $\xi_\phi \equiv \boldsymbol{\xi} \cdot \hat{\mathbf{e}}_\phi = (R\xi_R)'/in$. Inserting into the radial component of Eq. (2.5.7) we obtain

$$\left(PR \left(R\xi_R \right)' \right)' - Q\xi_R = 0, \tag{4.3.3}$$

where $P = \rho \omega_D^2 / n^2$ and

$$Q = \rho \omega_D^2 + R \left(\frac{2\rho \omega_D \Omega}{n} - \rho \Omega^2 \right)' + \rho' \Phi'. \tag{4.3.4}$$

For $\omega_D \approx 0$, which is appropriate for marginally stable radially highly localized modes, this reduces to

$$Q \approx \rho' \left(\Phi' - R\Omega^2 \right) = -p'\rho'/\rho. \tag{4.3.5}$$

This is the term responsible for the Rayleigh-Taylor instability, with the centrifugal acceleration added to the gravitational acceleration. We note the interesting cancellation of the MRI term $\rho \Omega^{2'}$ due to the radial variation in the Doppler shifted frequency

$\omega'_D = n\Omega'$. This cancellation can only occur for non-axisymmetric modes with $n \neq 0$. How exactly does the canceling term arise?

Equation (4.3.2) shows that an incompressible radial perturbation ξ_R is deflected in the $\hat{\mathbf{e}}_\phi$-direction by the Coriolis force or, especially when $\omega_D \approx 0$, gives rise to a pressure perturbation. Away from $\omega_D = 0$ the Coriolis force increases, giving rise to a radially varying perturbed pressure. The resulting force, from Eq. (4.3.2),

$$ -\delta p' \approx \frac{2\rho\Omega}{n}\omega'_D R\xi_R = \rho\Omega^{2'}R\xi_R, \tag{4.3.6} $$

is restoring for a radially decreasing angular rotation frequency. This stabilizing effect exactly cancels the destabilizing effect of the MRI.

4.3.2 Arbitrary vertical wavelength

In the preceding section we assumed no variation of the mode with the axial coordinate z. Here we take $\boldsymbol{\xi} \sim e^{-i(n\phi + k_z z + \omega t)}$ and for generality include an axial velocity component u_z. Solving for ξ_z, ξ_ϕ, and δp from projections of Eq. (2.5.7) in the $\hat{\mathbf{e}}_z$ and $\hat{\mathbf{e}}_\phi$-directions and the incompressibility condition gives

$$ \xi_\phi = -i\frac{n(R\xi_R)' + 2\frac{\Omega\omega_D}{\omega_D^2}k_z^2 R^2 \xi_R}{\bar{k}^2 R^2}, \tag{4.3.7} $$

$$ \delta p = \frac{\rho\omega_D^2 (R\xi_R)' - 2n\rho\omega_D\Omega\xi_R}{\bar{k}^2 R}, \tag{4.3.8} $$

where $\bar{k}^2 = n^2/R^2 + k_z^2$ and $\omega_D = \omega + n\Omega + k_z u_z$. The vertical perturbation $\xi_z = -ik_z\delta p/\rho\omega_D^2$ is not needed here. Inserting Eqs. (4.3.7) and (4.3.8) into the radial component of Eq. (2.5.7) gives again Eq. (4.3.3) with now

$$ P = \frac{\rho\omega_D^2}{R^2\bar{k}^2} \tag{4.3.9} $$

and

$$ Q = \rho\omega_D^2 + R\left(\frac{2n\rho\omega_D\Omega}{R^2\bar{k}^2} - \rho\Omega^2\right)' + \rho'\Phi' + \rho\mathcal{H}\frac{k_z^2}{\bar{k}^2}. \tag{4.3.10} $$

The only difference between Eqs. (4.3.10) and (4.3.4) is the final term, where

$$ \mathcal{H} = -\frac{(2\omega_D\Omega)^2}{\omega_D^2}. \tag{4.3.11} $$

Equation (4.3.10) can be rewritten as

$$ Q = \rho\omega_D^2 + 2n\omega_D R\left(\frac{\rho\Omega}{R^2\bar{k}^2}\right)' + \rho'\left(\Phi' - R\Omega^2\right) - \rho\kappa^2\frac{k_z^2}{\bar{k}^2}, \tag{4.3.12} $$

where $\kappa^2 = R\Omega^{2\prime} + 4\Omega^2$ is the squared epicyclic frequency, associated with inertial circles. The pressure-Coriolis term proportional to ω_D' now only partially cancels the centrifugal term $\rho\Omega^{2\prime}$, resulting in the prefactor $k_z^2/\bar{k}^2$. The cancellation is therefore only complete for $k_z = 0$.

4.3.3 Including a magnetic field

When imposing a vertical magnetic field, differential rotation will generate an azimuthal field as well. We therefore consider a general magnetic field $\mathbf{B} = B_z(R)\hat{\mathbf{e}}_z + B_\phi(R)\hat{\mathbf{e}}_\phi$. With $\nabla \times \mathbf{B} \times \mathbf{B} = -\frac{1}{2}\nabla B^2 + \mathbf{B} \cdot \nabla \mathbf{B}$ the radial component of the force balance equation (4.2.1) becomes

$$\left(p + \frac{B^2}{2}\right)' = \rho R \left(\Omega^2 - \omega_{A\phi}^2 - \frac{\Phi'}{R}\right), \tag{4.3.13}$$

where $\omega_{A\phi} = B_\phi/(R\sqrt{\rho})$. Here $-\omega_{A\phi}^2$ derives from the magnetic field line bending term $\mathbf{B} \cdot \nabla \mathbf{B}$ in the same way that Ω^2 derives from the inertial term $-\mathbf{u} \cdot \nabla \mathbf{u}$.

The structure of the mode equation (4.3.3) does not change upon the introduction of a magnetic field. Equations (4.3.7), (4.3.8) and the expressions for $P = \rho\omega_D^2/R^2\bar{k}^2$ and Q of Eq. (4.3.10) are unchanged, except for the replacements

$$\omega_D^2 \to \omega_D^2 - \omega_A^2, \tag{4.3.14}$$

$$\omega_D\Omega \to \omega_D\Omega + \omega_A\omega_{A\phi}, \tag{4.3.15}$$

$$\Omega^2 \to \Omega^2 - \omega_{A\phi}^2, \tag{4.3.16}$$

where the Alfvén frequency reads

$$\omega_A^2 = \frac{n^2 B_\phi^2/R^2 + k_z^2 B_z^2}{\rho}. \tag{4.3.17}$$

The resulting mode equation was first derived in Ref. [1] under the Boussinesq approximation. See for example Ref. [69] for a derivation. How the resulting P and Q relate to stability is elaborated in Appendix 4.B in which various stability criteria are derived.

We note that the replacements of Eqs. (4.3.14)–(4.3.16) should be made before the simplifications of Eq. (4.3.12) are made. This is because, with these replacements Eq. (4.3.11) reads

$$\mathcal{H} = -4\frac{\left(\omega_D\Omega + \omega_A\omega_{A\phi}\right)^2}{\omega_D^2 - \omega_A^2} = \begin{cases} -4\Omega^2 & (B = 0) \\ 4\omega_{A\phi}^2 & (B \neq 0, \omega_D \to 0) \end{cases}. \tag{4.3.18}$$

The loss of the stabilizing Coriolis term $-4\Omega^2$ upon the introduction of even a very small magnetic field can give rise to the MRI.

As we have seen, the Coriolis force induces a pressure perturbation that can exactly cancel the MRI term. A fraction $k_z^2/\bar{k}^2$ of the MRI drive remains so that long wavelengths will be less unstable than smaller wavelengths. Since this only holds for non-axisymmetric modes, the axisymmetric MRI will typically be more unstable than its non-axisymmetric counterpart.

Next we turn to a toroidal magnetically confined plasma, where we will see that things are very similar except that there the cancellation with the MRI term is incomplete.

4.4 Toroidal Analysis

We now switch to a toroidal geometry and will take into account plasma compressibility. We exclude a gravitational field so that the equilibrium is given by Eq. (4.2.1) with $\Phi = 0$. The nested magnetic surfaces are labeled by the poloidal magnetic flux ψ defined by the expression (2.2.4a). Normal to these surfaces, pressure forces are balanced by Lorentz forces as described by the extended Grad-Shafranov equation (2.2.9). Within the magnetic surfaces, solving the force balance analytically leads to expressions (2.2.10) and (2.2.11) for the pressure and density, respectively.

We perform an expansion in terms of the inverse aspect ratio $\epsilon = r/R_0$. We consider only the leading order terms in ϵ, so that the Shafranov shift does not enter and we can use simple polar coordinates (r, θ) in the poloidal plane. The approach we will follow is similar to that of Ref. [221]. We will however allow for an arbitrary value of the adiabatic constant of both the dynamics γ and the equilibrium γ_e, both of which are taken equal to one in [221]. For $\epsilon \ll 1$, poloidal Fourier harmonics $\propto e^{im\theta}$ couple weakly so that we can write

$$\xi_r = \sum_{m'=m,m\pm1} \xi_r^{m'} e^{i(m'\theta - n\phi - \omega t)}, \tag{4.4.1}$$

with $\xi_r^{m\pm1} \sim \epsilon \xi_r^m$ and similarly for the other components ξ_θ, ξ_ϕ. We order $\beta \equiv 2p_0/B_0^2 \sim \epsilon^2$ and $\omega_D \sim \Omega \sim \epsilon\sqrt{p_0/\rho_0}$ so that $\mathcal{M} \sim 1$ as in Refs. [221, 207, 204]. A consistent ordering turns out to require for the component parallel to the magnetic field $\xi_\parallel^m \sim \epsilon \xi_r^m$, but $\xi_\parallel^{m\pm1} \sim \xi_r^m \sim \xi_\theta^m$. The components ξ_R, ξ_z, and ξ_ϕ are ordered the same as $\xi_\parallel$.

Using the equilibrium relation (4.2.1), the projection of the Frieman-Rotenberg equation (2.5.7) in the direction of **B** can be written as [198]

$$-\rho\omega_D^2 (\mathbf{B} \cdot \boldsymbol{\xi}) + 2i\rho\omega_D\Omega (\mathbf{B} \times \hat{\mathbf{e}}_z) \cdot \boldsymbol{\xi} = \mathbf{B} \cdot \nabla (\gamma p \nabla \cdot \boldsymbol{\xi}) + \rho\Omega^2 \mathbf{B} \cdot (\nabla (\boldsymbol{\xi} \cdot \mathbf{R}) - \mathbf{R}\nabla \cdot \boldsymbol{\xi}). \tag{4.4.2}$$

To leading order in ϵ this becomes

$$-\rho_0\omega_D^2\xi_\parallel - 2i\rho_0\omega_D\Omega\xi_R = ik_\parallel \left(\gamma p_0 \nabla \cdot \boldsymbol{\xi} + \rho_0\Omega^2 R\xi_R\right), \tag{4.4.3}$$

where acting on an m' Fourier harmonic

$$k_\parallel^{m'} \equiv \frac{\mathbf{B}}{B} \cdot \nabla \approx \frac{1}{R_0} \left(\frac{m'}{q} - n \right) \sim \epsilon, \tag{4.4.4}$$

with the safety factor $q = r B_\phi / R_0 B_\theta + O(\epsilon)$.

To solve for $\xi_\parallel$ from Eq. (4.4.3) we need $\nabla \cdot \boldsymbol{\xi}$. For a low $\beta \sim \epsilon^2$ plasma, the toroidal magnetic field perturbation $\delta F = -R^2 \nabla \cdot \left(F \boldsymbol{\xi}_p / R^2 \right)$, with $\boldsymbol{\xi}_p = \boldsymbol{\xi} - \xi_\phi \hat{\mathbf{e}}_\phi$, creates such a large restoring force that for instabilities it has to vanish to order ϵ^2 [25, 46]. Therefore

$$\nabla \cdot \boldsymbol{\xi}_p \approx \boldsymbol{\xi}_p \cdot \left(\frac{2 \nabla R}{R} - \frac{\nabla F}{F} \right) = \frac{2 \xi_R}{R} + O(\epsilon^2), \tag{4.4.5}$$

where we used that the Grad-Shafranov equation (2.2.9) gives $F'/F \sim \beta' \sim \epsilon^2$. With Eq. (4.4.4) we thus obtain to leading order

$$\nabla \cdot \boldsymbol{\xi} = \frac{2 \xi_R}{R} + i k_\parallel \xi_\parallel \sim \epsilon. \tag{4.4.6}$$

Equation (4.4.3) now gives

$$\xi_\parallel^{m\pm 1} = \frac{2 i \rho_0 \omega_D \Omega + i k_\parallel^{m\pm 1} \left(\frac{2\gamma p_0}{R_0} + \rho_0 R_0 \Omega^2 \right)}{\gamma p_0 (k_\parallel^{m\pm 1})^2 - \rho_0 \omega_D^2} \xi_R^{m\pm 1},$$

$$\approx 2i \frac{\omega_D \Omega \pm q \omega_0^2 \left(1 + \frac{\mathcal{M}^2}{\gamma} \right)}{\omega_0^2 - \omega_D^2} \xi_R^{m\pm 1}, \tag{4.4.7}$$

with $\omega_0 = \sqrt{\gamma p_0 / \rho_0}/q R_0$. The approximation in Eq. (4.4.7) holds when we order $k_\parallel^m \sim \epsilon^2$ so that $k_\parallel^{m\pm 1} \approx \pm 1/q R_0 \sim \epsilon$. By ordering $k_\parallel^m$ an order lower than implied by Eq. (4.4.4), we focus on a region close to a rational surface where $q = m/n$. From Eq. (4.4.5) we have to zeroth order in ϵ that $\nabla \cdot \boldsymbol{\xi}_p = 0$ so that $\xi_\theta^m = i (r \xi_r^m)' / m$. Therefore, to leading order we find for $\xi_R = \cos \theta \xi_r - \sin \theta \xi_\theta$

$$\xi_R^{m\pm 1} = \frac{1}{2} \left(\xi_r^m \mp \frac{(r \xi_r^m)'}{m} \right). \tag{4.4.8}$$

In the following we will not take into account the effect of the magnetic field perturbations explicitly, so that $\mathbf{F}_s = -\nabla \delta p$. We take the divergence of the cross-product of Eq. (2.5.7) with $\tilde{\mathbf{B}} \equiv \mathbf{B}/B^2$, to obtain after various vector operations

$$\begin{aligned}
0 = \quad & \hat{\mathbf{e}}_R \times \tilde{\mathbf{B}} \cdot \nabla \rho \omega_D^2 \xi_R + \hat{\mathbf{e}}_z \times \tilde{\mathbf{B}} \cdot \nabla \rho \omega_D^2 \xi_z + 2i \hat{\mathbf{e}}_z \cdot \nabla \rho \omega_D \Omega \frac{\xi_\parallel}{B} \\
& + \frac{2 \tilde{\mathbf{B}} \times \nabla B}{B} \cdot \nabla \delta p + \frac{\tilde{\mathbf{B}} \times \hat{\mathbf{e}}_R}{R} \cdot \nabla \left(R^2 \nabla \cdot \left(\rho \Omega^2 \boldsymbol{\xi} \right) \right) \\
& + \rho \omega_D^2 \left(\xi_R \nabla \cdot \hat{\mathbf{e}}_R \times \tilde{\mathbf{B}} + \xi_z \nabla \cdot \hat{\mathbf{e}}_z \times \tilde{\mathbf{B}} \right) - 2i \nabla \cdot \left(\rho \omega_D \Omega \tilde{\mathbf{B}} \cdot \hat{\mathbf{e}}_z \boldsymbol{\xi} \right) \\
& + \frac{\nabla \times \mathbf{B}}{B^2} \cdot \nabla \delta p + R^2 \nabla \cdot \left(\rho \Omega^2 \boldsymbol{\xi} \right) \nabla \cdot \left(\frac{\tilde{\mathbf{B}} \times \hat{\mathbf{e}}_R}{R} \right).
\end{aligned} \tag{4.4.9}$$

69

We can write, using the covariant component $\xi_\psi \equiv \boldsymbol{\xi} \cdot \partial\mathbf{r}/\partial\psi$

$$\nabla \cdot \rho\Omega^2\boldsymbol{\xi} = \rho\Omega^2\nabla \cdot \boldsymbol{\xi} + \frac{R\left(\rho\Omega^2\right)^2}{\gamma_e p}\xi_R + \frac{\partial\rho\Omega^2}{\partial\psi}\xi_\psi, \tag{4.4.10}$$

$$\delta p = -\gamma p \nabla \cdot \boldsymbol{\xi} - \rho R\Omega^2\xi_R - \frac{\partial p}{\partial\psi}\xi_\psi. \tag{4.4.11}$$

The final terms of Eqs. (4.4.10) and (4.4.11) give rise to the centrifugal and pressure terms of Eq. (4.1.1). We will not take them into account here. To leading order, Eq. (4.4.9) then greatly simplifies. The last two lines vanish. We can approximate $\hat{\mathbf{e}}_R \times \tilde{\mathbf{B}} \approx -\hat{\mathbf{e}}_z/B$, and $\hat{\mathbf{e}}_z \times \tilde{\mathbf{B}} = \hat{\mathbf{e}}_R/B$ so that Eq. (4.4.9) can be written as $(2/B)\,\partial f/\partial z = 0$ where

$$f = -\rho_0\omega_D^2\xi_R + i\rho_0\omega_D\Omega\xi_\parallel + \frac{\gamma p_0}{R_0^2}\left(1 + \frac{\mathcal{M}^2}{\gamma}\right)R_0\nabla \cdot \boldsymbol{\xi} + \rho_0\Omega^2\left(1 + \frac{\mathcal{M}^2}{\gamma_e}\right)\xi_R. \tag{4.4.12}$$

To rewrite the second term of Eq. (4.4.9) we used that $\nabla \times \boldsymbol{\xi}_p = 0$ to zeroth order in ϵ, so that $\partial\xi_z/\partial R = -\partial\xi_R/\partial z$. Using Eqs. (4.4.6) and (4.4.7), the poloidal harmonics of f can be written as $f^{m\pm1} = (a \pm b)\xi_R^{m\pm1}$, where

$$a = \frac{\rho_0\left(\omega_D^2 - \omega_-^2\right)\left(\omega_D^2 - \omega_+^2\right)}{\omega_D^2 - \omega_0^2} = -\frac{B_0^2}{R_0^2}\tilde{A}_1, \tag{4.4.13}$$

$$b = \frac{4q\rho_0\omega_D\Omega\omega_0^2}{\omega_0^2 - \omega_D^2}\left(1 + \frac{\mathcal{M}^2}{\gamma}\right) = -m\frac{B_0^2}{R_0^2}\alpha_k. \tag{4.4.14}$$

and $\omega_\pm^2$ are again the zonal flow and geodesic acoustic mode frequencies previously derived in Eqs. (2.5.26a). To leading order, $\partial/\partial z = \sin\theta\,\partial/\partial r + \cos\theta\,\partial/r\partial\theta$ so that

$$2i\frac{\partial f}{\partial z} = \left(\frac{\partial}{\partial r} - \frac{m-1}{r}\right)f^{m-1} - \left(\frac{\partial}{\partial r} + \frac{m+1}{r}\right)f^{m+1}$$
$$= \frac{1}{r}\left(r\left(f^{m-1} - f^{m+1}\right)\right)' - \frac{m}{r}\left(f^{m-1} + f^{m+1}\right). \tag{4.4.15}$$

With $2f^{m\pm1} = (a \pm b)\left(\xi_r \mp (r\xi_r)'/m\right)$, we obtain

$$2imr\frac{\partial f}{\partial z} = \left(\left(ar(r\xi_r)' - bmr\xi_r\right)\right)' - \left(am^2\xi_r - bm(r\xi_r)'\right)$$
$$= \left(ar\,(r\xi_r)'\right)' - m^2\left(a + r\,(b/m)'\right)\xi_r = 0, \tag{4.4.16}$$

which is equal in structure to the cylindrical mode equation (4.3.3). The magnetorotational effect, from the final term of Eq. (4.4.10) that we did not take into account, effectively adds $\rho_0\Omega^2\left(1 + \mathcal{M}^2\right)$ to b/m [221, 207]. For $\mathcal{M} \ll 1$ this gives the second and third term on the right-hand side of Eq. (4.1.2). With Eq. (4.4.14), $(b/m)'$ gives only the Coriolis-pressure contribution. It derives from two equal contributions of

the Coriolis and perturbed pressure terms, the second and third terms of Eq. (4.4.12), respectively. For $\omega_D \approx 0$ and $\mathcal{M}^2 \ll 1$, Eq. (4.4.14) gives

$$\left(\frac{b}{m}\right)' \approx \frac{4\rho_0 \omega'_D \Omega}{n} = 2\rho_0 \Omega^{2\prime}, \tag{4.4.17}$$

which is the first term on the right-hand side of Eq. (4.1.2). Comparing this with the corresponding term in the cylindrical mode equation (4.3.3), we find that it is twice as large in a toroidal geometry. Consequently, only half of its effect is canceled by the magnetorotational effect. This allows flow shear to be stabilizing in a toroidal geometry.

4.5 Simulations

Next, we perform numerical computations using FINESSE [8] and PHOENIX [67, 15]. We take a circular equilibrium with $\epsilon = 0.3$ and use profiles $\beta_0 \approx 0.01(1 - \psi_n)^2$ and $\rho_0 \propto 1 - \psi_n$, where ψ_n is the poloidal flux scaled to zero on the magnetic axis and unity at the plasma edge. The profile $FF' \propto -0.95\psi_n - 0.1\psi_n + 3\psi_n^5$ gives $q \approx 1$ in the core of the plasma while increasing steeply near the edge to a value above 3.5. This is relevant for the 'hybrid scenario' envisioned for advanced operation of the ITER tokamak. In the entire core of the plasma, starting from $q = 0.995$ on axis, the magnetic shear is very low, with $q' = 0.03$ at $\psi_n = 0.1$ where $q = 1$.

With $q \approx 1$ in the center, the stability criterion of Eq. (4.1.1) for rigid rotation reads

$$\frac{r}{4}\left(\frac{q'}{q^2}\right)^2 > \frac{\rho'_0 \Omega^2}{\rho_0 \omega_A^2}, \tag{4.5.1}$$

where $\omega_A = B_0/R_0\sqrt{\rho_0}$. The destabilizing centrifugal term on the right-hand side results in modes similar to those of the previous chapter, with growth rates of several tens of a percent of ω_{A0} on the magnetic axis. We use a rotation profile

$$\Omega \approx 0.02\omega_{A0}\left(1 + k\left(\psi_n - 0.1\right)\right), \tag{4.5.2}$$

giving $\mathcal{M} = \sqrt{\beta}\Omega/\omega_A \approx 0.2$ at $\psi_n = 0.1$.

Near the plasma edge, a resistive computation with very high radial resolution is required to resolve the eigenfunctions. The growth rates were however found to be quite insensitive to applying ideally conducting wall boundary conditions at $\sqrt{\psi_n} = 0.8$, where $q \approx 1.1$. A resolution of 100 radial elements and seven poloidal Fourier harmonics was in this case found to be sufficient.

Figure 4.1 shows the growth rate of the most unstable modes as a function of the flow shear. It shows stabilization for radially decreasing rotation $k < 0$ and destabilization for radially increasing rotation $k > 0$, in correspondence with the theoretical analysis of this work. The second derivative of the growth rate with respect to k is negative. This may very well be due to the shearing effect investigated for ballooning
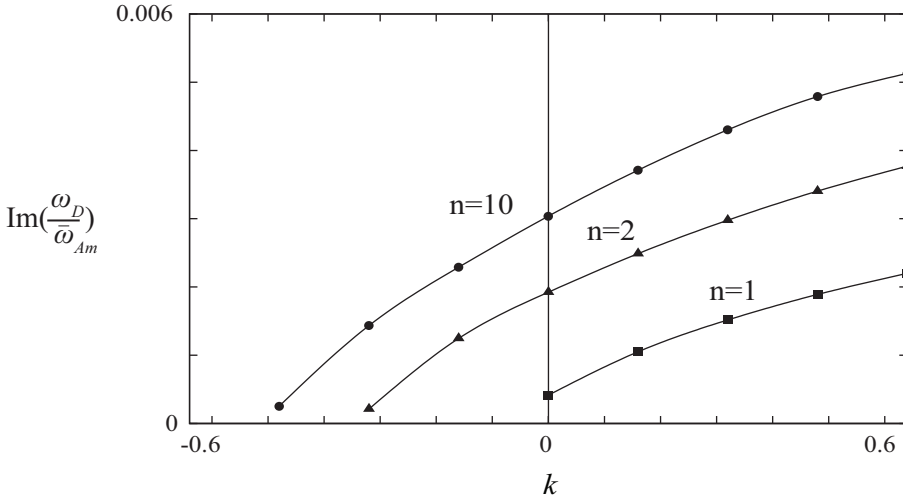
Figure 4.1: The normalized growth rate as a function of the flow shear $k = d\ln\Omega/d\psi_n$ at $\psi_n = 0.1$ for various toroidal mode numbers n.

modes in Refs. [199, 214], which is always stabilizing. Indeed, for a similar equilibrium with a higher value of $\beta \approx 0.05$ on axis, the growth rate of the higher n modes was found to *de*crease with increasing positive flow shear k.

4.6 Conclusions & Discussion

We showed that a stabilizing effect of a radially decreasing rotation frequency on non-axisymmetric modes originates from the Coriolis effect. In spite of being perpendicular to the displacement, the Coriolis effect can have a significant impact on stability through the mediating role of the perturbed pressure. In the uncommon case that the angular rotation frequency increases with minor radius, the effect can even be *de*stabilizing. In a rotating cylindrical plasma the effect on non-axisymmetric modes with no vertical variation is exactly canceled by the centrifugal effect responsible for the MRI. The effect may therefore be important for the recently observed non-axisymmetric MRI [105]. We expect modes with a long vertical wavelength to be highly suppressed. Since the effect results from a radial variation in the Doppler shifted mode frequency, it does not influence axisymmetric modes like the classical MRI.

The effect has often been missed in the literature. In Refs. [221, 207] ω'_D was incorrectly neglected along with ω_D. In Ref. [119] and later again in [209] an error was made in the WKB analysis as explained in [69]. In Ref. [150] the perturbed pressure δp was not included so that the effect was missed. In a cylindrical geometry the effect *is* included in the original analysis of [107] or more recently in for example [146, 161].

The fact that without axial variation the Coriolis force only modifies the pressure was already observed in Ref. [42].

Instability resulting from the Coriolis-pressure effect may be interpreted as a co-rotation instability. The part of the mode inside the co-rotation radius where $\omega_D = 0$ moves slower than the plasma and has negative energy [123, 115]. Energy transfer to the positive energy part of the mode outside the co-rotation radius can cause growth of the mode. See Appendix 4.C.

Relative to pressure effects, the effect discussed in this work scales with $\mathcal{M}^2$, so it will become particularly significant for high Mach number plasmas. In the plasma core of hybrid scenario plasmas, with a safety factor close to one, plasma pressure effects are small. Toroidal flow shear can therefore aid the formation of internal transport barriers, by stabilizing magnetohydrodynamic instabilities. Because of its dependence on the sign of the flow shear, the pressure-Coriolis effect can be discriminated from other effects like that of Ref. [199, 214], the parallel velocity gradient or Kelvin-Helmholtz instability, and non-linear flow shear suppression.

Also for stable modes, the Coriolis-pressure effect can be relevant. From Eq. (4.4.14), this particularly holds for modes with a frequency $\omega_D^2 \approx \omega_0^2$, although such a singularity is typically something that is "smoothed" in a more complete kinetic analysis. In chapter 6, the Coriolis-pressure effect will be shown to influence the existence of reversed shear Alfvén eigenmodes with $\omega_D^2 \approx \omega_+^2$, favoring modes propagating in the direction of the plasma rotation.

4.A   Frieman-Rotenberg equation

4.A.1   General

We adopt a Lagrangian viewpoint in which we move along with the flow. A Lagrangian perturbation of a quantity f with equilibrium value f_0 will be defined as $\delta_L f \equiv f(\mathbf{r} + \boldsymbol{\xi}) - f_0(\mathbf{r})$ [139], related to the Eulerian perturbation $\delta_E = \delta_L - \boldsymbol{\xi} \cdot \nabla$. Here the so-called Lagrangian displacement vector $\boldsymbol{\xi}(\mathbf{r}, t) = \delta_L \mathbf{r}$ gives the displacement of a fluid element that would have been at position $\mathbf{r}$ at time t in the unperturbed flow.

We introduce the advective derivative $D/Dt = \partial/\partial t + \mathbf{u} \cdot \nabla$ which commutes with δ_L [139]. It then follows from $\mathbf{u} = D\mathbf{r}/Dt$ that $\delta_L \mathbf{u} = D\boldsymbol{\xi}/Dt$. The Frieman-Rotenberg equation is obtained by acting with δ_L on the momentum equation $\rho D\mathbf{u}/Dt = \mathbf{f}$, giving

$$(\delta_L \rho) \frac{D\mathbf{u}}{Dt} + \rho \frac{D^2\boldsymbol{\xi}}{Dt^2} = \delta_L \mathbf{f}. \tag{4.A.1}$$

Similarly, acting with δ_L on the continuity equation $D\rho/Dt = -\rho \nabla \cdot \mathbf{u}$ gives $\delta_L \rho = -\rho \nabla \cdot \boldsymbol{\xi}$ so that the first term of Eq. (4.A.1) can be written as

$$-\rho \left(\nabla \cdot \boldsymbol{\xi} \right) \frac{D\mathbf{u}}{Dt} = -\nabla \cdot \left(\boldsymbol{\xi} \rho \frac{D\mathbf{u}}{Dt} \right) + \boldsymbol{\xi} \cdot \nabla \left(\rho \frac{D\mathbf{u}}{Dt} \right). \tag{4.A.2}$$

We define the static force operator $\mathbf{F}_s\left(\boldsymbol{\xi}\right) \equiv \delta_E\mathbf{f}$, where in the rest of the text we suppress the argument $\boldsymbol{\xi}$. Equation (4.A.1) now gives the Frieman-Rotenberg equation [58]

$$\rho\left(\frac{\partial}{\partial t} + \mathbf{u}\cdot\nabla\right)^2\boldsymbol{\xi} = \mathbf{F}_s + \nabla\cdot\left(\boldsymbol{\xi}\rho\mathbf{u}\cdot\nabla\mathbf{u}\right), \tag{4.A.3}$$

where we used that in equilibrium $D\mathbf{u}/Dt = \mathbf{u}\cdot\nabla\mathbf{u}$. We remark that the right-hand side of Eq. (4.A.3) actually represents the self-adjoint Galilean invariant generalized force operator deployed for example in Refs. [13, 2]. The total force operator of Frieman and Rotenberg [58] is given by

$$\mathbf{F} = \mathbf{F}_s + \nabla\cdot\left(\boldsymbol{\xi}\rho\mathbf{u}\cdot\nabla\mathbf{u}\right) - \rho\left(\mathbf{u}\cdot\nabla\right)^2\boldsymbol{\xi}, \tag{4.A.4}$$

so that Eq. (4.A.3) can be written as

$$\rho\frac{\partial^2\boldsymbol{\xi}}{\partial t^2} + 2\rho\mathbf{u}\cdot\nabla\frac{\partial\boldsymbol{\xi}}{\partial t} = \mathbf{F}. \tag{4.A.5}$$

4.A.2 Normal modes

Considering normal modes $\boldsymbol{\xi} \sim e^{-i(\omega t + n\phi + k_z z)}$ and a velocity $\mathbf{u} = R\Omega\hat{\mathbf{e}}_\phi + u_z\hat{\mathbf{e}}_z$ we have with $\omega_D = \omega + n\Omega + k_z u_z$ and $\boldsymbol{\Omega} = -\Omega\hat{\mathbf{e}}_z$

$$\frac{D\boldsymbol{\xi}}{Dt} = -i\omega_D\boldsymbol{\xi} + \boldsymbol{\Omega}\times\boldsymbol{\xi}, \tag{4.A.6}$$

so that

$$\frac{D^2\boldsymbol{\xi}}{Dt^2} = -\omega_D^2\boldsymbol{\xi} - i\omega_D\boldsymbol{\Omega}\times\boldsymbol{\xi} + \frac{D}{Dt}\left(\boldsymbol{\Omega}\times\boldsymbol{\xi}\right). \tag{4.A.7}$$

The final term reads

$$\boldsymbol{\Omega}\times\frac{D\boldsymbol{\xi}}{Dt} = -i\omega_D\boldsymbol{\Omega}\times\boldsymbol{\xi} + \boldsymbol{\Omega}\times\boldsymbol{\Omega}\times\boldsymbol{\xi}. \tag{4.A.8}$$

The first term of Eq. (4.A.8) combines with the second term of Eq. (4.A.7) to give the Coriolis force. For the right hand side of Eq. (4.A.3) we need

$$\nabla\cdot\left(\boldsymbol{\xi}\rho\mathbf{u}\cdot\nabla\mathbf{u}\right) = -\nabla\cdot\left(\boldsymbol{\xi}\rho\Omega^2\mathbf{R}\right) \tag{4.A.9}$$

$$= -\mathbf{R}\cdot\nabla\left(\rho\Omega^2\boldsymbol{\xi}\right) - \rho\Omega^2\boldsymbol{\xi}\cdot\nabla\mathbf{R}.$$

The last term can be written $-\Omega^2\left(\xi_R\hat{\mathbf{e}}_R + \xi_\phi\hat{\mathbf{e}}_\phi\right)$ and exactly cancels the last term of Eq. (4.A.8). The Frieman-Rotenberg equation (4.A.3) can then be written as Eq. (2.5.7).

4.B Stability Analysis

In this section we will investigate stability. First we show a very general criterion that determines stability a posteriori. Next we investigate how the coefficients P and Q of the mode equation (4.3.3) influence stability.

4.B.1 A general stability criterion

In the following we assume normal mode solutions $\boldsymbol{\xi} \sim e^{-i\omega t}$. Taking the inner product of Eq. (4.A.5) with the complex conjugate $\boldsymbol{\xi}^*$ and integrating over the plasma volume we can solve the resulting quadratic equation to give solutions $\omega = \omega^-$ and ω^+, where [58]

$$\omega^{\pm} = \bar{V} \pm \sqrt{\bar{V}^2 + \bar{W}}. \tag{4.B.1}$$

A bar denotes normalization with $I = \frac{1}{2} \int \rho \, |\boldsymbol{\xi}|^2 \, d^3\mathbf{r}$ and

$$V = \frac{1}{2} \int \boldsymbol{\xi}^* \cdot (-i\rho \mathbf{u} \cdot \nabla \boldsymbol{\xi}) \, d^3\mathbf{r}, \tag{4.B.2}$$

$$W = \frac{1}{2} \int -\boldsymbol{\xi}^* \cdot \mathbf{F} d^3\mathbf{r} \tag{4.B.3}$$

are both real [69]. Here $\bar{V}$ and W are the average Doppler-Coriolis shift and potential energy, respectively. The frequencies of Eq. (4.B.1) are real when $\bar{W} \geq -\bar{V}^2$, providing a necessary and sufficient criterion for stability. Equation (4.B.1) for general equilibrium flow may be compared with Eq. (4.B.1) for purely toroidal flow.

4.B.2 WKB analysis

We assume the radial variation of $\boldsymbol{\xi}$ is much faster than the length scale L over which the equilibrium quantities vary. In this case we can insert WKB solutions $R\xi_R \sim e^{i \int k_R dR}$ into Eq. (4.3.3) and neglect terms higher order in $1/L$ to obtain

$$-k_R^2 R^2 P - Q = 0. \tag{4.B.4}$$

We assume that either the magnetic field or k_z vanishes so that the term $\rho h k_z^2 / \bar{k}^2$ does not depend on the mode frequency. Then Eq. (4.B.4) becomes a quadratic equation in ω_D with solution

$$\omega_D = \bar{\mathcal{V}} \pm \sqrt{\bar{\mathcal{V}}^2 + \bar{\mathcal{W}}}, \tag{4.B.5}$$

where with $k^2 = k_R^2 + \bar{k}^2$,

$$\bar{\mathcal{V}} = -\frac{\bar{k}^2}{k^2} \frac{R}{\rho} \left(\frac{n\rho\Omega}{\bar{k}^2 R^2} \right)' \tag{4.B.6}$$

and

$$\bar{\mathcal{W}} = \omega_A^2 - \frac{k_z^2}{k^2} \left(h - R\Omega^{2\prime} \right) - 2\frac{nk_z}{Rk^2} u_z' \Omega \tag{4.B.7}$$

$$- \frac{\bar{k}^2}{k^2} \frac{R}{\rho} \left[\rho' \left(\frac{\Phi'}{R} - \Omega^2 \right) + \left(\rho \omega_{A\phi}^2 \right)' + \left(\frac{2n\rho\omega_A\omega_{A\phi}}{\bar{k}^2 R^2} \right)' \right].$$

The equilibrium is stable against the rapidly varying WKB modes when $\bar{\mathcal{W}} > -\bar{\mathcal{V}}^2$.

Equation (4.B.7) consists of a stabilizing Alfvén contribution, and several potentially destabilizing terms. The first of these is the inertial term that becomes equal

to $(k_z^2/k^2)\kappa^2$ in the absence of a magnetic field. The final term on the first line of Eq. (4.B.7) was already found in Ref. [107] and arises through the radial variation of the Doppler shift.

On the second line of Eq. (4.B.7) we have first the gravitational convective term augmented by the centrifugal force. Together with the next term, it may be rewritten using the equilibrium relation (4.3.13) as ρ' times the total pressure gradient. The remaining term proportional to $\left(\omega_{A\phi}^2\right)'$ was in Ref. [132] argued to be responsible for the helical MRI [104, 176]. This term is the magnetic field line bending analogue of the centrifugal MRI term proportional to $\Omega^{2'}$. The final term of Eq. (4.B.7) is then analogous to the pressure-Coriolis term that canceled part of the MRI term to give the prefactor k_z^2/k^2. Because of the sign difference in Eqs. (4.3.15) and (4.3.16), this term however always adds to the previous. For example, for $k_z = 0$ it reads $(2\rho\omega_{A\phi}^2)'$.

Comparing Eq. (4.B.1) with (4.B.5) we see that $\bar{V} = \bar{\mathcal{V}} - n\Omega - k_z u_z$. We would like to show, at least for $k_z = 0$, that our result for $\bar{\mathcal{V}}$ of Eq. (4.B.6) agrees with the definition of $\bar{V}$ given in Eq. (4.B.2). We first write

$$\boldsymbol{\xi}^* \cdot (-i\mathbf{u} \cdot \nabla \boldsymbol{\xi}) = \boldsymbol{\xi}^* \cdot (-n\Omega\boldsymbol{\xi} + i\Omega\hat{\mathbf{e}}_z \times \boldsymbol{\xi}) \tag{4.B.8}$$

$$= -n\Omega |\boldsymbol{\xi}|^2 + i\Omega\hat{\mathbf{e}}_z \cdot (\boldsymbol{\xi} \times \boldsymbol{\xi}^*), \tag{4.B.9}$$

where in (R, z, ϕ) coordinates

$$i\hat{\mathbf{e}}_z \cdot (\boldsymbol{\xi} \times \boldsymbol{\xi}^*) = i\left(\xi_\phi \xi_R^* - \xi_R \xi_\phi^*\right) = \frac{\left(|R\xi_R|^2\right)'}{nR}. \tag{4.B.10}$$

In the final step we used that incompressibility implies $\xi_\phi = (R\xi_R)'/in$. Therefore Eq. (4.B.2) can be written as

$$\bar{V} = -\frac{\int \rho\Omega \left(n|\boldsymbol{\xi}|^2 - \left(|R\xi_R|^2\right)'/nR\right) d^3\mathbf{r}}{\int \rho |\boldsymbol{\xi}|^2 d^3\mathbf{r}}, \tag{4.B.11}$$

$$= -\frac{\int \left(\rho n\Omega|\boldsymbol{\xi}|^2 + (\rho\Omega)' |R\xi_R|^2/nR\right) d^3\mathbf{r}}{\int \rho |\boldsymbol{\xi}|^2 d^3\mathbf{r}}, \tag{4.B.12}$$

$$\approx -n\Omega - \frac{n}{\rho Rk^2} (\rho\Omega)'. \tag{4.B.13}$$

On the second line we partially integrated using $d^3\mathbf{r} = RdRd\phi dz$ assuming that $|R\xi_R|$ vanishes at $R = 0$ and the plasma edge. Since we assume that the perturbation varies over a much smaller length scale, on the final line we took the equilibrium quantities out of the integrals. For evaluation of the remaining integrals we used that $\xi_\phi = k_R R\xi_R/n$. We thus find that indeed the result of Eq. (4.B.13) agrees with Eq. (4.B.6).

4.B.3 Cluster point analysis

Our mode equation (4.3.3) becomes singular for $P = 0$ ($\omega_D = \omega_A$), signaling the presence of a continuous spectrum. When also $P' = 0$ ($\omega'_D = \omega'_A$) a cluster point may exist, where global modes cluster towards the continuum [70]. To leading order in the distance x to this point, we can write Eq. (4.3.3) as $(x^2(R\xi_R)')' + DR\xi_R = 0$. Here

$$D \equiv -\frac{Q}{\frac{1}{2}R\,(RP)''} \tag{4.B.14}$$

is evaluated at $x = 0$. This equation has solutions of the form $R\xi_R = x^\nu$ with $\nu = -1/2 \pm \sqrt{1/4 - D}$. More formally we can perform a Frobenius expansion around $x = 0$. Either way, we find that oscillatory behaviour of the solutions cannot occur when $D < 1/4$ providing a sufficient criterion for local stability. Using $\omega'_D = n\Omega' + k_z u'_z$ this gives

$$D = -\frac{\rho\frac{k^2}{\bar{k}^2}\left(h - R\Omega^{2'}\right) + \rho'\left(\Phi' - R\Omega^2\right) + \frac{2n\rho k_z u'_z\Omega}{R\bar{k}^2}}{\frac{1}{2}\rho\left(\omega_A^2 - \omega_D^2\right)''R^2}$$

$$-\frac{\omega_D\left(\frac{2n\rho\Omega}{R^2 k^2}\right)' + \left(\rho\omega_{A\phi}^2 + \frac{2n\rho\omega_A\omega_{A\phi}}{R^2\bar{k}^2}\right)'}{\frac{1}{2}\rho\left(\omega_A^2 - \omega_D^2\right)''R} < \frac{1}{4}. \tag{4.B.15}$$

For highly localized modes, the Coriolis shift vanishes [69] so that at marginal stability $\omega_D = \omega_A = 0$ and $\frac{1}{2}\left(\omega_A^2 - \omega_D^2\right)'' = \omega_A'^2 - \omega_D'^2$. When positive, both sides of Eq. (4.B.15) can be multiplied with this quantity. The term $\omega_A'^2$ gives the stabilizing effect of magnetic field line bending while $-\omega_D'^2$ gives a destabilizing Kelvin-Helmholtz flow shear effect. The resulting stability criterion is the incompressible version of that derived in [85, 86, 18], which generalized the Suydam criterion [180] to include flow. Without magnetic and gravitational fields, and density gradients, Eq. (4.B.15) was first obtained in Ref. [107]. A magnetic field was included in this reference only for axisymmetric instabilities ($n = 0$) and pure rotation ($u_z = 0$). This generalized the result of Velikhov [195] whose analysis excluded an azimuthal magnetic field B_ϕ.

4.C Negative Energy Waves

In Appendix 4.B.1 we took the inner product of Eq. (4.A.3) with ξ^*. When instead we take the inner product of Eq. (4.A.3) with $\partial\xi^*/\partial t$ and use that **F** and $-i\rho\mathbf{u}\cdot\nabla$ are self-adjoint operators, we can obtain $\partial E/\partial t = 0$. Here, the mode energy [123, 115, 69]

$$E = \frac{1}{2}\int\left(\rho\left|\frac{\partial\xi}{\partial t}\right|^2 - \xi^*\cdot\mathbf{F}\right)d^3\mathbf{r} = \left(|\omega|^2 + \bar{W}\right)Ie^{2\mathrm{Im}(\omega)t}. \tag{4.C.1}$$

For unstable modes, Eq. (4.B.1) gives $|\omega_\pm|^2 = -\bar{W}$ so that $E = 0$. For stable modes however, Eq. (4.B.1) gives $|\omega^\pm|^2 = \bar{W} + 2\bar{V}\omega_\pm$ so that

$$E = 2\omega^\pm \left(\omega^\pm - \bar{V} \right) I = \pm 2\omega^\pm I \sqrt{\bar{V}^2 + \bar{W}}. \qquad (4.C.2)$$

This shows that when ω^+ and ω^- have the same sign, the two solutions of Eq. (4.B.1) correspond to a pair of modes with energies of opposite sign. A negative energy mode accompanied by one with positive energy. Note that this is only possible when

$$0 < -\bar{W} \leq \bar{V}^2. \qquad (4.C.3)$$

The stability criterion of Eq. (4.1.1) was derived in the previous chapter under the assumption that the Coriolis shift and the Doppler shifted mode frequency $\omega_D = \omega + n\Omega$ vanish. At marginal stability then $\bar{V}^2 = n^2\Omega^2 = -\bar{W}$, marginally satisfying Eq. (4.C.3). Before the system becomes unstable there will therefore be two modes, one with a small positive energy and one with an opposite negative energy, that combine to form an instability.

The condition $\omega_D = 0$ implies that the "pattern frequency" $-\omega/n$ locally equals the plasma rotation frequency Ω. This co-rotation condition holds quite generally for non-axisymmetric instabilities [1]. In instabilities like the Papaloizou-Pringle instability [156] or the Rossby wave instability [135], waves reflect at the boundaries or get trapped near a maximum of an equilibrium quantity, respectively. In a magnetized plasma we may speculate that the localizing effect of magnetic field line bending can play a similar role in confining waves with positive and negative energy.

Chapter 5

Low-frequency Alfvén Gap Modes in Rotating Tokamak Plasmas

As a result of toroidal rotation, sequences of new global modes are predicted to arise in magnetically confined plasmas. The frequencies of these Alfvén modes lie inside gaps of the continuous magnetohydrodynamic spectrum that are created or enlarged by toroidal flow. The numerically obtained results are compared with an analytical investigation, yielding a useful criterion for mode existence. Because of their low frequencies, these modes may be easily destabilized by energetic particles. Because of their sensitivity to the Mach number however, these modes can provide a valuable extension to MHD-spectroscopy by giving information on the rotational velocity.

5.1 Introduction.

In magnetically confined toroidal plasmas, such as tokamak plasmas for fusion energy research, high toroidal flow speeds can arise through neutral beam injection or intrinsic mechanisms. Such flow causes fundamental changes in the magnetohydrodynamic (MHD) stability and wave spectrum of the plasma. Centrifugal forces for example can stabilize various otherwise unstable modes [198, 206]. Toroidal rotation most significantly influences the low-frequency part of the spectrum, where at the same time MHD-stable waves are prone to destabilization by fast ions. Understanding the complete MHD spectrum of modes excited by fast ions [163] or antennas [68] is important for diagnostic purposes. Modes that are sensitive to rotation are of particular interest.

   Here we present a new class of low-frequency MHD modes that exhibit such sensitivity to toroidal plasma rotation. The modes were found numerically and investigated analytically. Toroidal rotation, plasma compressibility, and coupling between Alfvén waves and slow magnetosonic waves are taken into account.

   A pronounced consequence of plasma rotation is the appearance of a toroidal flow-induced (TFI) gap in the continuous MHD spectrum [190, 189]. In a toroidal plasma, coupling of Alfvén waves to slow magnetosonic waves gives rise to a second spectral gap [36, 187, 21]. This pressure, or β-induced Alfvén gap extends to the higher frequency of the Geodesic Acoustic Mode (GAM) [216, 203]. Contrary to singular continuum modes, radially extended 'global' modes may exist within these gaps, with discrete frequencies near an extremum in the continuous spectrum. The radial group velocity of these standing waves vanishes because of interference with either a counter-propagating wave or with its own reflection off some 'potential well' in the plasma [97]. An experimentally well-established example of the first type is the Toroidal Alfvén Eigenmode (TAE) [34] while the latter category includes the global Alfvén eigenmode [3] and the Reversed-Shear Alfvén Eigenmode (RSAE) [11, 171, 50]. Global modes called Beta-induced Alfvén Eigenmodes (BAEs) [98, 187] can exist near the GAM frequency. Recently, β-induced Alfvén acoustic eigenmodes were found both numerically and experimentally [74]. These modes also occur within the BAE/GAM gap, but at lower frequencies associated with extrema due to slow-Alfvén coupling. Toroidal rotation widens the BAE/GAM gap and a single global Toroidal Flow-induced Alfvén Eigenmode (TFAE) can appear [190, 189].

   We show that toroidal rotation can cause the formation of a new class of global Alfvén modes below the BAE/GAM gap, which are distinctly different from both the BAE and the TFAE. Similarly, modes are shown to arise within the TFI gap for sufficient rotation. Observation of such modes that are sensitive to rotation, can give detailed information on the rotation velocity, providing a valuable extension to MHD-spectroscopy [68, 171, 50]. Using a simplified mode equation, a total of four types of Alfvén modes occurring above and below the TFI and BAE/GAM gap are analyzed in a unified way. The analysis is therefore also relevant for the description of RSAEs in rotating plasmas. Simple criteria for mode existence are derived that agree with computations.
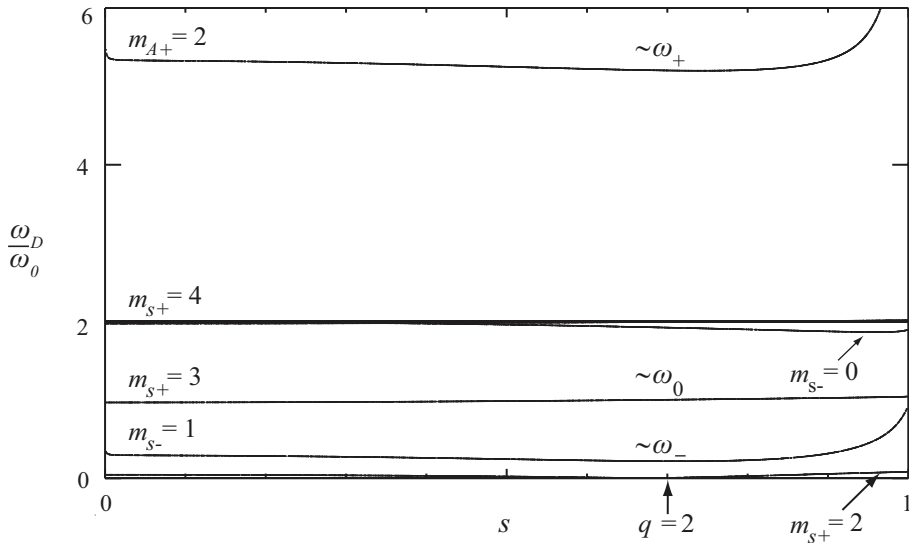
Figure 5.1: The low-frequency continuous spectrum for $M_0 = 1$. The poloidal mode number m is indicated for the Alfvén (A) and slow magnetosonic (s) waves, propagating in the co-rotating $(+)$ or counter-rotating $(-)$ direction. Global modes were found below $\omega_D^2 = \tilde{\omega}_\pm^2$.

5.2 Simulations

5.2.1 Equilibrium

The simplest configuration in which the newly discovered modes appear is that of an isothermal rigidly rotating plasma. With the assumptions of Eq. (2.3.2), the analytical equilibrium solution of Eq. (2.3.4) can be used. This equilibrium was accurately reconstructed numerically with FINESSE [8] for various $M_0 = \sqrt{2/\gamma}\mathcal{M}$. With $\gamma = 5/3$, $\epsilon = 0.1$, and β between zero at the plasma edge and a maximum $\beta \approx 5 \cdot 10^{-3}$, a relatively flat, monotonically increasing, safety factor profile was obtained, which was centered around $q \approx 2$. The coefficients c_1 and c_2 of Eq. (2.3.4) were adjusted to make the height of the plasma cross-section at $R = R_0$ equal its width $2a$.

5.2.2 Continuum modes

The MHD spectrum for $n = 1$ was investigated with PHOENIX [15], including the poloidal harmonics $m = 0, 1, 2, 3$, and 4. The low-frequency continuous spectrum is shown in Fig. 5.1 as a function of the dimensionless radial coordinate $s \approx r/a$ introduced in Eq. (2.6.1).

Due to rotation and other toroidal effects, the low-frequency continuous spectrum deviates significantly from the uncoupled cylindrical continuum. Due to an intricate
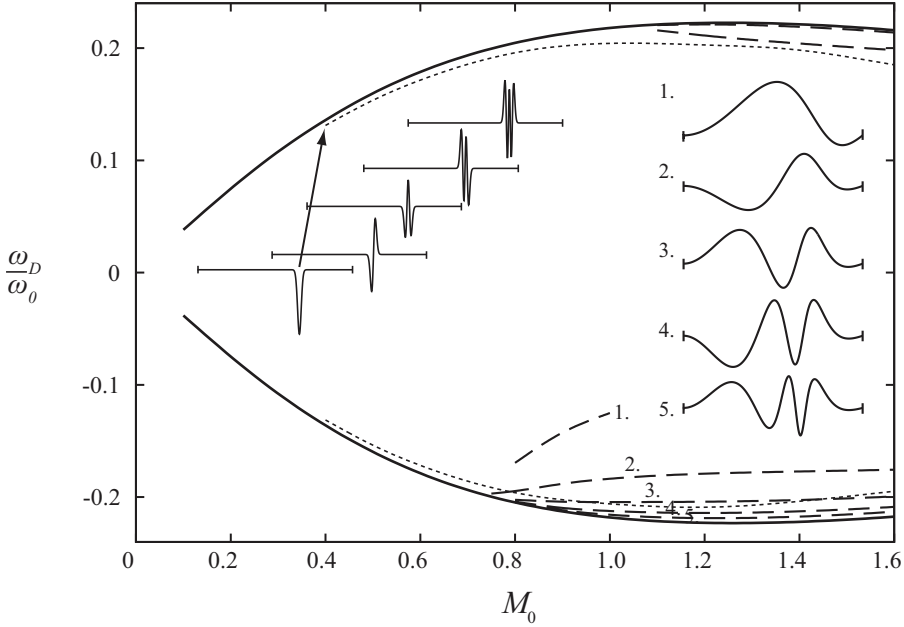
Figure 5.2: The frequencies of the toroidal flow-induced gap $\omega_D \approx \pm\tilde{\omega}_-$ (solid), the first zonal flow-like mode (dotted) and several global modes (dashed). The v_ϑ amplitudes of the first five zonal flow-like modes and the v_s amplitudes of the first five global modes are displayed for $M_0 = 1$. The first and second global modes were also found at the top of the gap.

coupling [189, 203] with the $m_A = 2$ and $m_s = 3$ continuum branches, the $m_s = 1$ continuum branch is dragged downwards in frequency near the rational surface and acquires an Alfvénic character. In a rotating equilibrium, the continuum does not reach $\omega_D = 0$ but is lifted to a finite Brunt-Väisälä frequency as discussed in chapter 2.

The modified $m = 2$ Alfvén and $m = 1$ slow-wave continuum frequencies are described well by the frequencies $\omega_D^2 = \omega_\pm^2$ for which A_1 vanishes so that the mode equation (3.2.2) becomes singular. The frequency range from $-\tilde{\omega}_+$ to $\tilde{\omega}_+$ is the BAE/GAM gap, modified by rotation. The gap between $-\tilde{\omega}_-$ and $\tilde{\omega}_-$ represents the TFI-gap caused by the buoyancy effect discussed in chapter 2. Both gaps are clearly visible in Fig. 5.1. In the range $0.1 \leq M_0 \leq 1.6$, the frequencies $\tilde{\omega}_-$ and $\tilde{\omega}_+$ given by Eq. (2.5.26a) were found to agree within a percent with the gap frequencies obtained numerically.

5.2.3   Global Alfvén modes

Above certain Mach numbers, sequences of global modes were found to arise near the bottom and the top of the TFI gap, as shown in Fig. 5.2. Because of the low magnetic shear, these modes extend radially over the entire tokamak. They first appear near the
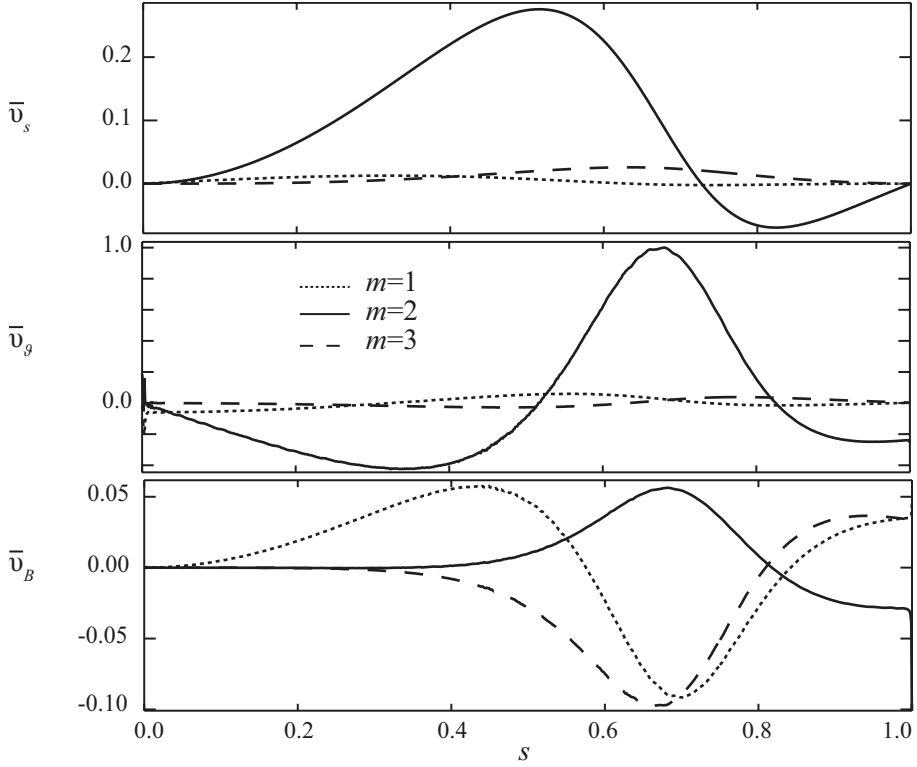
Figure 5.3: The velocity amplitudes $\bar{v}_i = \mathrm{Re}(v_i)/\mathrm{Re}(v_{\vartheta,\mathrm{max.}})$ of the first global mode near $\omega_D = -\tilde{\omega}_-$ for $M_0 = 0.8$.

bottom of the gap. At higher Mach numbers these modes also start to appear near the top of the gap.

Figure 5.3 shows the amplitudes of the first global mode. The Eulerian velocity perturbation $\mathbf{v} = -i\left(\omega + n\Omega\right)\boldsymbol{\xi}$ is expressed in components as $2s\mathbf{v} = v_s\mathbf{a}_s - iv_\vartheta\mathbf{a}_\vartheta - iv_B\mathbf{a}_B$. Here $\mathbf{a}_s$ and $\mathbf{a}_\vartheta$ are covariant base vectors of the coordinate system (s, ϑ, ϕ) and $\mathbf{a}_B = qR\mathbf{B}/B_\phi = \mathbf{a}_\vartheta + qR\hat{\mathbf{e}}_\phi$ [15]. The v_ϑ-component is much larger than both v_s and v_B. Because this is the dominant polarization for Alfvén waves, the observed modes can rightfully be called Alfvén modes. Figure 5.3 shows that the $m = 2$ component of v_s and v_ϑ, for which $(m/q - n)^2$ is minimal, is dominant. The v_B amplitude shows significant side-band amplitudes for $m = 1$ and $m = 3$ as well, because motion parallel to the magnetic field does not bend the field lines. Due to perfectly conducting wall boundary conditions at the plasma edge, the radial v_s velocity vanishes at $s = 1$.

Global modes also appear slightly below the BAE/GAM frequency. Above critical Mach numbers $M_0 \approx 0.9$ and $M_0 \approx 1.0$, these modes branch off the top and bottom of the continuum, respectively. The v_s and v_ϑ components are virtually indistinguishable
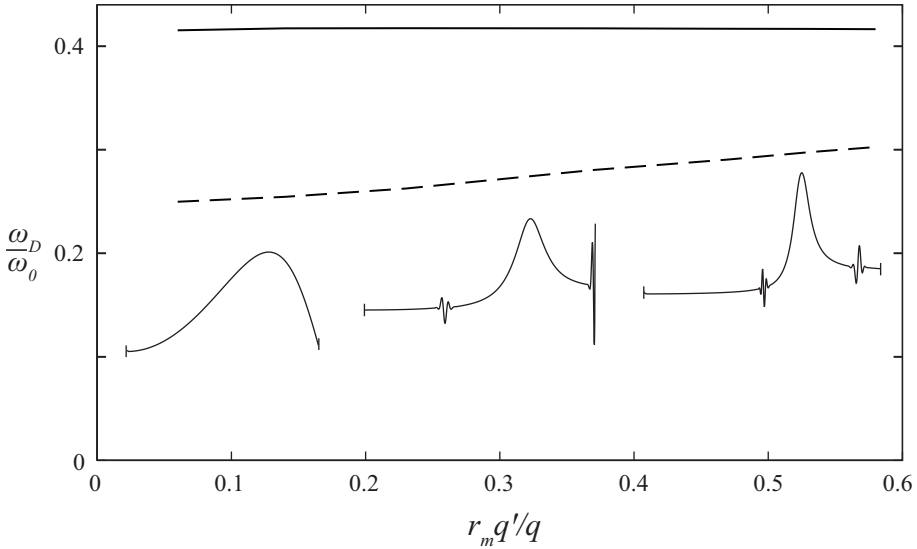
Figure 5.4: The frequencies of the $\tilde{\omega}_-$ continuum (solid) and the first $m = n = 1$ global Alfvén mode (dashed) as a function of the magnetic shear $r_s q'/q$ for $M_0 = 1$, $q(r_s) = 1$ and $S = 10^8$. The v_ϑ-amplitude of the modes is shown for $r_s q'/q \approx 0.06, 0.37$, and 0.58, respectively.

from those of the global modes present in the TFI gap. The v_B-velocity, however, is significantly smaller because the frequency of these modes is well above that of the 'sound frequency' ($\tilde{\omega}_+ > \omega_0$), which is too high for compressional wave motion in the direction of the magnetic field to be effective.

When the safety-factor profile is centered around $q = 1$ instead of 2, global $m = n = 1$ Alfvén modes appear near the bottom of the $\tilde{\omega}_-$-gap already above $M_0 \approx 0.15$. To investigate how the magnetic shear influences these modes, we deviated from the analytical solution of Eq. (2.3.4) and chose $FF' = (1 + \mu) J (1 - s^2)^\mu$. By increasing μ from 0 to 5, the magnetic shear was increased tenfold. From Fig. 5.4 we observe that, for the very low magnetic shear used in the foregoing simulations, the mode frequency seems to be fairly independent of the magnetic shear. For $r_s q'/q > 0.1$, with r_s the radius of the rational surface, the mode frequency increases approximately offset-linearly with the magnetic shear, towards the continuum frequency. Under the influence of magnetic shear, the modes also become more localized. Their frequency starts to overlap with the slow magnetosonic continuum so that under the influence of a finite resistivity η, the modes are damped [157]. For a Lundquist number $B_m R_m / \sqrt{\rho_m} \eta = 10^8$, the rate at which the modes are continuum-damped is about two orders of magnitudes smaller than their frequency. The interaction with the slow continuum was predominantly found to affect the parallel v_B component and only a tiny perturbation of the v_s-component was observed. Note from Fig. 5.4 that the influence on the v_ϑ-component is largest near the plasma edge, where the Alfvén frequency

diverges.

In order to test the robustness of these modes further, we increased the inverse aspect ratio and the dimensionless pressure to tokamak relevant values of $\epsilon = 0.3$ and a maximum $\beta \approx 0.04$. For these higher parameter values, the mode structure and frequency do not change substantially compared to the low-ϵ, low-β calculations. Also the modes discussed in the next section remain present.

5.2.4 Non-axisymmetric zonal flow modes

In Fig. 5.2 also localized but non-singular modes are shown that cluster near the continua. Their number of nodes increases when moving in frequency towards the continuum (Sturmian in ω_D^2 [64]). These modes have a negligible radial velocity so that their motion is practically within the magnetic surfaces. Unlike the global Alfvén modes of the previous subsection, which exist only for Mach numbers above a threshold value, these localized modes seem to exist for all values of M_0. The frequency of these modes goes to zero with vanishing toroidal rotation, allowing us to identify them as a type of finite mode-number zonal flows. These modes arise due to compressibility of poloidal $\mathbf{E} \times \mathbf{B}$ perturbations which, if fully compensated by a parallel return flow, yield a zero-frequency perturbation. In agreement with the result of chapter 2, these zonal flows acquire a finite oscillation frequency in the presence of toroidal rotation that can be attributed to the centrifugal convective effect. Simulations and analysis have shown [84] that a whole spectrum of finite-m, n zonal flows exist in general, that can condense into an axisymmetric $m = n = 0$ zonal flow. Similar to the modes found here, these flows were found to be radially located near rational surfaces.

5.3 Analysis

5.3.1 Mode existence criterion

Various features of the observed gap modes can be explained through the mode equation Eq. (3.2.2). Multiplying Eq. (3.2.2) by ξ^* and integrating over the entire plasma yields

$$\int_0^a r^2 A_2' \, |\xi|^2 \, dr = \int_0^a A_1 \left(r^3 \, |\xi'|^2 + r(m^2 - 1) \, |\xi|^2 \right) dr + C \, |I(\xi)|^2 , \qquad (5.3.1)$$

where the integrand $r^3 A_1 \, |\xi'|^2$ results from partial integration using $r^3 A_1 \xi' \xi^*|_0^a = 0$. The final term of Eq. (5.3.1) is equal to $\int_0^a h\xi^* dr$ and results from integration of the inhomogeneous term (3.2.6).

For $A_1 > 0$ the right hand side is manifestly positive. From Eq. (3.2.11) we see that A_1 is positive in the range $\omega_0^2 < \omega_D^2 < \omega_+^2$ and for $\omega_D^2 < \omega_-^2$. For global modes to exist within this frequency range, therefore, a necessary condition is that the left-hand side

of Eq. (5.3.1) is positive as well. For the isothermal rigidly rotating plasma considered in this chapter this requires

$$\int_0^a r^2 A_2' |\xi|^2 \, dr = \frac{A_2}{\beta} \int_0^a r^2 \beta' |\xi|^2 \, dr > 0. \qquad (5.3.2)$$

For physical profiles the latter integral will be negative. Hence, this condition requires $A_2 < 0$. Slightly below the continuum frequencies $\omega_D^2 = \omega_\pm^2$, where A_1 is positive but small, $A_2 < 0$ reads

$$1 - q^2(1 - \mathcal{M}^2 - \mathcal{M}^4) > \frac{2\gamma\Omega\omega_D/n}{\omega_0^2 - \omega_D^2} \left(1 + \frac{\mathcal{M}^2}{\gamma}\right), \qquad (5.3.3)$$

where $\omega_D = \pm\tilde{\omega}_-$ or $\pm\tilde{\omega}_+$. The Mercier term $1 - q^2$ ensures that for $q = m/n > 1$, modes just below $\omega_D^2 = \tilde{\omega}_\pm^2$ only exist for sufficiently high M_0. This term represents the combined interchange effects of the poloidal and toroidal field curvatures, which for $q > 1$ gives a net stabilizing effect.

5.3.2 Comparison with simulations

Near $q = m/n = 1$, the Mercier term vanishes so that Eq. (5.3.3) predicts that the rotation-induced Alfvén modes can already exist at relatively low Mach numbers. This was indeed found from simulations described in Section 5.2.3. Modes were in this case absent near $\omega_D = -\tilde{\omega}_+$, for which Eq. (5.3.3) is not satisfied. For $\omega_D = \tilde{\omega}_+$, the right-hand side of Eq. (5.3.3) is negative and modes were found for Mach numbers as low as $M_0 = 0.1$.

The right-hand side of Eq. (5.3.3) represents the Coriolis-pressure effect of the previous chapter. For $\Omega > 0$, the Coriolis force favors the existence of modes at the bottom of the gap $\omega_D^2 = \tilde{\omega}_-^2$, in agreement with Fig. 5.2. For $\omega_D^2 = \tilde{\omega}_+^2$, modes at the top of the gap more easily satisfy the existence criterion of Eq. (5.3.3). Evaluating Eq. (5.3.3) for $q = m/n = 2/1$, we find that it is satisfied for $M_0 \geq 0.69$ when $\omega_D = -\tilde{\omega}_-$, $M_0 \geq 0.92$ for $\tilde{\omega}_-$, $M_0 \geq 0.92$ for $-\tilde{\omega}_+$, and $M_0 \geq 0.62$ for $\tilde{\omega}_+$. These values are in agreement with the simulations and are very close to those for which modes appear in Fig. 5.2.

It is interesting to calculate the magnitude of the various terms of Eq. (5.3.1) from the simulations. For this purpose we use the $n = 1, m = 2, v_s$-component of the mode shown in Fig. 5.3. We find that numerically, the right-hand side approximately balances the left-hand side, with contributions more or less evenly distributed between the two integrals. The magnetic field-line bending contribution to the first integral of the right-hand side of Eq. (5.3.1) is an order of magnitude smaller, in agreement with the observation that the mode shown in Fig. 5.3 does not show localization due to the magnetic shear.

Perhaps even more interesting is to show how the various components of A_2' from Eq. (3.2.4b) contribute to the first integral of Eq. (5.3.1). The contribution of A_1' turns out to be negligible, in agreement with the assumption used in the analysis

of Section 5.3.1. The negative Mercier term $-\beta'(1-q^2)$ is only slightly smaller in magnitude than the positive flow-drive $-\beta'\left(\mathcal{M}^2+\mathcal{M}^4\right)$. There is also quite a large positive contribution, about one third of the flow drive, from the Coriolis-pressure term α_k' in A_2'. This explains why in Fig. 5.2 modes were not found for $M_0 = 0.8$ near the top of the gap, where this term has negative sign.

5.3.3   Origin of the global Alfvén modes

The radial 'potential well' (see App. 5.A.2) that enables the existence of global modes, is created by toroidal rotation through the term $r^2 A_2'$ in the mode equation (3.2.2). Apart from a stabilizing Mercier term and the Coriolis-pressure contribution, A_2' contains a centrifugal term proportional to $-\beta_k'$. This term is responsible for the existence of the global Alfvén modes. For the isothermal rigidly rotating equilibrium studied in this chapter, the variation in β_k is through the radial variation of the density. The physical origin is in this case very similar to the Rayleigh-Taylor instability of a heavy fluid on top of a lighter one. With the centrifugal force replacing the role of gravity.

In this simple picture a radially decreasing density profile $\rho' < 0$ is stabilizing at the low-field side of the plasma. At the high-field side however the density increases in the direction of the centrifugal force, forming a stable density distribution. This situation is similar to that of the interchange effect associated with the toroidal field curvature. An appropriate averaging of the stabilizing and destabilizing effects results for a low-β circular tokamak in the $q^2\beta'$ term. In a similar fashion, the average centrifugal effect results in the $-q^2\beta_k'$ term.

5.3.4   Modes above the continua

The coefficient A_1 is negative in the frequency ranges $\omega_-^2 < \omega_D^2 < \omega_0^2$ and for $\omega_D^2 > \omega_+^2$. At frequencies away from the continua, when magnetic shear is low enough, A_1 may become negative enough for the first integral on the right hand side of Eq. (5.3.1) to become negative. This is especially so when the mode frequency approaches $\omega_D^2 = \omega_0^2$ from below, for which A_1 diverges. In this case Eq. (5.3.1) gives, using $\int_0^a r^2 A_2' |\xi|^2 \, dr = -A_2 I(r^{1-m} |\xi|^2)/\tilde{\beta}$, the existence criterion

$$A_2 > -C\tilde{\beta} \frac{|I(\xi)|^2}{I\left(r^{1-m} |\xi|^2\right)} \geq -C\tilde{\beta} I(r^{m-1}). \tag{5.3.4}$$

In the second step we used Schwarz's inequality to obtain a bound based only on 'known' quantities. In this case, toroidal rotation creates a potential *hill* for modes. The condition Eq. (5.3.4) can be relevant for RSAEs, which accumulate above $\omega_D^2 = \tilde{\omega}_+^2$ when the safety factor has a minimum near $q = m/n$. These modes are routinely observed in magnetic spectrograms as up- or down-chirping Alfvén cascades [171, 50]. A characteristic bend in the spectral lines is observed near the minimum frequency $\tilde{\omega}_+$

[21] which, depending on whether Eq. (5.3.4) is satisfied, may not be attainable. We will investigate this in detail in the next chapter.

5.4 Conclusions & Discussion

In this chapter we have shown analytically and numerically that, depending on the Mach number, global Alfvén eigenmodes can accumulate below or above the continuum frequencies $\omega_D^2 = \tilde{\omega}_-^2$ and $\omega_D^2 = \tilde{\omega}_+^2$. These new modes are distinctly different from TFAEs, which are formed by the coupling between an m-Alfvén wave and two $(m \pm 1)$-slow magnetosonic waves. Instead, the modes described in this work only have a single dominant poloidal mode number m and arise due to a 'potential well', created by toroidal rotation, close to the continua. Also the dependence of the mode frequency on the rotation frequency, linear for TFAEs, can be used to discriminate between them. The modes accumulating at $\omega_D^2 = \tilde{\omega}_+^2$ are in the same frequency range as BAEs. Because the mode equation, Eq. (3.2.2), is linear in β however, these modes cannot be said to be induced by a threshold value of β. Instead it is shown here that centrifugal forces are essential for their formation. An existence criterion Eq. (5.3.3), derived for negligible magnetic shear, shows that modes can exist below $\omega_D^2 = \tilde{\omega}_\pm^2$, near $q = 1$ at practically relevant toroidal rotation velocities. Simulations show that these modes remain present for practically relevant magnetic shear, aspect ratio, and β.

Very localized but non-singular modes observed in the simulations near $\omega_D^2 = \tilde{\omega}_-^2$ were identified as non-axisymmetric zonal flow modes. Because their motion is primarily within the magnetic surfaces, they do not contribute to radial transport and can play a role in storing some of the turbulent energy. Their negligible radial component is also the reason why they are not described by the mode existence criterion Eq. (5.3.3) for the radial component of the plasma perturbation. Because their amplitude is non-zero only in a small region around the magnetic surface these modes may escape strong continuum damping. When a small but finite resistivity was introduced the modes disappeared however from their original frequency range, while the global Alfvén modes were merely slightly damped.

In order to assess whether the global Alfvén modes described in this work can actually be experimentally observed, the implications of the various simplifying assumptions made in the present work have to be investigated further. The effects of a finite temperature gradient and rotational shear, which were not taken into account in this work, enter the mode equation primarily through the Mach number. Ordinarily the Mach number decreases towards the plasma edge so that the term $r^2 A_2'$, responsible for the formation of modes, will only be larger than in the present case of constant M_0. A larger variation of the equilibrium quantities, or a smaller aspect ratio, will modify the continuum significantly, making continuum damping [223, 157] of the global modes inescapable. Ion Landau damping of the lower frequency modes is probably very small because their frequency $\tilde{\omega}_- \ll 1$ is well below that of thermal

ions. Similar to BAE modes [98], the modes near $\omega_D^2 = \tilde{\omega}_+^2$ may be destabilized by energetic (beam) ions. These modes may therefore arise in a hybrid regime, which is included as a third operating scenario for ITER. In this advanced tokamak operating regime, a broad low-shear region near $q = 1$ exists at the center of a tokamak plasma.

When they are not destabilized, the newly discovered global modes may also prove to be useful. Because the frequencies $\omega_D^2 = \tilde{\omega}_\pm^2$ at which these modes accumulate depend sensitively on the Mach number, they can provide accurate information on the rotation velocity. Similar to how the sweeping of Alfvén cascades in reversed-shear plasmas provides information on the q-profile, an extension of MHD-spectroscopy can be envisioned in which the evolution of these modes provides information on the plasma rotation.

5.A   Appendix

The isothermal rigidly rotating low-shear plasma considered in this chapter is particularly amenable to analytical investigations. The following appendices exploit this simplification to provide more insight into the low-frequency spectrum. First, the mode equation is transformed to Sturm-Liouville form, which allows us to see what happens for modes with frequencies away from the continua. Next we will transform the mode equation to Schrödinger form. This will allow us to say something about the shape of the eigenfunctions.

These appendices were added to this thesis and are not part of the original publication [93].

5.A.1   Sturm Liouville form

The main reason for the many simplifications that arise for an isothermal rigidly rotating shearless plasma is that for a given frequency, A_1/β and A_2/β are constants. A particular solution to Eq. (3.2.2) is then given by $\xi_0 r^{m-1}$, where $\xi_0 = m^2 \tilde{\beta} C_+ / ((m-1) A_1 + A_2)$. Introducing $\tilde{\xi} = \xi - \xi_0 r^{m-1}$ and dividing Eq. (3.2.2) by A_1/β gives

$$(u\tilde{\xi}')' - v\tilde{\xi} + \lambda w \tilde{\xi} = 0, \tag{5.A.1}$$

where $u = r^3 \beta$, $v = r(m^2 - 1)\beta$, $w = -r^2 \beta'$, and the eigenvalue $\lambda = -A_2/A_1$. When u and w are positive and v is non-negative, Eq. (5.A.1) constitutes a Sturm-Liouville equation. For this type of equations many useful theorems can be proven, among which is Sturm's fundamental oscillation theorem discussed in Section 6.2.1.

Multiplying Eq. (5.A.1) by $\tilde{\xi}^*$ and integrating over the entire plasma, we obtain the Rayleigh quotient

$$\lambda = \frac{\int_0^a \left(u|\tilde{\xi}'|^2 + v|\tilde{\xi}|^2 \right) dr}{\int_0^a w|\tilde{\xi}|^2 dr}, \tag{5.A.2}$$

where $u|\tilde{\xi}'|^2$ results from partial integration using $u\tilde{\xi}^*\tilde{\xi}'|_0^a = 0$. At $r = 0$ we have that $\tilde{\xi}^*\tilde{\xi}' = \xi^*\xi' = 0$ for all eigenfunctions. At $r = a$ we have to assume that $\beta(a) = 0$ so that u vanishes at the plasma edge.

From Eq. (5.A.2) we conclude that for $\beta' < 0$ positivity of the eigenvalue λ is a necessary condition for the existence of global modes. We can however obtain more information by making use of a well-known variational principle. This states that when λ is calculated for all continuous functions satisfying the boundary conditions of (5.A.1), the smallest obtainable value is the actual lowest eigenvalue. This theorem can be used to obtain an upper estimate of the lowest eigenvalue by using reasonable test-functions. Inserting $\tilde{\xi} \propto r(1 - r/a)$ into Eq. (5.A.2) and assuming $\beta \propto 1 - (r/a)^2$ for $m = 1$ gives for example $\lambda = 9/5$. With different test functions this value can only be slightly reduced, so that we seem to be close to the lowest eigenvalue $\lambda_{\min.} \approx 1.8$.

In order to find the frequency corresponding to an eigenvalue λ, we have to solve

$$\lambda = -\frac{A_2}{A_1}. \tag{5.A.3}$$

for ω_D. We neglect the Coriolis-pressure term α_k' so that A_2 of Eq. (3.2.4b) becomes independent of ω_D. With $A_1 = \tilde{A}_1$ from Eq. (3.2.5a) we can solve Eq. (5.A.3) to give

$$\omega_D^2 = \frac{\omega_0^2}{2}\left(a_1 + \mathcal{A} \pm \sqrt{(a_1 + \mathcal{A})^2 - a_2 - 4\mathcal{A}}\right), \tag{5.A.4}$$

where $\mathcal{A} \equiv \left(\omega_A^2/\omega_0^2\right)\left(A_2 - A_1\right)/\left(1 + \lambda\right)$. Note that with $\mathcal{A} = 0$ the continuum frequencies $\omega_D^2 = \tilde{\omega}_\pm^2$ of Eq. (2.5.26a) are recovered. Without the Coriolis-pressure term α_k, Eq. (5.A.4) predicts stability when

$$0 < a_2 + 4\mathcal{A} < (a_1 + \mathcal{A})^2. \tag{5.A.5}$$

Next we plot λ from Eq. (5.A.3) as a function of ω_D/ω_0. We use $q = m = n = 1$, $\gamma = 5/3$, $\gamma_e = 1$, and $\mathcal{M} = 0.8$. Fig. 5.5 shows λ both including and excluding the Coriolis term α_k. The continua are clearly visible as the positions where λ diverges. The fundamental eigenmode is expected at those frequencies where the graph of λ crosses $\lambda_{\min.}$. Without the Coriolis-pressure term this happens at frequencies just below $\omega_D^2 = \tilde{\omega}_\pm^2$, inside the TFI and GAM/BAE gaps. The Coriolis-pressure term α_k however breaks the symmetry around $\omega_D = 0$. Modes inside the BAE/GAM gap near $\omega_D = -\tilde{\omega}_+$ are now no longer possible. This is in agreement with what was observed in the simulations of Section 5.3.2. The graph indicates that just outside this gap, the situation is the opposite. Modes can be expected near $-\tilde{\omega}_+$ but not near $tilde\omega_-$. This will however require reversed magnetic shear, which will be the subject of the next chapter.

Note that contrary to what was focused on in chapter 4, the effect of the Coriolis-pressure term $\alpha_k' \sim \left(\rho_0\omega_D\Omega\right)'$ arises here because of a variation in the density, not a variation in the rotation frequency. Because of the proportionality with ω_D, the effect is much smaller for the lower frequencies near the ω_- gap than near ω_+, in agreement with Fig. 5.5.
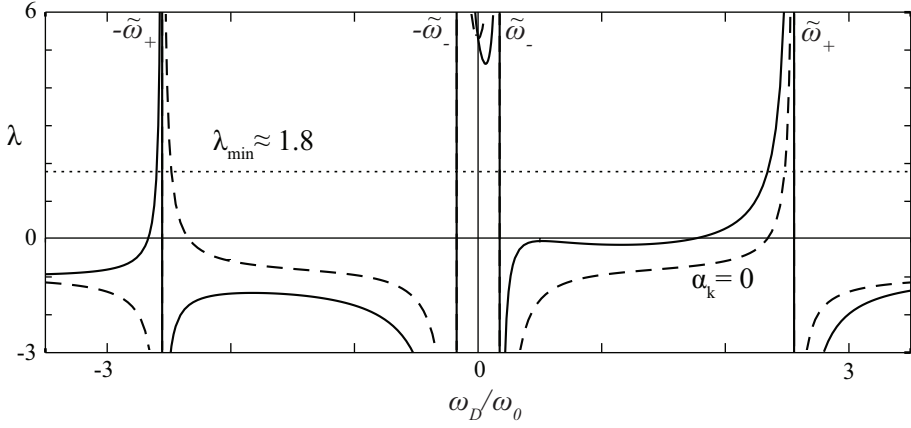
Figure 5.5: The eigenvalue $\lambda = -A_2/A_1$ versus ω_D/ω_0 for an isothermal shearless plasma with $q = 1$ and $\mathcal{M} = 0.8$. ($\gamma = \frac{5}{3}$, $\gamma_e = 1$).

5.A.2 Schrödinger form

Under the transformation $\psi = \sqrt{f}\xi$ the homogeneous part of the mode equation (3.2.2) becomes

$$\psi'' - V\psi = 0, \tag{5.A.6}$$

with the 'potential'

$$V = -\frac{1}{4}\frac{f'^2 - 2ff'' + 4gf}{f^2}. \tag{5.A.7}$$

Equation (5.A.6) closely resembles the one-dimensional time-independent Schrödinger equation. The eigenvalue ω_D however appears in some complicated nonlinear way in the potential, instead of linearly. For the isothermal shearless mode equation (5.A.1) the eigenvalue λ can actually be made to appear linearly using a coordinate transformation and a coordinate dependent re-normalization of the eigenfunction.

By analogy with the Schrödinger equation we expect a discrete spectrum of 'bound states'. For Eq. (5.A.6), this requires that the 'potential' V is negative somewhere. The eigenfunctions are then confined between the 'turning points' where V becomes positive and the eigenfunction will have to go to zero there exponentially. Or, again by analogy from quantum mechanics, the eigenmode can 'tunnel' through the potential barrier to another potential well. Such a potential barrier can for example be the continuum for which f vanishes. This situation was actually considered in Ref. [72] where it was shown to lead to 'double-gap Alfvén eigenmodes'.

Another turning point is usually present near the plasma center. The final term $-g/f$ of Eq. (5.A.7) with g from Eq. (3.2.3b) will give a term $(m^2 - 1/4)/r^2$ that will constitute a potential barrier near $r = 0$. This is reminiscent to the 'centrifugal term'

proportional to $l(l+1)/r^2$, with l the azimuthal quantum number, that appears in the radial part of the spherically symmetric Schrödinger equation.

For the isothermal shearless plasma considered in this chapter, the potential (5.A.7) reads

$$V = \lambda \frac{\beta'}{r\beta} + \frac{\beta'' + 3\beta'/r - \beta'^2/2\beta}{2\beta} + \frac{m^2 - 1/4}{r^2}. \tag{5.A.8}$$

A necessary condition for the existence of discrete modes is that $V < 0$ somewhere in the plasma. Note that this requires variation in β; the overall magnitude of β does not matter. When β goes to zero at the edge smoothly, a second turning point can arise near the edge, forcing the eigenfunction to go down smoothly there as well.

Chapter 6

The Effect of Toroidal Plasma Rotation on Low-frequency Reversed Shear Alfvén Eigenmodes in Tokamaks

The influence of toroidal plasma rotation on the existence of Reversed Shear Alfvén Eigenmodes (RSAEs) near their minimum frequency is investigated analytically. An existence condition is derived showing that a radially decreasing kinetic energy density is unfavorable for existence of RSAEs. The Coriolis-pressure effect is typically unfavorable for modes moving slower than the plasma or moving in the opposite direction. The generality of the analysis allows for the description of down-sweeping RSAEs and also rotation-induced modes in regular shear plasmas.

6.1 Introduction.

To describe Alfvén waves associated with the bending of magnetic field lines in toka-mak plasmas, the theory of magnetohydrodynamics has been very successful. The continuous MHD spectrum contains various gaps and extrema introduced by toroidal effects, plasma shape, and rotation. When specific criteria are met, global modes can cluster at these extrema. An example of such cluster modes are Reversed Shear Alfvén Eigenmodes (RSAEs). They are often observed in magnetic spectrograms when the safety factor profile has an extremum. These modes have been used as an accu-rate diagnostic for the safety factor [68, 171, 50]. Besides their usefulness in MHD-spectroscopy, RSAEs can also have a negative effect on the confinement of energetic ions [99]. The expulsion of fast particles can lead to decreased plasma performance and even damage to plasma facing components.

Reversed shear Alfvén eigenmodes were first observed in JT-60U [125] and later thoroughly investigated at JET [171, 11], where they were called Alfvén Cascades (ACs). They have also been observed in various other tokamaks like Alcator C-mod [50], TFTR [160], ASDEX Upgrade [19], DIII-D [192], and spherical tokamaks like NSTX [57] and MAST [80]. Recently they have also been found in the LHD stel-larator [185]. RSAEs are observed to terminate at the Geodesic Acoustic Mode (GAM) frequency, primarily caused by geodesic curvature [216, 64, 21]. When this minimum frequency exceeds the maximum (Toroidal Alfvén Eigenmode) frequency, RSAEs can-not exist [57]. Toroidal rotation can significantly increase the GAM frequency, an effect that might be observable in spectrograms. Besides such quantitative changes, rotation can also modify the structure of the spectrum. At very low frequencies, new flow-induced gaps and modes appear in the continuous spectrum, see Ref. [189] and chapter 5.

Whether cluster modes exist or not, depends both on whether certain cluster crite-ria are met and whether a free energy source is available to destabilize the modes. A radially decreasing density of large orbit energetic particles can play a role in satisfy-ing both these conditions. This effect was shown to favor the existence of modes with a ratio of poloidal and toroidal mode numbers m/n slightly above the minimum value q_0 of the safety factor q [11]. Typically in experiments q_0 is decreasing due to current diffusion so that these modes chirp upwards in frequency. Second order toroidal ef-fects were found to further favor up-sweeping cascades [20]. Simulations showed that plasma pressure gradients provide an additional drive [126]. Terms quadratic in the pressure gradient were found to play a negative role for the existence of RSAEs [21]. Inclusion of the average toroidal curvature in the interchange term resulted in a mode existence criterion that, close to a rational surface, is similar to Mercier's stability crite-rion [59]. This criterion contains a term linear in the pressure gradient that is favorable for both stability and RSAE existence when $q > 1$.

Here we extend these useful existing cluster criteria to take into account the effect of toroidal rotation. The results are limited to modes near a rational surface, where the mode frequency is close to the GAM frequency. New terms due to rotation appear,

the physical origin of which was discussed in chapter 3.

6.2 Analysis

6.2.1 Oscillation properties

Sturm's fundamental oscillation theorem with the modification due to Picone [116] states that in a given interval the homogeneous solution ξ_2 of Eq. (3.2.2) has the same number of nodes or more than ξ_1 when

$$f_1 \leq f_2 < 0 \text{ and } g_1 \geq g_2. \tag{6.2.1}$$

Since RSAEs have frequencies $\omega_D^2 \geq \omega_+^2$, from Eq. (3.2.11) we find that $f = r^3 A_1 \leq 0$. When α_k' can be neglected, for example for high m, f and g of Eqs. (3.2.3a)-(3.2.3b) satisfy the conditions (6.2.1) when $\omega_{D2}^2 < \omega_{D1}^2$. Therefore, the number of nodes of these solutions increases with decreasing ω_D^2. This is in agreement with simulations and observations of higher harmonics of RSAEs [75, 191].

More generally, when α_k' can be neglected, the theorem implies that ω_D^2 increases with the number of nodes (Sturmian) when $A_1 > 0$ and decreases when $A_1 < 0$ (anti-Sturmian). This agrees with the finding of Sturmian sequences of modes in the frequency ranges $\omega_D^2 \leq \omega_-^2$ and $\omega_0^2 \leq \omega_D^2 \leq \omega_+^2$ in chapters 3 and 5, respectively. Note that we used here a mathematical argument since for rotating toroidal plasmas no analogue exists to the physics-based Goedbloed-Sakanaka oscillation theorem for static cylindrical plasmas [71].

6.2.2 Time variation

For high poloidal mode numbers m, the time variation of q in the field line bending terms $(m/q - n)^2$ dominates the time variation of ω_+ so that from Eqs. (3.2.9)-(3.2.10b)

$$\frac{d\omega_+}{dt} = \frac{\omega_A^2}{\omega_+} \frac{\omega_+^2 - \omega_0^2}{\omega_+^2 - \omega_-^2} \left(\frac{m}{q} - n \right) m \frac{dq^{-1}}{dt}. \tag{6.2.2}$$

When q decreases and drops below m/n, there is an initially slow but accelerating increase in ω_+, explaining the hockey-stick-shaped spectral lines of RSAEs observed in spectrograms [50, 21, 191, 127]. Measured slopes $d\omega_+/dt$ can be used to discriminate between different poloidal mode numbers m and obtain the time variation of the q profile.

At the low-frequency tip of these spectral lines, when $q = m/n$ so that $\omega_+ = \tilde{\omega}_+$, we have

$$\frac{d\omega_+}{dt} = \frac{\omega_+}{\omega_0} \frac{d\omega_0}{dt} + \frac{\omega_0^2}{\omega_+^2 - \omega_-^2} \left(\frac{\omega_+}{2} \frac{d\tilde{a}_1}{dt} - \frac{\omega_0^2}{8\omega_+} \frac{d\tilde{a}_2}{dt} \right). \tag{6.2.3}$$

When $\tilde{a}_2 \ll \tilde{a}_1^2$ this approximately reduces to $d\sqrt{\tilde{a}_1}\omega_0/dt$. In spectrograms the continuum frequency ω_+ itself is generally not visible. However, the global RSAEs with

approximately the same frequency *can* be observed. The goal of the following analysis will be to establish under which conditions RSAEs can cluster above the ω_+ continuum.

6.2.3 Cluster point analysis

The nature of the differential equation (3.2.2), changes when at a radial position where $x \equiv r - r_c = 0$ the 'Mercier index' D satisfies [9, 70]

$$D \equiv \lim_{x \to 0} x^2 \frac{g}{f} > \frac{1}{4}. \tag{6.2.4}$$

In this case the local homogeneous solutions $x^{\nu\pm}$, with the complex 'Frobenius indices' $\nu_\pm = -\frac{1}{2} \pm \sqrt{1 - 4D}$, rapidly oscillate and diverge near $x = 0$. This signals the presence of an infinite sequence of modes near the cluster point at $r = r_c$. By investigating D for Eq. (3.2.2) in plasmas with a reversed magnetic shear ($q' < 0$), we obtain criteria for the existence of RSAEs near the point of shear reversal ($q' = 0$).

We note that Eq. (6.2.4) can only be satisfied when $A_1 = A_1' = 0$ and only the behaviour of A_1 to second order in x is of importance. In this case Eq. (6.2.4) becomes

$$D = \frac{2A_2'}{rA_1''}\bigg|_{r=r_c} > \frac{1}{4}. \tag{6.2.5}$$

Because of the magnetic field line bending term in A_1, A_1'' will typically be positive. In this case Eq. (6.2.5) shows that the clustering of modes requires $A_2' > 0$. When $A_2' < 0$ potentially unstable modes cannot cluster below the ω_- continuum, ensuring local stability as investigated in chapter 3.

However, when at $r = r_0$ the safety factor has a minimum $q_0 < m/n$, magnetic field line bending decreases away from $r = r_0$ so that A_1'' is negative (see Fig. 6.1). This allows, in locally stable plasmas with $A_2' < 0$, the appearance of RSAEs.

Note that with $A_1 = A_1' = 0$ and $A_1'' < 0$, Eq. (3.2.11) implies that $\omega_D^{2\,''} > \omega_+^{2\,''}$. This will allow the sequence of RSAEs with frequencies $\omega_D^2 \geq \omega_+^2$ to avoid strong overlap with the continuum and associated continuum damping, see Fig. 6.1(a). When q_0 decreases in time, field line bending will increase, as will the mode frequency according to Eq. (6.2.2). This explains why for decreasing q_0 typically up-sweeping RSAEs are found.

6.2.4 Reversed magnetic shear

We consider a plasma with a minimum q_0 in the safety factor, close ($m/q_0 - n \sim \epsilon$) to a rational surface $q = m/n$. To second order in $r - r_0$ we can write $q = q_0 + \frac{1}{2}q_0''(r - r_0)^2$ so that

$$\left(\frac{m}{q} - n\right)^2 = \left(\frac{m}{q_0} - n\right)^2 - \frac{(r - r_0)^2}{\Delta r^2}, \tag{6.2.6}$$
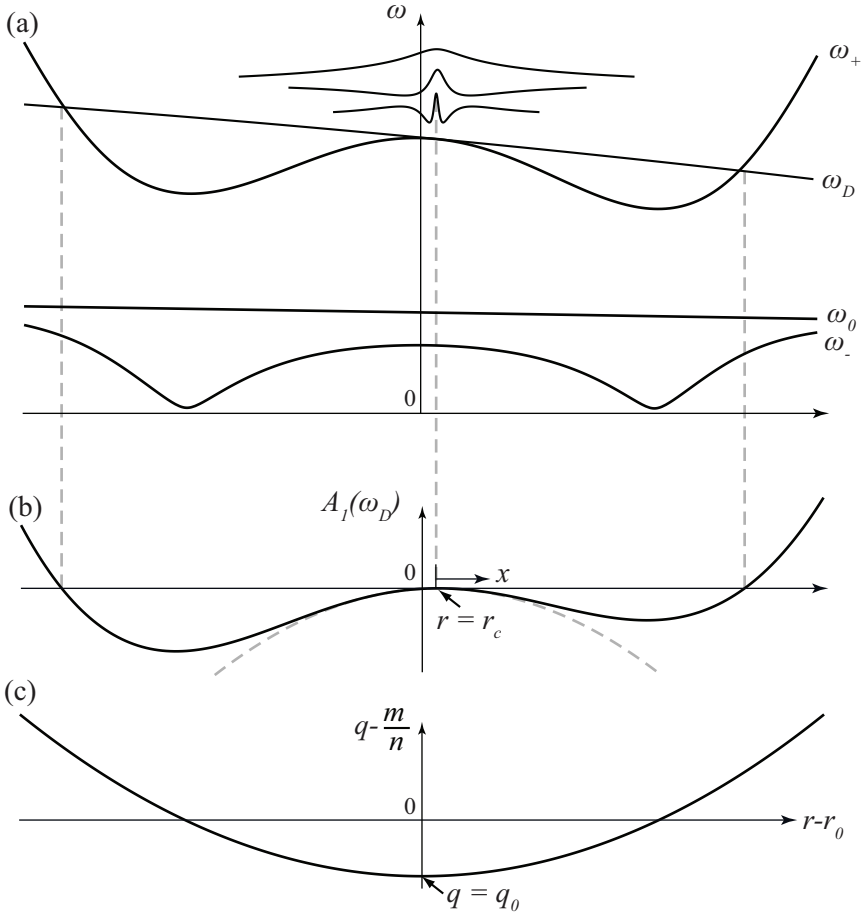
Figure 6.1: Schematic illustration of the typical circumstances under which RSAEs cluster at a position $r = r_c$ and frequency (a) $\omega_D^2 = \omega_+^2$ where $(\omega_D^2)' = (\omega_+^2)'$ so that (b) $A_1 = A_1' = 0$. This clusterpoint is not necessarily at the position (c) $r = r_0$ where the safety factor q has its minimum q_0.

where we introduced a squared shear length-scale

$$\Delta r^2 \equiv \frac{q_0^2}{mq_0''} \frac{1}{m/q_0 - n}. \tag{6.2.7}$$

The parallel wave number $-\left(m/q_0 - n\right)/R_0$ is positive when $q_0 > m/n$, so that $(m/q - n)^2$ increases quadratically away from $r = r_0$. When however $q_0 < m/n$, field line bending *decreases* away from $r = r_0$ up to the rational surface $q = m/n$, after which it increases again. This causes the 'double well' of Fig. 6.1(b), the description of which requires the inclusion of terms of higher order in $r - r_0$.

Note that in this case the continuum frequencies $\omega_{\pm}^2$ have a similar double well shape, see Fig. 6.1(a). Sufficiently localized modes may therefore avoid strong continuum damping.

The cluster point is characterized by the two conditions $A_1 = 0$ and $A_1' = 0$. These are satisfied when either $\omega_D = \omega_+$ and $\omega_D' = n\Omega' = \omega_+'$ as in Fig. 6.1(a) or $\omega_D = -\omega_+$ and $\omega_D' = n\Omega' = -\omega_+'$. When these criteria cannot be satisfied, RSAEs cannot exist. The expression for A_1'' at $r = r_c$

$$A_1'' = \left(\tilde{A}_1 + (m/q - n)^2 \right)'' = 2\frac{N-1}{\Delta r^2}, \tag{6.2.8}$$

is naturally split into a term from Eq. (6.2.6) due to field line bending, and other effects due to $\tilde{A}_1''$ incorporated in N

$$N \equiv \frac{\Delta r^2}{2} \frac{\tilde{\omega}_+^2 - \tilde{\omega}_-^2}{\omega_A^2 \left(\omega_0^2 - \tilde{\omega}_+^2\right)} \left(\omega_D^2 - \tilde{\omega}_+^2\right)'', \tag{6.2.9a}$$

$$\approx \Delta r^2 \frac{\tilde{a}_1^{3/2}}{1 - \tilde{a}_1} \frac{\omega_0}{\omega_A} \frac{n\Omega'' - \tilde{\omega}_+''}{\omega_A}, \tag{6.2.9b}$$

where in the second line we assumed $\tilde{a}_2 \ll \tilde{a}_1^2$ and used Eq. (2.5.26a). Note that in writing Eq. (6.2.8) we assumed that r_c is sufficiently close to r_0 that higher order terms in Eq. (6.2.6) can be neglected, for example $|r_c - r_0| \ll q_0''/q_0'''$.

6.2.5 Existence criterion for RSAEs

Using Eq. (6.2.8), the cluster condition Eq. (6.2.5) is given by

$$D = \frac{A_2'}{N-1} \frac{\Delta r^2}{r} > \frac{1}{4}. \tag{6.2.10}$$

As discussed previously, RSAEs can avoid strong continuum damping when $A_1'' < 0$. In this case the existence condition (6.2.10) is given by

$$(1 - N) \frac{r}{4\Delta r^2} < -A_2'. \tag{6.2.11}$$

Therefore $-A_2'$ should be sufficiently large and positive for the existence of RSAEs near their minimum frequency. With Eq. (3.2.4b) and Eq. (6.2.7) we can write this as

$$(1 - N) \left(\frac{m}{q_0} - n \right) \frac{r}{4} \frac{m}{n^2} \frac{q_0''}{q_0^2} < \beta' \left(1 - q^2 \right) + q^2 \alpha_k' + q^2 \beta_k'. \tag{6.2.12}$$

Equation (6.2.12) agrees with the previous result of [126, 59, 75] that in a static plasma, where $\alpha_k = \beta_k = 0$, a radially decreasing pressure is favorable for the existence of RSAEs provided that $q > 1$. When however in a toroidally rotating plasma

$$\mathcal{M}^2 \left(1 + \mathcal{M}^2/\gamma_e \right) > 1 - 1/q^2, \tag{6.2.13}$$

the combination of the first and last terms on the right-hand side of Eq. (6.2.12) becomes negative. When this holds, a decreasing plasma pressure is unfavorable for RSAE existence.

6.2.6 Physical interpretation

The first term on the right-hand side of Eq. (6.2.12) for $q > 1$ represents the well-known 'magnetic well', representing the interchange effect due to the average field curvature.

For a large aspect ratio tokamak, β_k is associated with the variation of the kinetic energy density with major radius, see Eq. (3.4.1). When $\beta_k' < 0$, the kinetic energy density decreases radially. This constitutes an unstable density distribution in the presence of the centrifugal force.

The term α_k arises due to the Coriolis-pressure effect, elucidated in chapter 4. For $\omega_0^2 < \omega_D^2$ and radially decreasing profiles, α_k' is negative and thus unfavorable for the existence of modes with $\omega_D/n > 0$. From Eq. (3.2.1), the toroidal phase velocity $-\omega R/n$ is in this case smaller than the plasma velocity $R\Omega$. Observed from a frame locally moving along with the flow, these modes will move in the direction opposite to the plasma rotation. The effect is in this case favorable for modes with $\omega_D/n < 0$. Note that this term will be less significant for higher toroidal mode numbers n.

6.3 Experimental Implications

After shortly considering some effects lying outside the ideal MHD description used here, we will discuss the experimental implications of the present analysis.

6.3.1 Adiabatic constant

Since we apply MHD to a plasma that is not strongly collisional, we must allow for a value of the adiabatic constant γ that deviates from the ideal gas value $\gamma = 5/3$. For the description of RSAEs in a low-β tokamak plasma this is likely to be an overestimate

and a value of $\gamma \approx 1.4$ seems more appropriate [49]. Since $\sqrt{\gamma T}$ is the sound speed c_s in an ideal gas, we may write $\omega_0 = c_s/qR_0$ and replace c_s with a more general expression:

$$c_s^2 = \frac{\sum_j \gamma_j n_j T_j}{\sum_j n_j},$$ (6.3.1)

which is a weighted average over species j including both electrons (e) and ions (i) with number densities n_j. For a mono-component plasma with $\gamma_e = 1$ and $\gamma_i = 7/4$ we obtain $\omega_0^2 = (T_e + 7T_i/4)/q^2R_0^2$ as in [21]. Note that the definition of temperature used here includes a factor k_B/m_j with k_B Boltzmann's constant and m_j the component's particle mass.

6.3.2 Energetic ions

Without rotation, D of Eq. (6.2.10) equals $Q_{p(ressure)}$ of [59, 75] when evaluated near the rational surface at low frequency. We may follow the approach of [20, 21, 59] and add independently derived toroidal and hot particle terms, Q_{tor} and Q_{hot}, respectively, to obtain an extended criterion for mode existence. Near a rational surface Q_{tor} is negligible compared to Q_p [59] and the expression of Q_{hot} from [20] writes

$$\frac{Q_{hot}}{D} = (1 - N)\,\frac{\omega\omega_h}{\omega_A^2}\,\frac{\langle\rho_h\rangle'/\rho}{A_2'/m}.$$ (6.3.2)

In a tokamak ω_A typically exceeds both the RSAE frequency ω and the hot ion gyrofrequency ω_h by several orders of magnitude. Therefore, the flux surface averaged hot particle density $\langle\rho_h\rangle$ has to be peaked and must be a significant fraction of the plasma density ρ to compete with the plasma pressure and rotation effects of $A_2'/m \sim \epsilon^2$.

6.3.3 Frequency

The primary effect of toroidal rotation on the RSAE frequency that is often observed is the Doppler shift $n\Omega$. It can be used to determine the mode numbers and the angular rotation frequency Ω. For high n it can even dominate the RSAE frequency [127].

In current tokamaks the Mach number can be a significant fraction of one. In JET for example, NBI heated plasmas can have $\mathcal{M} \approx 0.5$, see for example [196]. This approximately doubles $\tilde{a}_1$, causing an increase of about 40 percent in the minimum RSAE frequency $\tilde{\omega}_+ \approx \sqrt{\tilde{a}_1}\omega_0$. Such a change should be observable.

Near the minimum RSAE frequency, when magnetic field line bending is still small, changes in temperature and the safety factor enter the frequency evolution according to Eq. (6.2.3). When however magnetic field line bending is the primary source of the RSAE frequency change, Eq. (6.2.2) shows that $d\omega_+^2/dt$ approximately scales with ω_A^2.

6.3.4 Existence

Recently RSAEs have been observed between sawtooth crashes when the magnetic shear was very low and $q_0 \approx 1$ [50]. Near $q = 1$, the average magnetic well term $-\beta'(1 - q^2)$ in the existence criterion Eq. (6.2.12) is small. Shaping effects like ellipticity and triangularity are known to 'deepen' the magnetic well, making that it vanishes at a somewhat lower q. In this case the rotational terms α'_k and β'_k can be critical for RSAE existence in shots with significant toroidal rotation.

For RSAEs near a rational surface $\omega_D \approx \pm\tilde{\omega}_+ \approx \pm\sqrt{\tilde{a}_1}\omega_0$ so that

$$\alpha_k \approx \pm\sqrt{8\gamma}\frac{\sqrt{\tilde{a}_1}}{\tilde{a}_1 - 1}\frac{\beta\mathcal{M}}{m}\left(1 + \frac{\mathcal{M}^2}{\gamma}\right). \tag{6.3.3}$$

With $\gamma = 1.4$, $q = 1$, and $\mathcal{M} = 0.5$ this gives $\alpha_k \approx \pm 1.7\beta/m$. Typically both β and $\mathcal{M}$ are decreasing functions of minor radius, so that $\alpha'_k > 0$ for RSAEs with $\omega_D/m < 0$. According to Eq. (6.2.12) a radially increasing α_k is favorable for mode existence. Therefore, modes with a toroidal phase velocity exceeding the plasma rotation velocity so that $\omega_D/m < 0$, are favored. Modes with a toroidal phase velocity below the plasma rotation velocity receive a strong negative contribution to the right-hand side of the existence criterion (6.2.12). They may therefore not exist. According to Eq. (6.3.3) this Coriolis effect is strongest for low m.

For $\mathcal{M} = 0.5$, the centrifugal term $\beta_k \approx 0.3\beta$ is a bit smaller, but does not decrease with m. From Eq. (6.3.2), it becomes more significant compared to fast particle effects for higher m. Typically $\beta'_k < 0$ so that according to Eq. (6.2.12) it is always unfavorable for the existence of RSAEs. It should therefore be possible to see RSAEs in the GAM frequency range disappear with increasing rotation. First the modes moving slower than the plasma, lowest-m modes first.
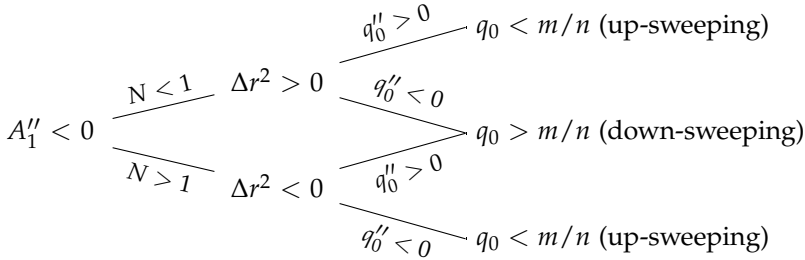
6.3.5 Downwards sweeping cascades

In the vast majority of cases, RSAEs are observed to increase in frequency with time. Occasionally however downward sweeping cascades are observed. In experiments with significant toroidal rotation, up-sweeping RSAEs propagating in the direction opposite to the plasma rotation *appeared* to sweep downwards in frequency due to the Doppler shift $n\Omega$ [127]. In other cases the observation of downwards chirping cascades required the introduction of energetic particles, kinetic effects, and 'quasi-modes' to be explained [11, 73, 22]. Here we show that also within the present MHD framework there are circumstances under which down-sweeping cascades can arise.

The typical situation for which up-sweeping cascades occur is shown in Fig. 6.1. When $q_0 < m/n$ decreases, field line bending increases and the mode frequency shifts upwards. When however q_0 is *above* m/n, field line bending decreases when q_0 decreases, resulting in down-sweeping cascades. The increasing field line bending away from $r = r_0$ will however generally lead to a local minimum in the continuum, instead of a maximum as in Fig. 6.1(a). The anti-Sturmian sequence of modes clustering above

this continuum will unavoidably overlap in frequency with the continuum. This will lead to heavy continuum damping, providing an explanation for why these down-sweeping cascades are rarely observed. Note that a Sturmian sequence of modes below the continuum with $\omega_D^2 < \omega_+^2$ (BAEs in regular shear plasmas) may still avoid continuum damping and sweep downwards.

Reversed shear Alfvén eigenmodes with frequencies $\omega_D^2 > \omega_+^2$ can thus avoid strong continuum damping when $A_1'' < 0$. Depending on N, there are several possibilities for this to happen, summarized by the following diagram

$$A_1'' < 0 \quad \begin{array}{c} \xrightarrow{N < 1} \Delta r^2 > 0 \\ \xrightarrow{N > 1} \Delta r^2 < 0 \end{array} \quad \begin{array}{c} \overset{q_0'' > 0}{\nearrow} \; q_0 < m/n \; \text{(up-sweeping)} \\ \underset{q_0'' < 0}{} \\ \xrightarrow{} q_0 > m/n \; \text{(down-sweeping)} \\ \overset{q_0'' > 0}{} \\ \underset{q_0'' < 0}{\searrow} \; q_0 < m/n \; \text{(up-sweeping)} \end{array}$$

where the conclusions regarding up-sweeping or down-sweeping frequency assume decreasing $q_0(t)$. The first case with $N < 1$ and a minimum in the safety factor profile, resulting in upwards shifting frequencies, is the typical case for RSAEs. The second case shows that strong continuum damping may also be avoided ($A_1'' < 0$) when there is a local maximum q_0 in the safety factor profile ($q_0'' < 0$) that exceeds m/n. These are precisely the conditions under which simulations showed down-chirping RSAEs [51]. Also in experiments at the LHD stellarator with $q_0'' < 0$, RSAEs with decreasing frequency were found [185].

The above diagram also shows another instance in which down-sweeping may occur, namely when $N > 1$. According to Eq. (6.2.9b) this can happen, for example when n is high and the rotation frequency is locally concave ($\Omega'' > 0$). In this case the Doppler shift ensures that, at least locally, ω_D curves away from the continuum so that strong continuum damping can be avoided.

6.3.6 Other modes

Equation (6.2.10) is also a necessary condition for the existence of modes clustering above the ω_- continuum. This would predict, at low frequencies very close to the Doppler shift, the possibility of a second cascade of RSAEs. For these low frequencies α_k' is somewhat smaller and favors positive instead of negative Doppler shifted frequency modes. Note that in this case, N is obtained by interchanging ω_+ and ω_- in Eq. (6.2.9a).

For positive shear plasmas, Eq. (6.2.6) is replaced by $(m/q - n)^2 = (nq'/q)^2(r - r_0)^2$. By replacing Δr^2 with $-(q/nq')^2$, therefore, Eq. (6.2.10) becomes a criterion for

the existence of modes clustering below the $\omega_{\pm}$ continua of regular shear plasmas:

$$\frac{r}{4}\left(\frac{q'}{q}\right)^2 < \frac{-\beta'\left(1 - q^2\right) - q^2\alpha'_k - q^2\beta'_k}{1 - N}. \tag{6.3.4}$$

This criterion improves on the derived integral condition for the flow driven "BAEs" found in chapter 5 by taking into account the effect of magnetic shear. When $\gamma = 1$, the cluster frequency $\tilde{\omega}_{-} = 0$ is marginally stable. Modes clustering below this continuum are therefore automatically unstable. In this case the reverse of Eq. (6.3.4) provides a stability criterion for localized (Mercier) modes, see chapter 3.

6.4   Conclusions & Discussion

We derived an existence condition, Eq. (6.2.12), for reversed shear Alfvén eigenmodes near a rational surface using a clusterpoint analysis. Toroidal plasma rotation enters through a centrifugal effect and an effect depending on the Doppler-shifted mode frequency. The latter Coriolis-pressure effect is typically unfavorable for RSAEs with a toroidal phase velocity that is below the plasma velocity or in the opposite direction. Neglecting this term, we showed that RSAEs form an anti-Sturmian sequence with their number of nodes decreasing with increasing frequency. We finally showed that the sometimes observed RSAEs sweeping downwards in frequency can avoid strong continuum damping when the safety factor contains a local maximum, or the flow profile is strongly concave.

   We note that local existence criteria of the kind discussed here, neglect coupling between poloidal harmonics allowing the (weak) ballooning of a mode towards the low-field side of the plasma. This destabilizing ballooning effect is even stronger in the presence of rotation, as the kinetic energy adds to the pressure in the coupling terms. When the magnetic shear is low enough for the sideband harmonics to be located away from their respective resonance, the effect of the coupling term h of Eq. (3.2.2) will however be stabilizing, see chapter 5. The influence of this coupling on the derived existence criterion (6.2.10) for RSAEs is therefore somewhat non-trivial.

   Besides the influence on the existence of RSAEs, toroidal rotation also increases their clusterpoint frequency given by Eq. (3.2.9). Thereby, a changing toroidal rotation weakly enters the time variation of the RSAE frequency as described by Eqs. (6.2.2) and (6.2.3). Effects associated with the compression of Alfvén waves are also included here. Taking all of these effects into account leads to improved predictions and a better understanding of the low-frequency MHD spectrum.

Chapter 7

Implementation and Verification of the Nonlinear Viscoresistive Full Magnetohydrodynamic Equations in the JOREK code

The nonlinear finite element code JOREK has previously successfully been used to simulate various aspects of tokamak plasmas using the reduced magnetohydrodynamic (MHD) model. Here we report on our effort of extending this code to the full MHD equations. Some problems regarding pollution, stability, and regularity of the solutions are discussed, together with our proposed solutions. Various analytical test cases are performed that verify our implementation. We show that highly anisotropic diffusion can be treated with the same accuracy as isotropic diffusion, even on non-aligned grids, as long as these grids are created with sufficient care. We show that this property is associated with our use of a magnetic vector potential to describe the magnetic field. The linear growth rate of an internal kink mode and a tearing mode are benchmarked against the result of a linear MHD code. The evolution of a tearing mode and the resulting magnetic islands are simulated well into the nonlinear regime. The results are compared with predictions from the reduced MHD model. Finally, a simulation of a ballooning mode illustrates the possibility to use JOREK as an ideal MHD code without the need to add any physical dissipation.

7.1 Introduction

The hot plasma in a tokamak knows many ways to escape the grip of the confining magnetic field. Most of these have been long understood and this understanding has led to a tremendous progress in the time a plasma can be kept in place. A first understanding of the development of instabilities in tokamak plasmas starts with an understanding of their linear phase. The theory of magnetohydrodynamics (MHD) has been successful in understanding many linear instabilities like kink-, tearing-, and ballooning modes. The kink mode is at the basis of what is called the sawtooth instability, named after the shape of the resulting magnetic signals. Tearing modes grow to form magnetic islands, while the ballooning mode plays an important role in the formation of Edge Localized Modes (ELMs). An accurate description of these phenomena typically requires the inclusion of effects outside of the MHD model, like the effects of fast particles or neoclassical effects. Linear MHD instabilities and their nonlinear development can however already account for many aspects of the observations.

While purely theoretical analyses are arguably still the most important tool for understanding the linear phase of instabilities, for their nonlinear development this role is more and more taken over by numerical simulations. Over the last few decades the computing power has increased to a level that with a fluid model like MHD, the nonlinear development of instabilities are routinely simulated with sufficient resolution in both space and time. As a result, many codes have been developed that can solve a sub- or super-set of the MHD equations. Codes used for tokamak applications include NIMROD [174, 175], BOUT++ [47, 48], M3D(-C^1) [54, 23], XTOR(-2F) [137, 138], FAR [33], MEGA [184], and JOREK.

The JOREK code was initially developed as a reduced MHD code. It has been used to calculate various instabilities like the peeling(-tearing) mode [110], ballooning modes [109], and their combined nonlinear development in the form of ELMs [112, 114, 155, 106]. The influence of flows on ELMs [112, 154] and various mechanisms to trigger or mitigate instabilities through resonant magnetic perturbations [149, 151], pellet injection [114], and massive gas injection [162] have also been studied extensively with JOREK.

These simulations were all performed using the reduced MHD model. In this model typically only one or two variables are used to describe the velocity. The primary difference with the full MHD model however is that the toroidal magnetic field function RB_ϕ does not allow for variation in space and time, but is a constant. This eliminates the possibility of supporting fast magneto-acoustic waves, which require compression of the toroidal magnetic field. Since this wave is very stable and has a high frequency that is much higher than most phenomena of interest, this is typically considered to be an advantage.

There are however situations in which compression of the toroidal magnetic field can be important. A particular instance may be the accurate description of fast poloidal rotation, for which 'magnetic pumping' acts as a damping mechanism. Since in this case anisotropic pressure and diamagnetic effects are expected to be impor-

tant as well, the present extension to full MHD can perhaps be considered as a step towards a more complete tokamak modeling with the JOREK code.

The basic numerical framework behind the JOREK code has been described elsewhere [43, 111]. Here we focus primarily on issues related to our implementation of the full MHD equations. In Section 7.2 we first describe the strong form of the equations and how the gauge freedom introduced by the use of a magnetic vector potential was used. Next, after discussing the simple boundary conditions used in this work, we derive a suitable weak form of the equations.

Some numerical aspects relevant to this work are presented in Section 7.3. The spatial discretization is discussed only insofar this is required for what follows, while the time integration and its properties are discussed in more detail. In Section 7.4 we discuss our solution to a problem encountered with spectral pollution. Section 7.5 discusses a problem and a potential solution related to the grid axis.

Next, we thoroughly verify our implementation through a series of tests. We test the equations individually in Section 7.6 and the combined set of equations in Section 7.7. As test cases we look at the most well-known MHD instabilities. First an internal kink mode, whose growth rate we compare with that what is obtained with a linear MHD code. We do the same for a tearing mode, for which we also make a comparison with reduced MHD, also in the nonlinear regime. We end with some first results for ballooning modes.

7.2 Theoretical Model

7.2.1 The equations

Our goal is to implement the following set of viscoresistive MHD equations

$$\frac{\partial \rho}{\partial t} = -\nabla \cdot (\rho \mathbf{u} + \mathbf{q}_m) + S_m, \tag{7.2.1a}$$

$$\frac{\partial \rho \mathbf{u}}{\partial t} = -\mathbf{u} \nabla \cdot (\rho \mathbf{u}) - \rho \mathbf{u} \cdot \nabla \mathbf{u} - \nabla p + \mathbf{J} \times \mathbf{B} + \nabla \cdot \mathbf{T}_v, \tag{7.2.1b}$$

$$\frac{\partial p}{\partial t} = -\nabla \cdot [\gamma p \mathbf{u} + (\gamma - 1) \mathbf{q}_h] + (\gamma - 1) \left(\mathbf{u} \cdot \nabla p + \eta J^2 + \mathbf{T}_v : \nabla \mathbf{u} + S_h \right), \tag{7.2.1c}$$

$$\frac{\partial \mathbf{A}}{\partial t} = -\eta \mathbf{J} + \mathbf{u} \times \mathbf{B}, \tag{7.2.1d}$$

for the primitive variables $\rho, T, \mathbf{u}$ and $\mathbf{A}$, the density, temperature, velocity, and magnetic vector potential respectively. In this chapter we will use the ideal gas value $\gamma = 5/3$ for the adiabatic constant. For describing other plasma phenomena different values may however be more appropriate [49]. As secondary variables we use the current density $\mathbf{J} = \nabla \times \mathbf{B}$, and pressure $p = \rho T$. The magnetic field $\mathbf{B}$ is expressed in terms of a magnetic vector potential $\mathbf{A}$ as

$$\mathbf{B} = \nabla \times \mathbf{A} + \mathbf{F}, \tag{7.2.2}$$

where we allow for the addition of a divergence-free vector $\mathbf{F}$ that is constant in time, see section 7.2.8. The continuity and heat equation are supplemented with mass and heat sources S_m and S_h. The constitutive relations for the fluxes $\mathbf{q}_m$ and $\mathbf{q}_h$ are given by

$$\mathbf{q}_m = -\left(D_\perp \nabla_\perp \rho + D_\| \nabla_\| \rho \right) - D_h \nabla \nabla^2 \rho, \tag{7.2.3a}$$

$$\mathbf{q}_h = -\left(K_\perp \nabla_\perp T + K_\| \nabla_\| T \right), \tag{7.2.3b}$$

where $\nabla_\| = (\mathbf{B}/B^2)\mathbf{B} \cdot \nabla$ and $\nabla_\perp = \nabla - \nabla_\|$. The parallel conductivity $K_\|$ and mass diffusion coefficient $D_\|$ can in principle depend on the temperature. The perpendicular diffusion coefficients $D_\perp$ and $K_\perp$ and the hyperdiffusion coefficient D_h can be used to phenomenologically model turbulence effects beyond MHD, which can be useful for simulations on a transport time scale. Hyperdiffusive terms may also be introduced in the temperature equation, or the induction equation as in Refs. [48, 217].

The right-hand side of the momentum equation (7.2.1b) can be written as the divergence of the stress tensor

$$\mathbf{T} = -\left(p + \frac{1}{2} B^2 \right) \mathbf{g} - \rho \mathbf{u}\mathbf{u} + \mathbf{B}\mathbf{B} + \mathbf{T}_v. \tag{7.2.4}$$

Under the assumptions of isotropy and a linear relation between stress and strain, the most general viscous stress tensor $\mathbf{T}_v$ is given by

$$\mathbf{T}_v = \mathbf{T}_N + \lambda (\nabla \cdot \mathbf{u})\mathbf{g}, \tag{7.2.5a}$$

$$\mathbf{T}_N = \mu \left(\nabla \mathbf{u} + (\nabla \mathbf{u})^T \right). \tag{7.2.5b}$$

Here $\mathbf{T}_N$ is the Newtonian part of the stress tensor proportional to the dynamic viscosity μ, and $\mathbf{g}$ is the metric tensor. In Cartesian coordinates this is the identity. Very little is accurately known about the second coefficient of viscosity λ. When it is not taken to be zero, it is most often assigned its ideal gas value of $\lambda = -2\mu/3$. For this value the trace of the viscous stress tensor vanishes. The quantity $\mu_B = \lambda + 2\mu/3$ is sometimes called the 'bulk viscosity' or 'dilational viscosity'. For thermodynamic reasons, this quantity must, like μ, be non-negative. The viscous force density becomes

$$\nabla \cdot \mathbf{T}_v = \mu \nabla^2 \mathbf{u} + (\mu + \lambda)\nabla(\nabla \cdot \mathbf{u}) + \frac{\nabla \mu}{\mu} \cdot \mathbf{T}_N + (\nabla \cdot \mathbf{u})\nabla \lambda, \tag{7.2.6}$$

where we used that $\nabla \cdot (\nabla \mathbf{u})^T = \nabla(\nabla \cdot \mathbf{u})$. The assumptions underlying the derivation of Eq. (7.2.5a), in particular that of isotropy, do not hold in a magnetized plasma. The present viscous stress tensor should therefore be considered to be only a crude first approximation of the relevant collisional processes.

Equations (7.2.1a)-(7.2.1b) express the conservation of mass and momentum, respectively. Divergence terms like $-\nabla \cdot \mathbf{q}$ merely redistribute these quantities. The

viscous and resistive terms in the pressure equation (7.2.1c) describe the generation of heat by viscous and resistive dissipation. The density of the total energy that is conserved is given by

$$\mathcal{E} = \frac{p}{\gamma - 1} + \frac{1}{2}\rho v^2 + \frac{1}{2}B^2. \tag{7.2.7}$$

Without any non-ideal terms, Eq. (7.2.1c) can be transformed to a conservation equation for $p\rho^{1-\gamma}$, a quantity related to the entropy density. In the absence of resistivity η, the induction equation (7.2.1d) expresses the conservation of magnetic flux, see for example Ref. [70].

7.2.2 Gauge

Equation (7.2.1d) for the magnetic field, results from 'uncurling' Faraday's law 2.2.1d

$$\frac{\partial \mathbf{B}}{\partial t} = -\nabla \times \mathbf{E}. \tag{7.2.8}$$

Using Eq. (7.2.2) with $\partial \mathbf{F}/\partial t = 0$ gives

$$\frac{\partial \mathbf{A}}{\partial t} = -\mathbf{E}. \tag{7.2.9}$$

Equation (7.2.1d) is obtained after using Ohm's law for moving media

$$\mathbf{J} = \eta^{-1}\left(\mathbf{E} + \mathbf{u} \times \mathbf{B}\right), \tag{7.2.10}$$

where $\mathbf{E}$ is the electric field. The additional magnetic force proportional to $\mathbf{u} \times \mathbf{B}$ disappears in a reference frame moving along with the flow to transform into an electric force. To Eq. (7.2.9) the gradient of an arbitrary time-dependent scalar field Φ can be added, without changing Eq. (7.2.8). We have used this 'gauge freedom' to set $\Phi = 0$, with obvious advantages. This gauge is called the Weyl gauge, also known as the Hamiltonian or temporal gauge. In the Weyl gauge, a time-independent gradient of a scalar field can still be added. Therefore the gauge is not completely fixed, which is sometimes referred to as an 'incomplete gauge'.

Equation (7.2.9) displays how, for example, the toroidal electric field that drives the toroidal current in a tokamak is generated, namely through induction by a time-varying magnetic field in the central solenoid. The electric fields generated by plasma motion are often however more conveniently described in terms of an electrostatic potential. We will come back to this point in Section 7.2.8 when discussing the initial conditions in JOREK. Here we just note that an electric potential Φ can always be reintroduced by replacing a part of $\partial \mathbf{A}/\partial t$ with $\nabla \Phi$. This gauge transformation leaves both the electric and magnetic fields unchanged.

Several other choices for Φ, like the Coulomb gauge in which $\nabla \cdot \mathbf{A} = 0$, require solving a costly Poisson equation. Some numerical aspects of the various gauges in a finite volume setting are described in Ref. [100]. An interesting option specifically

for tokamak applications is implemented in M3D-C^1 [23]. Instead of introducing an additional variable Φ to fix the gauge, they do with one variable less. The freedom in **A** introduced by $\nabla \cdot \mathbf{B} = 0$ is used to describe the magnetic vector potential in terms of only two scalar components instead of three.

7.2.3 Weak forms

To obtain the weak formulation of the equations (7.2.1a)-(7.2.1d) we multiply them with a test function and integrate over the entire domain. We then have the choice of partially integrating some or all of the terms. This choice potentially influences stability and accuracy. Also, a smart choice of which terms to partially integrate can lead to a more convenient implementation of the equations.

The continuity equation

We multiply Eq. (7.2.1a) for the density ρ with a test function ρ^* and integrate over the entire domain

$$\int \rho^* \frac{\partial \rho}{\partial t} dV = \int \left[-\rho^* \nabla \cdot (\rho \mathbf{u} + \mathbf{q}_m) + \rho^* S_m \right] dV, \tag{7.2.11a}$$

$$= \int \left[(\rho \mathbf{u} + \mathbf{q}_m) \cdot \nabla \rho^* + \rho^* S_m \right] dV - \oint \rho^* (\rho \mathbf{u} + \mathbf{q}_m) \cdot d\mathbf{S}, \tag{7.2.11b}$$

where the surface element $d\mathbf{S}$ is oriented normal to the boundary in the outward direction. The weak formulation of the pressure equation (7.2.1c) follows in a similar way.

For the hyperdiffusive term $-D_h \nabla \nabla^2 \rho$ in $\mathbf{q}_m$ we can perform one more partial integration to write[1]

$$-\int D_h \nabla \nabla^2 \rho \cdot \nabla \rho^* dV = \int \nabla^2 \rho \nabla \cdot (D_h \nabla \rho^*) \, dV - \int D_h \nabla^2 \rho \nabla \rho^* \cdot d\mathbf{S}. \tag{7.2.13}$$

The momentum equation

To implement the vector equations we eventually have to project them in three independent directions. We have the choice of first multiplying the strong form of the equations with a scalar test function and then after any desired partial integration take projections of these weak formulations. Alternatively we can project the equations first and then transform to weak form. The second option, at least in principle, provides

---

[1]An alternative weak formulation can be obtained for the hyperdiffusive term. Integrating by parts with respect to the divergence operators acting on $D_h \nabla \rho^*$, we obtain the alternative weak form

$$-\int D_h \nabla \nabla^2 \rho \cdot \nabla \rho^* dV = \int \nabla \nabla \rho : \nabla D_h \nabla \rho^* dV - \int D_h \left(\nabla \rho^* \cdot \nabla \nabla \rho \right) \cdot d\mathbf{S}. \tag{7.2.12}$$

the opportunity to choose different test functions for different projections. Therefore we will here follow this approach.

Taking the inner product of Eq. (7.2.1b) with a vectorial test function $\mathbf{m}^*$ and integrating by parts we get

$$\int \mathbf{m}^* \cdot \frac{\partial \rho \mathbf{u}}{\partial t} dV = \int -\mathbf{T} : \nabla \mathbf{m}^* dV + \int \mathbf{T} \cdot \mathbf{m}^* \cdot d\mathbf{S}. \tag{7.2.14}$$

For the stress tensor (7.2.4) the boundary term reads

$$\int \mathbf{T} \cdot \mathbf{m}^* \cdot d\mathbf{S} = \int \left[-\left(p + \frac{1}{2} B^2 - \lambda (\nabla \cdot \mathbf{u}) \right) \mathbf{m}^* + (-\rho \mathbf{u} \mathbf{u} + \mathbf{B} \mathbf{B} + \mathbf{T}_N) \cdot \mathbf{m}^* \right] \cdot d\mathbf{S}. \tag{7.2.15}$$

This surface integral represents the total stress in the direction of $\mathbf{m}^*$, normal to the boundary. The integrand of the first term on the right-hand side of Eq. (7.2.14) reads

$$-\mathbf{T} : \nabla \mathbf{m}^* = \rho \mathbf{u} \cdot (\mathbf{u} \cdot \nabla \mathbf{m}^*) - \mathbf{B} \cdot (\mathbf{B} \cdot \nabla \mathbf{m}^*) + \left(p + \frac{B^2}{2} - \lambda \nabla \cdot \mathbf{u} \right) \nabla \cdot \mathbf{m}^* - \mathbf{T}_N : \nabla \mathbf{m}^*, \tag{7.2.16}$$

where we used that $\mathbf{g} : \nabla \mathbf{m}^* = \nabla \cdot \mathbf{m}^*$.

The induction equation

Transforming Eq. (7.2.1d) to weak form, using

$$\eta \mathbf{A}^* \cdot \nabla \times \mathbf{B} = \nabla \cdot (\mathbf{B} \times \eta \mathbf{A}^*) + \mathbf{B} \cdot \nabla \times \eta \mathbf{A}^*, \tag{7.2.17}$$

we obtain

$$\int \mathbf{A}^* \cdot \frac{\partial \mathbf{A}}{\partial t} dV = \int \left[\mathbf{A}^* \cdot (\mathbf{u} + \nabla \eta) \times \mathbf{B} - \eta \mathbf{B} \cdot \nabla \times \mathbf{A}^* \right] dV + \int \eta \mathbf{A}^* \times \mathbf{B} \cdot d\mathbf{S}. \tag{7.2.18}$$

7.2.4   Boundary conditions

Eqs. (7.2.1a)-(7.2.1d) constitute a set of eight second-order partial differential equations. Because of the double periodicity in a toroidal geometry, we only have to consider the outer boundary in the radial direction. The inner radial boundary is an interior point of the domain that does not require boundary conditions.

In a finite element method there are two different types of boundary conditions, natural and essential boundary conditions. The first type are typically Neumann conditions for the gradients of quantities. They naturally arise by evaluating the boundary integrals in the weak formulation. Essential boundary conditions are typically of the Dirichlet type, where the unknowns are forced to a certain value at the boundary.

In this paper we will primarily use the simplest possible boundary conditions. We will fix all the primitive variables at the boundary:

$$\frac{\partial}{\partial t} (\rho, T, \mathbf{u}, \mathbf{A}) = 0. \tag{7.2.19}$$

More general boundary conditions will have to be taken into account in the future when modeling for example the divertor, where plasma can freely flow out of the domain. Such outflow conditions have already been implemented for the reduced MHD models in JOREK [113].

The conditions (7.2.19) can be shown to describe an ideally conducting wall, impenetrable for both plasma and current.

When no current can penetrate the boundary, Ohm's law (7.2.10) with $\mathbf{u} = 0$ shows that the normal component of the electric field vanishes. When the boundary of the domain consists of an ideally conducting wall also the tangential component of the electric field vanishes. With Eq. (7.2.9) the boundary condition $\partial \mathbf{A}/\partial t = 0$ then follows.

The unknowns in JOREK are the changes of the primitive variables from one time-step to the next. Therefore the boundary conditions (7.2.19) constitute simple Dirichlet boundary conditions. Because the test functions should live in the same space as the unknowns, Dirichlet boundary conditions also hold for the test functions. We can use this property to neglect almost all boundary integrals of the weak formulations derived in the previous section. In the code this is implemented in the matrix equation that results from the discretization by taking out those lines corresponding to the basis functions that do not satisfy the boundary conditions. These lines are then replaced by conditions that implement the boundary conditions (7.2.19).

The only surface term that does not necessarily vanish is the hyperdiffusive term in Eq. (7.2.13). By not taking into account this boundary term, the natural boundary condition $\nabla^2 \rho = 0$ is implemented. This is a boundary condition that seems reasonable in the sense that it will probably not alter the interior solution too much.

7.2.5 Summary of the weak forms

When the test functions vanish at the boundary, all the surface integrals in the above weak formulations disappear. The integrands of the weak formulation can be summarized as

$$\rho^* \frac{\partial \rho}{\partial t} = (\rho \mathbf{u} + \mathbf{q}_m) \cdot \nabla \rho^* + \rho^* S_m, \tag{7.2.20a}$$

$$\mathbf{m}^* \cdot \frac{\partial \rho \mathbf{u}}{\partial t} = \rho \mathbf{u} \cdot (\mathbf{u} \cdot \nabla \mathbf{m}^*) - \mathbf{B} \cdot (\mathbf{B} \cdot \nabla \mathbf{m}^*) + (p + \frac{1}{2}B^2 - \lambda \nabla \cdot \mathbf{u}) \nabla \cdot \mathbf{m}^* - \mathbf{T}_N : \nabla \mathbf{m}^*, \tag{7.2.20b}$$

$$p^* \frac{\partial p}{\partial t} = [\gamma p \mathbf{u} + (\gamma - 1) \mathbf{q}_h] \cdot \nabla p^* + (\gamma - 1) p^* \left(\mathbf{u} \cdot \nabla p + \eta J^2 + \mathbf{T}_v : \nabla \mathbf{u} + S_h \right), \tag{7.2.20c}$$

$$\mathbf{A}^* \cdot \frac{\partial \mathbf{A}}{\partial t} = (\nabla \times \mathbf{A}^*) \cdot \eta \mathbf{B} - \mathbf{A}^* \cdot (\mathbf{u} + \nabla \eta) \times \mathbf{B}, \tag{7.2.20d}$$

where the hyperdiffusive term in $\mathbf{q}_m$ will be partially integrated once more as indicated in Eq. (7.2.13).

Alternatively, we also implement a more primitive formulation in which only partial integration is used when it reduces the order. The magnetic terms are left unaltered:

$$\rho^* \frac{\partial \rho}{\partial t} = \rho^* \left[-\nabla \cdot (\rho \mathbf{u}) + S_m \right] + \mathbf{q}_m \cdot \nabla \rho^*, \tag{7.2.21a}$$

$$\mathbf{m}^* \cdot \frac{\partial \rho \mathbf{u}}{\partial t} = \mathbf{m}^* \cdot \left[-\mathbf{u} \nabla \cdot (\rho \mathbf{u}) - \rho \mathbf{u} \cdot \nabla \mathbf{u} - \nabla p \right] + \left(\frac{1}{2} B^2 - \lambda \nabla \cdot \mathbf{u} \right) \nabla \cdot \mathbf{m}^* \tag{7.2.21b}$$
$$- \mathbf{B} \cdot (\mathbf{B} \cdot \nabla \mathbf{m}^*) - \mathbf{T}_N : \nabla \mathbf{m}^*,$$

$$p^* \frac{\partial p}{\partial t} = p^* \left[-\gamma p \nabla \cdot \mathbf{u} - \mathbf{u} \cdot \nabla p + (\gamma - 1) \left(\eta J^2 + \mathbf{T}_v : \nabla \mathbf{u} + S_h \right) \right] \tag{7.2.21c}$$
$$+ (\gamma - 1) \mathbf{q}_h \cdot \nabla p^*,$$

$$\mathbf{A}^* \cdot \frac{\partial \mathbf{A}}{\partial t} = \nabla \times \mathbf{A}^* \cdot \eta \mathbf{B} - \mathbf{A}^* \cdot (\mathbf{u} + \nabla \eta) \times \mathbf{B}, \tag{7.2.21d}$$

where we left out the same surface integrals as before.

7.2.6 Coordinate system

We use the cylindrical coordinate system for toroidal problems (R, Z, ϕ). In this coordinate system the components g_{ij} of the metric tensor are given by $\text{diag}(1, 1, R^2)$. The contravariant and covariant toroidal basis vectors are given by

$$\mathbf{a}^3 \equiv \nabla \phi = \frac{\hat{\mathbf{e}}_\phi}{R}, \tag{7.2.22a}$$

$$\mathbf{a}_3 \equiv \frac{\partial \mathbf{r}}{\partial \phi} = R \hat{\mathbf{e}}_\phi, \tag{7.2.22b}$$

respectively. Here $\hat{\mathbf{e}}_\phi$ is the unit vector in the toroidal direction. We thus have

$$A_3 = \mathbf{a}_3 \cdot \mathbf{A} = R A_\phi. \tag{7.2.23}$$

Furthermore, the only non-zero Christoffel symbols Γ^i_{jk} are associated with

$$\frac{\partial \hat{\mathbf{e}}_R}{\partial \phi} = \hat{\mathbf{e}}_\phi \quad \rightarrow \Gamma^3_{31} = \Gamma^3_{13} = \frac{1}{R}, \tag{7.2.24a}$$

$$\frac{\partial \hat{\mathbf{e}}_\phi}{\partial \phi} = -\hat{\mathbf{e}}_R \quad \rightarrow \Gamma^1_{33} = -R. \tag{7.2.24b}$$

Because in an axisymmetric equilibrium A_3 can be identified with the poloidal magnetic flux function ψ, we use this covariant component of $\mathbf{A}$ as a primitive variable. For the velocity however we use the physical component $u_\phi = \hat{\mathbf{e}}_\phi \cdot \mathbf{u}$. Our primitive variables then read

$$\mathbf{y} = \left(A_R, A_Z, A_3, u_R, u_Z, u_\phi, \rho, T \right). \tag{7.2.25}$$

In the Galerkin method, for scalar test functions like ρ^* the basis functions are used. For the vectorial test functions $\mathbf{m}^*$ and $\mathbf{A}^*$ we use

$$\mathbf{m}^* = u_R^* \hat{\mathbf{e}}_R + u_Z^* \hat{\mathbf{e}}_Z + u_\phi^* \hat{\mathbf{e}}_\phi, \tag{7.2.26a}$$

$$\mathbf{A}^* = A_R^* \hat{\mathbf{e}}_R + A_Z^* \hat{\mathbf{e}}_Z + A^{3*} \mathbf{a}_3. \tag{7.2.26b}$$

Inserting these expressions into the weak formulations and subsequently choosing only one of the six test functions to be non-zero gives six scalar equations. After this step it is a matter of working out the integrands of the weak formulation explicitly in the (R, Z, ϕ)-coordinate system to obtain a formulation that is suitable for implementation.

7.2.7 Dimensions

As in the reduced MHD version of JOREK we introduce a normalization in which μ_0 disappears. This can be done using the standard ideal MHD non-dimensionalization in which we introduce a characteristic length l_0, magnetic field strength B_0, and a characteristic density ρ_0. When velocities are then normalized by the Alfvén velocity $v_0 = v_A = B_0/\sqrt{\mu_0 \rho_0}$ and pressures by $\rho_0 v_0^2 = B_0^2/\mu_0$, the only difference in the ideal MHD equations is that μ_0 is divided out [70]. The non-ideal terms can be non-dimensionalized by dividing the diffusion coefficients by

$$D_0 = \nu_0 = \frac{K_0}{\rho_0} = \frac{\eta_0}{\mu_0} = \frac{l_0^2}{t_0} = l_0 v_0. \tag{7.2.27}$$

In this way η/η_0 becomes an inverse Lundquist number.

By writing $\mathbf{J} = \nabla \times \mathbf{B}$ we implicitly assumed that our quantities are non-dimensionalized in this way. In JOREK, nothing special is done to non-dimensionalize the input or output. Characteristic values l_0, B_0, and ρ_0 can be chosen to re-scale the variables based on preference. Unlike the SI units $l_0 = 1\text{m}$ and $B_0 = 1\text{T}$, a characteristic density $\rho_0 = 1\text{kgm}^{-3}$ is not an appropriate value for tokamak applications. Still, the density in JOREK is typically chosen to have a value of one on the magnetic axis. In this case, to convert the output to SI units, a re-scaling with a relevant ρ_0 should be performed as in Ref. [106].

Often in tokamak physics, in linear MHD codes for example, units are used in which the characteristic length scale is given by the minor radius $l_0 = a$ and the characteristic magnetic field and density by their value on the magnetic axis $B_0 = B_M$ and $\rho_0 = \rho_M$. Growth rates are then expressed in terms of the Alfvén frequency $\omega_A = v_A/a = B_M/a\sqrt{\mu_0 \rho_M}$ and resistivities as inverse Lundquist numbers $\eta/\mu_0 a v_A$. To transform JOREK results to such units, growth rates should be divided by B_M/a in order to get the growth rate in these Alfvén units and the resistivity η should be divided by $\eta_A \equiv aB_M/\sqrt{\rho_M}$ to get a standard inverse Lundquist number based on the minor radius.

We finally comment on the way we defined the temperature $T = p/\rho$. This should be compared with the ideal gas law $p = nk_BT$, where the particle number density $n = \rho/m$ with m the average particle mass. From this we see that we effectively absorbed the factor k_B/m in our definition of the temperature.

7.2.8 Initial conditions

As input to JOREK, we then have to supply the parametric dependencies of T_0, ρ_0, F, and Ω on ψ_n, which is ψ normalized between zero and one. The extended Grad-Shafranov equation (2.2.9) is then solved with the boundary condition $\psi = 0$. We implemented the parameterizations of Eqs. (2.2.10) and (2.2.11) for the pressure and the density for a general equilibrium adiabatic constant γ_e. The resulting $\psi(R, Z)$, $T(\psi, R)$, $\rho(\psi, R)$, $F(\psi)$, and $\Omega(\psi)$ are then used as initial conditions for the simulation, in particular $A_3 = \psi$, $u_\phi = R\Omega$, and

$$\mathbf{F} = F(\psi)\nabla\phi. \tag{7.2.28}$$

The equilibrium is calculated on a polar grid of N_r elements in the radial direction and N_θ elements in the poloidal direction. The grid used for the simulations is typically aligned with the equilibrium magnetic field and can have a different number of radial and poloidal elements N_ψ and N_θ respectively. Also available in JOREK is a square grid, or a combination of a square grid and a polar grid.

In an ideal equilibrium with toroidal rotation $\mathbf{u} = R\Omega\hat{\mathbf{e}}_\phi$ there exists an electric field (2.2.1g)

$$\mathbf{E} = -\mathbf{u} \times \mathbf{B} = \Omega\nabla\psi. \tag{7.2.29}$$

A scalar potential $\Phi(\psi) = \int \Omega(\psi)d\psi$ can be conveniently introduced to describe such an electric field. In the present gauge (7.2.9), this equilibrium electric field is described by a magnetic vector potential $\mathbf{A}$ that increases linearly in time. A time-varying quantity is therefore an inherent part of the equilibrium.

A problem with this is that sometimes we want to study for example the linear growth rate of a instability, while keeping fixed the $n = 0$ harmonic provided by the initial conditions. If we do this by restraining the primitive variables from changing in time, we effectively remove the equilibrium electric field. Another problem is that when there is plasma flow near the boundary, the normal component of $\mathbf{A}$ has to change in time, in violation of our boundary conditions (7.2.19). For these reasons, when including equilibrium rotation, we prefer to add the static equilibrium electric field $\Omega\nabla\psi$ directly as a source to the right-hand side of Eq. (7.2.1d).

Often a next step is to run JOREK axisymmetrically, using only $n = 0$. When the ideal MHD equations are used, the variables should not evolve in this case. This is because the initial conditions are an equilibrium solution of these equations. With the Dirichlet boundary conditions this equilibrium is also stable to $n = 0$ perturbations. To verify that this is indeed the case actually provided a good first test of the implementation of the equations.

Often we want to start a simulation from a non-ideal equilibrium with various diffusivities and resistivities. In the corresponding steady state however some of the profiles may have completely diffused away. To avoid this we can introduce sources in the equations that balance the diffusion. In tokamak simulations, the diffusivities are often so low, and the time scales of interest so fast, that for practical purposes the ideal initial conditions provide a sort of quasi-equilibrium.

7.3   Numerical Model

JOREK uses a mixed spectral / finite element spatial representation. A real sine-cosine Fourier expansion is used in the toroidal direction. Finite elements are used in the poloidal plane [43].

A general multi-step method was implemented in JOREK that allows for second-order accurate fully implicit time integration. This is an important feature, since the MHD equations can be quite stiff. The three fundamental waves in MHD for example, can have widely varying frequencies. When we are not interested in the highest of these frequencies, a very attractive feature of implicit methods is that the time-step can be chosen much larger than what is required to resolve the highest frequencies.

The physics is reasonably separated from the linear algebra in JOREK. The physics of the problem enters through the geometry of the mesh, the initial and boundary conditions, and obviously through the equations. The integrals of the weak formulation are calculated per element and put into an 'element matrix'. These element matrices are then combined in an assembly stage after which the Dirichlet boundary conditions (7.2.19) are applied. The resulting sparse system of linear equations is saved in coordinate format and is solved using the direct solver Pastix [101].

In addition, an iterative solver has been implemented based on the Generalized Minimal RESidual (GMRES) method. A preconditioner has been implemented based on the fact that, because of the axisymmetry of the initial conditions, the various Fourier harmonics are initially primarily influenced by the $n = 0$ equilibrium component [111]. Because the inversion of the sub-matrices for different harmonics can be done independently, this allows for an easily parallelizable solver.

7.3.1   Spatial discretization

A nice feature of the finite element method is that the integrals of the weak formulation can be split into separate contributions from the individual elements. Because the basis functions used are nonzero only in the elements bordering the node at which the unknown is defined, this gives a small element matrix and element vector. These can be constructed on separate processors for separate elements.

The finite element method in JOREK is a fourth-order accurate Galerkin method based on the Bézier formalism. This approach has been described in detail in the
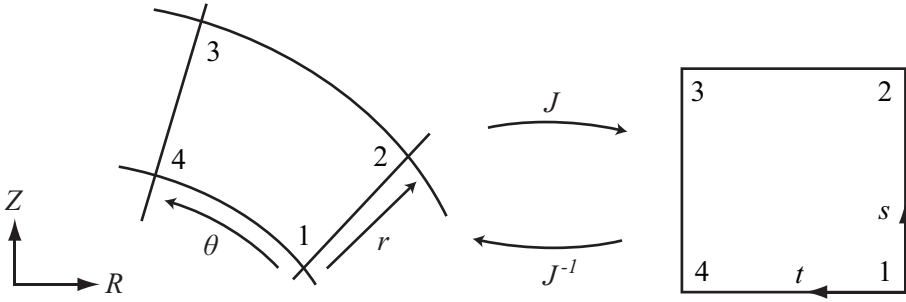
Figure 7.1: A schematic representation of the coordinate transformation from an element in (R, Z) to a reference unit square with coordinates (s, t).

original reference [43]. Here we recollect only those details relevant for the present exposition.

The integrals of the weak formulation are evaluated not in (R, Z, ϕ)-coordinates, but after a coordinate transformation to a unit square. An isoparametric formulation is used in which the coordinates are transformed using the same basis functions as those used for the other variables. An arbitrary quantity, coordinate or variable, is expanded on a unit square as

$$P(s,t) = \sum_{i=1}^{4} \sum_{j=1}^{4} p_{i,j} \sigma_{i,j} b_{i,j}(s,t), \tag{7.3.1}$$

where the coordinates s and t run from 0 to 1. The outer sum runs over the four vertices of the element, while the inner sum runs over the four basis functions $b_{i,j}(s,t)$ per vertex. The coefficients $p_{i,j}$ are the unknowns living on the vertices, while the quantities $\sigma_{i,j}$ arrange the continuity of P across elements. In the local coordinates (s,t) this continuity is only 'geometric' [43]. In the Cartesian coordinates (R, Z) however, the variables are continuously differentiable or C^1. The basis functions or 'shape functions' $b_{i,j}(s,t)$ are products of cubic polynomials in s and t. They follow from so-called Bernstein polynomials after taking into account continuity requirements at the edges of the elements [43]. For the first vertex $i = 1$

$$b_{1,1}(s,t) = (1-s)^2(1-t)^2(1+2s)(1+2t), \tag{7.3.2a}$$

$$b_{1,2}(s,t) = 3(1-s)^2(1-t)^2(1+2t)s, \tag{7.3.2b}$$

$$b_{1,3}(s,t) = 3(1-s)^2(1-t)^2(1+2s)t, \tag{7.3.2c}$$

$$b_{1,4}(s,t) = 9(1-s)^2(1-t)^2 st. \tag{7.3.2d}$$

For the second vertex, referring to Fig. 7.1 for the labeling of the vertices, we have the same basis functions with $s \to 1 - s$. That is $b_{2,j}(s,t) = b_{1,j}(1-s,t)$. For the other two basis functions we have $b_{3,j}(s,t) = b_{1,j}(1-s,1-t)$ and $b_{4,j}(s,t) = b_{1,j}(s,1-t)$.

The basis functions are zero in elements to which the vertex does not belong. All basis functions labeled i vanish on the two edges opposite of the vertex i.

Non-axisymmetric variables acquire an additional dependence on the toroidal angle ϕ by multiplication of the parameterization (7.3.1) with $\cos(n_k\phi)$ or $\sin(n_k\phi)$. This adds another index to the unknowns $p_{i,j} \rightarrow p_{i,j,k}$ and the basis functions $b_{i,j} \rightarrow b_{i,j,k}$. The toroidal mode numbers $n_k = (k-1)/2$ typically run from $n_k = 0$ for $k = 1$ to to $n_k = n$ for $k = 2n + 1$. It is however also possible to use only a fraction of the full toroidal angle, so that mode numbers n_k that are not a multiple of some integer periodicity are excluded. This allows us to focus on a single mode number n, only even n, only multiples of 3, etc.

In the Galerkin method, the test functions are equal to the basis functions. The integrands of the weak formulation (7.2.20a)-(7.2.20d) will therefore contain Fourier harmonics of at most a toroidal mode number $2n$ and polynomials of fourth-order in s and t. Such integrals can be evaluated exactly using a four point Gaussian integration method [43]. The toroidal integration can be done in JOREK using a fast Fourier transform. Alternatively, the integral over the toroidal angle can be done exactly with a Riemann sum using $N = 4n$ points. These points are chosen to be evenly distributed over the full toroidal angle so that $\phi_k = 2\pi(k-1)/2n$. The volume integral of a quantity f is then given by

$$\int f dV \approx \sum_{\text{elements}} \frac{1}{N} \sum_{k=1}^{N} \sum_{j=1}^{4} \sum_{i=1}^{4} f(s_i, t_j, \phi_k) w_i w_j 2\pi R \det(J), \qquad (7.3.3)$$

with w_i the weights. The evaluation points satisfy $0 < s_1 < s_2$ and $s_3 = 1 - s_2$ and $s_4 = 1 - s_1$. The fact that none of the integration points lie on the boundary of the elements has a clear advantage when the elements tend to a position where the determinant

$$\det(J) = \begin{vmatrix} R_s & R_t \\ Z_s & Z_t \end{vmatrix} = R_s Z_t - R_t Z_s \qquad (7.3.4)$$

vanishes. The Jacobian matrix J provides the coordinate transformation from the poloidal plane in (R, Z) to the unit square in (s, t), see Fig. 7.1. The inverse provides the back-transformation for, for example, the derivatives:

$$\begin{pmatrix} \partial_R \\ \partial_Z \end{pmatrix} = J^{-1} \begin{pmatrix} \partial_s \\ \partial_t \end{pmatrix} = \frac{1}{\det(J)} \begin{pmatrix} Z_t & -Z_s \\ -R_t & R_s \end{pmatrix} \begin{pmatrix} \partial_s \\ \partial_t \end{pmatrix}. \qquad (7.3.5)$$

For second-order derivatives we have to apply this operation twice, taking into account derivatives of $\det(J)$ as well.

7.3.2 Time integration

Derivation

We consider the most general two-step time integration method. We present a derivation similar that of Ref. [7], but allow for a variable time-step. We introduce six un-

knowns p_-, p_0, p_+, q_-, q_0, and q_+ to discretize $\dot{P} = Q$ as

$$p_- P^{n-1} + p_0 P^n + p_+ P^{n+1} = \Delta t_+ \left(q_- Q^{n-1} + q_0 Q^n + q_+ Q^{n+1} \right), \qquad (7.3.6)$$

where Δt_+ is the time-step when going from the time level n to $n+1$. This can be different from the time-step Δt_- used to go from $n-1$ to n. To second-order in the time-step we can Taylor expand to write

$$p_- \left(P^{n-1} - \Delta t_- \dot{P}^n + \frac{1}{2} \Delta t_-^2 \ddot{P}^n \right) + p_0 P^n + p_+ \left(P^n + \Delta t_+ \dot{P}^n + \frac{1}{2} \Delta t_+^2 \ddot{P}^n \right) \qquad (7.3.7a)$$

$$= \Delta t_+ \left[q_- \left(Q^n - \Delta t_- \dot{Q}^n \right) + q_0 Q^n + q_+ \left(Q^n + \Delta t_+ \dot{Q}^n \right) \right], \qquad (7.3.7b)$$

where a dot denotes a time derivative. To leading order in the time-step we have $p_- + p_0 + p_+ = 0$. To first-order we can use $\dot{P}^n = Q^n$ to obtain a relation between q_i and p_i:

$$\frac{p_+ \Delta t_+ - p_- \Delta t_-}{\Delta t_+} = q_- + q_0 + q_+. \qquad (7.3.8)$$

We will make use of the freedom in the magnitude of the coefficients to equate these terms separately to unity. Defining $\zeta \equiv p_-$, $\phi \equiv -q_-$, and $\theta \equiv q_+$, the resulting three equations are solved by

$$p_0 = - \left(1 + \zeta \left(1 + r \right) \right), \quad p_+ = 1 + \zeta r, \quad q_0 = 1 + \phi - \theta, \qquad (7.3.9)$$

where $r \equiv \Delta t_- / \Delta t_+$. The resulting two-step time integration scheme (7.3.6) becomes

$$\left(1 + \zeta r \right) P^{n+1} - \left(1 + \zeta \left(1 + r \right) \right) P^n + \zeta P^{n-1} = \Delta t_+ \left(\theta Q^{n+1} + \left(1 + \phi - \theta \right) Q^n - \phi Q^{n-1} \right). \qquad (7.3.10)$$

For $r = 1$ the scheme of Beam-Warming [7] is obtained. The derivation can equally well be performed centered around $t = t^{n-1}$ or t^{n+1}, in which case the same result is obtained. To second-order in the time-step, Eq. (7.3.7) can be re-written using $\ddot{P}^n = \dot{Q}^n$ as

$$\frac{1}{2} r^2 \left(p_- + p_+ \right) = q_- - r q_-, \qquad (7.3.11)$$

with the solution

$$\phi r + \theta - \zeta r \left(1 + r \right) = \frac{1}{2}. \qquad (7.3.12)$$

Equation (7.3.10) gives the most general two-step method for variable time-step. In general it is only first-order accurate in time. When Eq. (7.3.12) holds it is at least second-order accurate. Equation (7.3.10) includes the well-known θ-schemes for $\zeta = \phi = 0$, of which forward Euler $\theta = 0$, backward Euler $\theta = 1$, and Crank-Nicolson $\theta = 1/2$ are examples.

Properties

Stability   To establish some properties of the general time integration scheme (7.3.10) we investigate the model eigenvalue equation $\dot{P} = Q = \lambda P$ [44], with exact solution $P \propto \exp \lambda t$. We limit ourselves to the case $r = 1$ so that the growth factor $P^{n+1}/P^n = P^n/P^{n-1} \equiv G$. Dividing Eq. (7.3.10) by P^n we obtain

$$(1 + \zeta)\, G^2 - (1 + 2\zeta)\, G + \zeta = z \left(\theta G^2 + (1 + \phi - \theta)\, G - \phi \right), \tag{7.3.13}$$

where $z \equiv \lambda \Delta t$. This quadratic equation is solved by $G = a \pm \sqrt{a^2 + b}$ where

$$a = \frac{1}{2} \frac{1 + 2\zeta + z\,(1 - \theta + \phi)}{1 + \zeta - z\theta}, \quad b = -\frac{\zeta + z\phi}{1 + \zeta - z\theta}. \tag{7.3.14}$$

An interesting limit is that of very large time-steps. We note that in this case λ is irrelevant because it appears linearly in both the numerator and denominators of a and b. The result is

$$\lim_{\Delta t \to \infty} G = \frac{1 + \phi - \theta}{2\theta} \mp \sqrt{\frac{\phi}{\theta} + \left(\frac{1 + \phi - \theta}{2\theta} \right)^2}, \tag{7.3.15}$$

which is independent of ζ. This quantity vanishes for $\phi = 0$, $\theta = 1$, which is the backwards-differencing second-order scheme (BDF2, or Gear's scheme). In this scheme the solution component corresponding to any large eigenvalue λ, real or imaginary, is heavily damped, unless the time-step is sufficiently small. This scheme is therefore suitable for example for marching towards an equilibrium. The scheme can also be useful in stiff problems, such as the simulation of a tokamak plasma. With a suitably chosen time-step, the fastest waves will be damped while the slower dynamics can be resolved.[2] Regarding stability of these numerical schemes, it is highly desirable that $|G|^2 \leq 1$ when $\mathrm{Re}\,(\lambda) \leq 0$, in which case the scheme is called A-stable. It can be show [7] that this holds when

$$\frac{1}{2} + \phi \leq \theta \quad \text{and} \quad -\frac{1}{2} \leq \zeta \leq \theta + \phi - \frac{1}{2}. \tag{7.3.16}$$

When next to A-stability also $G \to 0$ when $|z| \to \infty$, as is the case for BDF2, the scheme is called L-stable.

Accuracy   For $\zeta = \phi = 0$, the solution to Eq. (7.3.13) becomes

$$G = \frac{1 + z(1 - \theta)}{1 - z\theta} = 1 + z + \theta z^2 + \theta^2 z^3 + \dots \tag{7.3.17}$$

---

[2] When instead of $\dot{P} = \lambda P$ we investigate the linear wave equation $\dot{P} + c\partial_x P = 0$, with central differences we write $\partial_x P = (P_{i+1} - P_{i-1})/2\Delta x$. Inserting a spatial dependence $P \propto \exp(ikx)$ we obtain the same equation as (7.3.13), but with $Q = -ic\Delta \sin(kx)/\Delta x$.

Comparing with the exact analytical solution $G = \exp z = 1 + z + \frac{1}{2}z^2 + \frac{1}{6}z^3 + ...$, we see that the θ-methods are only second-order accurate for $\theta = 1/2$, in agreement with Eq. (7.3.12). With $\theta = 1/2$ the error for the third order term is $(1/2)^2 - 1/6 = 1/12$. This can be shown to be the smallest truncation error of all second-order A-stable schemes. Note that even though the local error is $O(\Delta t^3)$, over a finite time interval a number of time-steps inversely proportional to Δt has to be taken, lowering the global order of convergence to two.

Positivity   For the Crank-Nicolson scheme $\theta = 1/2$, $\zeta = \phi = 0$, the limit of Eq. (7.3.15) gives -1. This implies that the solution can display numerical oscillations $P^{n+1} = -P^n = P^{n-1}$. This provides a warning that the time-step is too large to resolve all the time scales present.

It is important that when a quantity cannot be negative, as holds for example for the density, the time integration is such that when the quantity starts out positive it stays positive everywhere. We assume real eigenvalues λ, since otherwise it would not be physical to demand positivity. From the solution of Eq. (7.3.13) the growth factor G is non-negative when $b \leq 0$, or from Eq. (7.3.14)

$$
G \geq 0 \quad \text{when either} \quad
\begin{cases}
-\frac{\zeta}{\phi} \leq z \leq \frac{1+\zeta}{\theta} & \text{or} \\
-\frac{\zeta}{\phi} \geq z \geq \frac{1+\zeta}{\theta}
\end{cases}. \tag{7.3.18}
$$

When $\phi = 0$ and $\zeta > 0$ the bottom criterion cannot be satisfied while the top criterion only gives a time-step restriction for exponentially growing solutions with $\lambda > 0$. In this case the time-step is restricted by $\Delta t < (1 + \zeta) / \lambda \theta$.

When besides ϕ also ζ vanishes, we growth factor G is given by Eq. (7.3.17) which gives, assuming $0 \leq \theta \leq 1$,

$$
G \geq 0 \quad \text{when either} \quad
\begin{cases}
0 \leq -z \leq \frac{1}{1-\theta} & \text{or} \\
0 \leq z \leq \frac{1}{\theta}
\end{cases}. \tag{7.3.19}
$$

The first option is relevant for damped solutions with $\lambda < 0$. Unless $\theta = 1$, ever smaller time-steps are required to assure positivity with decreased damping. The second option is relevant for exponential growth. Unless $\theta = 0$, ever smaller time-steps are required to avoid oscillations when the growth rate increases.

The spatial discretization will be important to determine what the eigenvalues λ will be. In any case the sufficient criteria (7.3.18) provide rather demanding conditions on the time-step for assuring positivity.

Implementation in JOREK

The integrands of the weak formulation (7.2.20a)-(7.2.20d) or (7.2.21a)-(7.2.21d) can in matrix/operator form be written as

$$
\frac{\partial \mathbf{P}(\mathbf{y})}{\partial t} = \mathbf{Q}(\mathbf{y}, t), \tag{7.3.20}
$$

with each of the entries of this vector equation representing one of the scalar MHD equations.

Nonlinear terms are treated in JOREK using linearization,

$$\mathbf{Q}^{n+1} = \mathbf{Q}^n + \left(\frac{\partial \mathbf{Q}}{\partial \mathbf{y}}\right)^n \cdot \delta \mathbf{y}^n + O(\Delta t^2), \tag{7.3.21}$$

where $\delta \mathbf{y}^n \equiv \mathbf{y}^{n+1} - \mathbf{y}^n$. Similarly for $\mathbf{Q}^{n-1}$, $\mathbf{P}^{n+1}$ and $\mathbf{P}^{n-1}$. The matrix $\partial \mathbf{Q}/\partial \mathbf{y}$ is the Jacobian that contains the derivatives of all the right-hand sides of the equations with respect to all the primitive variables. These derivatives are evaluated analytically in JOREK.

After linearization, the two-step scheme (7.3.10) reads with $\Delta t = \Delta t_+$

$$\left[(1 + \zeta r)\left(\frac{\partial \mathbf{P}}{\partial \mathbf{y}}\right)^n - \Delta t\theta\left(\frac{\partial \mathbf{Q}}{\partial \mathbf{y}}\right)^n\right] \cdot \delta \mathbf{y}^n = \Delta t\mathbf{Q}^n + \left(\zeta\left(\frac{\partial \mathbf{P}}{\partial \mathbf{y}}\right)^n + \phi\Delta t\left(\frac{\partial \mathbf{Q}}{\partial \mathbf{y}}\right)^n\right) \cdot \delta \mathbf{y}^{n-1}. \tag{7.3.22}$$

This matrix equation is solved for the unknowns $\delta \mathbf{y}^n$. In the remainder of this chapter we will use $\phi = 0$.

Startup and changing time-step

Whenever ζ is nonzero, the time integration scheme (7.3.10) requires P^{n-1}, or equivalently Eq. (7.3.22) requires $(\partial \mathbf{P}/\partial \mathbf{y})^{n-1}$. At the startup of a simulation this information of the previous time level is not available, which can endanger the properties of the scheme. It is well-known that the accuracy of the approximation for P^{n-1} can be at most an order lower in the time-step than that required for the rest of the time-evolution. For example, P^{n-1} should be supplied with an accuracy of at least first-order in time to ensure second-order accuracy of the rest of the time evolution. To supply such an approximation we can use any first-order scheme, like explicit Euler. Also the second-order Crank-Nicolson scheme can be used, since this scheme has $\zeta = 0$ and does not require an approximation for P^{n-1}.

This behavior is illustrated by the following simple test case. In Fig. 7.2 we show the error after numerically integrating

$$\frac{d\rho(t)}{dt} = \rho(t) \quad \text{with} \quad \rho(0) = 1, \tag{7.3.23}$$

from $t = 0$ up to $t = 1$. We show two second-order time integration schemes: Crank-Nicolson ($\theta = 0.5, \zeta = 0$) and BDF2 ($\theta = 1$, $\zeta = 0.5$); and two first-order schemes: implicit Euler ($\theta = 1, \zeta = 0$) and explicit Euler ($\theta = \zeta = 0$). These schemes indeed nicely show the expected behavior. The BDF2 scheme only shows the desired second-order behavior when we use for the first time-step a scheme with $\zeta = 0$ to start up.

Using a single time-step, the implicit Euler scheme diverges. This can be understood from Eq. (7.3.22), because with $\partial P/\partial y = \partial Q/\partial y = \partial \rho/\partial \rho = 1$, $\theta = 1$, $\zeta = \phi = 0$,
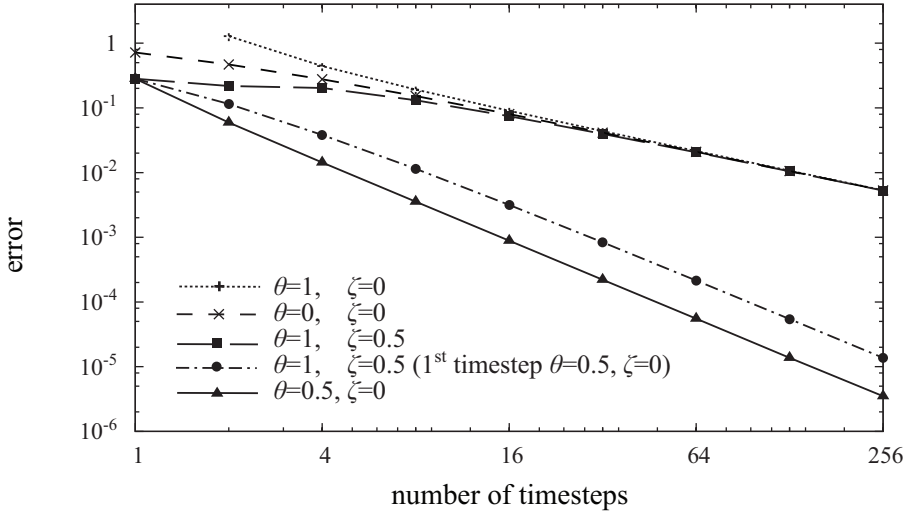
Figure 7.2: The error $|\rho(1) - e|$, when calculating $d\rho(t)/dt = \rho$ with $\rho(0) = 1$, using various time integration schemes. The first two methods give first-order convergence, while the final Crank-Nicolson method shows second-order convergence. The BDF2 scheme with $\theta = 1$ and $\zeta = 0.5$ only shows second-order convergence when for the first time-step a different method with $\zeta = 0$ is used.

and $\Delta t = 1$, the term between square brackets vanishes, while the right-hand side is finite. This actually corresponds to the limiting case of the lower solution of Eq. (7.3.19) for which positivity is guaranteed.

More generally, the top solution of Eq. (7.3.18) guarantees that oscillations are avoided when $\Delta t \leq \frac{1+\zeta}{\lambda\theta}$. Note that this corresponds to a condition for when the expression between square brackets in Eq. (7.3.22) is positive. For Eq. (7.3.23), $\lambda = 1$ so that oscillatory motion is expected for $\Delta t > 2$ with Crank-Nicolson and for $\Delta t > 1.5$ with BDF2. Indeed exactly above these values of the time-step, the solutions started to oscillate.

Sometimes we want to adjust the time-step during a simulation, which for BDF2 gives the same problem as during startup. The final term of Eq. (7.3.22) is not a first-order approximation to $\mathbf{P}^n - \mathbf{P}^{n-1}$ and the scheme reduces to first-order in time. When changing the time-step, we should use a scheme that has $\zeta = 0$ for at least one new time-step before proceeding with a scheme that has ζ nonzero.

Finally we note that in the limit $\Delta t \to \infty$ Eq. (7.3.22) reads

$$0 = \theta \left(\frac{\partial \mathbf{Q}}{\partial \mathbf{y}} \right)^n \cdot \delta \mathbf{y}^n + \mathbf{Q}^n. \tag{7.3.24}$$

For $\theta = 1$ this is equal to Newton's method for solving $\mathbf{Q} = 0$. The parameter θ can be used for successive over-relaxation, which may be useful in the case of multiple roots.
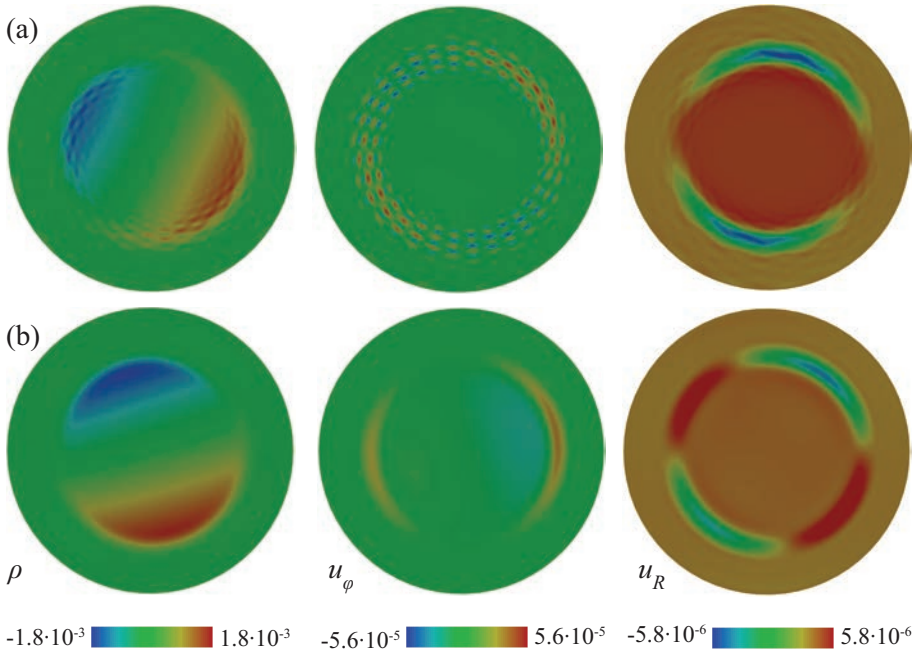
Figure 7.3: The results from an internal kink mode simulation with $\eta = 10^{-5}$. The numerical artifacts in the variables are caused by small noise in the Lorentz force. This was found to be avoided when instead of a projection of the momentum equation in (a) the toroidal direction, a projection in (b) the direction of the magnetic field is used.

7.4 Parallel Projection

MHD instabilities in tokamak plasmas to a large degree avoid compression of the toroidal magnetic field because of the large amount of energy this requires. It can require some special care to accurately represent such perturbations numerically. This problem of 'spectral pollution' is the primary reason why for example in M3D-C^1 the choice is made for a representation of the velocity in terms of a stream function that does not compress the magnetic field [23].

Our simulations of linear MHD instabilities were found to be polluted by spurious fluctuations in the magnetic vector potential components A_R and A_Z making up the toroidal magnetic field. This small noise primarily influences the solution through the Lorentz force in the toroidal component of the momentum equation. Before we discuss our internal kink mode simulations in more detail in Section 7.7.1, in Fig. 7.3(a) we already show results from this test case. In particular the toroidal velocity can be seen to be dominated by non-physical noise.

This was found to be avoided when instead of projecting the momentum equation in the toroidal direction, we project it in the direction of the magnetic field. Under

such a parallel projection the Lorentz force vanishes. The resulting solutions are much smoother, as is shown in Fig. 7.3(b).

With the test function

$$\mathbf{m}_B^* = \bar{m}_B^* \mathbf{B} = \bar{m}_B^* \left(B_R \hat{\mathbf{e}}_R + B_Z \hat{\mathbf{e}}_R + B_\phi \hat{\mathbf{e}}_\phi \right), \qquad (7.4.1)$$

we obtain a scalar equation that contains terms from projections in all three directions. Partial integration results in derivatives of the test function, which now include also the magnetic field components B_R, B_Z, and B_ϕ. Because the magnetic field is expressed in terms of a magnetic vector potential, this will require the use of second derivatives. This is very well possible in JOREK, but requires more function evaluations, and is therefore preferably avoided, if possible. Instead, we will not partially integrate the terms of the momentum equation. In this case the equation resulting from the use of Eq. (7.4.1) will simply be a linear combination of the three projections in the $\hat{\mathbf{e}}_R$, $\hat{\mathbf{e}}_Z$, and $\hat{\mathbf{e}}_\phi$-directions weighed by the magnetic field components.

Without partial integration, the viscous force (7.2.6) now does require the evaluation of second derivatives. The Laplacian first term of Eq. (7.2.6) requires derivatives like $\partial^2 u_R / \partial R^2$, whereas the second term requires mixed terms like $\partial^2 u_R / \partial R \partial Z$. To minimize the amount of second derivatives that have to be calculated, we choose to partially integrate

$$\int \mathbf{m}_B^* \cdot \nabla \left(\nabla \cdot \mathbf{u} \right) dV = \int \left(\nabla \cdot \mathbf{m}_B^* \right) \left(\nabla \cdot \mathbf{u} \right) dV + \int \left(\nabla \cdot \mathbf{u} \right) \mathbf{m}_B^* \cdot d\mathbf{S}. \qquad (7.4.2)$$

Since $\nabla \cdot \mathbf{B} = 0$ we have that $\nabla \cdot \mathbf{m}_B^* = \mathbf{B} \cdot \nabla m_B^*$, which does not require the calculation of derivatives of the magnetic field.

There might be some concern regarding whether the use of implicit time integration for an equation like

$$\mathbf{B} \cdot \frac{\partial \rho \mathbf{u}}{\partial t} = \mathbf{B} \cdot \mathbf{f} \qquad (7.4.3)$$

requires special care, because the projection operator can change during a time-step. Following the derivation leading up to the time integration scheme (7.3.22) we find that with $\partial \rho u_R / \partial t = f_R$ and $\partial \rho u_Z / \partial t = f_Z$ solved, what remains of Eq. (7.4.3) is $B_\phi \partial \rho u_\phi / \partial t = B_\phi f_\phi$. With $\partial \rho u_\phi / \partial t = f_\phi$ and $\partial^2 \rho u_\phi / \partial t^2 = \dot{f}_\phi$ to balance the different orders in the time-step, the derivation proceeds as before, leading to the same time integration scheme. To show that indeed the second-order time behavior of the parallel projected momentum equation can be guaranteed, in Section 7.6.4 we show results for an appropriate test case.

Note that it will be different if we want to solve for example

$$\rho \frac{\partial \mathbf{u}}{\partial t} = \mathbf{f}, \qquad (7.4.4)$$

since ρ now appears only on the left-hand side. To second-order in the time-step the derivation requires the time derivative of both sides, where $\dot{\rho}$ enters.

7.5 Grid Axis

Near the axis of the grid, the quadrilateral elements are deformed into triangular elements. At the grid axis, there will typically be much more than the usual four nodes per vertex. Therefore, there will be more equations than unknowns, rendering the system of equations underdetermined. The corresponding freedom in the solutions sometimes gives rise to numerical instability, starting with oscillations near the axis. The solution is to either increase the number of equations, or to decrease the number of degrees of freedom. In principle, the same issue holds also for the X-point grids often used in JOREK, where six elements come together in a single point.

Additional equations can be obtained by imposing regularity of the solution at the axis. Expanding a continuous function $f(R, Z)$ to first-order in the distance to the axis at $R = R_0$ and $Z = Z_0$ gives

$$f(R, Z) \approx f(R_0, Z_0) + \frac{\partial f}{\partial R}(R - R_0) + \frac{\partial f}{\partial Z}(Z - Z_0). \tag{7.5.1}$$

The scalar function f can be any of our primitive variables (7.2.25). Introducing a polar coordinate system $R = R_0 + r \cos \theta$, $Z = Z_0 + r \sin \theta$ we have for $r \to 0$

$$\frac{\partial f}{\partial \theta} = 0, \tag{7.5.2a}$$

$$\frac{\partial f}{\partial r} = \frac{\partial f}{\partial R} \cos \theta + \frac{\partial f}{\partial Z} \sin \theta, \tag{7.5.2b}$$

$$\frac{\partial^2 f}{\partial r \partial \theta} = -\frac{\partial f}{\partial R} \sin \theta + \frac{\partial f}{\partial Z} \cos \theta. \tag{7.5.2c}$$

The first of these equations shows the trivial fact that functions do not vary with θ at the single point in space corresponding to $r = 0$. Equation (7.5.2b) shows that for $r \to 0$ the radial derivative is only nonzero for functions with a periodicity of 2π. For such functions, $\partial f / \partial r$ changes sign when rotating over an angle of π.

The regularity conditions (7.5.2a)-(7.5.2c) can provide the additional constraints required to reduce the redundancy in the degrees of freedom on the grid axis. Equation (7.5.2a) for example excludes the use of the third basis function $b_{1,3}$ and $b_{4,3}$ for vertex 1 and 3 of the elements near the axis. This is because $\partial b_{1,3}/\partial t$ and $\partial b_{4,3}/\partial t$ do not vanish for $s \to 0$. Since the coordinates s and t locally become proportional to r and θ respectively, these basis functions therefore violate Eq. (7.5.2a). Writing down Eq. (7.5.2b) and (7.5.2c) for two values of θ, we can solve for

$$\frac{\partial f}{\partial R} = \frac{\partial f}{\partial r}\bigg|_{\theta_1} \cos \theta_1 - \frac{\partial^2 f}{\partial r \partial \theta}\bigg|_{\theta_1} \sin \theta_1 = \frac{\partial f}{\partial r}\bigg|_{\theta_2} \cos \theta_2 - \frac{\partial^2 f}{\partial r \partial \theta}\bigg|_{\theta_2} \sin \theta_2, \tag{7.5.3a}$$

$$\frac{\partial f}{\partial Z} = \frac{\partial f}{\partial r}\bigg|_{\theta_1} \sin \theta_1 + \frac{\partial^2 f}{\partial r \partial \theta}\bigg|_{\theta_1} \cos \theta_1 = \frac{\partial f}{\partial r}\bigg|_{\theta_2} \sin \theta_2 + \frac{\partial^2 f}{\partial r \partial \theta}\bigg|_{\theta_2} \cos \theta_2. \tag{7.5.3b}$$
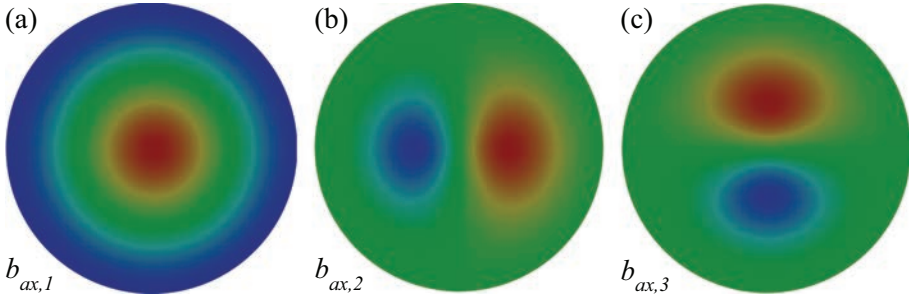
Figure 7.4: The three basis functions that satisfy the regularity conditions at the axis describe: (a) the function value f, (b) $\partial f/\partial R$, and (c) $\partial f/\partial Z$ at the axis

For $s \to 0$ and $t = 0$ we have $\partial^2 b_{1,4}/\partial s \partial t = 9$ and $\partial b_{1,2}/\partial s = 3$. With θ_1 and θ_2 the values of θ for two consecutive axis nodes, Eqs. (7.5.3) give additional conditions for the coefficients of these basis functions.

Instead of adding these conditions as additional equations, we can also impose them on the basis functions themselves. We then look for basis functions that are local to all the elements near the axis and satisfy the above regularity conditions. Additionally they should allow for continuity of the variables along element boundaries, and preferably also be exactly integrable with the Gauss quadrature presently used. Obvious candidates are linear combinations of our basis functions. A first one, $b_{ax,1}$ is easy. The union of all $b_{1,1}$ and $b_{4,1}$ of the elements that border the axis satisfies these conditions. A second basis function follows from Eq. (7.5.3a) as

$$b_{ax,2} = \cos\theta_1 b_{1,2} - \frac{1}{3}\sin\theta_1 b_{1,4} + \cos\theta_2 b_{4,2} + \frac{1}{3}\sin\theta_2 b_{4,4}. \qquad (7.5.4)$$

A third one follows from (7.5.3b) as

$$b_{ax,3} = \sin\theta_1 b_{1,2} + \frac{1}{3}\cos\theta_1 b_{1,4} + \sin\theta_2 b_{4,2} - \frac{1}{3}\cos\theta_2 b_{4,4}. \qquad (7.5.5)$$

These three basis functions are shown in Fig. 7.4. The coefficients of these basis functions represent the respective values of f, $(\partial f/\partial R)(\partial r/\partial s)$, and $(\partial f/\partial Z)(\partial r/\partial s)$ at the axis. Note that the basis function $b_{ax,3}$ is equal to $b_{ax,2}$ when rotated over 90 degrees. As such, taking a linear combination of these two new basis functions amounts to a rotation and scaling.

What is presently being done in JOREK is to ensure unique function values at the axis by making the coefficients of the first basis functions of all axis nodes equal. This is equivalent to introducing the single axis basis function of Fig. 7.4. This already reduces a lot of the redundancy in the degrees of freedom and is often enough to ensure stable and accurate solutions. However, the coefficients of the $b_{1,3}$ and $b_{4,3}$ basis functions can sometimes still become significant. Therefore in what follows we

effectively remove these inadmissible basis functions by forcing their coefficients to be zero.

For the test cases performed in this paper, these combined measures turned out to be sufficient to ensure both stability and accuracy. Therefore we did not proceed with the implementation of the other two axis basis functions $b_{ax,2}$ and $b_{ax,3}$, shown in Fig. 7.4(b) and (c) respectively. If, in the future, regularity at the axis becomes an issue, then the solution proposed in this section can be fully implemented.

7.6 Testing Individual Equations

In this section we test our implementation of the various equations and their boundary conditions, primarily by comparison with analytical solutions.

7.6.1 The momentum equation

To test aspects of our implementation of the momentum equation, we use the analytical solution of Ref. [38]. An incompressible Newtonian fluid with constant density is considered in a toroidal domain of which the walls are moving with an angular frequency Ω_{wall}. The flow velocity $\mathbf{u} = u_\phi \hat{\mathbf{e}}_\phi + \nabla \times (\Psi \hat{\mathbf{e}}_\phi)$ satisfies no-slip boundary conditions $u_\phi = R\Omega_{\text{wall}}$ and $\Psi = d\Psi/dr = 0$ at the wall at $\bar{r} \equiv \sqrt{(R-R_0)^2 + Z^2}/a = 1$. A toroidal pressure gradient $\nabla p = dp/d\phi \hat{\mathbf{e}}_\phi / R$ can potentially make the fluid in the core move in a direction opposite to the fluid near the wall. An analytical solution can be obtained by expanding u_ϕ and Ψ in the inverse aspect ratio ϵ and solving order by order, giving [38]

$$u_\phi = \frac{G}{4}\left(1 - \bar{r}^2\right)\left[1 + \epsilon\frac{Z}{4}\left(3 - \frac{GF\text{Re}^2}{1152}\left(\bar{r}^4 - 3\bar{r}^2 + 3\right)\right.\right. \tag{7.6.1a}$$

$$\left.\left. + \frac{G^2\text{Re}^2}{4608}\left(\bar{r}^6 - 9\bar{r}^4 + 21\bar{r}^2 - 19\right)\right) + O(\epsilon^2)\right],$$

$$\Psi = -\frac{G\text{Re}}{192}(R - R_0)(1 - \bar{r}^2)^2\left(F + \frac{G}{24}\left(4 - \bar{r}^2\right)\right) + O(\epsilon^2), \tag{7.6.1b}$$

with $G = a^2\left(dp/d\phi\right)/R_0\mu$, $F = R_0\Omega_{\text{wall}}$, and $\text{Re} = \rho R_0/\mu$. The leading order term of u_ϕ can be recognized as the classical parabolic Poiseuille solution for a cylindrical
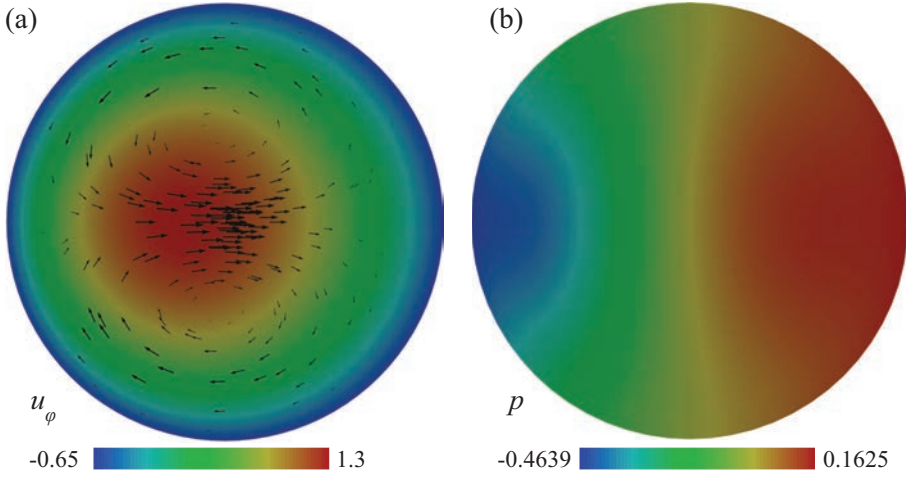
Figure 7.5: (a) The toroidal velocity (color) and spanwise velocity (vectors) in a toroidally rotating tokamak. (Re $= 1$, $G = 8$, $F = -0.63$, $\epsilon = 0.5$). (b) The pressure is calculated using an artificial compressibility model.

pipe flow. For the spanwise velocities we obtain to first-order

$$u_R = -\frac{\partial \Psi}{\partial Z} \quad = \epsilon \frac{G \mathrm{Re}}{4608} \left(1 - \bar{r}^2\right) \left[\left(1 - \bar{r}^2\right)\left(24F + G\left(4 - \bar{r}^2\right)\right)\right. \tag{7.6.2a}$$
$$\left. +6Z^2 \left(G\left(\bar{r}^2 - 3\right) - 16F\right)\right],$$

$$u_Z = \frac{1}{R}\frac{\partial (R\Psi)}{\partial R} \quad = \epsilon \frac{G \mathrm{Re}}{4608}\frac{Z}{R}\left(1 - \bar{r}^2\right)\left[-\left(1 - \bar{r}^2\right)\left(24F + G\left(4 - \bar{r}^2\right)\right)\right. \tag{7.6.2b}$$
$$\left. +R\left(R - R_0\right)\left(6G\left(3 - \bar{r}^2\right) + 96F\right)\right].$$

In order to ensure $\nabla \cdot \mathbf{u} = 0$ numerically, we adopt a penalty method for the momentum equation, see for example [78]. From Eq. (7.2.5a), the second coefficient of viscosity λ multiplies any nonzero deviation from $\nabla \cdot \mathbf{u} = 0$. Comparing with Eq. (7.2.4), this gives rise to a 'penalty pressure' $P = -\lambda \nabla \cdot \mathbf{u}$. When $\lambda \to \infty$, the associated force ensures $\nabla \cdot \mathbf{u} \to 0$. Taking $\lambda = 10^6$ was found to give good results.

We take $a = 1$, $\mu = 1$, $F = -0.63$, and $G = 8$. In this case the fluid in the core moves in a direction opposite to the direction in which the wall moves. The numerical solution for $\epsilon = 0.5$, is shown in Fig. 7.5. The center of the torus is to the left of the figure. The maximum fluid velocity is moved inwards rather than outwards, contrary to what is expected from the centrifugal force. This is because the driving pressure gradient force decreases with major radius.

We choose a grid with a larger number of poloidal elements $N_\theta = 4N_r$ than radial elements because the error primarily originates from the edge. This is due to the fact that the polynomial basis functions used in JOREK cannot describe circular bound-
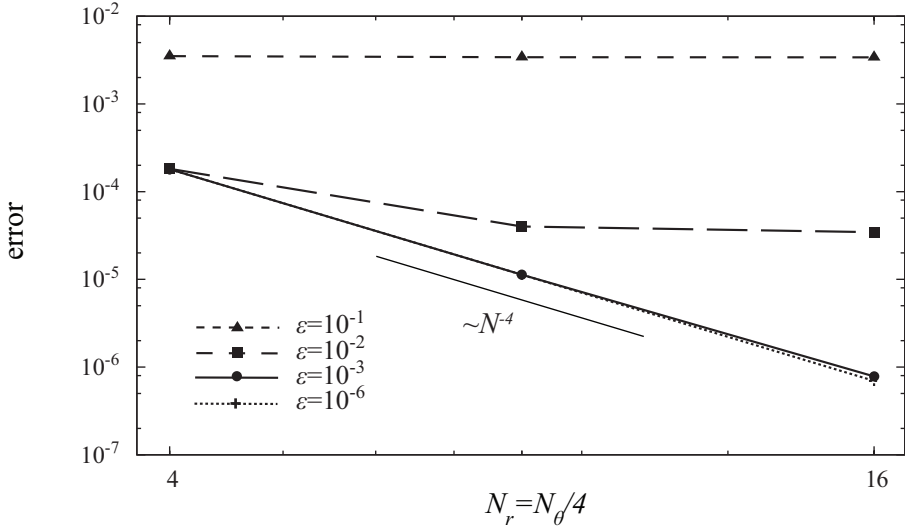
Figure 7.6: The maximum fractional difference between the numerical and analytical solution for the toroidal velocity u_ϕ as a function of the number of radial elements $N_r = N_\theta/4$. The analytical solution is first-order accurate in ϵ only.

aries exactly [43]. Therefore, the essential boundary condition $\mathbf{u} = 0$ is not exactly prescribed on a circle but on a shape that converges to a circle with an error of order $1/N_\theta^4$. In M3D-C^1 the boundary is described by straight lines so that a circle can be described only to first-order in the number of poloidal elements [55].

We vary R_0 so that $10^{-1} \leq \epsilon \leq 10^{-6}$. The result of such a scan in aspect ratio is presented in Fig. 7.6, which shows the maximum fractional difference between the analytical and numerical toroidal velocity component as a function of the number of radial elements N_r.

It can be seen that the analytical solution is only accurate to $O(\epsilon^2)$, providing rather a validation of the analytical solution than of the numerical solution. Fourth-order convergence between the numerical and the analytical solution down to the highest investigated resolution of $N_\theta = 4N_r = 64$ elements can be observed for the smallest $\epsilon = 10^{-6}$. Both the advective and viscous terms play a role in the solution. This test case provides a quantitative verification of the axisymmetric part of the implemented momentum equation and its boundary conditions.

7.6.2 The pressure equation

In an incompressible fluid it is typically the pressure rather than the viscous stress that ensures incompressibility. We therefore now turn our attention to the so-called artificial compressibility method for the same test case as used in the previous section.

In an incompressible fluid the only role of the pressure is to ensure that the velocity field remains divergence-free. The boundary conditions for the pressure are obtained by imposing $\nabla \cdot \mathbf{u} = 0$ at the edge [78]. Here it turns out that we can get away without imposing any boundary conditions for the pressure. We only keep the value of the pressure fixed on axis, to ensure uniqueness of the solution.

With $K_\perp = K_\parallel = S_h = 0$ the pressure equation (7.2.1c) reads

$$\frac{\partial p}{\partial t} = -\mathbf{u} \cdot \nabla p - \gamma p \nabla \cdot \mathbf{u}. \tag{7.6.3}$$

In the limit $\gamma \to \infty$, its steady state solution gives $\nabla \cdot \mathbf{u} = 0$.

Using a very large value of γ, the velocity field indeed becomes divergence-free in steady state. The resulting pressure field is shown in Fig. 7.5(b). Again fourth-order convergence of the velocity field was found. We did however find the weak formulation of Eq. (7.2.21c), without partial integration of the first-order terms, to be more stable for very high values of γ than that of Eq. (7.2.20c). Therefore in the following we will use the formulation of Eqs. (7.2.21a)-(7.2.21d).

7.6.3 The induction equation

With $\mathbf{u} \times \mathbf{B} = 0$ and constant resistivity, the induction equation for the magnetic field is a pure diffusion equation. Inserting $\mathbf{E} = \eta \nabla \times \mathbf{B}$ from Eq. (7.2.10) into Eq. (7.2.9) gives

$$\frac{\partial \mathbf{B}}{\partial t} = \eta \nabla^2 \mathbf{B}, \tag{7.6.4}$$

where we used $\nabla \cdot \mathbf{B} = 0$ so that $\nabla \times \nabla \times \mathbf{B} = -\nabla^2 \mathbf{B}$. With $\mathbf{B}$ a velocity and η a viscosity, Eq. (7.6.4) is Stokes equation, the viscous Re$= 0$ limit of the incompressible Navier-Stokes equations. There is no analogue to the pressure force in Eq. (7.6.4). In the poloidal direction its only role would be to keep the velocity field divergence-free, for which we have our vector potential formulation.

We can therefore again use the analytical solution of the previous section. For Re=0 there will be no secondary flows. We add a source term $-GZ\hat{\mathbf{e}}_R/R$ to Eq. (7.2.1d) to give the required source term $\nabla \times (-GZ\hat{\mathbf{e}}_R/R) = \hat{\mathbf{e}}_\phi G/R$ in Eq. (7.6.4). We now need $\mathbf{B} = 0$ as a boundary condition. Luckily this is the 'natural boundary condition' of the weak form (7.2.18). It is easily implemented by not taking into account the boundary term. To ensure uniqueness of the vector potential, we do fix $\mathbf{A} = 0$ at the axis of the grid. In Fig. 7.7 the components A_R and A_Z and the corresponding magnetic field are shown. Without imposing essential boundary conditions, the toroidal magnetic field $B_\phi = \partial_R A_Z - \partial_Z A_R$ can be seen to satisfy the homogeneous Dirichlet boundary conditions. Fourth-order convergence was obtained for the error in B_ϕ.

The surface term of Eq. (7.2.18) can also be made to vanish using essential boundary conditions for $\mathbf{A}$. This allows us to test the toroidal component of the induction equation, by adding a source term $GR_0\hat{\mathbf{e}}_\phi/R$ and comparing the resulting $A_\phi = A_3/R$ with the analytical solution (7.6.1a). Convergence of the solution was again verified.
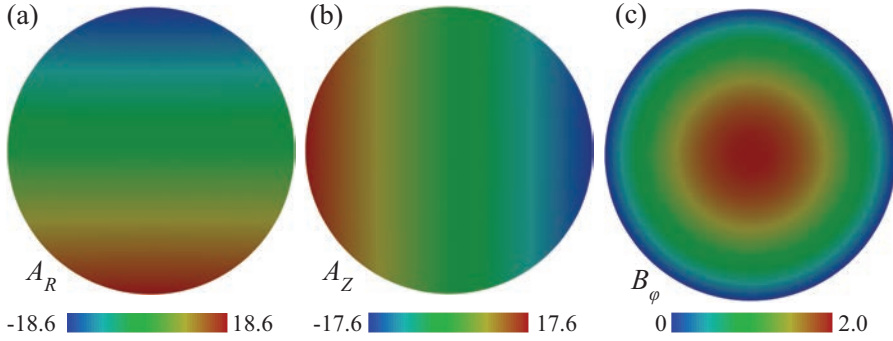
Figure 7.7: The magnetic vector potential components (a) A_R and (b) A_Z, and (c) the associated toroidal magnetic field $B_\phi = \partial_R A_Z - \partial_Z A_R$ for the incompressible Navier-Stokes test case with $F = \text{Re} = 0$, $G = 8$, $\epsilon = 10^{-4}$ on a mesh with $N_\theta = 4N_r = 32$.

The resistive term $-\eta \mathbf{J}$ in the induction equation can, with $\nabla \times \nabla \times \mathbf{A} = -\nabla^2 \mathbf{A} + \nabla\nabla \cdot \mathbf{A}$ and partial integration, also be cast into the weak form:

$$\int -\eta \mathbf{A}^* \cdot \mathbf{J} dV = - \int (\nabla \mathbf{A})^T : \nabla (\eta \mathbf{A}^*) \, dV + \int \eta \mathbf{A}^* \cdot \nabla \mathbf{A} \cdot d\mathbf{S}. \qquad (7.6.5)$$

We did not include the constant vector $\mathbf{F}$ and also used the gauge freedom to leave out the gradient term $\nabla\nabla \cdot \mathbf{A}$. This weak formulation of the Laplacian is similar to what we did with the viscous stress tensor in the momentum equation. The error obtained with this formulation was found to be virtually indistinguishable from that of Eq. (7.2.18).

7.6.4 Parallel projection

In Section 7.4 it was shown through analysis that the order of accuracy of the time integration is not at risk when one component of the projection operator of the weak formulation varies in time. To show that this is indeed the case, we perform the following test case. It consists of a combination of the test cases used individually to test the momentum equation and the toroidal component of the induction equation in the previous subsections. We add a source term for both the equation for A_3 and u_ϕ. This will introduce toroidal rotation and secondary flows, but also a time varying magnetic field with an associated Lorentz force interacting with the flow. We use $\nu = \eta = 1$, $G_\psi = G_{u_\phi} = 8$, $\Omega_{wall} = 0$, an inverse aspect ratio of $\epsilon = 1/10$, and a grid with $N_\theta = 4N_r = 16$. The simulation was started from a static Grad-Shafranov equilibrium with $FF' = 20$ and $p_0 = 0.001 \, (1 - \psi_n)$. The pressure and constant density were not evolved in time.

We simulated over a time $t = 0.1$ using Crank-Nicolson, and looked at the maximum secondary flow velocity in the R-direction. We estimated the time-resolved value
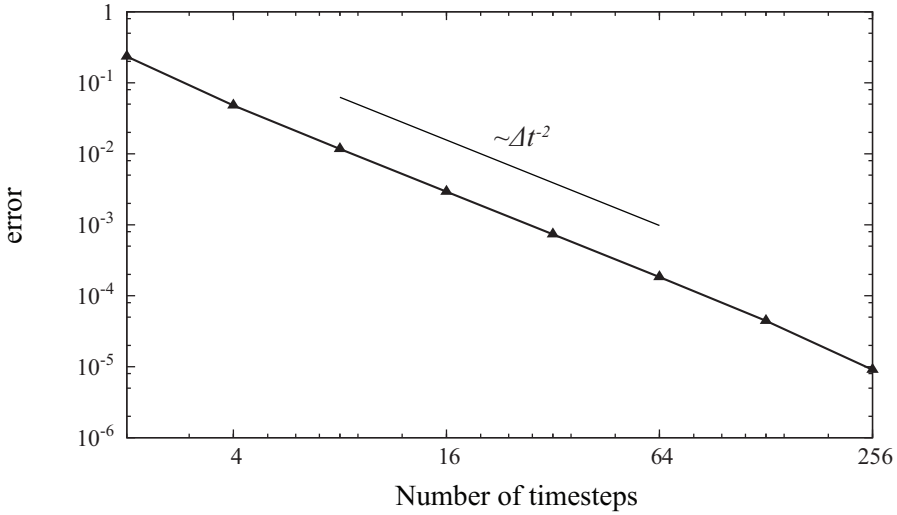
Figure 7.8: The relative temporal error in the maximum secondary velocity u_R as a function of the number of time-steps.

for this quantity based on a Richardson-extrapolation of the finest two time-steps assuming second-order convergence. The fractional difference between this extrapolated value and the numerically obtained value is shown in Fig. 7.8 for various numbers of time-steps. It shows clear second-order convergence, showing that the order of accuracy of the scheme can be maintained even with a time-varying magnetic field as a projection operator.

7.6.5   Scalar equations

Hyperdiffusivity

To test some aspects of our implementation of the hyperdiffusive term in the continuity equation we investigate a circular tokamak in the cylindrical limit. We look for an analytical solution to the stationary inhomogeneous hyperdiffusion equation $0 = \nabla^4 \rho + S_\rho$ for constant S_ρ. In polar coordinates (r, θ), assuming symmetry in the θ and ϕ direction, this equation reads

$$\frac{1}{r}\frac{d}{dr}\left(r\frac{d}{dr}\left(\frac{1}{r}\frac{d}{dr}\left(r\frac{d\rho(r)}{dr}\right)\right)\right) = -S_\rho. \tag{7.6.6}$$

The solution that is regular for $r \to 0$ is given by

$$\rho(r) = \frac{1}{64}\left(\bar{r}^2 - \bar{r}^4\right)a^4 S_\rho + \rho_0\left(1 - \bar{r}^2\right) + \rho_a \bar{r}^2, \tag{7.6.7}$$
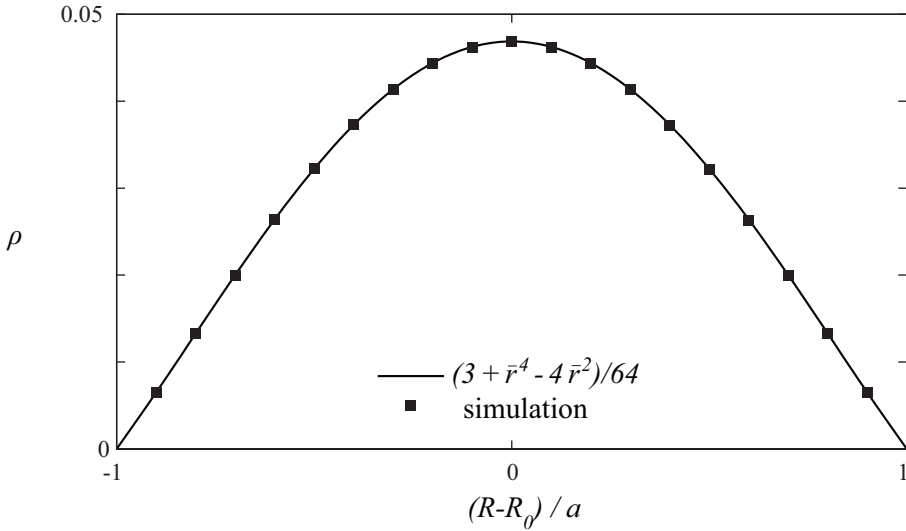
133

Figure 7.9: The profile resulting from solving the stationary hyperdiffusive equation $\nabla^4 \rho = 1$ with JOREK on a mesh with $N_r = N_\theta = 10$ elements, compared with the analytical solution.

where $\bar{r} \equiv r/a$. With $\rho_a = \rho(r = a) = 0$ we see that

$$\nabla^2 \rho \Big|_{\bar{r}=1} = \frac{1}{r}\frac{d}{dr}\left(r\frac{d\rho(r)}{dr}\right) = -4\left(\rho_0 + \frac{3}{64}S_\rho\right). \tag{7.6.8}$$

When the natural boundary condition is such that $\nabla^2 \rho$ vanishes at $\bar{r} = 1$ the central density therefore becomes $\rho_0 = -3S_\rho/64$. Taking a constant density source $S_\rho = -1$ and a large aspect ratio $\epsilon^{-1} = 100$, the resulting density distribution along a line $Z = 0$ is plotted in Fig. 7.9. The central value can indeed be seen to approach $\rho_0 = 3/64 \approx 0.047$. The overall agreement with the analytical result is also good, even on the relatively coarse grid with $N_r = N_\theta = 10$ elements that is used.

Anisotropic diffusion

In a fusion plasma the diffusivities in the direction parallel to the magnetic field can easily be many orders of magnitude larger than those perpendicular to the magnetic surfaces. Anisotropies of the order of 10^9 are not uncommon. A potential problem in numerically simulating such conditions is that a small error in the calculation of the parallel diffusion 'pollutes' the much smaller perpendicular diffusion. Since one of the most valued properties of a fusion device is its ability to keep heat and matter locked up, for some purposes it is important to make sure this can also be made to hold numerically.

A good two-dimensional stationary test case was devised for the NIMROD code

in Ref. [174] based on the anisotropic heat diffusion equation

$$\frac{\partial T}{\partial t} = \nabla \cdot \left[\left(\kappa_{\parallel} - \kappa_{\perp} \right) \nabla_{\parallel} T + \kappa_{\perp} \nabla T \right] + S_T. \tag{7.6.9}$$

The temperature T and poloidal magnetic flux ψ were chosen to have the same analytical dependence on a unit square $-\frac{1}{2} \leq x \leq \frac{1}{2}$, $-\frac{1}{2} \leq y \leq \frac{1}{2}$:

$$T, \psi \sim \cos\left(\pi x\right) \cos\left(\pi y\right). \tag{7.6.10}$$

Since the magnetic field $\mathbf{B} = \nabla\phi \times \nabla\psi$ is oriented parallel to the iso-contours of the temperature, the parallel diffusion should exactly vanish. When increasing the parallel diffusion coefficient, any deviation from the isotropic case can then be attributed to numerical pollution. Performing this test case with JOREK, we find no dependence of the error on the amount of parallel diffusion for anisotropies as large as 10^9. The fourth-order convergence is completely unaffected by the parallel diffusion coefficient, as it should of course. Interestingly, we do find that the error increases dramatically with increasing anisotropy when we enter the analytical expressions for $B_x = \partial\psi/\partial y$, $B_y = -\partial\psi/\partial x$ directly, instead of obtaining them as numerical derivatives from the analytical expression for ψ. In this case we lose as much as four orders of accuracy for an anisotropy of 10^9 compared to the error for the isotropic case. The reason for the fact that this pollution does not occur when we use ψ, must lie in the fact that the polluting term,

$$\mathbf{B} \cdot \nabla T = B_x \frac{\partial T}{\partial x} + B_y \frac{\partial T}{\partial y} = \frac{\partial \psi}{\partial y} \frac{\partial T}{\partial x} - \frac{\partial \psi}{\partial x} \frac{\partial T}{\partial y}, \tag{7.6.11}$$

can be represented very accurately in this case. We would like to test the accuracy with which anisotropic diffusion can be calculated on other grids available in JOREK as well.

For a constant source S_T, the isotropic diffusion equation (7.6.9) with $\kappa_{\perp} = \kappa_{\parallel}$ and boundary condition $T = 0$ is solved on a circular domain by $T(\bar{r}) = (S_T/4)\left(1 - \bar{r}^2\right)$. With ψ also proportional to $1 - \bar{r}^2$, the solution of the anisotropic heat equation is again independent of the parallel conductivity $\kappa_{\parallel}$. We run the diffusion equation to steady state for a single very large time-step with $\theta = 1$ as discussed below Eq. (7.3.24). It was found that again the error is not influenced by the anisotropy.

The polar grid that is used in this test case is however aligned with the magnetic field. Since anisotropy usually causes problems when the grid is not aligned, we should test this as well. To create an unaligned grid we make use of the machinery in JOREK that is normally used to create a flux-aligned grid. We set up a toroidal equilibrium with $\epsilon^{-1} = 3$ and a Shafranov shift of approximately $0.15a$ to which we align our grid. This is done using an interpolation from the polar grid on which the equilibrium is calculated. Now we re-run the anisotropic diffusion equation to steady state on this grid that is misaligned with the isocontours of our analytical ψ. Now the error *does* increase with the anisotropy. Fig. 7.10 compares the case where the grid is aligned with the magnetic field with the case where the grid and magnetic field
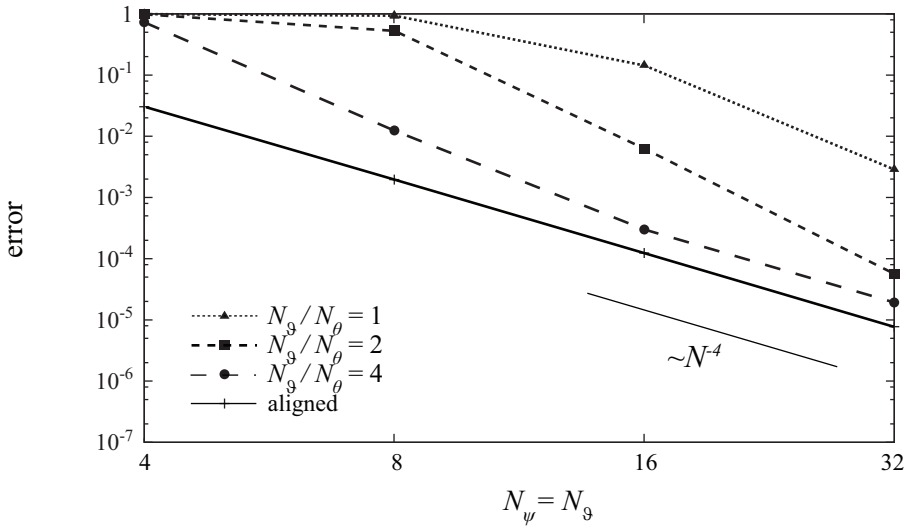
Figure 7.10: The maximum difference between the numerical and analytical solution for an anisotropy of $\kappa_\parallel / \kappa_\perp = 10^9$ as a function of the number of elements $N_\psi = N_\vartheta$, interpolated from a mesh with a potentially different number of poloidal elements N_θ.

are not aligned, using an anisotropy of $\kappa_\parallel / \kappa_\perp = 10^9$. The figure also shows what happens when we poloidally refine the initial polar grid from which the misaligned grid is obtained by interpolation. What is found is that when a poloidally much finer mesh is used for this initial polar mesh, the error can be greatly reduced. For an initial mesh that is four times finer in the poloidal direction, the curve approaches that of the aligned mesh, which is again the same as the curve for isotropic diffusion.

This leads us to the conclusion that accurately capturing highly anisotropic diffusion is not a problem in JOREK when the mesh that is used is of sufficient quality. It does not have to be aligned with the magnetic field, but it has to be set up either from an analytical representation or an accurate numerical interpolation.

7.7 Integrated Test Cases

The various tests performed in the previous sections were necessary to provide confidence that the equations are implemented correctly. Next, we deploy the newly implemented full MHD equations to show that they can be used to simulate various well-known MHD instabilities.
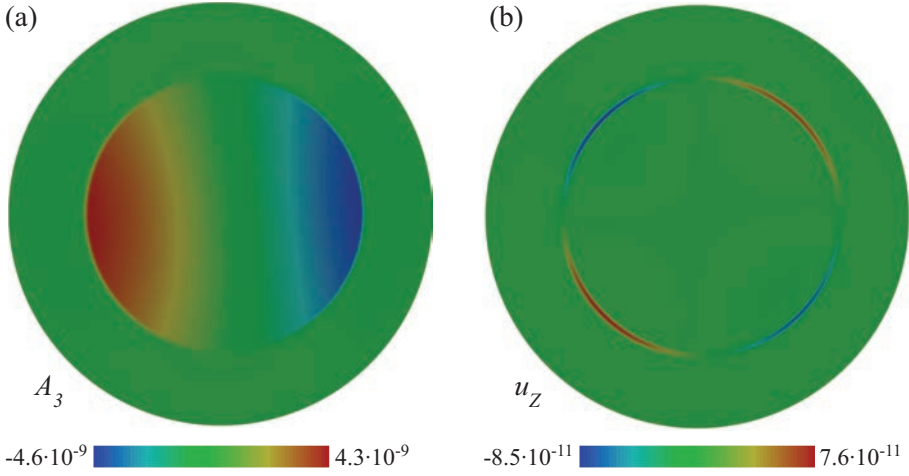
Figure 7.11: The perturbed poloidal flux ψ and vertical velocity u_Z of an internal kink mode after 50 time-steps of $\Delta t = 400$ with Crank-Nicolson. Shown is a poloidal cut of the Fourier harmonic $\sim \cos\phi$ at $\phi = 0$.

7.7.1 Resistive $m = n = 1$ internal kink mode

We start from an ideal equilibrium with circular cross-section and $\epsilon = 0.1$ with the profiles

$$\rho/\rho_0 = 1 - 0.9\psi_n, \tag{7.7.1a}$$

$$T/T_0 = 1 - 0.8\psi_n, \tag{7.7.1b}$$

$$F^2 = F_0^2 - 4\left(\psi_e - \psi_m\right)\left(\psi_n - 0.5\psi_n^2\right), \tag{7.7.1c}$$

where $\rho_0 = 1$, $T_0 = 2 \cdot 10^{-3}$, $F_0 = R_0 = 10$ so that $B_0 = 1$ and $\beta \sim 4 \cdot 10^{-3}$. In this case the units are essentially Alfvén units. The enclosed poloidal flux $\psi_e - \psi_m \approx 0.48$ is an integral part of the solution to the Grad-Shafranov equation. The safety factor monotonically increases from 0.73 at the axis to 1.6 at the plasma edge.

We use the resistive MHD equations without any additional diffusivities. Under these conditions, the $q = 1$ surface becomes unstable against an $n = m = 1$ internal kink mode. Kink modes perturb the plasma in a shift-tilt fashion that displaces rather than bends the field lines. In the absence of resistivity the source of their instability is a critical pressure gradient. Resistivity can however greatly enhance their growth rate. We fix the equilibrium $n = 0$ component and take into account only a single toroidal Fourier harmonic $n = 1$. We used an aligned grid of approximately $N_\psi = 30$ radial and $N_\vartheta = 30$ poloidal elements, which was refined when necessary to obtain a grid-independent solution. As can be seen from Fig. 7.11 the structures in the solution can
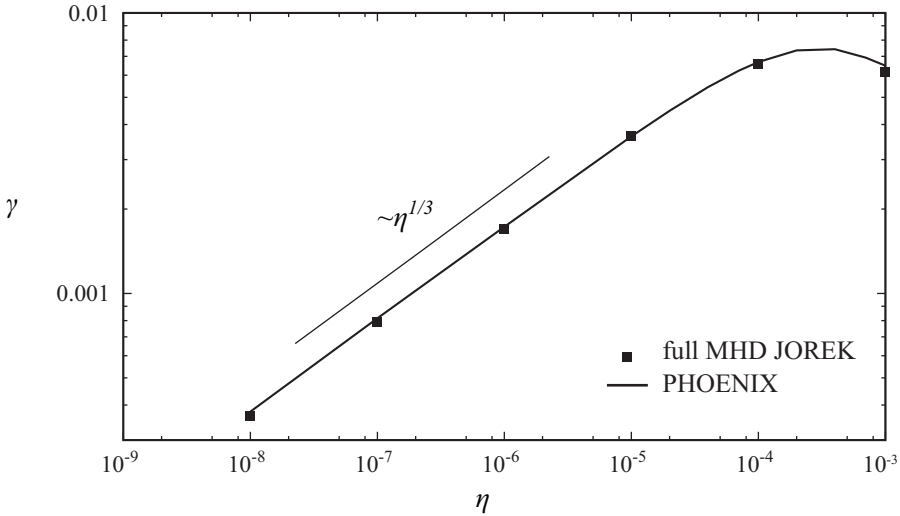
Figure 7.12: A comparison of the internal kink mode growth rate as a function of resistivity between JOREK and PHOENIX.

become very fine. Therefore we used local grid refinement. Figure 7.11 was obtained for $\eta = 10^{-8}$ on a grid of $N_\psi = N_\vartheta = 30$ elements, using Gaussian grid accumulation with a width of $0.03a$.

The structures become finer with smaller resistivity. Both the unstable layer size and the growth rate are known to scale as $\eta^{1/3}$. We start from an initial perturbation in the $n = 1$ harmonic of the toroidal velocity given by

$$u_\phi^{n=1} = 10^{-12}\psi_n \left(1 - \psi_n\right). \qquad (7.7.2)$$

Next we let the equilibrium develop in time, keeping the axisymmetric $n = 0$ component fixed. After some time all solution components y show exponential growth with the same growth rate $\gamma = (\partial y/\partial t)/y$. This growth rate is shown in Fig. 7.12 for various resistivities. Also shown is the growth rate as calculated from the linear MHD code PHOENIX [67, 15]. This code uses Fourier harmonics in the poloidal direction. The inclusion of only five poloidal mode numbers was found to be sufficient for accurate results, therefore requiring significantly less computational effort than JOREK. The equilibrium was calculated with the ideal MHD equilibrium code FINESSE [8] using the same parameters as in Eqs. (7.7.1a)-(7.7.1c). JOREK and PHOENIX results show good agreement for the full range of resistivities tested. For $\eta < 10^{-4}$ the growth rate nicely follows the $\eta^{1/3}$ scaling. For higher values of the resistivity, $\eta > 10^{-4}$, the mode width becomes comparable to the machine size and the scaling is lost entirely. This is therefore a good test case of the ideal wall boundary conditions that are also present in PHOENIX. Instead of driving the tearing mode, resistivity starts to damp the mode. These resistivities are much too high to be relevant for most tokamak plasmas.

7.7.2 Tearing modes

A next test case is the simulation of tearing modes. These are resistive, current-driven modes, that can become unstable around a rational surface. Tearing modes are primarily driven by the radial variation in the toroidal current density and are typically stabilized by pressure. The growth of these modes is much slower than that of the internal kink mode. Since their growth relies on the 'tearing' of field lines which is only possible for a finite resistivity, the time scale associated with their growth is closer to the resistive time scale than to the Alfvén time scale. For small resistivities this results in a scaling of the growth rate proportional to $\eta^{3/5}$.

Linear simulations

Zero pressure We start from the same equilibrium as was used for the internal kink simulations of Section 7.7.1, only for now with zero temperature. We also modify the toroidal magnetic field function to

$$F^2 = F_0^2 - 4 \left(\psi_e - \psi_m \right) \left(\psi_n - 0.35 \psi_n^2 \right). \tag{7.7.3}$$

With $F_0 = 18$ and $\psi_e - \psi_m \approx 0.4$, this results in a safety factor between $1.8 < q < 2.9$. The $q = 2$ surface is located at $\psi_n \approx 0.28$. The $q = 3$ surface was intentionally positioned outside the plasma to avoid the occurrence of a second tearing mode. We first only take into account the evolution of a single $n = 1$ harmonic, fixing the axisymmetric $n = 0$ component. We start from the same initial perturbation as in Eq. (7.7.2), but now for the $n = 1$ component of A_3. The required radial resolution for accurate tearing mode calculations was found to be substantially higher than for the internal kink mode. We restricted ourselves to the calculation of the growth rate for three resistivities, just to demonstrate agreement with the result obtained by FINESSE / PHOENIX as shown in Fig. 7.13. Both the resistivity and the growth rate were multiplied by the characteristic magnetic field strength $B_0 = F_0/R_0 = 1.8$ to convert the standard dimensionless Alfvén units used in PHOENIX to the units of JOREK.

Figure 7.13 also shows a comparison with the simplest reduced MHD model included in JOREK. This model uses a single stream function to describe the velocity perturbation in the poloidal plane. The model does not allow a velocity component in the toroidal direction. The figure shows good agreement with the PHOENIX results.

For the full MHD model we used a mesh of $N_\psi = 104$, $N_\vartheta = 36$ elements, for which the growth rates are approximately converged to their grid-independent values. We used Gaussian grid refinement with a width depending on the resistivity. It seems to be a general characteristic of JOREK, that convergence is achieved from the stable side. That is, the growth rate converges to its grid-independent value from below. This can usually be considered to be a favorable property.

The reduced MHD simulations were performed on a mesh with $N_\psi \geq 101$, $N_\vartheta \geq 41$; at this resolution the growth rate has converged. As the resistivity increases beyond some critical value, damping becomes more important than driving and the growth
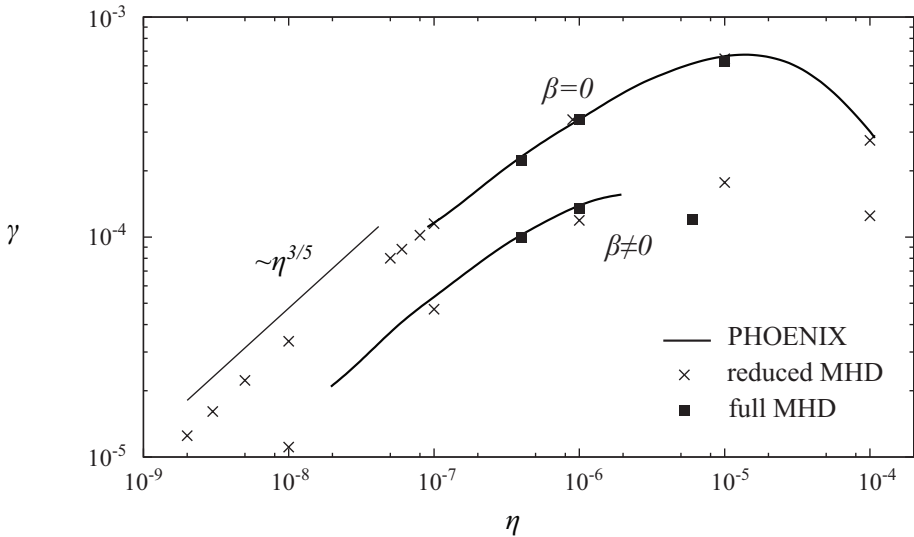
Figure 7.13: The growth rate of an $n = 1$ tearing mode as a function of the resistivity. Results from full MHD JOREK are compared with both PHOENIX and a reduced MHD model available in JOREK. For the $\beta = 0$ and $\beta \neq 0$ curves a reduced MHD model without and with a toroidal velocity were used respectively.

rate decreases. At the same time, the eigenvalue obtained by PHOENIX acquires an imaginary component, representing oscillatory behavior. These oscillations were indeed also observed in the JOREK simulations. The growth rates shown for the higher resistivities represent an average over several of these oscillations.

Outside of a reasonable middle-range of tokamak resistivities, PHOENIX exhibited difficulty converging to an eigenvalue with a sufficiently small residual. For this reason the PHOENIX results in Fig. 7.13 are not shown over the full broad range of resistivities where JOREK results were calculated.

Nonzero pressure   Next we introduce a small equilibrium pressure. When the safety factor is above one, the average magnetic field curvature becomes favorable, causing a finite pressure to exert a stabilizing influence. We design a pressure profile that is small enough to allow the instability to grow, but large enough to have a significant influence on the tearing mode growth rate. We choose the same temperature profile as in Eq. (7.7.1b). With $T_0 = 4.3 \cdot 10^{-4}$ and $B_0 = F_0/R_0 = 19.5/10$ this resulted in a value of β on the magnetic axis of $\beta_m = 2p_m/B_0^2 = 2.3 \cdot 10^{-4}$. Using the same parameters in an equilibrium constructed with FINESSE, allowed again a comparison with the growth rates calculated by PHOENIX.
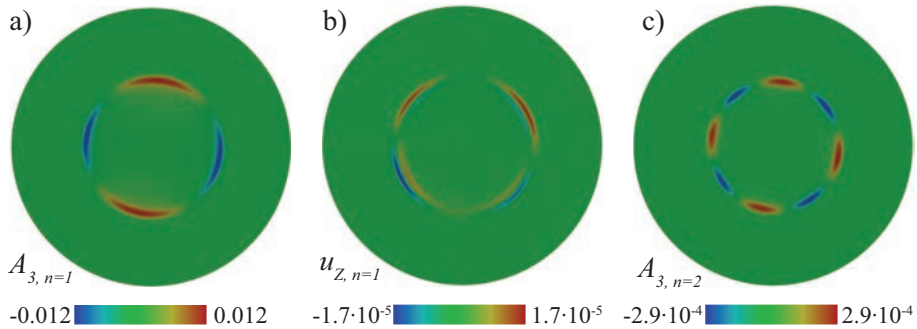
Figure 7.14: The $\cos\phi$ component of (a) the perturbed A_3, (b) u_Z, and (c) the $\cos 2\phi$ component of the perturbed A_3 of a tearing mode in the finite pressure equilibrium.

Comparing the zero and finite-β curves in Fig. 7.13 we see that indeed the growth rates are lowered by the finite pressure. The growth rates obtained with the full MHD equations in JOREK for three different resistivities were again found to converge to the PHOENIX result.

Finite-beta growth rates calculated with the simplest reduced MHD model in JOREK, that was successfully used to obtain the zero-beta tearing mode growth rates, were almost an order of magnitude smaller than those of the full MHD model. A second reduced MHD model, that includes a toroidal velocity component, produced results that agree reasonably well with the PHOENIX and the full MHD JOREK results. These are the finite-beta results plotted in Fig 7.13. The growth rates using this reduced MHD model are still slightly lower than those obtained with the full MHD model. Special care has been taken to ensure convergence in the number of elements and the time-step. Therefore this small deviation may be attributed to a genuine difference between full and reduced MHD models.

Fig. 7.14(a)-(b) shows the $n = 1$ mode structure, which has a clear dominant $m = 2$ structure that can be compared with the internal kink mode structure in Fig. 7.11.

Nonlinear simulations

$n = 2$ During the linear growth phase of the tearing mode, we added another toroidal Fourier harmonic $n = 2$. This harmonic is not unstable by itself, but arises due to nonlinear coupling with the $n = 1$ harmonic. After some time, the magnitude of the physical variables of the $n = 2$ harmonic were found to be approximately given by the square of those of the dominant $n = 1$ harmonic. Correspondingly the growth rate was found to be double that of the $n = 1$ harmonic. Fig. 7.14(c) clearly shows the $m = 4$ structure that is expected for a mode that is resonant with $q = m/n = 4/2$.

$n = 0$ When we follow the evolution of a tearing mode into the nonlinear phase, we would like to take into account the evolution of the axisymmetric component as well.
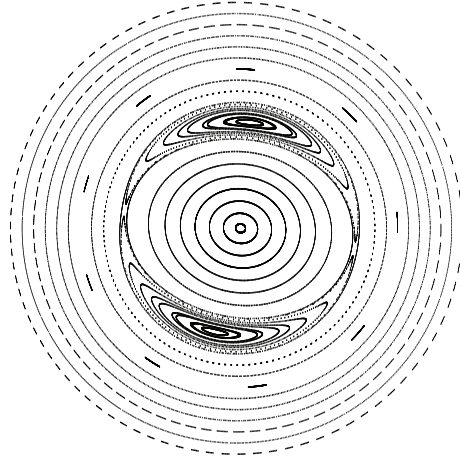
Figure 7.15: A Poincaré plot of the magnetic island at its maximum width. The starting values are homogeneously distributed radially, but with a higher density near the island. The magnetic field lines are followed for only 1000 turns, explaining why at certain radii close to rational magnetic surfaces the magnetic surfaces are not yet fully traced out.

Using $\eta = 10^{-6}$, the force equilibrium quickly changes. As the current resistively diffused, the safety factor went up and the $q = 3$ surface entered the plasma. This allowed an associated 3/1 tearing mode to grow. Because the resonant surface now changes location, adaptive grid refinement or an impractically high resolution over the whole domain is required in this case. To counteract the resistive diffusion of the $n = 0$ component we added a current source. This was effected by changing the resistive term in the induction equation from $\eta \mathbf{J} \rightarrow \eta \left(\mathbf{J} - \mathbf{J}_{eq} \right)$ with $\mathbf{J}_{eq}$ the equilibrium current density. This change allows the ideal equilibrium solution to be an equilibrium solution of the resistive static equations as well.

$n = 1$ We followed the evolution of the tearing mode for $\eta = 10^{-6}$ into the nonlinear regime using $N_\psi = 84$, $N_\vartheta = 36$ for the full MHD simulations and $N_\psi = 91$, $N_\vartheta = 45$ for the reduced MHD model. By perturbing the magnetic field, the instability changes the topology of the previously nested magnetic surfaces. By tracing the magnetic field lines around the torus for many times, new magnetic surfaces become visible. The resulting Poincaré plot is shown in Fig. 7.15. The field lines form new nested surfaces inside what are called magnetic islands.

In reduced MHD the magnetic field is described by Eq. (2.2.4a) with F constant in space and time. We consider a single helical perturbation $f(\psi_0, m\vartheta - n\phi)$ with ψ_0 the equilibrium value of ψ and the coordinate ϑ such that the equilibrium field lines satisfy $d\phi/d\vartheta = q(\psi_0)$. Then we can show that $\mathbf{B} \cdot \nabla \psi^* = 0$ with the helical flux

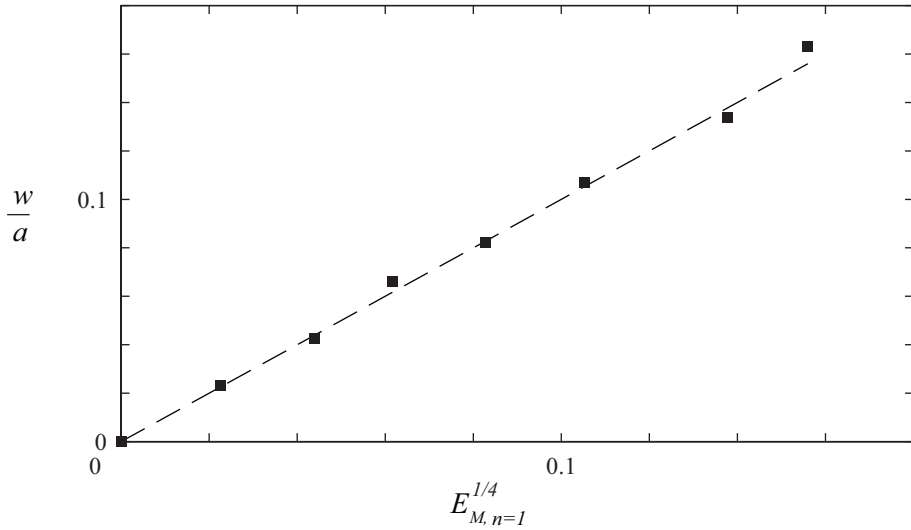$$\psi^* = \psi - \frac{n}{m} \int q(\psi_0) d\psi_0. \tag{7.7.4}$$

Figure 7.16: The normalized island width w/a as estimated from Poincaré plots compared to the quartic root of $E_{M,n=1}$, the normalized magnetic energy in the $n = 1$ Fourier harmonic.

For tearing modes this quantity can be nicely used to visualize the magnetic islands. In full MHD however this is no longer true. It turns out that at a given time in the tearing mode simulations the perturbed A_3 of the full MHD model is much larger than the perturbed ψ in the reduced MHD models. The other components A_R and A_Z of the magnetic vector potential grow along with A_3 to cancel part of the poloidal field associated with A_3. Neither the perturbed ψ relative to the equilibrium value nor the helical flux in this case are a measure of how much the magnetic topology is affected.

Instead we measure the island widths 'by hand' from Poincaré plots, the result of which is shown as a function of the quartic root of the perturbed magnetic energy $E_{M,n=1} = \frac{1}{2}B_{n=1}^2$ in Fig. 7.16. In reduced MHD, the island width is proportional to the square root of ψ^* so that the magnetic energy, which is proportional to the square of ψ^*, is proportional to the fourth power of the island width. From Fig. 7.16 the resulting scaling can been seen to hold well also in full MHD. Therefore we can from now on use the quartic root of the normalized magnetic energy as a measure of the island width.

The island width as a function of time is shown in Fig. 7.17. Since the magnetic energy is proportional to the square of the magnetic field, the island width initially grows with twice the linear growth rate. Actually this is the way that growth rates are typically calculated in JOREK:

$$E \sim e^{2\gamma t} \rightarrow \gamma = \frac{\ln\left(E_1/E_0\right)}{2(t_1 - t_0)}, \tag{7.7.5}$$

where for the energy E any quadratic quantity of a Fourier harmonic can be used.
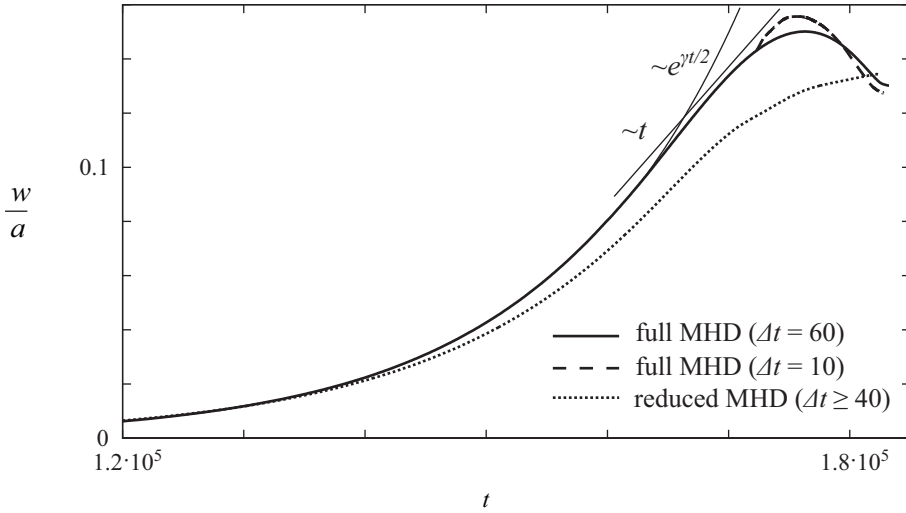
143

Figure 7.17: The normalized island width w/a as a function of time for the full and a reduced MHD model including a toroidal velocity. In contrast to the full MHD curve shown, the reduced MHD result allowed the $n = 0$ harmonic to evolve.

Using for example the kinetic energy $E_k = \frac{1}{2}\rho v^2$ or the magnetic energy $E_M = \frac{1}{2}B^2$ should give the same linear growth rate.

The island width initially grows with half the linear growth rate γ, as is shown in Fig. 7.17. After some time this exponential growth stalls and eventually the island width decreases again. Especially after increasing the time resolution, there seems to be a clear region in which the island width grows linearly in time, as in the so-called Rutherford regime. Note that in the full MHD simulations the $n = 0$ harmonic was kept fixed. Apparently there are also other mechanisms that make the tearing mode saturate besides a flattening of the $n = 0$ current density.

What is shown from the reduced MHD model in the figure is the island evolution when allowing the axisymmmetric component of all variables to evolve in time. To counteract resistive diffusion, the equilibrium current was subtracted from the current in the resistive term. Most of the $n = 0$ variables now do not significantly change in time. There is however a clear flattening of the temperature and density profiles. This is expected as a consequence of the changed magnetic topology.

The simulations were stopped when structures started to appear in the solution that were too small to resolve on the grid used. The final island sizes of both models compare quite well.
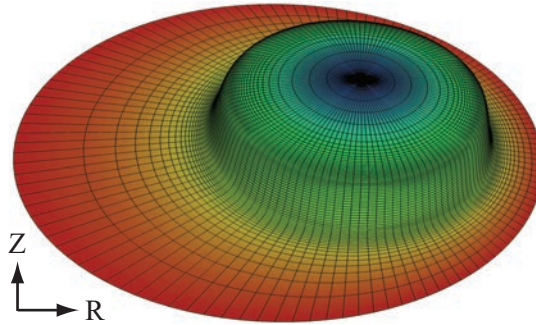
144

Figure 7.18:   A typical grid with radial grid accumulation. The height profile gives the equilibrium temperature, while the coloring denotes the equilibrium ψ.

7.7.3   Ballooning modes

As a final illustration we take a first look at the ballooning mode instability. A standardized set of equilibria to study these instabilities was developed by P. B. Snyder. Here we use the cbm18_dens8 equilibrium used for benchmarking NIMROD [24], M3D-C^1 [56], and BOUT++ [48, 217] against various linear stability codes.

We leave a full benchmark and a comparison with the reduced MHD model for future work, and present here the result for a single toroidal mode number $n = 12$. The growth rate for this case shows reasonable agreement with values reported in literature.

The equilibrium has an ideally conducting circular wall with an aspect ratio $\epsilon^{-1} = 3/2$. The density is constant, but the temperature profile has a strong H-mode-like pedestal gradient in a narrow layer. This profile is shown as an elevation in Fig. 7.18. The coloring denotes the equilibrium poloidal magnetic flux ψ and a typical computational mesh is shown. The peak value of β is approximately one percent. The safety factor profile ranges from around one on axis, to between two and three in the pedestal region, while continuing to grow to large values outside this region.

The large pressure gradient in combination with unfavorable magnetic field curvature at the low field side leads to an instability in which the plasma 'balloons' outwards. Many poloidal harmonics that are resonant on different rational q-values overlap to form structures that are dominant on the low-field side. The total perturbed $n = 12$ velocity and magnetic field are depicted in Fig. 7.19, showing the ballooning character of the mode and the strong radial and poloidal localization. Note how the structures get much more narrow near the high-field side where the local magnetic shear is higher.

Fig. 7.20 shows the perturbed density and plasma velocity at the low field side, revealing vortical structures of plasma motion. Note however the net plasma motion to the left of the figure, the top of the plasma. Because of symmetry in the top-bottom direction there should be an eigenmode with the exact same growth rate but with a
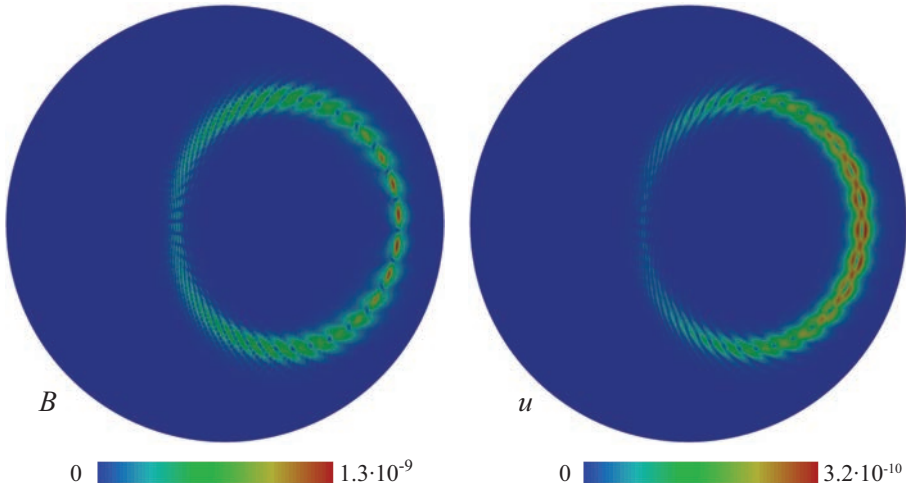
Figure 7.19: The magnitude of the perturbed $n = 12$ (a) velocity and (b) magnetic field.

net plasma motion towards the bottom of the plasma.

As was shown in Ref. [24] the linear instabilities of this equilibrium experience a significant kink drive, particularly impacting the smallest-n modes. The combination of external kink / peeling and ballooning effects is at the basis of Type-I ELMs.

7.8   Conclusions & Discussion

We presented an overview of our implementation of the full MHD equations in the finite element code JOREK. To ensure a divergence-free magnetic field we used a vector potential formulation. The resulting gauge freedom was used to set the electrostatic potential to zero. Small noise in the components of the magnetic vector potential was found to pollute the solutions of linear MHD instabilities. This problem was solved by projecting the momentum equation in a direction parallel to the magnetic field instead of in the toroidal direction. We identified a potential numerical problem with the grid axis, where many quadrilateral elements come together in one point. Additional conditions were derived that can be imposed on the coefficients of the basis functions to ensure regularity.

Various test cases based on analytical solutions were used to verify the implementation of the individual equations. Test cases with highly anisotropic diffusion showed that the same convergence as for isotropic diffusion can be obtained. This does not require the grid to be aligned with the magnetic field, as long as the grid is of good quality. This can be achieved by constructing the grid analytically or by accurate interpolation. The description of the magnetic field in terms of a stream function was shown to be essential for this good convergence.
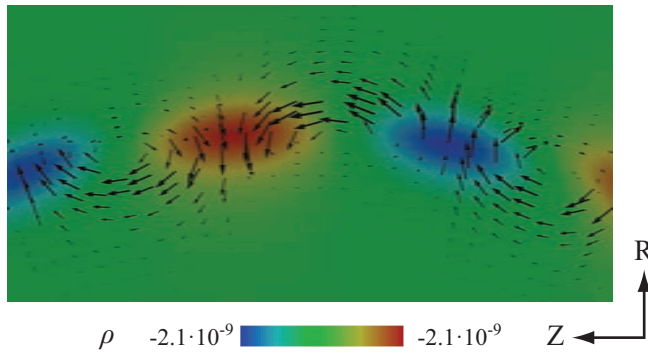
Figure 7.20: The perturbed $n = 12$ density at the low-field side together with the perturbed plasma velocity showing vortical structures with the same poloidal periodicity.

The complete system of full MHD equations was verified by studying what are arguably the three most important MHD instabilities in a tokamak: an internal kink mode, a tearing mode, and a ballooning mode. The resulting growth rates were successfully compared with the result from linear stability codes. Our implementation does not necessarily require a source of physical dissipation. Ballooning modes are driven by large pressure gradients and as such have a finite extended structure. These modes have been simulated without any resistivity, viscosity, or other diffusivity.

For the time integration, most often we used the Crank-Nicolson scheme. Sometimes the growth rate showed oscillations that could be effectively suppressed by switching to the L-stable BDF2 scheme,

The tearing mode simulations were extended into the nonlinear regime and a comparison was made with the reduced MHD models. For zero pressure, the reduced MHD models were found to be accurate in reproducing the full MHD growth rates. The inclusion of a toroidal velocity component was required to approach the full MHD growth rates when including a finite pressure. Only small differences remained.

By and large these tearing mode simulations confirm what has been long known from tearing mode research, namely that the reduced MHD model can give a reasonably accurate description of the predictions of the full MHD model. For other phenomena the differences between the two models can be much larger. With the present extension of JOREK to the full MHD model we now have the possibility to verify this.

Chapter 8

Summary

Magnetohydrodynamic Waves and Instabilities in Rotating Tokamak Plasmas

The effect of toroidal rotation on the equilibrium and the waves and instabilities in tokamak plasmas was investigated within the framework of magnetohydrodynamics (MHD). A comprehensive analysis was performed of the effects of toroidal plasma rotation on the low-frequency MHD spectrum of a large aspect ratio, low-beta, tokamak plasma with a circular cross-section. Continuum modes, waves, and instabilities were investigated both analytically and numerically.

We introduced an adiabatic constant of the equilibrium γ_e that may deviate from the dynamical adiabatic constant γ. All analytical results in this thesis hold for general γ_e. Analytical expressions were obtained for the continuum frequencies ω_- and ω_+ corresponding to zonal flow modes and geodesic acoustic modes, respectively. When $\gamma_e > \gamma$ the zonal flow modes acquire a finite Brunt-Väisälä frequency in the presence of toroidal rotation. For $\gamma_e < \gamma$ they become convectively unstable. The analytical results were successfully compared to the results from numerical simulations.

When modes have a significant component normal to the magnetic surfaces, profile variation in this direction can influence their existence and stability. A stability criterion was derived for localized modes. The terms in this criterion were interpreted in terms of well-known hydrodynamic and MHD instabilities.

A regime was identified in which toroidal rotation is stabilizing. This occurs when the flow shear is low enough to avoid the destabilizing Kelvin-Helmholtz effect but the rotation frequency squared decreases faster radially than the density so that the centrifugal Rayleigh-Taylor instability is avoided. The term that is responsible for this stabilization has the same form as that of the magnetorotational instability, but is of opposite sign and in a toroidal geometry is twice as large. It exists only for non-axisymmetric modes. The physical origin of this flow shear stabilization was elucidated as a Coriolis-pressure effect.

Close to when the derived stability criterion predicts *instability*, stable global modes

arise near the ω_+ frequency. These may be interpreted as the rotation-driven coun-
terpart of beta-induced Alfvén eigenmodes. In the absence of resistivity, global but
radially highly localized modes are present close to the ω_- frequency. These may be
interpreted as the non-axisymmetric counterparts of the axisymmetric zonal flows.

Close to when the stability criterion predicts *stability*, stable modes arise above
the ω_+ continuum frequency when the magnetic shear is reversed. Toroidal rotation
can make these reversed-shear Alfvén eigenmodes disappear through the Coriolis-
pressure effect when they move at a lower velocity than the plasma or propagate in
the opposite direction. The generality of the analysis also allows for the description
of downwards cascading modes that are sometimes observed, reversed-shear modes
above ω_-, and regular-shear modes below both ω_+ and ω_-.

Finally, the full viscoresistive MHD equations were implemented in the reduced-
MHD finite element code JOREK. With this code, it was found to be possible to sim-
ulate extremely anisotropic diffusion phenomena with high accuracy. This property
seems to be associated with the use of a magnetic vector potential to describe the mag-
netic field. Numerical pollution of the components of this magnetic vector potential
could be avoided by choosing a weak formulation in which the momentum equation
is projected in the direction parallel to the magnetic field rather than in the toroidal
direction. Conditions were derived to ensure regularity at the grid axis, where many
nodes can come together in one point. The implementation of the equations was thor-
oughly tested using both analytical solutions and benchmarks with MHD instabilities.
The linear growth rates of an internal kink mode, a tearing mode, and a ballooning
mode were used. The tearing mode evolution was followed well into the nonlinear
regime and the results were compared with those of the reduced MHD models. The
implemented equilibrium description allows for toroidal rotation with arbitrary γ_e.
This code will in the future allow further investigation of the nonlinear evolution of
MHD phenomena, also in the presence of toroidal rotation.

Chapter 9

Conclusions, Discussion, and Outlook

9.1 Conclusions

Detailed conclusions have been presented in the respective chapters of this thesis. Here we will return to the goals and research objectives that were formulated in section 1.4.1 and provide more global conclusions.

1. In a toroidally rotating equilibrium, in order to balance the centrifugal force, the pressure must vary within the magnetic surfaces. Due to the high thermal conductivity along the field lines, the magnetic surfaces of tokamak plasmas can typically be assumed to be isothermal. In the presence of significant poloidal flows however, isentropic magnetic surfaces may be more appropriate. A general equilibrium description of the thermodynamic state of the magnetic surfaces can be introduced to accommodate this, without the additional complications of actually including poloidal rotation and heat flow. See section 2.2.2.

2. A local stability criterion was derived that can be interpreted in terms of a combination of well-known hydrodynamic and MHD instabilities. See Eqs. (3.3.22), (3.5.2), or (4.1.1). Rotation effects enter as the square of the ratio between the kinetic energy density and the pressure. When the flow shear is large enough to overcome the centrifugal destabilization of a radially decreasing density profile, but small enough to avoid destabilization by the Kelvin-Helmholtz effect, a Coriolis-pressure effect can positively affect plasma stability. See chapter 4. For very fast rotation, the Brunt-Väisälä-effect can provide a further stabilizing influence.

3. Toroidal rotation can give the zonal flow continuum modes a finite 'Brunt-Väisälä-frequency' or make them convectively unstable. Analytical expressions

are provided in Eq. (2.5.26a). Non-axisymmetric zonal flow modes were found at approximately these frequencies as well, see section 5.2.4. New modes were found to be created, and well-known modes were found to be influenced by rotation in chapters 5 and 6 respectively. These changes to the MHD spectrum can potentially be used as a diagnostic for rotation.

4. The full viscoresistive nonlinear MHD equations have been implemented in the JOREK code. A formulation in terms of a magnetic vector potential allows for an accurate calculation of extremely anisotropic diffusion phenomena. The differences with reduced MHD models were found to be small for tearing mode simulations, but can be much larger for other phenomena.

9.2   Discussion

The continuity equation and the adiabatic energy equation of MHD are trivially satisfied for axisymmetric equilibria with purely toroidal rotation, and therefore do not impose any constraints. The slightest amount of poloidal rotation, however, dictates that the magnetic surfaces should be isentropic. Such a discontinuous change in the solutions often indicates something is missing from the model. Including thermal diffusion, a more physical picture arises. Poloidal advection of entropy competes with thermal diffusion over the thermodynamic state of the magnetic surfaces. A back-of-the-envelope calculation shows that in a tokamak this competition is not a-priori decided in favor of either of these effects. The sizable poloidal flows that can occur, in particular near the edge of H-mode plasmas, can cause significant deviations from isothermality of the magnetic surfaces. The generality offered by the introduction of a separate adiabatic constant for the equilibrium and the dynamics allows the modeler to decide which of these processes is more important. These adiabatic 'constants' do not even have to be constant and can assume different values on different magnetic surfaces. In this way, aspects of poloidal flows and thermal transport can be taken into account without introducing significant additional complexity to the model. Of course, the full implications of poloidal flow can only be taken into account by including it as an integral part of the equilibrium description.

There may be some concern about whether the introduction of two adiabatic constants does not alter the mathematical structure of the model in such a way that the resulting stability analysis becomes invalid. The use of a different set of equations for the equilibrium and the subsequent stability analysis is for example not guaranteed to give an energy principle in general. Luckily in our case it can be shown that the force operator remains self-adjoint so that the stability analysis still has a solid mathematical basis.

For the localized modes that are studied in detail in this thesis, rotation primarily influences stability through the interchange contribution that arises due to the magnetic field curvature. The proportionality with q^2 in Eq. (3.3.15) seems to indicate that

the modifications of toroidal rotation act only through the *toroidal* field curvature. This may be in part due to an actual change in this curvature, caused by the effect of the centrifugal force on the equilibrium force balance. This can for example explain why the kinetic energy density is effectively subtracted from the pressure in the stability criterion. Part of the rotation-induced toroidal curvature terms can, however, only be explained by reconsidering the dynamics of the perturbations. This is the case, for example, for the Coriolis-pressure term.

Under normal tokamak conditions the Coriolis-pressure effect constitutes one of the very few stabilizing influences of toroidal rotation in MHD. The stabilizing convective effect only becomes significant for very high rotation. The flow-shear stabilization that was previously found for ballooning modes [199, 214] becomes important only for high β and high mode numbers. This effect is missing from our analysis because of our low-beta ordering $\beta \sim \epsilon^2$. In the analyses of this thesis we also did not take into account the toroidal coupling between poloidal Fourier harmonics, which is required for the description of such effects.

Many of the assumptions that have to be made in mathematical analyses can be avoided in numerical simulations, like those performed in chapter 7. The implemented extension of the JOREK code to the full MHD equations will allow tests of whether the assumptions made in the reduced MHD models lead to significant deviations from the predictions of the full MHD model. In its turn, the full MHD equations may be extended with a variety of additional effects to investigate their influence on the predictions made by MHD.

9.3 Outlook

Depending on the profiles for the rotation and the density, rotation can be destabilizing or stabilizing through the centrifugal Rayleigh-Taylor or Coriolis-pressure effect respectively. In the core of a rotating tokamak plasma, the influence of these effects can perhaps be inferred from internal kink mode stability data. It may however turn out to be easier to single out the effects of rotation in the data of stable modes like reversed-shear Alfvén eigenmodes. The analysis of chapter 6 in particular leads to predictions that should be experimentally verifiable.

The kind of analyses performed in this thesis should in principle still be possible when besides toroidal rotation also poloidal rotation is included. The influence of poloidal rotation on the continuous spectrum was investigated in Refs. [67, 130, 52]. A mode equation valid for non-continuum modes, including the effects of both poloidal and toroidal rotation, still has to be derived however.

It would be very interesting to investigate experimentally how the temperature over a magnetic surface varies as a function of poloidal and toroidal rotation. This can provide information on the equilibrium adiabatic constant. Also numerical experiments can provide insight in this matter. The implementation of the full MHD equations into the JOREK code described in this thesis is very well suited for this

purpose.

This implementation still allows for various generalizations and extensions. The isotropic viscous stress tensor may be replaced by formulations that are more appropriate for highly anisotropic tokamak plasmas. Various other extensions like an anisotropic pressure, two-fluid effects, or neoclassical and diamagnetic terms can also be considered.

Acknowledgements

List of Publications

Chapters 2-7 are adapted from the following journal publications:

- J. W. Haverkort, H. J. de Blank, and B. Koren. Low-frequency Alfvén gap modes in rotating tokamak plasmas. *Plasma Phys. Control. Fusion.*, 53:045004, 2011

- J. W. Haverkort and H. J. de Blank. Local stability of rotating tokamak plasmas. *Plasma Phys. Control. Fusion*, 53:045008, 2011

- J. W. Haverkort, H. J. de Blank, and B. Koren. The Brunt-Väisälä frequency of rotating tokamak plasmas. *J. Comp. Phys.*, 231:981–1001, 2012

- J. W. Haverkort. The effect of toroidal plasma rotation on low-frequency reversed shear Alfvén eigenmodes in tokamaks. *Plasma Phys. Control. Fusion*, 54:025005, 2012

- J. W. Haverkort and H. J. de Blank. Flow shear stabilization of rotating plasmas due to the Coriolis effect. *Physical Review E*, 86(1):016411, 2012

- J. W. Haverkort, G. T. A. Huysmans, H. J. de Blank, J. Pratt, E. V. van der Plas, B. Nkonga, and B. Koren. Implementation and verification of the nonlinear viscoresistive full magnetohydrodynamic equations in the JOREK code. *To be submitted to J. Comp. Phys.*, 2013

Curriculum Vitae

On the tenth of January 1984 I was born in Ruhengeri, Rwanda. I grew up in Wageningen, the Netherlands, where I went to primary and secondary school. For my university education I moved to Delft, the Netherlands. Here I completed my bachelor's and master's degree in Applied Physics with honors. During my master's phase I completed an honors track in theoretical physics, primarily consisting of courses taught at the University of Amsterdam.

During an internship at Corus, now Tata Steel, I developed an interest in magnetohydrodynamics. I investigated the influence of magnetic fields on insulating bubbles and inclusions in liquid steel. My graduation research consisted of the analysis and simulation of a technique in which drugs attached to magnetized particles can be specifically targeted using magnetic fields. These projects resulted in four journal publications. For my graduation work I received the Unilever Research Prize and the VerDelFT "best thesis" award.

On the first of February 2009, I started the PhD research for this thesis. I have been employed by the FOM Institute for Plasma Physics Rijnhuizen, which in 2012 changed its name to the Dutch Institute For Fundamental Energy Research, DIFFER. During the four years of this PhD research I have been seconded at the Centrum Wiskunde & Informatica (CWI) in Amsterdam.

Bibliography

[1] D. J. Acheson. Hydromagnetic wavelike instabilities in a rapidly rotating stratified fluid. *J. Fluid Mech.*, 61:609–624, 1973.

[2] J. Andries. The eigenfrequency spectrum of linear magnetohydrodynamic perturbations in stationary equilibria: A variational principle. *Phys. Plasmas*, 17:112106, 2010.

[3] K. Appert, R. Gruber, F. Troyon, and J. Vaclavik. Excitation of global eigenmodes of the Alfvén wave in tokamaks. *Plasma Phys.*, 24:1147, 1982.

[4] C. V. Atanasiu, S. Günter, K. Lackner, and I. G. Miron. Analytical solutions to the Grad-Shafranov equation. *Phys. Plasmas*, 11(7):3510–3518, 2004.

[5] K. Avinash, S. N. Bhattacharyya, and B. J. Green. Axisymmetric toroidal equilibrium with incompressible flows. *Plasma Phys. Controlled Fusion*, 11(4):465–473, 1992.

[6] S. A. Balbus and J. F. Hawley. A powerful local shear instability in weakly magnetized disks. I. Linear analysis. *Astrophys. J.*, 376:214–222, 1991.

[7] R. M. Beam and R. F. Warming. Alternating direction implicit methods for parabolic equations with a mixed derivative. *SIAM J. Sci. Stat. Comput.*, 1(1):131–159, 1980.

[8] A. J. C. Beliën, M. A. Botchev, J. P. Goedbloed, B. van der Holst, and R. Keppens. FINESSE: Axisymmetric MHD equilibria with flow. *J. Comp. Phys.*, 11(182):91–117, 2002.

[9] C. M. Bender and S. A. Orszag. *Advanced Mathematical Methods for Scientists and Engineers*. McGraw-Hill, 1978.

[10] D. Berger, L. C. Bernard, R. Gruber, and F. Troyon. Numerical study of the unstable MHD spectrum of a small aspect ratio, flat current, non-circular tokamak. *J. Appl. Math. Phys.*, 31:113–132, 1980.

[11] H. L. Berk, D. N. Borba, B. N. Breizman, S. D. Pinches, and S. E. Sharapov. Theoretical interpretation of Alfvén cascades in tokamaks with nonmonotonic q profiles. *Phys. Rev. Lett.*, 87:185002, 2001.

[12] I. B. Bernstein, E. A. Frieman, M. D. Kruskal, and R. M. Kulsrud. An energy principle for hydromagnetic stability problems. *Proc. Roy. Soc. London*, 244:17–40, 1958.

[13] A. Bhattacharjee, R. Iacono, J. L. Milovich, and C. Paranicas. Ballooning stability of axisymmetric plasmas with sheared equilibrium flows. *Phys. Fluids B*, 11:2207–2212, 1989.

[14] J. W. S. Blokland, R. Keppens, and J. P. Goedbloed. Unstable magnetohydrodynamical continuous spectrum of accretion disks. *Astronomy Astrophys.*, 467:21–35, 2007.

[15] J. W. S. Blokland, B. van der Holst, R. Keppens, and J. P. Goedbloed. PHOENIX: MHD spectral code for rotating laboratory and gravitating astrophysical plasmas. *J. Comp. Phys.*, 226:509–533, 2007.

[16] J. W. S. Blokland, E. van der Swaluw, R. Keppens, and J. P. Goedbloed. Magneto-rotational overstability in accretion disks. *Astronomy Astrophys.*, 444:337–346, 2005.

[17] A. Bondeson and R. Iacono. Ideal stability of cylindrical plasma in the presence of mass flow. *Phys. Fluids B*, 1:1431, 1989.

[18] A. Bondeson, R. Iacono, and A. Bhattacharjee. Local magnetohydrodynamic instabilities of cylindrical plasma with sheared equilibrium flows. *Phys. Fluids*, 30:2167, 1987.

[19] I. G. J. Classen J. E. Boom, W. Suttrop, E. Schmid, B. Tobias, et al. 2D electron cyclotron emission imaging at ASDEX upgrade. *Rev. Sc. Instr.*, 81:10D929, 2010.

[20] B. N. Breizman, H. L. Berk, M. S. Pekker, S. D. Pinches, and S. E. Sharapov. Theory of Alfvén eigenmodes in shear reversed plasmas. *Phys. Plasmas*, 10:3649–3660, 2003.

[21] B. N. Breizman and M. S. Pekker. Plasma pressure effects on Alfvén cascade eigenmodes. *Phys. Plasmas*, 12:112506, 2005.

[22] B. N. Breizman and S. E. Sharapov. Major minority: energetic particles in fusion plasmas. *Plasma Phys. Controll. Fusion*, 53:054001, 2011.

[23] J. Breslau, N. Ferraro, and S. Jardin. Some properties of the M3D-C^1 form of the three-dimensional magnetohydrodynamics equations. *Phys. Plasmas*, 16:092503, 2009.

[24] B. J. Burke, S. E. Kruger, C. C. Hegna, P. Zhu, P. B. Snyder, C. R. Sovinec, and E. C . Howell. Edge localized linear ideal magnetohydrodynamic instability studies in an extended-magnetohydrodynamic code. *Phys. Plasmas*, 17:032103, 2010.

[25] M. N. Bussac and R. Pellat. Internal kink modes in toroidal plasmas with circular cross sections. *Phys. Rev. Lett.*, 35:1638–1641, 1975.

[26] A. J. Cerfon and J. P. Freidberg. "One size fits all" analytic solutions to the Grad-Shafranov equation. *Phys. Plasmas*, 17:032502, 2010.

[27] S. Chandrasekhar. The stability of non-dissipative Couette flow in hydromagnetics. *Proc. Nat. Ac. Sc.*, 46:253–257, 1960.

[28] I. T. Chapman, T. C. Hender, S. Saarelma, S. E. Sharapov, R. J. Akers, et al. The effect of toroidal plasma rotation on sawteeth in MAST. *Nucl. Fusion*, 46:1009–1016, 2006.

[29] I. T. Chapman, M. D. Hua, S. D. Pinches, R. J. Akers, A. R. Field, et al. Saturated ideal modes in advanced tokamak regimes in MAST. *Nucl. Fusion*, 50:045007, 2010.

[30] I. T. Chapman, S. D. Pinches, J. P. Graves, R. J. Akers, C. Appel, et al. The physics of sawtooth stabilization. *Plasma. Phys. Controlled Fusion*, 49:B358, 2007.

[31] I. T. Chapman, S. D. Pinches, H. R. Koslowski, Y. Liang, A. Krämer-Flecken, et al. Sawtooth stability in neutral beam heated plasmas in TEXTOR. *Nucl. Fusion*, 48:035004, 2008.

[32] L. A. Charlton, R. .J. Hastie, and T. C. Hender. Resistive "infernal" modes. *Phys. Fluids B*, 1:798, 1989.

[33] L. A. Charlton, J. .A. Holmes, H. R. Hicks, V. E. Lynch, and B. A. Carreras. Numerical calculations using the full MHD equations in toroidal geometry. *J. Comp. Phys*, 63:107–129, 1986.

[34] C. Z. Cheng and M. S. Chance. Low-n shear Alfvén spectra in axisymmetric toroidal plasmas. *Phys. Fluids*, 29(11):3695, 1986.

[35] M. S. Chu. Shear flow destabilization of a slowly rotating tokamak. *Phys. Plasmas*, 5(1):183, 1998.

[36] M. S. Chu, J. M. Greene, L. L. Lao, A. D. Turnbull, and M. S. Chance. A numerical study of the high-n shear Alfvén spectrum gap and the high-n gap mode. *Phys. Fluids B*, 4:3713–3721, 1992.

[37] M. S. Chu and M. Okabayashi. Stabilization of the external kink and the resistive wall mode. *Plasma Phys. Controlled Fusion*, 52:123001, 2010.

[38] A. Chupin and R. Stepanov. Full perturbation solution for the flow in a rotating torus. *Phys. Rev. E*, 77:057301, 2008.

[39] R. A. Clemente and R. Farengo. A class of rotating compact tori equilibria. *Phys. Fluids*, 27(4):776–778, 1984.

[40] J. W. Connor, R. J. Hastie, and A. J. Webster. A destabilizing effect of rotation shear on magnetohydrodynamic ballooning modes. *Phys. Plasmas*, 14:044504, 2007.

[41] W. A. Cooper and S. P. Hirshman. Axisymmetric MHD equilibria with isothermal toroidal mass flow by variational steepest descent method. *Plasma Phys. Controlled Fusion*, 29:933–943, 1987.

[42] T. G. Cowling. The condition for turbulence in rotating stars. *Astrophys. J.*, 114:272–286, 1951.

[43] O. Czarny and G. Huysmans. Bézier surfaces and finite elements for MHD simulations. *J. Comp. Physics*, 227:7423–7445, 2008.

[44] G. G. Dahlquist. A special stability problem for linear multistep methods. *BIT Num. Math.*, 3:27–43, 1963.

[45] N. D'Angelo and S. V. Goeler. Investigation of the Kelvin-Helmholtz instability in a cesium plasma. *Phys. Fluids*, 9:309, 1966.

[46] H. J. de Blank. *Theory of the m=1 kink mode in toroidal plasmas*. PhD thesis, Utrecht University, 1990.

[47] B. D. Dudson, M. V. Umansky, X. Q. Xu, P. B. Snyder, and H. R. Wilson. BOUT++: A framework for parallel plasma fluid simulations. *Comp. Phys. Comm.*, 180:1467–1480, 2009.

[48] B. D. Dudson, X. Q. Xu, M. V. Umansky, H. R. Wilson, and P. B. Snyder. Simulation of edge localized modes using BOUT++. *Plasma Phys. Contr. Fusion*, 53:054005, 2011.

[49] E. M. Edlund, M. Porkolab, G. J. Kramer, L. Lin, Y. Lin, N. Tsujii, and S. J. Wukitch. Experimental study of reversed shear Alfvén eigenmodes during the current ramp in the Alcator C-Mod tokamak. *Plasma Phys. Control. Fusion*, 52:115003, 2010.

[50] E. M. Edlund, M. Porkolab, G. J. Kramer, L. Lin, Y. Lin, and S. J. Wukitch. Observation of reversed shear Alfvén eigenmodes between sawtooth crashes in the Alcator C-Mod tokamak. *Phys. Rev. Lett.*, 102:165003, 2009.

[51] E. M. Edlund, M. Porkolab, G. J. Kramer, L. Lin, Y. Lin, and S. J. Wukitch. Phase contrast imaging measurements of reversed shear Alfvén eigenmodes during sawteeth in alcator c-mod. *Phys. Plasmas*, 16:056106, 2009.

[52] A. G. Elfimov, R. M. O. Galvão, and R. J. F. Sgalla. Rotation effect on geodesic and zonal flow modes in tokamak plasmas with isothermal magnetic surfaces. *Plasma Phys. Control. Fusion*, 53:105003, 2011.

[53] K. Elsasser and A. Heimsoth. Axisymmetric plasma equilibria with incompressible flow. *Zeitschr. Naturforsch. A*, 41(7):883–896, 1986.

[54] N. M. Ferraro and S. C. Jardin. Calculations of two-fluid magnetohydrodynamic axisymmetric steady-states. *J. Comp. Phys.*, 228:7742–7770, 2009.

[55] N. M. Ferraro, S. C. Jardin, and X. Luo. Essential boundary conditions with straight C^1 finite elements in curved domains. Technical Report PPPL-4497, PPPL, Feb. 2010.

[56] N. M. Ferraro, S. C. Jardin, and P. B. Snyder. Ideal and resistive edge stability calculations with M3D-C^1. *Phys. Plasmas*, 17:102508, 2010.

[57] E. D. Fredrickson, N. A. Crocker, N. N. Gorelenkov, W. W. Heidbrink, S. Kubota, et al. β suppression of Alfvén cascade modes in the national spherical torus experiment. *Phys. Plasmas*, 14:102510, 2007.

[58] E. Frieman and M. Rotenberg. On hydromagnetic stability of stationary equilibria. *Rev. Mod. Phys.*, 32(4):898–902, 1960.

[59] G. Y. Fu and H. L. Berk. Effects of pressure gradient on existence of Alfvén cascade modes in reversed shear tokamak plasmas. *Phys. Plasmas*, 13:052502, 2006.

[60] M. Furukawa and S. Tokuda. Mechanism of stabilization of ballooning modes by toroidal rotation shear in tokamaks. *Phys. Rev. Lett.*, 94:175001, 2005.

[61] M. Furukawa, Z. Yoshida, M. Hirota, and V. Krishan. MHD stability in flowing plasmas: Connection between fusion plasma and astrophysics research. *Plasma Fusion Res.*, 2:016, 2007.

[62] X. Garbet, C. Fenzi, H. Capes, P. Devynck, and G. Antar. Kelvin-Helmholtz instabilities in tokamak edge plasmas. *Phys. Plasmas*, 6:3955, 1999.

[63] J. P. Goedbloed. Generalization of Suydam's criterion. *Phys. Fluids*, 16(11):1927, 1973.

[64] J. P. Goedbloed. Spectrum of ideal magnetohydrodynamics of axisymmetric toroidal systems. *Phys. Fluids*, 18(10):1258–1268, 1975.

[65] J. P. Goedbloed. Some remarks on computing axisymmetric equilibria. *Comp. Phys. Comm.*, 31:123–135, 1984.

[66] J. P. Goedbloed. New construction of the magnetohydrodynamic spectrum of stationary plasma flows. I. solution path and alternator. *Phys. Plasmas*, 16:122110, 2009.

[67] J. P. Goedbloed, A. J. C. Beliën, B. van der Holst, and R. Keppens. Unstable continuous spectra of transonic axisymmetric plasmas. *Phys. Plasmas*, 11:28–54, 2004.

[68] J. P. Goedbloed, H. A. Holties, S. Poedts, G. T. A. Huysmans, and W. Kerner. MHD spectroscopy: free boundary modes (ELMs) and external excitation of TAE modes. *Plasma Phys. Control. Fusion*, 35:B277, 1993.

[69] J. P. Goedbloed, R. Keppens, and S. Poedts. *Advanced Magnetohydrodynamics*. Cambridge University Press, 2010.

[70] J. P. Goedbloed and S. Poedts. *Principles of Magnetohydrodynamics*. Cambridge University Press, 2004.

[71] J. P. Goedbloed and P. H. Sakanaka. New approach to magnetohydrodynamic stability: I. a practical stability concept. *Phys. Fluids*, 17(5):908–918, 1974.

[72] N. N. Gorelenkov. Double-gap Alfvén eigenmodes. *Phys. Rev. Lett.*, 95:265003, 2005.

[73] N. N. Gorelenkov. Existence of weakly damped kinetic Alfvén eigenmodes in reversed shear tokamak plasmas. *Phys. Plasmas*, 15:110701, 2008.

[74] N. N. Gorelenkov, H. L. Berk, E. Fredrickson, S. E. Sharapov, and JET EFDA Contributors. Predictions and observations of low-shear beta-induced shear Alfvén-acoustic eigenmodes in toroidal plasmas. *Phys. Lett. A*, 370:70, 2007.

[75] N. N. Gorelenkov, G. J. Kramer, and R. Nazikian. Interpretation of the finite pressure gradient effects in the reversed shear Alfén eigenmode theory. *Plasma Phys. Control. Fusion*, 48:1255–1269, 2006.

[76] H. Grad. Magnetofluid-dynamic spectrum and low shear stability. *Proc. Nat. Acad. Sci. USA*, 70:3277, 1973.

[77] H. Grad and H. Rubin. *Proceedings of the Second United Nations Conference on the Peaceful Uses of Atomic Energy*, 21:190–197, 1958.

[78] P. M. Gresho and R. L. Sani. *Incompressible flow and the finite element method*. Wiley & Sons, 2000.

[79] R. C. Grimm, R. L. Dewar, and J. Manickam. Ideal MHD stability calculations in axisymmetric toroidal coordinate systems. *J. Comp. Phys.*, 49:94–117, 1983.

[80] M. P. Gryaznevich, S. E. Sharapov, M. Lilley, S. D. Pinches, and A. R. Field. Recent experiments on Alfvén eigenmodes in MAST. *Nucl. Fusion*, 48:084003, 2008.

[81] L. Guazzotto, R. Betti, J. Manickam, and S. Kaye. Numerical study of tokamak equilibria with arbitrary flow. *Phys. Plasmas*, 11:604, 2004.

[82] L. Guazzotto and J. P. Freidberg. A family of analytic equilibrium solutions for the Grad-Shafranov equation. *Phys. Plasmas*, 14:112508, 2007.

[83] S. Gupta, J. D. Callen, and C. C. Hegna. Violating Suydam criterion produces feeble instabilities. *Phys. Plasmas*, 9:3395, 2002.

[84] K. Hallatschek. Condensation of microturbulence-generated shear flows into global modes. *Phys. Rev. Lett.*, 84:5145, 2000.

[85] E. Hameiri. *The Stability of a Particular MHD Equilibrium with Flow*. PhD thesis, New York University, 1976.

[86] E. Hameiri. Spectral estimates, stability conditions, and the rotating screw-pinch. *J. Math. Phys.*, 22:2080, 1981.

[87] E. Hameiri. The equilibrium and stability of rotating plasmas. *Phys. Fluids*, 26:230–237, 1983.

[88] E. Hameiri and P. Laurence. The ballooning spectrum of rotating plasmas. *J. Math. Phys.*, 25:396, 1984.

[89] A. B. Hassam. Nonlinear stabilization of the Rayleigh-Taylor instability by external velocity shear. *Phys. Fluids B*, 4:485, 1992.

[90] J. W. Haverkort. The effect of toroidal plasma rotation on low-frequency reversed shear Alfvén eigenmodes in tokamaks. *Plasma Phys. Control. Fusion*, 54:025005, 2012.

[91] J. W. Haverkort and H. J. de Blank. Local stability of rotating tokamak plasmas. *Plasma Phys. Control. Fusion*, 53:045008, 2011.

[92] J. W. Haverkort and H. J. de Blank. Flow shear stabilization of rotating plasmas due to the Coriolis effect. *Physical Review E*, 86(1):016411, 2012.

[93] J. W. Haverkort, H. J. de Blank, and B. Koren. Low-frequency Alfvén gap modes in rotating tokamak plasmas. *Plasma Phys. Control. Fusion.*, 53:045004, 2011.

[94] J. W. Haverkort, H. J. de Blank, and B. Koren. The Brunt-Väisälä frequency of rotating tokamak plasmas. *J. Comp. Phys.*, 231:981–1001, 2012.

[95] J. W. Haverkort, G. T. A. Huysmans, H. J. de Blank, J. Pratt, E. V. van der Plas, B. Nkonga, and B. Koren. Implementation and verification of the nonlinear viscoresistive full magnetohydrodynamic equations in the JOREK code. *To be submitted to J. Comp. Phys.*, 2013.

[96] C. C. Hegna. Linear resistive layer equations in the presence of sheared toroidal rotation. Technical Report UW-CPTC 03-5, Center for Plasma Theory and Computation, University of Wisconsin-Madison, Dec. 2003.

[97] W. W. Heidbrink. Basic physics of Alfvén instabilities driven by energetic particles in toroidally confined plasmas. *Phys. Plasmas*, 15:055501, 2008.

[98] W. W. Heidbrink, E. J. Strait, M. S. Chu, and A. D. Turnbull. Observation of beta-induced Alfvén eigenmodes in the DIII-D tokamak. *Phys. Rev. Lett.*, 71(6):855, 1993.

[99] W. W. Heidbrink, M. A. van Zeeland, M. E. Austin, K. H. Burrell, and N. N. Gorelenkov. Central flattening of the fast-ion profile in reversed-shear DIII-D discharges. *Nucl. Fusion*, 48:084001, 2008.

[100] C. Helzel, J. A. Rossmanith, and B. Taetz. An unstaggered constrained transport method for the 3D ideal magnetohydrodynamic equations. *J. Comp. Phys.*, 230:38303–3829, 2011.

[101] P. Hénon, P. Ramet, and J. Roman. On finding approximate supernodes for an efficient block-ILU(k) factorization. *Parallel Computing*, 34(6):345–362, 2008.

[102] F. Herrnegger. On the equilibrium and stability of the belt pinch. *Proc. 5th Europ. Conf. Controlled Fusion Plasma Phys.*, 1:26, 1972.

[103] M. J. M. Hill. On a spherical vortex. *Phyl. Trans. Roy. Soc. London. A*, 185:213–245, 1894.

[104] R. Hollerbach and G. Rüdiger. New type of magnetorotational instability in cylindrical Taylor-Couette flow. *Phys. Rev. Lett.*, 95:124501, 2005.

[105] R. Hollerbach, V. Teeluck, and G. Rüdiger. Nonaxisymmetric magnetorotational instabilities in cylindrical Taylor-Couette flow. *Phys. Rev. Lett.*, 104:044502, 2010.

[106] M. Hölzl, S. Günter, R. P. Wenninger, W. C. Müller, G. T. A. Huysmans, et al. Reduced-magnetohydrodynamic simulations of toroidally and poloidally localized edge localized modes. *Phys. Plasmas*, 19(8):082505–082505, 2012.

[107] L. N. Howard and A. S. Gupta. On the hydrodynamic and hydromagnetic stability of swirling flows. *J. Fluid Mech.*, 14:463–476, 1962.

[108] Y. M. Huang and A. B. Hassam. Velocity shear stabilization of centrifugally confined plasma. *Phys. Rev. Lett.*, 87:235002, 2001.

[109] G. T. A. Huysmans. ELMs: MHD instabilities at the transport barrier. *Plasma Phys. Controll. Fusion*, 47:B165–B178, 2005.

[110] G. T. A. Huysmans. External kink (peeling) modes in x-point geometry. *Plasma Phys. Controll. Fusion*, 47:2107–2121, 2005.

[111] G. T. A. Huysmans. Implementation of an iterative solver in the non-linear MHD code JOREK. Technical report, ANR, 2006.

[112] G. T. A. Huysmans. MHD stability in X-point geometry: simulation of ELMs. *Nuclear Fusion*, 47:659–666, 2007.

[113] G. T. A. Huysmans, R. Abgrall, M. Becoulet, R. Huart, B. Nkonga, et al. Non-linear MHD simulations of ELMs. *35rd EPS Conference on Plasma Physics*, 32D:2.065, 2008.

[114] G. T. A. Huysmans, S. Pamela, E. van der Plas, and P. Ramet. Non-linear MHD simulations of edge localized modes (ELMs). *Plasma Phys. Controll. Fusion*, 51:124012, 2009.

[115] V. I. Ilgisonis, I. V. Khalzov, and A. I. Smolyakov. Negative energy waves and MHD stability of rotating plasmas. *Nucl. Fusion*, 49:035008, 2009.

[116] E. L. Ince. *Ordinary Differential Equations*. Dover Publications Inc., 1956.

[117] D. L. Jassby. Transverse velocity shear instabilities within a magnetically confined plasma. *Phys. Fluids*, 15:1590, 1972.

[118] R. Keppens and J. W. S. Blokland. Computing ideal magnetohydrodynamic equilibria. *Trans. Fusion Sc. Techn.*, 49:131–138, 2006.

[119] R. Keppens, F. Casse, and J. P. Goedbloed. Waves and instabilities in accretion discs: Magnetohydrodynamic spectroscopic analysis. *Astrophys. J.*, 569:L121–L126, 2002.

[120] W. Kerner, J. P. Goedbloed, G. T. A. Huysmans, S. Poedts, and E. Schwarz. CASTOR: Normal-mode analysis of resistive MHD plasmas. *J. Comp. Phys.*, 142:271–303, 1998.

[121] W. Kerner and O. Jandl. Axisymmetric MHD equilibria with flow. *Comp. Phys. Comm.*, 31:269–285, 1984.

[122] W. Kerner and S. Tokuda. Computation of tokamak equilibria with steady flow. *Zeitschr. Naturforsch. A*, 42:1154–1166, 1987.

[123] I. V. Khalzov, A. I. Smolyakov, and V. I. Ilgisonis. Energy of eigenmodes in magnetohydrodynamic flows of ideal fluids. *Phys. Plasmas*, 15:054501, 2008.

[124] A. H. Khater and S. M. Moawad. Exact solutions for axisymmetric nonlinear magnetohydrodynamic equilibria of aligned magnetic field and plasma flow with applications to astrophysics and plasma confinement devices. *Phys. Plasmas*, 16:052504, 2009.

[125] H. Kimura et al. Alfvén eigenmode and energetic particle research in JT-60U. *Nucl. Fusion*, 38:1303–1314, 1998.

[126] G. J. Kramer, N. N. Gorelenkov, R. Nazikian, and C. Z. Cheng. Finite pressure effects on reversed shear Alfvén eigenmodes. *Plasma Phys. Control. Fusion*, 46:L23–L29, 2004.

[127] G. J. Kramer, R. Nazikian, B. Alper, M. de Baar, H. L. Berk, et al. Interpretation of core localized Alfvén eigenmodes in DIII-D and Joint European Torus reversed magnetic shear plasmas. *Phys. Plasmas*, 13:056104, 2006.

[128] R. J. La Haye et al. Islands in the stream: The effect of plasma flow on tearing stability. *Phys. Plasmas*, 17:056110, 2010.

[129] C. S. Lai and M. Verleun. An exact solution for toroidal plasma in equilibrium. *Phys. Fluids*, 19(7):1066–1067, 1976.

[130] V. P. Lakhin and V. I. Ilgisonis. Continuum modes in rotating plasmas: General equations and continuous spectra for large aspect ratio tokamaks. *Phys. Plasmas*, 18:092103, 2011.

[131] V. P. Lakhin, V. I. Ilgisonis, and A. I. Smolyakov. Geodesic acoustic modes and zonal flows in toroidally rotating tokamak plasmas. *Phys. Lett. A*, 374:4872–4875, 2010.

[132] V. P. Lakhin and E. P. Velikhov. Instabilities of highly-resistive rotating liquids in helical magnetic fields. *Phys. Lett. A*, 369:98–106, 2007.

[133] L. L. Lao. Variational moment method for computing magnetohydrodynamic equilibria. *Comp. Phys. Comm.*, 31:201–212, 1984.

[134] B. Levitt. Excitation of the centrifugally driven interchange instability in a plasma confined by a magnetic dipole. *Phys. Plasmas*, 12:055703, 2005.

[135] R. V. E. Lovelace. Rossby wave instability of Keplerian accretion disks. *Astroph. J.*, 513:805–810, 1999.

[136] H. Lütjens, A. Bondeson, and A. Roy. Axisymmetric MHD equilibrium solver with bicubic Hermite elements. *Comp. Phys. Comm.*, 69:287–298, 1992.

[137] H. Lütjens and J.-F. Luciani. The XTOR code for nonlinear 3D simulations of MHD instabilities in tokamak plasmas. *J. Comp. Phys.*, 227:6944–6966, 2008.

[138] H. Lütjens and J.-F. Luciani. XTOR-2F: a fully implicit Newton-Krylov solver applied to nonlinear 3D extended MHD in tokamaks. *J. Comp. Phys.*, 229:8130–8143, 2010.

[139] D. Lynden-Bell and J. P. Ostriker. On the stability of differentially rotating bodies. *Mon. Not. R. astr. Soc.*, 136:293–310, 1967.

[140] J. Manickam, N. Pomphrey, and A. M. M. Todd. Ideal MHD stability properties of pressure driven modes in low shear tokamaks. *Nuclear Fusion*, 27:1461, 1987.

[141] F. Masaru, N. Yuji, H. Satoshi, and W. Masahiro. Tokamak equilibria with toroidal flows. *J. Plasma Fusion Res.*, 76:937–948, 2000.

[142] E. K. Maschke. Exact solutions of the MHD equilibrium equation for a toroidal plasma. *Plasma Phys.*, 15:535–541, 1973.

[143] E. K. Maschke and H. Perrin. Exact analytic solution of the stationary M.H.D. equilibrium equation of a toroidal plasma in rotation. *Plasma Phys.*, 22:579, 1980.

[144] P. J. Mc Carthy. Analytical solutions to the Grad-Shafranov equation for tokamak equilibrium with dissimilar source functions. *J. Plasma Fusion Res.*, 6:937–948, 1999.

[145] C. Mercier. Un critère nécessaire de stabilité hydromagnétique pour un plasma en symétrie de révolution. *Nuclear Fusion*, 1:47–53, 1960.

[146] A. B. Mikhailovskii, J. G. Lominadze, R. M. Galvão, A. P. Churikov, N. N. Erokhin, et al. Nonaxisymmetric magnetorotational instability in ideal and viscous plasmas. *Phys. Plasmas*, 15:052103, 2008.

[147] R. L. Miller, F. L. Waelbroeck, A. B. Hassam, and R. E. Waltz. Stabilization of ballooning modes with sheared toroidal rotation. *Phys. Plasmas*, 2:3676, 1995.

[148] O. Missiato and J. P. Sudano. Exact analytic solution of the stationary M.H.D. equilibrium equation of a toroidal plasma in rotation. *Rev. Bras. Fis. Journal; Conference: Latin-American workshop on plasma physics and controlled nuclear fusion research, Cambuquira, Brazil, 8 Feb 1982*, 1:264–275, 1982.

[149] E. Nardon, M. Bécoulet, G. Huysmans, and O. Czarny. Magnetohydrodynamics modelling of H-mode plasma response to external resonant magnetic perturbations. *Phys. Plasmas*, 14:092501, 2007.

[150] G. I. Ogilvie and J. E. Pringle. The non-axisymmetric instability of a cylindrical shear flow containing an azimuthal field. *Mon. Not. R. Astron. Soc.*, 279:152–164, 1996.

[151] F. Orain, M. Bécoulet, G. Huysmans, G. Dif-Pradalier, V. Grandgirard, et al. Interaction of resonant magnetic perturbations with flows in toroidal geometry. In *39th EPS Conference on Plasma Physics*, volume 4, page 065, 2012.

[152] T. Ozeki, M. Azumi, S. Tokuda, and S. Ishida. Effects of a hollow current profile on the ideal MHD stability of high beta$_p$ plasmas in a tokamak. *Nucl. Fusion*, 33:1025, 1993.

[153] P-Y Longaretti. Pressure-driven instabilities in MHD cylindrical columns: another general criterion. *Phys. Lett. A*, 320:215, 2003.

[154] S. Pamela, G. Huysmans, and S. Benkadda. Influence of poloidal equilibrium rotation in MHD simulations of edge-localized modes. *Plasma Phys. Controll. Fusion*, 52(7):075006, 2010.

[155] S. J. P. Pamela, G. T. A. Huysmans, M. N. A. Beurskens, S. Devaux, T. Eich, et al. Nonlinear MHD simulations of edge-localized-modes in JET. *Plasma Phys. Controll. Fusion*, 53(5):054014, 2011.

[156] J. C. B. Papaloizou. The dynamical stability of differentially rotating discs with constant specific angular momentum. *Mon. Not. R. Astr. Soc.*, 208:721–750, 1984.

[157] S. Poedts, W. Kerner, J. P.Goedbloed, B. Keegan, G. T. A. Huysmans, and E. Schwarz. Damping of global Alfvén waves in tokamaks due to resonant absorption. *Plasma Phys. Control. Fusion*, 34(8):1397, 1992.

[158] S. Poedts and E. Schwarz. Computation of the ideal-MHD continuous spectrum in axisymmetric plasmas. *J. Comp. Phys.*, 105:165–168, 1993.

[159] R. Qilong and Z. Cheng. Numerical study of tokamak equilibrium with toroidal flow on EAST. *Plasma Sc. Techn.*, 8:511–515, 2006.

[160] C. Z. Cheng R. Nazikian, G. J. Kramer and N. N. Gorelenkov. New interpretation of alpha-particle-driven instabilities in deuterium-tritium experiments on the tokamak fusion test reactor. *Phys. Rev. Lett.*, 91:125003, 2003.

[161] H. Ren, Z. Wu, J. Cao, C. Dong, and P. .K. Chu. Density gradient effects on the magnetorotational instability. *Plasma Phys. Control. Fusion*, 53:035012, 2011.

[162] C. Reux, G. Huysmans, J. Bucalossi, and M. Bécoulet. Non-linear simulations of disruption mitigation using massive gas injection on tore supra. In *38th EPS Conf. Plasma Phys.*, volume 3, page 117, 2011.

[163] M. N. Rosenbluth and P. H. Rutherford. Excitation of Alfvén waves by high-energy ions in a tokamak. *Phys. Rev. Lett.*, 34:1428, 1975.

[164] J. Scheffel. Linear MHD equilibria in toroidal geometry-exact and approximate solutions. *Phys. Scripta*, 30:350–365, 1984.

[165] A. R. Schellhase and R. G. Storer. Spectral analysis of resistive MHD in toroidal geometry. *J. Comp. Phys.*, 123:15–31, 1996.

[166] F. Schwander, G. Chiavassa, G. Ciraolo, Ph. Ghendrih, L. Isoardi, et al. Parallel shear flow instability in the tokamak edge. *J. Nucl. Mat.*, 415:S601–S604, 2011.

[167] S. Semenzato, R. Gruber, and H. P. Zehrfeld. Computation of symmetric ideal MHD flow equilibria. *Comp. Phys. Rep.*, 1:389–425, 1984.

[168] A. K. Sen. Stabilization of interchange type instabilities in tokamaks via inverted flow profiles. *Nucl. Fusion*, 34:459–463, 1994.

[169] V. D. Shafranov. On magnetohydrodynamic equilibrium configurations. *Soviet Phys. JETP*, 33:710–722, 1957.

[170] V. D. Shafranov and E. I. Yurchenko. Condition for flute instability of a toroidal-geometry plasma. *Sov. Phys. JETP*, 26:682–686, 1968.

[171] S. E. Sharapov, D. Testa, B. Alper, D. N. Borba, A. Fasoli, et al. MHD spectroscopy through detecting toroidal Alfvén eigenmodes and Alfvén wave cascades. *Phys. Lett. A*, 289:127, 2001.

[172] G. L. G. Sleijpen and H. A. van der Vorst. A Jacobi-Davidson iteration method for linear eigenvalue problems. *SIAM J. Matrix Anal. Appl.*, 17:401–425, 1996.

[173] L. S. Solov'ev. The theory of hydromagnetic stability of toroidal plasma configurations. *Soviet Phys. JETP*, 26(2):400–407, 1968.

[174] C. R. Sovinec, A. H. Glasser, T. A. Gianakon, D. C. Barnes, R. A. Nebel, et al. Nonlinear magnetohydrodynamics simulations using high-order finite elements. *J. Comp. Phys.*, 195:355–386, 2004.

[175] C. R. Sovinec, J. R. King, and the NIMROD Team. Analysis of a mixed semi-implicit/implicit algorithm for low-frequency two-fluid plasma modeling. *J. Comp. Phys.*, 229:5803–5819, 2010.

[176] F. Stefani, T. Gundrum, G. Gerbeth, G. Rüdiger, M. Schultz, J. Szklarski, and R. Hollerbach. Experimental evidence for magnetorotational instability in a Taylor-Couette flow under the influence of a helical magnetic field. *Phys. Rev. Lett.*, 97:184502, 2006.

[177] J. P. Sudano. Equilibrium of a toroidal plasma. *Phys. Fluids*, 17:1915–1916, 1974.

[178] H. Sugai, A. Komori, T. Sawafuzi, N. Sato, and Y. Hatta. Observation of velocity-shear flute instability in the region of bad curvature. *Phys. Fluids*, 20:90, 1977.

[179] S. Sugita, M. Yagi, S-I. Itoh, and K. Itoh. Interchange turbulence and radial transport in tokamak scrape-off layer dominated by meso scale structure. *J. Phys. Soc. Japan*, 79:044502, 2010.

[180] B. R. Suydam. Stability of a linear pinch. *Proc. second UN Int. Conf. on Peaceful Uses of Atomic Energy*, 31:157, 1958.

[181] H. Tasso and G. N. Throumoulopoulos. Axisymmetric ideal magnetohydrodynamic equilibria with incompressible flows. *Phys. Plasmas*, 5(6):2378, 1998.

[182] G. N. Throumoulopoulos and G. N. Pantis. Analytic axisymmetric magnetohydrodynamic equilibria of a plasma torus with toroidal mass flow. *Phys. Fluids B*, 1(9):1827–1833, 1989.

[183] G. N. Throumoulopoulos, G. Poulipoulis, G. Pantis, and H. Tasso. Exact magnetohydrodynamic equilibria with flow and effects on the Shafranov shift. *Phys. Lett. A*, 317:463–469, 2003.

[184] Y. Todo, K. Shinohara, M. Takechi, and M. Ishikawa. Nonlocal energetic particle mode in a JT-60U plasma. *Phys. Plasmas*, 12:012503, 2005.

[185] K. Toi, F. Watanabe, T. Tokuzawa, K. Ida, S. Morita, et al. Observation of reversed-shear Alfvén eigenmodes excited by energetic ions in a helical plasma. *Phys. Rev. Lett.*, 105:145003, 2010.

[186] K. H. Tsui. Toroidal equilibria in spherical coordinates. *Phys. Plasmas*, 15:112506, 2008.

[187] A. D. Turnbull, E. J. Strait, W. W. Heidbrink, M. S. Chu, H. H. Duong, et al. Global Alfvén modes: Theory and experiment. *Phys. Fluids B*, 5(7), 1993.

[188] M. Tuszewski, G. A. Barnes, M. H. Baron, R. E. Chrien, W. N. Hugrass, et al. The n=1 rotational instability in field-reversed configurations. *Phys. Fluids B*, 2:2541, 1990.

[189] B. van der Holst, A. J. C. Beliën, and J. P. Goedbloed. Low frequency Alfvén waves induced by toroidal flows. *Phys. Plasmas*, 7(10):4208–4222, 2000.

[190] B. van der Holst, A. J. C. Beliën, and J. P. Goedbloed. New Alfvén continuum gaps and global modes induced by toroidal flow. *Phys. Rev. Lett.*, 84(13):2865–2868, 2000.

[191] M. A. van Zeeland, W. W. Heidbrink, R. Nazikian, M. E. Austin, C. Z. Cheng, et al. Measurements, modelling and electron cyclotron heating modification of Alfvén eigenmode activity in DIII-D. *Nucl. Fusion*, 49:065003, 2009.

[192] M. A. van Zeeland, G. J. Kramer, M. E. Austin, R. L. Boivin, W. W. Heidbrink, et al. Radial structure of Alfvén eigenmodes in the DIII-D tokamak through electron-cyclotron-emission measurements. *Phys. Rev. Lett.*, 97:135001, 2006.

[193] V. Varadarajan, W. H. Choe, and G. H. Miley. Rapid calculation of tokamak equilibria with toroidal rotation via minimization of a functional. *Appl. Math. Comp.*, 43:145–163, 1991.

[194] V. D. Varadarajan and G. H. Miley. Linear instability analysis for toroidal plasma flow equilibria. *J. Comp. Phys.*, 123:415–434, 1996.

[195] E. P. Velikhov. Stability of an ideally conducting liquid flowing between cylinders rotating in a magnetic field. *Sov. Phys. JETP*, 36:995–998, 1959.

[196] T. W. Versloot, P. C. de Vries, C. Giroud, M.-D. Hua, M. N. A. Beurskens, et al. Effect of ELMs on rotation and momentum confinement in H-mode discharges in JET. *Plasma Phys. Control. Fusion*, 52:045014, 2010.

[197] R. L. Viana, R. A. Clemente, and S. R. Lopes. Spherically symmetric stationary MHD equilibria with azimuthal rotation. *Plasma Phys. Control. Fusion*, 39:415–434, 1997.

[198] F. L. Waelbroeck. Gyroscopic stabilization of the internal kink mode. *Phys. Plasmas*, 3(3):1047–1053, 1996.

[199] F. L. Waelbroeck and L. Chen. Ballooning instabilities in tokamaks with sheared toroidal flows. *Phys. Fluids B*, 3:601, 1991.

[200] F. L. Waelbroeck and R. D. Hazeltine. Stability of low-shear tokamaks. *Phys. Fluids*, 31:1217, 1988.

[201] F. Wagner, G. Becker, K. Behringer, D. Campbell, A. Eberhagen, et al. Regime of improved confinement and high beta in neutral-beam-heated divertor discharges of the ASDEX tokamak. *Phys. Rev. Lett.*, 49(19):1408–1412, 1982.

[202] C. Wahlberg. Stabilization of the quasi-interchange instability in low-shear tokamak plasmas by toroidal rotation. *Plasma Phys. Controlled Fusion*, 47:757–775, 2005.

[203] C. Wahlberg. Geodesic acoustic mode induced by toroidal rotation in tokamaks. *Phys. Rev. Lett.*, 101:115003, 2008.

[204] C. Wahlberg. Low-frequency magnetohydrodynamics and geodesic acoustic modes in toroidally rotating tokamak plasmas. *Plasma Phys. Control. Fusion*, 51:085006, 2009.

[205] C. Wahlberg. private communication, 2012.

[206] C. Wahlberg and A. Bondeson. Isothermal internal kink instability in a toroidally rotating tokamak plasma. *Phys. Lett. A*, 271:285–290, 2000.

[207] C. Wahlberg and A. Bondeson. Stabilization of the Mercier modes in a tokamak by toroidal plasma rotation. *Phys. Plasmas*, 8:3595, 2001.

[208] C. Wahlberg, I. T. Chapman, and J. P. Graves. Importance of centrifugal effects for the internal kink mode stability in toroidally rotating tokamak plasmas. *Phys. Plasmas*, 16:112512, 2009.

[209] C. Wang, J. W. S. Blokland, R. Keppens, and J. P. Goedbloed. Local analysis of MHD spectra for cylindrical plasmas with flows. *J. Plasma Phys.*, 70:651–669, 2004.

[210] S. Wang. Erratum: Zonal flows in tokamak plasmas with tororidal rotation. *Phys. Rev. Lett.*, 97:129902, 2006.

[211] S. Wang. Zonal flows in tokamak plasmas with toroidal rotation. *Phys. Rev. Lett.*, 97:085002, 2006.

[212] S. Wang and J. Yu. An exact solution of the Grad-Shafranov-Helmhotz equation with central current density reversal. *Phys. Plasmas*, 12:062501, 2005.

[213] A. A. Ware and F. A. Haas. Stability of a circular toroidal plasma under average magnetic well conditions. *Phys. Fluids*, 9:956–964, 1966.

[214] A. J. Webster and H. R. Wilson. Role of flow shear in the ballooning stability of tokamak transport barriers. *Phys. Rev. Lett.*, 92:165004, 2004.

[215] J. A. Wesson. Sawtooth oscillations. *Plasma. Phys. Control. Fusion*, 28:243, 1986.

[216] N. Winsor, J. L. Johnson, and J. M. Dawson. Geodesic acoustic waves in hydromagnetic systems. *Phys. Fluids*, 11(11):2448–2450, 1968.

[217] X. Q. Xu, B. D. Dudson, P. B. Snyder, M. V. Umansky, H. R. Wilson, and T. Casper. Nonlinear ELM simulations based on a nonideal peeling-ballooning model using the BOUT++ code. *Nucl. Fusion*, 51(10):103040, 2011.

[218] C. Yarim, U. Daybelge, and A. Nicolai. Modelling of rotating plasma states and their stability accounting for neutral beam injection and helical perturbations. Technical report, Juelich Research Center, 2003.

[219] L. E. Zakharov. The theory of hydromagnetic stability of a tokamak plasma. *Nuclear Fusion*, 18:335, 1978.

[220] H. P. Zehrfeld and B. J. Green. Stationary toroidal equilibria at finite beta. *Nucl. Fusion*, 12:569–575, 1972.

[221] L. J. Zheng, M. S. Chu, and L. Chen. Effect of toroidal rotation on the localized modes in low beta circular tokamaks. *Phys. Plasmas*, 6(4):1217, 1999.

[222] S. B. Zheng, A. J. Wootton, and E. R. Solano. Analytical tokamak equilibrium for shaped plasmas. *Phys. Plasmas*, 3(3):1176–1178, 1996.

[223] F. Zonca and L. Chen. Resonant damping of toroidicity-induced shear-Alfvén eigenmodes in tokamaks. *Phys. Rev. Lett.*, 68:592, 1992.